Table of Contents

Welcome to the Eighth Edition of CMDITR's Review of "Hooked on Photonics" Undergraduate Research

This volume features extended abstracts written by student participants in the National Science Foundation (NSF) Center on Materials and Devices for Information Technology Research (CMDITR) Summer 2011 Research Experiences for Undergraduates (REU) program: Hooked on Photonics (HoP).

The REU experience is intended to serve as a catalyst for undergraduates to enter into careers involving science, technology, engineering, and mathematics. Hooked on Photonics placed undergraduate students from across the United States in research laboratories at the University of Washington, the University of Arizona, and Georgia Institute of Technology. All of the participants worked on interdisciplinary research projects that contributed to advancements in information technology encompassing activities in chemistry, physics, optics, materials science and engineering. The program emphasized the teamwork nature of scientific research, and was supplemented by a collection of activities including ethics training and workshops in scientific communication.

HoP provides a rich learning opportunity not only for the undergraduate participants who experience hands-on research prior to committing to graduate study, but also for the student's mentors, be they faculty members, research scientists, post-doctoral fellows or graduate students. While working with REU students, mentors develop teaching and mentoring skills, and benefit from reflecting on the excitement of the cutting-edge research upon which their careers have been built.

This publication offers a forum for participants to share their research with their peers, future students, CMDITR graduate students and faculty, and others interested in the research activities of CMDITR. To learn more about Hooked on Photonics please visit *hookedonphotonics.org*.

A special thanks to all of the students for their hard work, to their mentors for their time and patience, and to the REU program coordinators Denise Bale-Mushatt, Olanda Bryant, Kimberly Sierra-Cajas and April Wilkinson for their organizational efforts. A final but important thanks goes to Ly Pham for her work on the production of this volume.

The extended abstracts included here are presented in alphabetical order by the participant's last name.

Philip Reid, CMDITR Director

The Effect of Gold Nanoparticles on the Efficiency of Organic Solar Cells

DANA DEMENT, Rice University
Shiva Shahin, Robert Norwood, University of Arizona

Introduction

As fossil fuels continue to be depleted at an ever increasing rate it is critical that suitable alternative energy sources are researched. While solar energy is perhaps our most abundant energy source, the photovoltaic technology currently available to convert sunlight into electricity is not yet economically viable. While inorganic, silicon based devices have the capability of being highly efficient, they also are expensive to manufacture. This has led to the investigation of other, potentially cheaper photovoltaic alternatives. Organic, polymer based photovoltaic devices are one such technology.

Organic solar cells have several attractive characteristics. They have lower material costs than the typical silicon based solar cell and have the potential to be easily manufactured on a large scale (e.g. roll-to-roll processes). In addition, the materials used are chemically flexible, meaning that their properties could be changed through chemical synthesis. However, there are still many weaknesses that must be overcome before organic solar cells can achieve efficiencies suitable to make them a viable commercial technology. Namely, the efficiency of organic solar cells is many times less than that of silicon based cells. Through the use of gold nanoparticles, we hope to improve the efficiency of bulk-heterojunction (BHJ), P3HT/PCBM based solar cells.

When light hits a gold nanoparticle, the oscillating electric vector component of the electromagnetic wave not only excites the gold's electrons to higher individual energy states, it also causes the nanoparticles to exhibit localized surface plasmon resonance or collective oscillations of conduction electrons on the metal's surface. Surface plasmons produce strong, broad absorption peaks. The absorption peaks occur about resonance wavelengths characteristic of the particular plasmons involved. In this case, spherical gold nanoparticles with a diameter of 50 nm with an absorption peak around 534 nm were used.

A key problem in organic solar cells is their poor charge carrier mobility and the relatively short diffusion length of excitons (electron-hole pairs). The bulk hetero-junction (BHJ) design was introduced to solve the diffusion length problem by ensuring that electron donor and acceptor molecules are mixed such that they are within a distance of each other less than the diffusion length of the exciton. However there is still the problem of light absorption versus charge carrier recombination. While an increased thickness of the active layer will increase incident light absorption in the solar cell, it will also make it less likely that charge carriers will reach the electrodes. This is because of the increased path length they must travel.

When gold nanoparticles are incorporated into organic solar cells, it is hoped that the localized plasmon resonance they exhibit will both increase the number of excitons created in the cell due to the localized electric fields and cause enhanced scattering of the light, leading to higher absorption. Further, these enhancements could allow the thickness of the BHJ active layer of the solar cell to be decreased. This would be advantageous because organic photovoltaic devices generally have poor charge carrier mobility. If the active layer could be thinned but still maintain its high absorption, the fraction of charge carriers (electrons and holes) that reach the electrodes of the solar cell before recombining should increase.

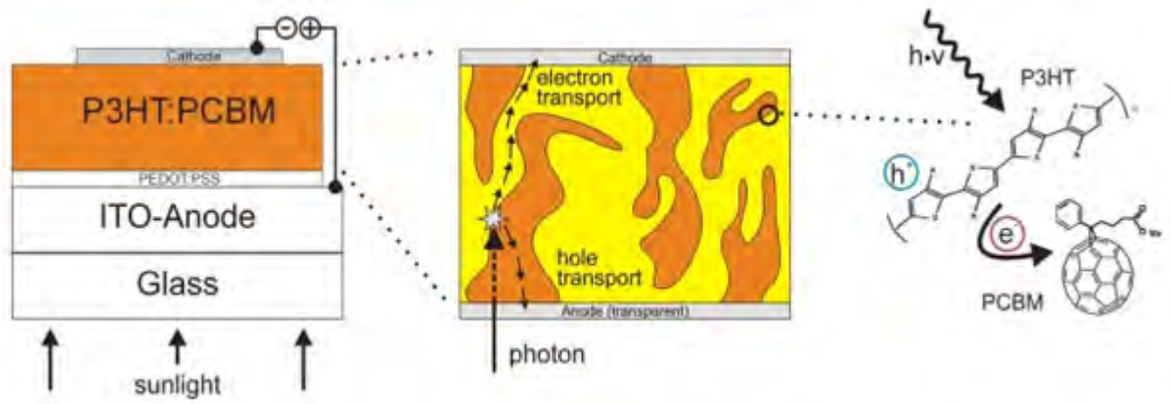

Figure 1: Layers of an BHJ Organic Solar Cell.

Experimental Methods

Before the gold nanoparticles could be properly utilized, various parameters in the synthesis of the P3HT/PCBM solar cell had to be adjusted and optimized. Firstly, a new layer was added to the solar cell.

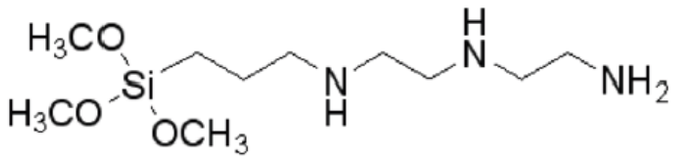

Figure 2: DETA (trimethoxysilylpropyl-diethylenetriamine).

DETA, a silane, was deposited on top of the ITO coated glass substrate in order to attach the gold nanoparticles to the ITO surface (see Figure 3).

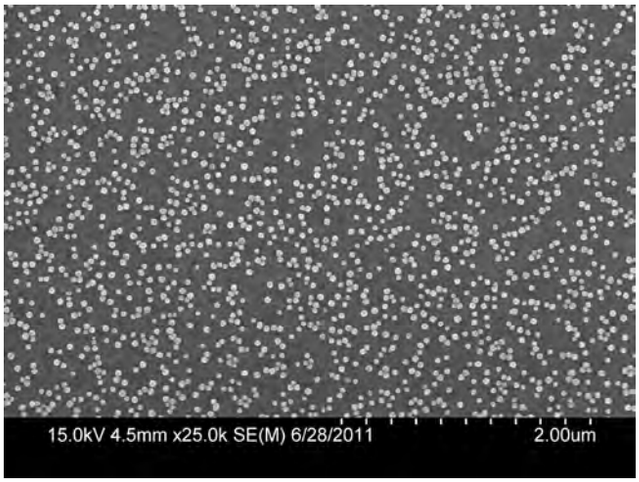

Figure 3: SEM of AuNP on ITO surface.

A stable covalent bond with the activated ITO surface is formed while the amine groups attach to the gold nanoparticles. While DETAS worked well to attach the gold, it also affected the next deposited layer, PEDOT:PSS a hole conducting, water soluble polymer. PEDOT:PSS also helps smooth the ITO surface, decreasing the density of pinholes and lessening the likelihood of shunts.

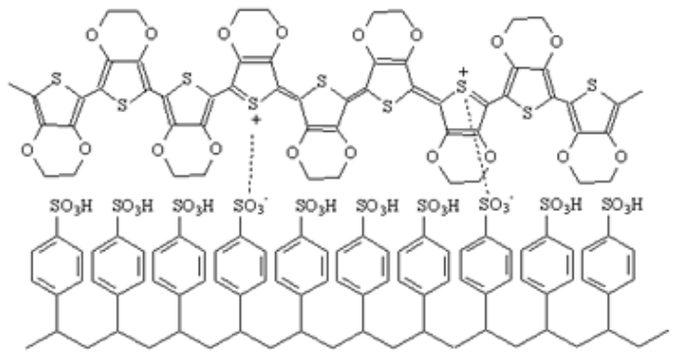

Figure 4: PEDOT:PSS.

The presence of DETAS resulted in the spin coated layer of PEDOT:PSS increasing by about 20 nm. Thus new data had to be obtained so that the spin coating parameters needed to achieve a 40 nm PEDOT layer could be utilized (Figure 5).

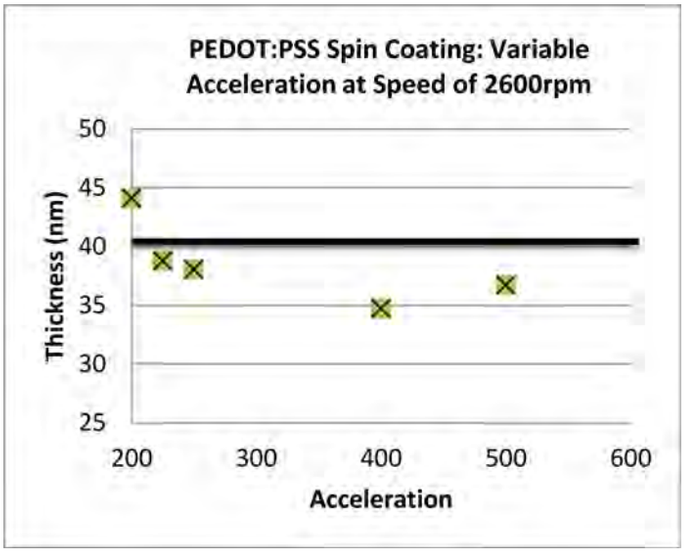

Figure 5a: Spin Curve for PEDOT:PSS layer.

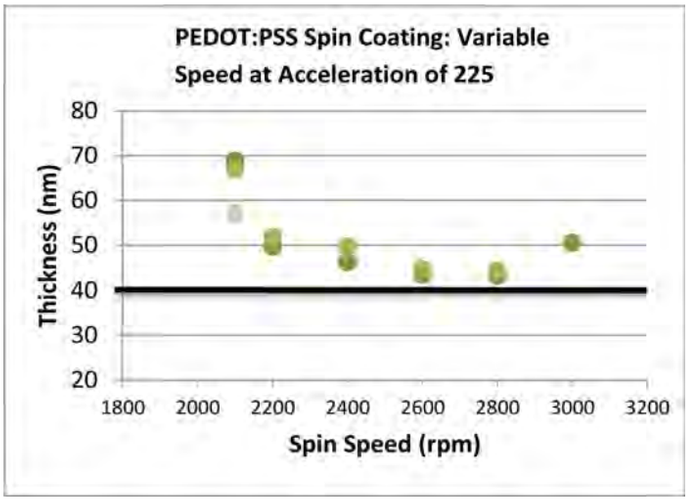

Figure 5b: Spin Curve for PEDOT:PSS layer.

The thickness of the BHJ active layer of P3HT/PCBM also had to be changed. Typically 120 nm of P3HT:PCBM is used. However, at this thickness the absorption of the polymer layer would obscure any absorption improvements caused by the presence of the gold nanoparticles. Using the modeling software Lumerical, 50 nm was determined to be the new ideal active layer thickness. Since the polymer mixture of P3HT/PCBM is also deposited via spin coating, a spin curve for this layer was also created. All thickness measurements were taken using a Dektak profiliometer.

Once the polymer layers were adjusted to accommodate the gold nanoparticles, the complete solar cells were created. LiF, and Al were deposited through thermal evaporation.

Results and Discussion

UV-Vis spectroscopy was used to compare the absorption and transmission of three variations of the solar cell.

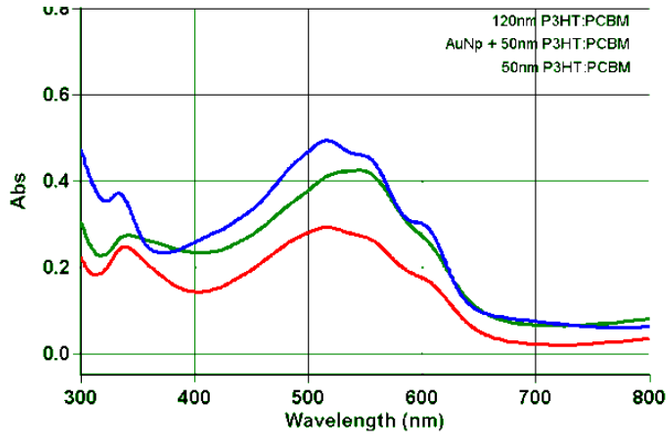

Figure 6: Solar cells Absorption Comparison

While absorption was increased with the addition of the gold nanoparticles, the overall efficiency was decreased. This could be caused by a number of different factors. This includes the fact that cells without gold nanoparticles were not activated with HCl before DETA was applied. This probably lessened the DETA deposition and, since DETA is a dielectric, this may have caused the results seen above. Also, direct contact between plasmonic materials and ITO, or between the plasmonic materials and the active layer may have led to the quenching of the generated excitions, thus causing a efficiency decrease. More samples must be created before the results may be fully understood.

Conclusion

Before any conclusion can be made, more results must be obtained. Possible reasons for our results not being what was expected are that the cells without gold nanoparticles were not activated with HCl before DETAS was applied. This probably lessened the DETAS deposition and, since DETAS is a dielectric, this may have caused the results seen above. Also, direct contact between plasmonic materials and ITO or with the active layer may have led to quenching of the generated excitions.

In future work, all samples should be activated before applying the DETAS layer. Also the deposition of gold nanoparticles with different sizes and shapes should be investigated as well the incorporation of a buffer layer on top of the ITO such as polyelectrolyte or thin NiO to prevent excition quenching.

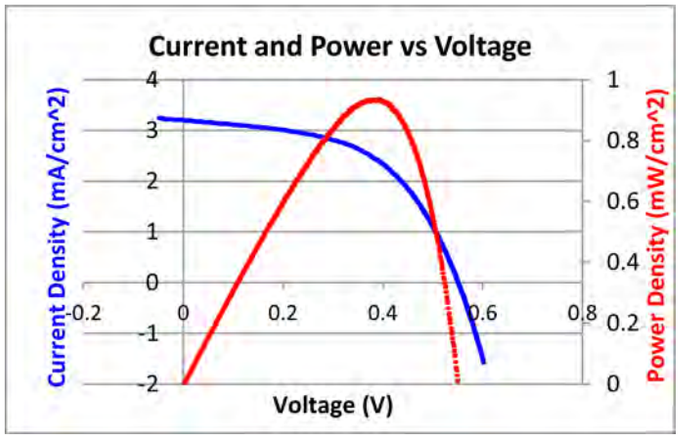

Figure 7: Solar cells with AuNPs Efficiency 1.0%.

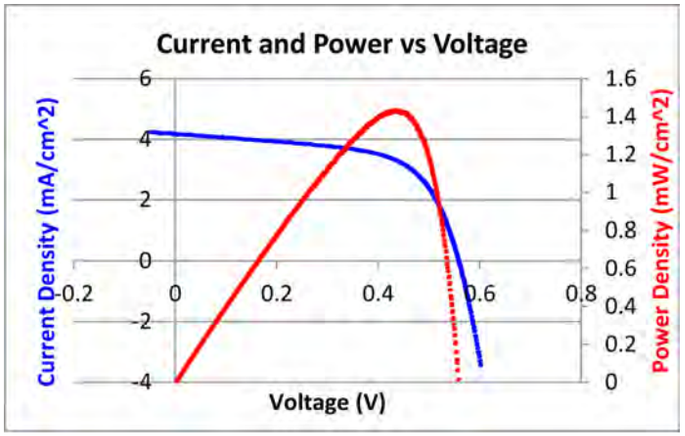

Figure 8: Solar cell without AuNP Efficiency 1.5%.

References

1. H. A. Atwater and A. Polman, “Plasmonics for improved photovoltaic devices ” Nature Materials 9, 205 (2010).
2. H. Shen, P. Bienstman, and B. Maes, “Plasmonic absorption enhancement in organic solar cells with thin active layers,” J. Appl. Phys. 106(7), 073109 (2009).

Acknowledgments

I would like to thank Shiva Shahin and Dr. Robert Norwood in addition to the other members of the organic solar cell group for all the assistance they provided during my research. In addition thanks goes to the University of Arizona and the Hooked on Photonics REU program for giving me this opportunity. Funds for this research were provided by the Center on Materials and Devices for Information Technology Research (CMDITR), the NSF Science and Technology Center No. DMR 0120967.

DANA DEMENT is currently an undergraduate at Rice University where she is working to complete her B.S. in Chemical Engineering. She plans to pursue a PhD in either Materials Science or Chemical Engineering.

Study of the n-Doping Reaction Mechanism for Organic Semiconductor Materials in Solution

WALLACE DERRICOTTE, Morehouse College
Song Guo, Stephen Barlow, Seth Marder, Georgia Institute of Technology

Introduction

Doping an organic semiconductor is essential to alter its electrical properties; extensive research has gone into the efficiency of this reaction.[1-4] N-type doping involves an electron rich dopant transferring electrons to an intrinsic semiconductor. N-doping modulates the free electron concentration of the semiconductor which will change its inherent electrical properties. The n-doping process is kinetically handicapped by the activation energy requirement of the electron transfer from the dopant to the acceptor. Conventional n-dopants are alkali metals with low ionization energies. However, the small sizes of these alkali metal cations are problematic because they diffuse readily in an organic environment, making the resulting devices unstable. Through photoemission (PES) and inverse photoemission (IPES) analysis, it has been demonstrated that using a bulkier donor such as decamethylcobaltocene (DMC) yields a more stable doped semiconductor with respect to the diffusion of ions.[1] Although this compound is more stable in solution than the previously used alkali metals, DMC is air sensitive and the device must be prepared under ultra high vacuum (UHV). An air-stable compound would be more ideal, as it provides a multitude of advantages such as low power consumption and greater device stability.[2]

In the Marder group, it has been discovered that a particular type of metal dimer complexes (M_2) are promising candidates as n-dopants.

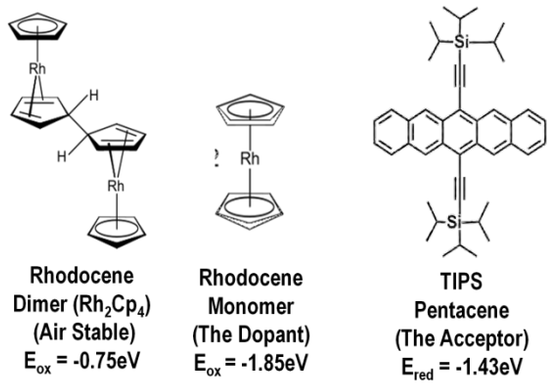

Figure 1: The structure of the compounds used, and the role they play in the reaction. The corresponding redox potential for each compound is also given.

The rhodocene dimer as shown in Figure 1 has a low oxidation potential and is used as an air stable pre-cursor to the n-doping reaction. As the reaction proceeds, the dimer may convert to the rhodocene monomer which has a lower oxidation potential and will readily dope an acceptor such as TIPS pentacene. The n-doping reaction with M_2 is normally a multi-step reaction. Having an understanding of this n-doping mechanism may facilitate future device developments. In a multi-step reaction mechanism, there will always be one step that will require the most activation energy; this step is the slowest step and determines the overall rate of the chemical reaction. In order to use these air-stable dimers in devices or materials, it is necessary to understand how they work and what mechanistic pathway they follow.

The reaction rate of a general reaction involving two reactants can be modeled by the rate law:

$$r=k[M_2]^m[A]^n$$

Where k is the rate constant, $[M_2]$ and [A] are the concentrations of each reactant, and the exponents m and n are the rate order with respect to each reactant. When one reactant is in great excess,

$$\text{when } [A] >> [M_2]$$

very little of it is consumed during the reaction and basically stays constant, and the rate is dependent only upon the concentration of the other reactant.

$$[A]^n \approx \text{ constant}$$
$$r = k' [M_2]^m$$

This yields a pseudo single reactant reaction which reveals the reaction's overall dependency on the limiting reactant.

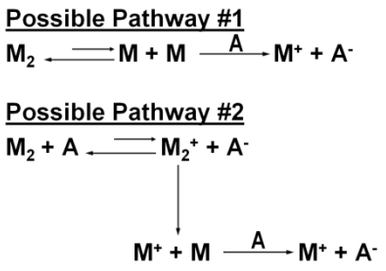

Figure 2: Two pathways that are possible for this reaction. M_2 represents any generic dimer compound while A represents any acceptor.

Two possible pathways are displayed in Figure 2, in Pathway #1, the rate limiting step of the reaction is the dissociation of the dimer into its monomer form. If the reaction follows this pathway, the rate of the reaction should show a dependence upon the concentration of the dimer alone.

In Pathway #2, the rate limiting step of the reaction is an initial electron transfer between the dimer and the acceptor. If the reaction follows this mechanism, then the rate of the reaction will be dependent upon the concentration of both the dimer and the acceptor.

$$r = k\,[M_2][A]$$

In order to model this with rhodocene and TIPS pentacene, two separate solutions were created. In one solution, the concentration of the rhodocene dimer was 1.68×10^{-3} M and the concentration of TIPS pentacene was 2.39×10^{-4} M, thus creating a 14:1 ratio of rhodocene to TIPS pentacene. In the other solution, the concentration of rhodocene was 1.52×10^{-4} M and the concentration of TIPS pentacene was 3.41×10^{-3} M, thus creating an 11:1 ratio of TIPS pentacene to rhodocene. By tracking the change in concentration over time of both solutions, the rate order with respect to each reactant can be determined. Ultraviolet-visible-Near Infrared Absorption Spectroscopy (UV-Vis-NIR) is widely used to study the reaction kinetics of compounds in solution. In an ideal case, the reactants and products will have distinct absorption peaks at well separated wavelengths. According to Beer-Lambert's Law, a compound's absorption is directly proportional to its concentration. Thus by monitoring the change in absorption over time, the kinetics can be studied.

Research Methods

Experiments are conducted using a UV-Vis-NIR spectrometer in order to observe the changes in the absorption over time. Dry and deoxygenated chlorobenzene is the solvent used in this study. Solutions are prepared in a N_2 protected glove box in order to eliminate the side reaction resulting from oxygen and water; the solutions are then transferred to a cuvette for absorption observations. The cuvette containing the solution is placed in the UV-Vis spectrometer and a light resistant sheet is placed over the UV-Vis spectrometer to block out any ambient light. By plotting the absorption over time and determining a best fit line, the k' for the reaction may be determined. Using this along with the concentrations for the reagents, the rate of the reaction can be calculated using the rate law equation. To further explore temperatures effect on the reaction rate, an Arrhenius plot is made from the experimental k values at different temperatures.

In order to determine where the product peak is located UV-vis-NIR spectra were taken of both solutions individually and a mixture of the two.

As shown in Figure 3, the TIPS pentacene anion has absorption at 738 nm; rhodocene shows a weak absorption around 340 nm, and neutral TIPS pentacene has a peak at 645 nm. Thus, the reaction can be fully monitored by looking at the TIPS pentacene neutral peak (the reactant) at 645 nm and the TIPS pentacene anion peak (the product) at 738 nm.

To monitor the reaction kinetics, the absorption spectra of the solutions were taken in the range of 600 nm – 790 nm to observe the TIPS pentacene neutral peak (the reactant) at 645 nm and the TIPS pentacene anion peak (the product) at 738 nm.

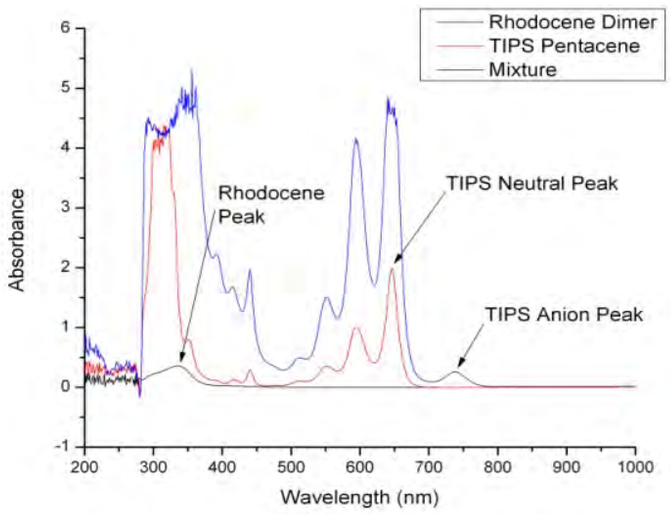

Figure 3: UV-Vis absorption data showing the neutral spectra of rhodocene and TIPS pentacene, as well as a mixture of the two in solution.

Rate of the Reaction

Figure 4 shows the spectra taken at different times for a mixture of 1.68×10^{-3} M of rhodocene and 2.39×10^{-4} M of TIPS pentacene at 55°C. As shown in Figure 4, this reaction is yielding very little product. The intensity of the TIPS pentacene anion peak is low and has little variation over time. Ideally, the rate of decay of the neutral peak and the appearance of the anion peak should be directly proportional to each other. However, since they are not, in this case, it suggests that the anion is participating in another side reaction. Upon qualitative analysis of the cuvette, an insoluble solid was forming. This solid, is likely a salt formed between the two ionic species (the monomer cation and the TIPS pentacene anion). Although the concentration of the anion peak is low, the decaying neutral peak should yield significant kinetic data from the reaction.

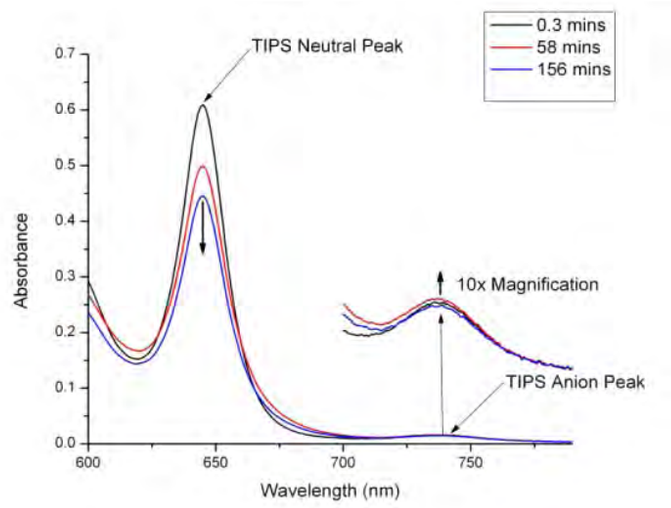

Figure 4: UV-Vis absorption Spectra of the n-doping solution containing excess rhodocene. The rhodocene concentration was 1.68×10^{-3} M and the concentration of TIPS pentacene was 2.39×10^{-4} M.

As shown in Figure 5, the decay of the TIPS pentacene neutral peak can be approximated by a first order exponential best fit line that can be expressed as:

$$Abs = 0.161e^{-t/5388} + 0.440$$

Due to the high concentration of the rhodocene in this solution, a small amount of it is consumed, which means its concentration is approximately constant throughout the reaction. Thus the reaction rate is first order in TIP Spentacene and n = 1, since the rate of the reaction is dependent upon the consumption of TIPS pentacene.

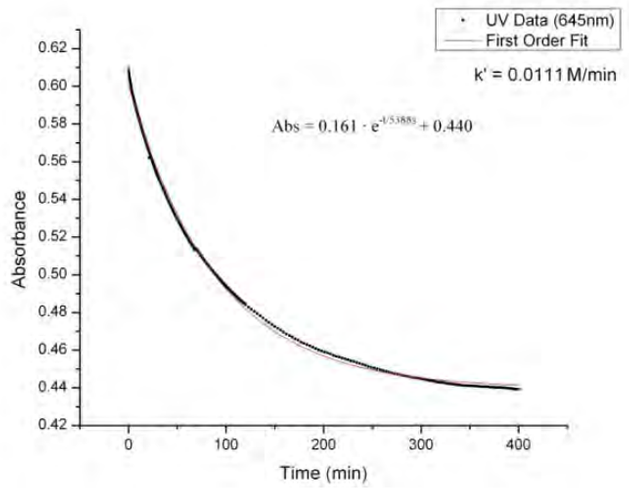

Figure 5: Change in absorption over time at the TIPS neutral peak (645 nm). UV Spectra of the n-doping solution containing excess rhodocene. The rhodocene concentration was 1.68×10^{-3} M and the concentration of TIPS pentacene was 2.39×10^{-4} M.

Figure 6 shows the spectra at different times for a mixture of 3.41×10^{-3} M of TIPS pentacene and 1.52×10^{-4} M of rhodocene at 55°C. In the case of excess TIPS, the TIPS anion peak shows slightly higher absorption and more variation over time.

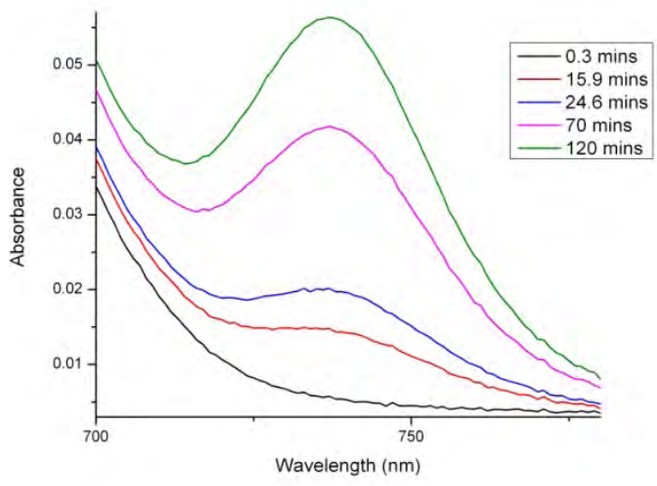

Figure 6: The TIPS pentacene anion peak from the spectra of the n-doping solution containing excess rhodocene. The concentration of rhodocene was 1.52×10^{-4} M and the concentration of TIPS pentacene was 3.41×10^{-3} M.

As shown in figure 7, the growth of the TIPS pentacene anion peak can be approximated by a first order exponential best fit line that can be expressed as:

$$Abs = 0.05003e^{t/4907.48} + 0.05562$$

Due to the high concentration of the TIPS pentacene in this solution, a small amount of it is consumed, which means its concentration is approximately constant throughout the reaction. Thus the reaction rate is first order in rhodocene and m = 1, since the rate of the reaction is dependent upon the consumption of rhodocene.

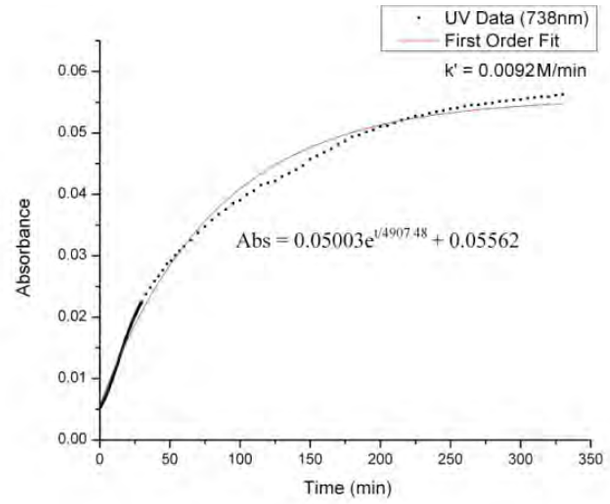

Figure 7: Change in absorption over time at the TIPS anion peak (738 nm). UV-Vis absorption spectra of the n-doping solution containing excess TIPS. The concentration of rhodocene was 1.52×10^{-4} M and the concentration of TIPS was 3.41×10^{-3} M.

Since m = 1 and n = 1, the reaction rate is dependent upon the concentration of both reactants. The overall reaction rate can be modeled by the second order rate law:

$$r = k[Rh_2Cp_4][TIPS]$$

Since the reaction is first order in TIPS pentacene and first order in rhodocene, the rate limiting step of the reaction must involve both reactants. Therefore, Pathway #2 (refer to Figure 2) is the more likely reaction pathway.

Excess Rhodocene

$$k = \frac{k'}{2[Rh_2Cp_4]}$$

$$k = \frac{8.7\cdot10^{-3}M/min}{2(1.68\cdot10^{-3}M)}$$

$$k = 2.59min^{-1}$$

Excess TIPS

$$k = \frac{k'}{[TIPS]}$$

$$k = \frac{9.2\cdot10^{-3}M/min}{3.41\cdot10^{-3}M}$$

$$k = 2.7min^{-1}$$

Figure 8: Calculation of the k values for both solutions.

Figure 8 shows the calculation of k values for both solutions. The k values for both solutions in this reaction are similar. This suggests that the reaction mechanisms are similar for the two extreme cases at 55°C.

Temperature	k value (min^{-1}) Excess Rhodocene (Anion Peak)	k value(min^{-1}) Excess Rhodocene (Neutral Peak)	k value(min^{-1}) Excess Tips (Anion Peak)
55°C	2.59	3.3	2.7
65°C	N/A	6.07	9.9
75°C	8.69	11.79	15
85°C	N/A	15.5	N/A
105°C	18.81	31.85	N/A

Table 1: All temperatures this reaction was conducted and the corresponding k values at different absorption peaks.

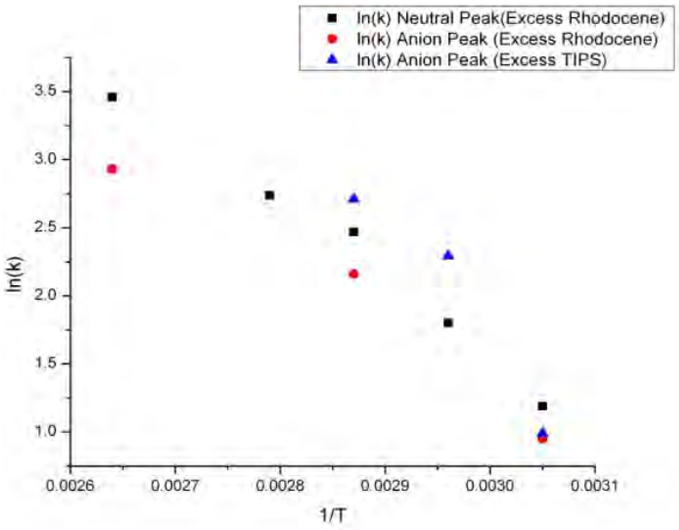

Figure 9: A scatter plot of all k values corresponding to Table 1.

As shown in Figure 9, an Arrhenius plot was attempted with the k values from the neutral peak of the solution with excess rhodocene at 55°C, 65°C, and 75°C. The main focus is on the first three temperatures because they have a near perfect linear fit. This suggests that they might follow the same mechanism. Also the data for the TIPS pentacene anion peak may be misleading since the anion could participate in other "side reactions" that won't be consistent with the decay of the neutral peak. The activation energy shown is 0.60 eV; this is close to the Gibbs free energy (ΔG) between rhodocene and TIPS pentacene which is 0.68 eV.

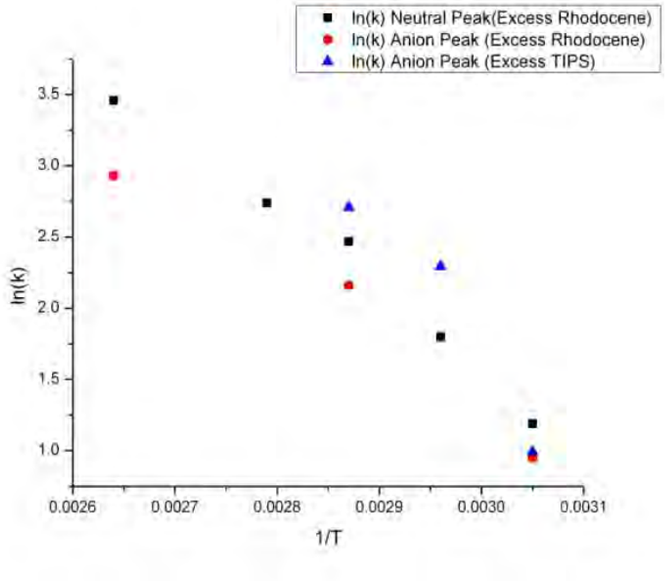

Figure 10: An Arrhenius plot of the k values at 55°C, 65°C, and 75°C.

Temperature Effects

In order to further study the kinetics of this reaction it is necessary to observe its behavior at different temperatures. By doing so, it is possible to make an Arrhenius plot based on the inverse of temperature and natural log of the k values. The Arrhenius relationship is governed by Arrhenius' equation:

$$k = Ae^{-Ea/RT}$$

Where Ea is the activation energy barrier of the reaction. So essentially, by studying the reaction at different temperatures, it is possible to determine the activation energy barrier of the reaction. The concentrations used were the same as the ones used for the study at 55°C. The same experiment was conducted at 65°C, 75°C, 85°C, and 105°C respectively.

Based on the data displayed in Table 1 and Figure 8, there is very little consistency in the k values at different temperatures. Although the k values were practically the same at 55°C, that same relationship is not seen at higher temperatures. So although Pathway #2 is a likely mechanism for this reaction, there is no doubt that the mechanism is more complicated at elevated temperatures. However plotting an Arrhenius plot of the most consistent fit could give more information about the reaction.

Conclusion

These experiments answer a few key questions about the n-doping mechanism. When the dimer is in excess, the reaction is first order in the acceptor. When the acceptor is in excess, the reaction is first order in the dimer. This is important to know going forward, so that predictions can be made on how the concentration will affect the rate of the reaction. Also, these experiments suggest that there are, at least, two competing mechanistic pathways the reaction can follow. Two likely mechanisms were discussed earlier; it is possible that they are representative of the competing mechanisms shown in the data. Going forward it may be possible to run the reaction under conditions that will allow one mechanism to dominate. Being able to isolate one mechanism is favorable for further kinetic study.

Possible Future Project

It has been proven through UV-Vis spectroscopy that TIPS pentacene has a definitive absorption at 646 nm. Since the dopant has no absorption between 600 nm – 700 nm, it should be possible to selectively excite the acceptor without disturbing the dopant. The selective excitation of the acceptor can possibly increase the reaction rate.

References

1. C. Chan, W. Zhao, S. Barlow, S. Marder, A. Kahn, Organic Electronics 9 (2008) 575.
2. J. Hak Oh, P. Wei, Z. Bao, Applied Physics Letters 97 (2010) 24.
3. W. Zhao, Y. Qi, T. Sajoto, S. Barlow, S. Marder, A. Kahn, Applied Physics Letters 97 (2010) 12.
4. Y. Qi, T. Sajoto, M. Kroger, A. Kandabarow, W. Park, S. Barlow, E. Kim, L. Wielunski, L.C. Feldman, R. A. Bartynski, J. Bredas, S. Marder, A. Kahn, Chemistry of Materials 22 (2009) 524.

WALLACE DERRICOTTE is currently a Junior chemistry major/ mathematics minor at Morehouse College. Upon graduation he plans to pursue a Ph.D. in chemical physics.

Application of Tuned Range-Separated Functionals to Low Optical-Gap Polymers

CURTIS FRANCIS DOIRON, University of Oklahoma
Laxman Pandey, John Sears, Jean-Luc Brédas, Georgia Institute of Technology

Bulk heterojunction (BHJ) organic photovoltaic (OPV) cells based on materials with low optical gaps are desirable for renewable energy production. One way of obtaining a low-optical gap material is through the use of a donor-acceptor (DA) polymer (which plays the role of the donor of in the heterojunction while PCBM is typically used as the acceptor). By combining electron-poor acceptor moieties with electron-rich donor moieties, the optical gap of the polymer will be lowered. In the DA polymer, electronic transitions occur primarily from the HOMO (mostly donor units) to the LUMO (mostly acceptor units) and thus have significant charge-transfer (CT) characteristics. Due to the short-range nature of modern Density Functional Theory (DFT) functionals there are severe deficiencies when describing molecules with significant CT character. In this work we have investigated the ability of optically-tuned long-range-corrected (ω) functionals to describe the CT characteristics of the low-lying excited states in seven low optical-gap donor-acceptor (DA) copolymers. The tuned long-range-corrected functionals ωb97 and BNL have been compared to results from the commonly used B3LYP functional as well as to untuned long-range-corrected functionals for their ability to describe experimental absorption spectra.

Introduction and Objectives

In the year 2050 the population is expected to reach 10 billion people. To maintain current standards of living, energy production will need to be increased from 13 TW to 23 TW.[4] To provide this power renewable energy sources are preferred because of the environmental damage and dwindling supply of traditional fossil fuels. Photovoltaics have been proposed as a renewable method for power generation, but implementation is hindered by high cost and inadequate efficiencies. Organic photovoltaics (OPV) have the potential to provide power from low-cost, flexible, and large-scale solar panels. The potential benefits of OPVs have encouraged the development of new materials that take advantage of the optical and electronic properties of organic molecules. In order to produce desirable devices several properties are needed. First, it is desirable for the optical band gap to be in the near-infrared (~1.2 eV) to allow for absorption of a broad range of the solar spectrum. Second, high absorption coefficients are desirable which can be obtained by using polymers with large transition-dipole moments. BHJ OPVs will usually consist of a hole-transport material (HTM) that has a small ionization potential and is easily ionized and an electron-transport material (ETM) with a large electron affinity. To obtain low optical gaps, a donor-acceptor (DA) polymer is sometimes used as the HTM, examples are shown in Figure 1. By combining electron-poor acceptor moieties with electron-rich donor moieties the optical gap of the polymer will be reduced lowering the energy needed to create the photoexcited state (exciton), which will be separated at the ETM-HTM interface to generate current.

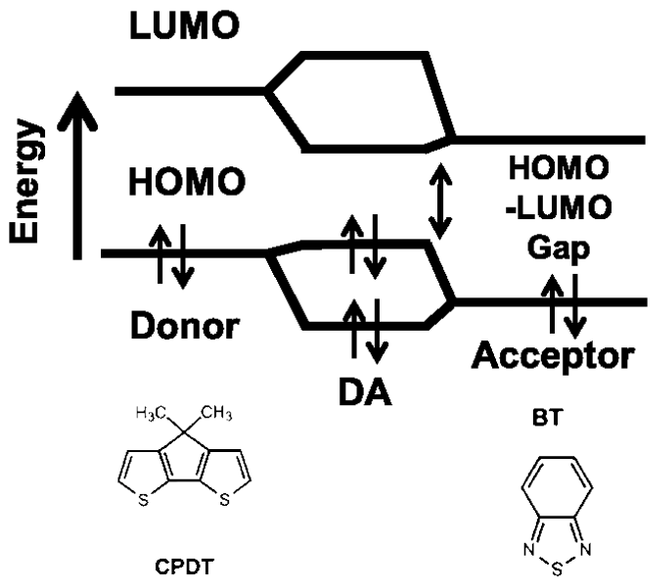

Figure 1: Donors and acceptors studied.

Using quantum-chemical methods, theoretical estimates for DA-copolymer properties, such as structures, dipole moments, and energy levels can be found. These properties are useful for the design of new DA-copolymers. The most popular QM methods today are based upon DFT. The unknown part of the functional comes from the term for the exchange-correlation energy, $E_{XC}(\rho)$. Because this is unknown approximations must be used, with the simplest being the local density approximation (LDA) where the exchange-correlation energy is dependent on the local electron density corresponding to a homogeneous electron gas. This approximation, unlike the Hartree-Fock method, fails to find the exact exchange energy. Hybrid functionals were developed that partly contain the exchange interaction from HF theory. The most commonly used functional, B3LYP, is of this class of functionals and like all hybrid functionals has a constant percentage of HF exchange. B3LYP performs well for many chemical properties, although difficulties exist for CT excitations. To correct for this long-range-corrected (LRC) functionals were developed. Long range-corrected-functionals split the exchange-correlation functional into two parts view a Coulomb operator. This is done by creating a partition based on the error

function (shown in Equation 1). For LRC functionals the parameter ω is the same for all systems. Because of this, the exchange-correlation interactions are poorly modeled for some systems. To correct for this error, tunable long-range-corrected (ω) functionals were developed to allow for the "strength" of long-range and short-range components to be tuned by varying ω for a specific system. The first term in Equation 1 controls the strength of HF while the second is for the strength of the short-range component. The tuning is performed by finding the ω value that allows the system to best satisfy Koopman's theorem in DFT form. This means that the ionization potentials and electron affinities are forced to be consistent. Time dependent DFT (TDDFT) can be used to find the energies of excited states, which can be used to simulate optical spectra.

$$\frac{1}{r_{12}} = \frac{erf(\omega r)}{r_{12}} + \frac{1 - erf(\omega r)}{r_{12}}$$

Long-Range Short-Range

Equation 1: Long-range and short-range separation with the error function.

Because the transitions are from the HOMO (donor moieties) to the LUMO (acceptor moieties) there is a large amount of charge-transfer (CT) characteristics (Figure 2). Because of this, DFT is a poor method for modeling DA copolymers. This project investigated the ability of tuned long-range-corrected (ω) functionals to describe the CT characteristics of the low-lying excited states in P3HT and six low optical-gap DA copolymers. The DA copolymers studied were PBDTTPD, PBDTTT-C, PBDTTT-CF, PBDTTT-E, PCDTBT, and PCPDTBT. The molecular structures of the donor and acceptor units are shown in Figure 3 and DA-copolymers in Figure 4.

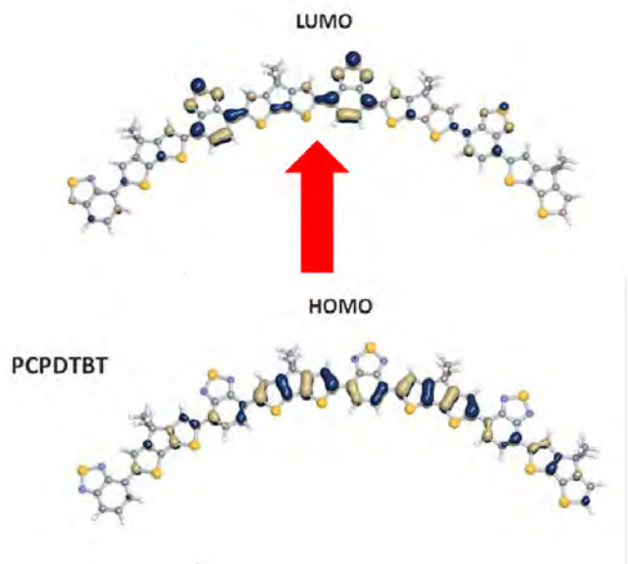

Figure 2: HOMO and LUMO energy levels with CT characteristics in PCPDTBT.[3]

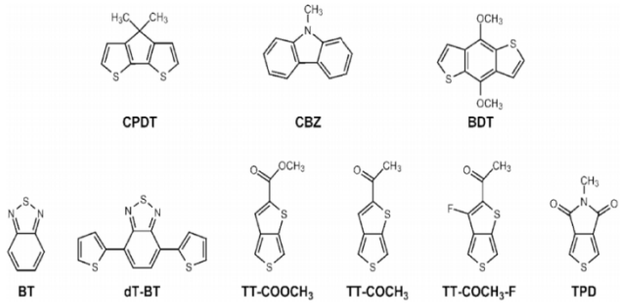

Figure 3: Donors and acceptors studied.

Methods

For this project a quantum chemistry package, QChem, was used to model P3HT and six DA copolymers shown in Figure 3. The first process is to use energy minimization to find the optimized structures for monomers, dimers, trimers, and tetramers. To optimize the structures, QChem uses a variety of algorithms. These algorithms move the atoms in the molecule in such a way as to iteratively decrease the energy of the molecule. The goal is to find the molecular geometry with the lowest energy, which represents the most energetically favorable geometry. The functional used for optimizing the molecular structures was B3LYP, which has been found to provide accurate structures for organic systems. The optimized structures were used for all single-point and TDDFT calculations.

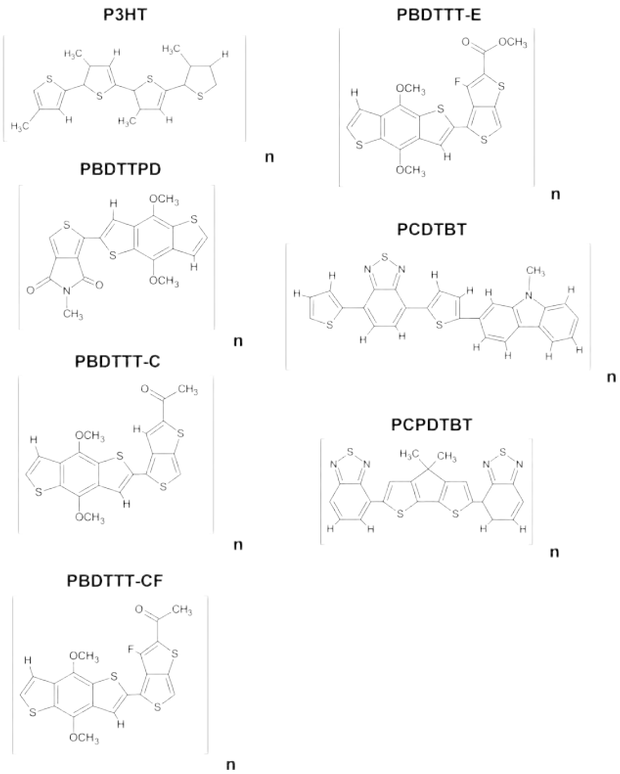

Figure 4: Monomers. Note: The P3HT monomer is an oligomer with three thiophene rings. This was done so as to keep oligomers of different systems about the same length. The functional groups of P3HT were removed because of the reduction in computational complexity with no effect on the electronic structure.

$$|IP(N) + \alpha(N)| + |IP(N+1) + \alpha(N+1)|$$

Equation 2: "Error" from Koopman's theorem.

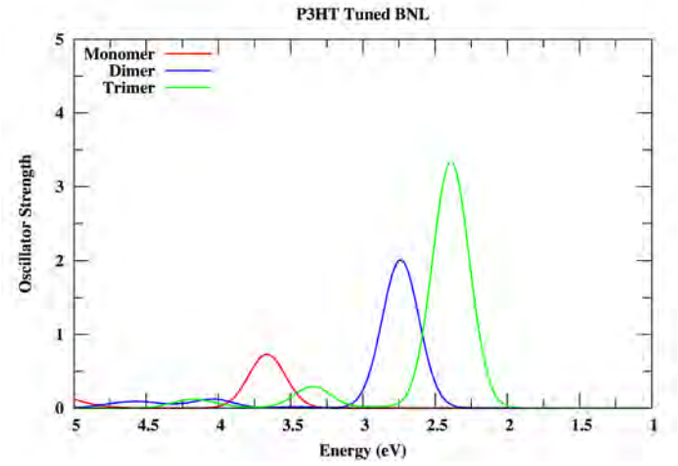

Figure 5: Effect of number of repeat units on P3HT using tuned BNL.

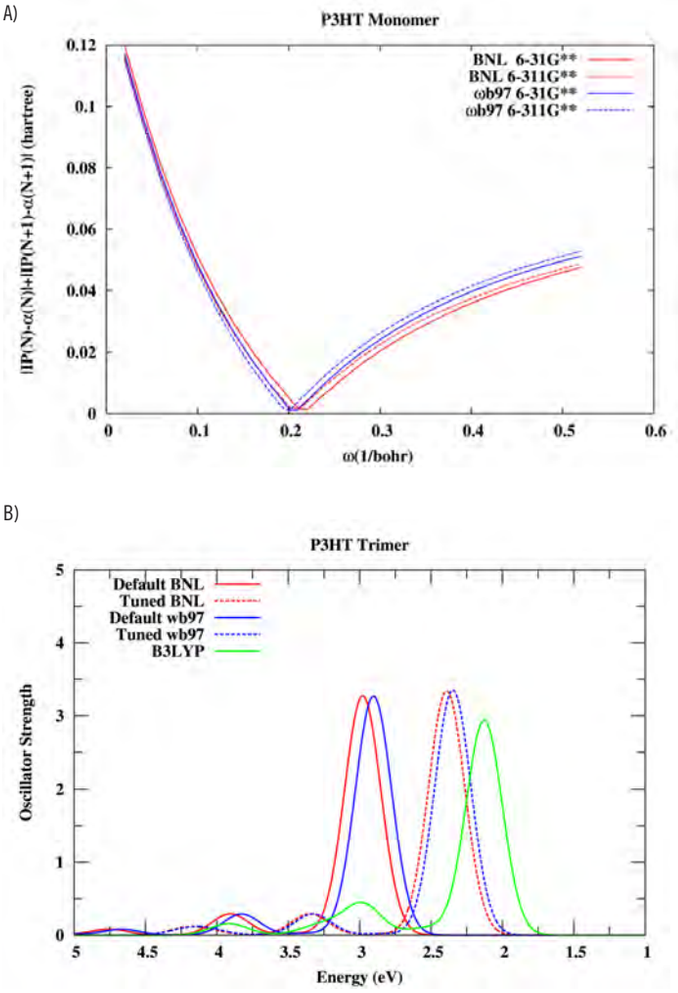

Figure 6: A) Error from Koopman's Theorem on P3HT monomer B) Simulated absorption spectra comparison of all functionals studied on P3HT trimer.

Once optimized, single-point energies were calculated using two range-tuned functionals, ωb97 and BNL. The objective was to find the ω value that best satisfies Koopman's theorem. A rigorous criterion (Equation 2) for judging the best ω was used to find the tuned ω.

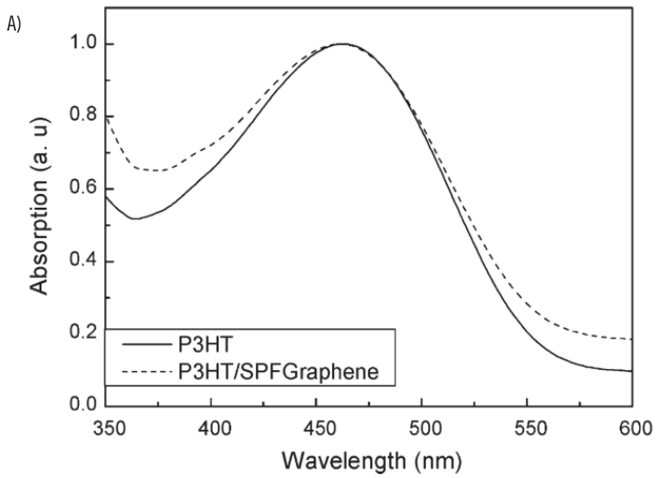

B)

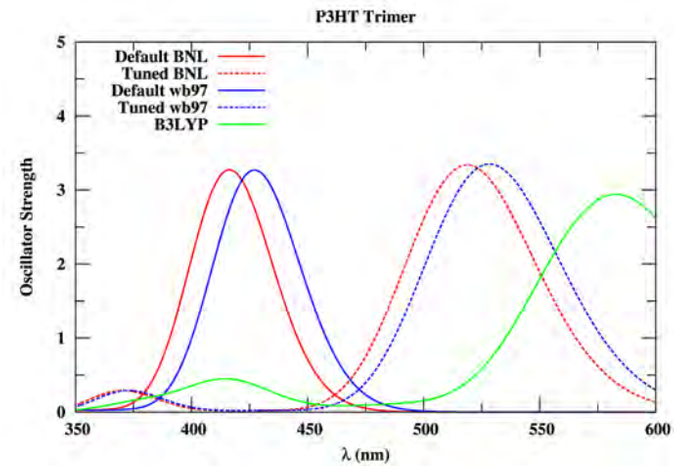

Figure 7: A) Experimental P3HT solution absorption spectra[5] B) Simulated spectra from TDDFT.

In Equation 2 IP(N) is the ionization potential of the Nth energy state and α(N) is the HOMO energy. By minimizing Equation 2, the electron affinity and ionization potentials are forced to be consistent, therefore satisfying Koopman's theorem. Once the optimized ω value was found TDDFT calculations were performed using B3LYP, BNL, and ωb97 functionals. From the TDDFT the excited energy levels and oscillator strengths were found. From this information, simulated absorption spectra were plotted.

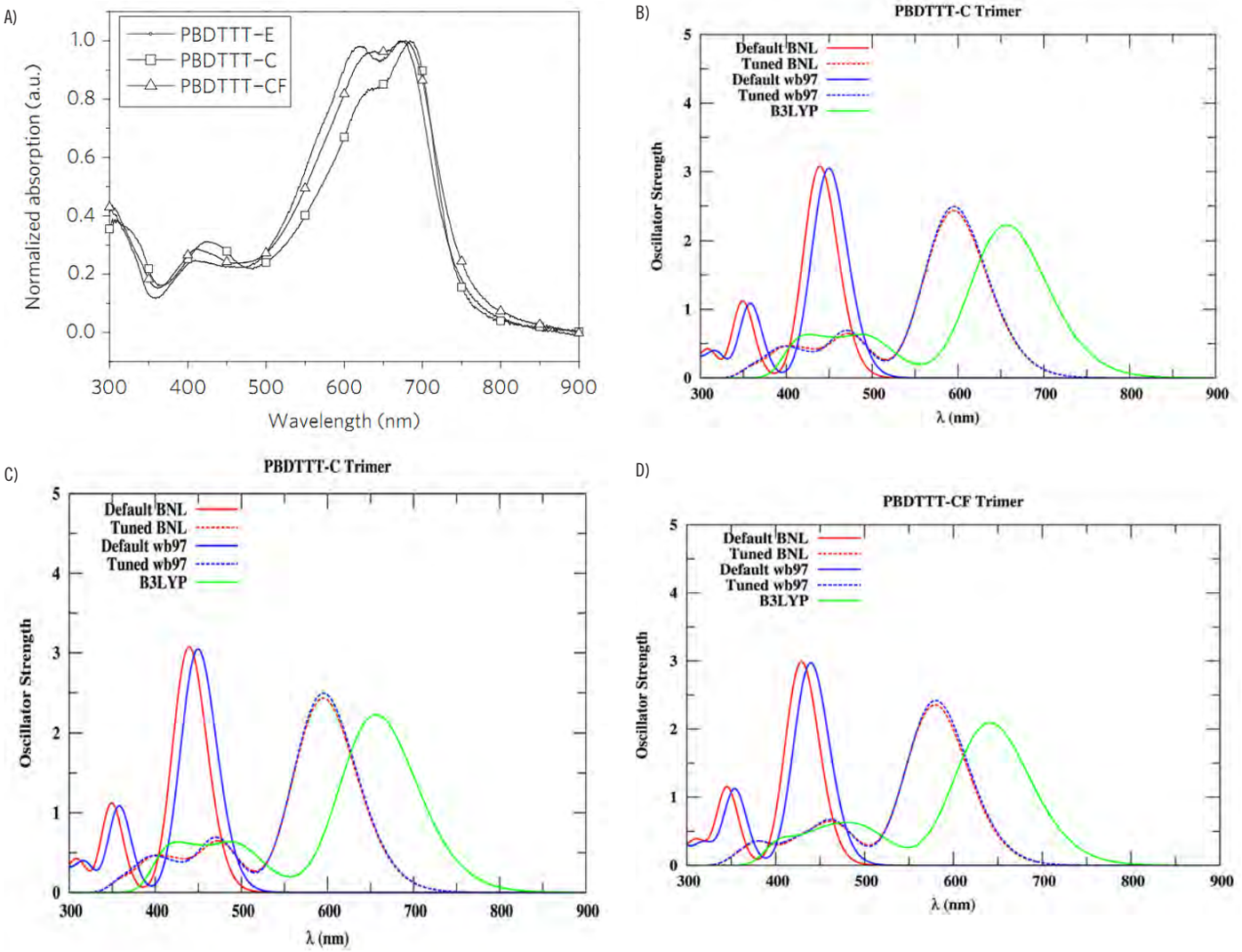

Figure 8: A) Experimental PBDTTT-E, PBDTTT-C, and PBDTTT-CF solution absorption spectra.[6] B-D) Simulated spectra from TDDFT.

Results and Discussion

The optimization of each oligomer structure was performed separately using the B3LYP functional and a 6-31G** basis set.

Figure 6A shows the error from Koopman's theorem (Eq. 2) as a function of ω. From these types of plots the tuned omega values were found and used for TDDFT calculations to find the energy levels of the first 15 excited states. The tuned ω occurs when the curve is at a minimum and Koopman's theorem is best satisfied. Simulated spectra were created by using the energy levels found using TDDFT and generating Gaussian curves with a width of 0.3 eV. The simulated spectra from the P3HT trimer are shown in Figure 7. From Figure 7A, it can be seen that the tuned functionals provide energy levels between the untuned functionals and B3LYP. This is to be expected, since by tuning the functionals the CT characteristics can be described. From the computed absorption spectrum using a 6-31G** and 6-311G** basis, we found that both basis sets provide very similar results. Because of this and the extra computational requirements of the 6-311G** basis set for the dimers, trimers, and tetramers only the 6-31G** basis set was used.

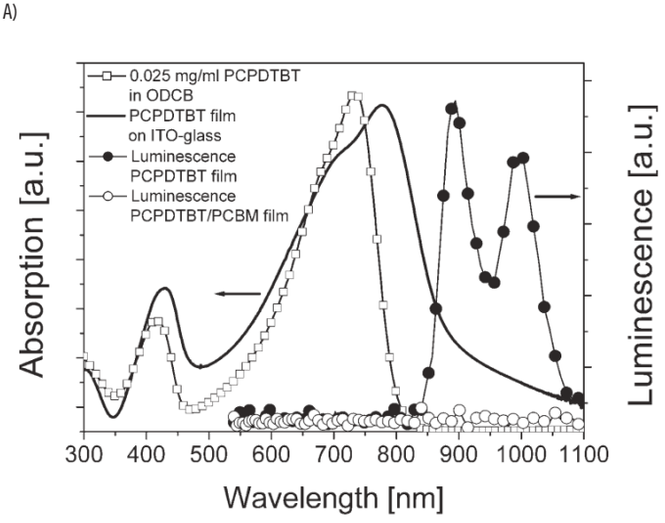

Figure 9: A) Experimental PCPDTBT solution absorption spectra.[7]

B)

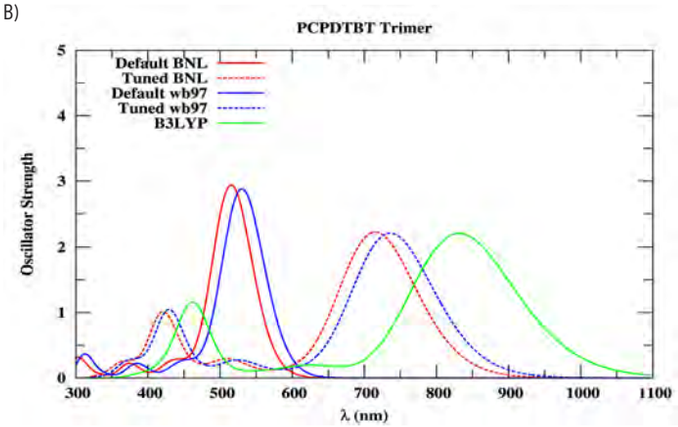

Figure 9: B) Simulated spectra from TDDFT.

When the systems size was increased the tuned omega values shifted downwards, which is to be expected as the number of repeat units is increased. The energy levels of the first excited state lowered and the absorption spectra (Figure 5) energy levels and qualitative feature better match the experimental results, which makes intuitive sense because the molecules are closer to the polymer limit.

Comparisons with experimental solution spectra and simulated spectra from TDDFT using tuned and untuned functionals are shown in Figures 7-10. From these it can be seen that tuning does a good job of increasing semi-quantitative accuracy by shifting the energy levels lower. These shifts were around 0.5 eV. With tuning, the calculated energies were still larger than those found using B3LYP. It should be noted that the experimental absorption spectra were measured in solution, while the TDDFT calculations modeled gas-phase absorption spectra. Qualitative aspects were also improved, for example the absorption peak for the third excited state for PCPDTBT increases.

A)

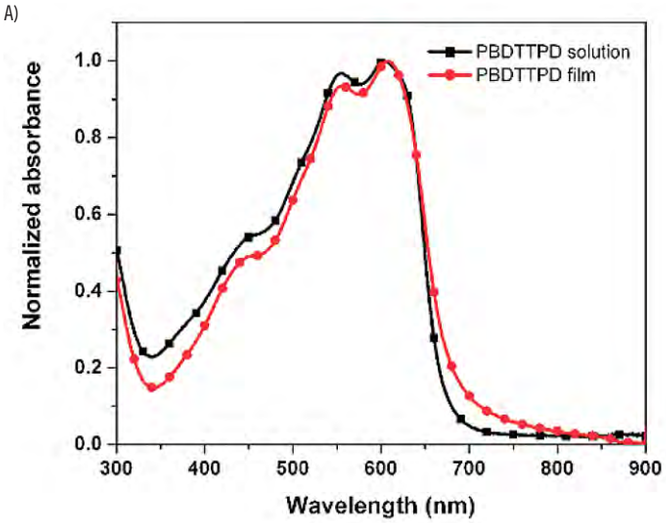

B)

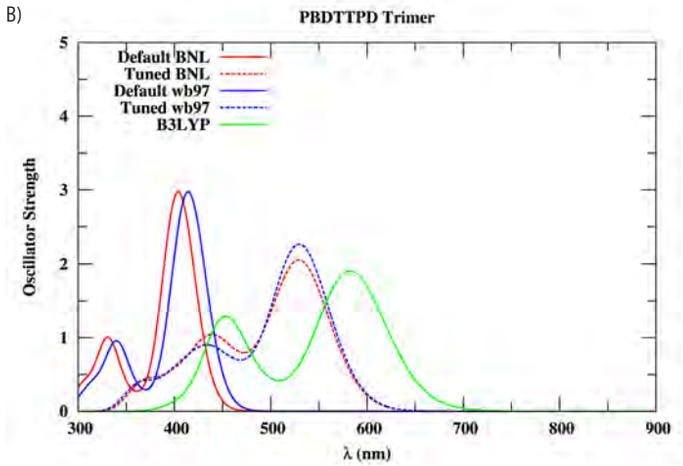

Figure 10: A) Experimental PBDTTPD solution absorption spectra.[8]
B) Simulated spectra from TDDFT

Conclusions

Based on the results we found that tuning long-range-corrected functionals increases qualitative and semi-quantitative accuracy of simulated absorption spectra found using TDDFT. The agreement between ωb97 and BNL after tuning may imply that the difference between results using untuned ωb97 and BNL functionals may come from range effects, which become consistent after tuning. In the future TDDFT will be performed in solution environment. This will more accurately model solution spectra measurements. Pentamers of all the systems will be studied to investigate how close to the polymer limit our calculations were.

References

1. Roi Baer, Ester Livshits, and Ulrike Salzner. Tuned range-separated hybrids in density functional theory. Annual Review of Physical Chemistry, 61:85–109, March 2010.
2. A Karolewski, T Stein, R Baer, Kummel, and S. Communication: Tailoring the optical gap in light-harvesting molecules. The Journal of Chemical Physics, 134(15):151101, April 2011.
3. Chad Risko, Michael D. McGehee, and Jean-Luc Brédas. A quantum-chemical perspective into low optical-gap polymers for highly-efficient organic solar cells. Chemical Science, (ii), 2011.
4. Kehan Yu and Junhong Chen. Enhancing Solar Cell Efficiencies through 1-D Nanostructures. Nanoscale Research Letters, 4(1):1– 10, November 2008.
5. Q. Liu, Z. Liu, X. Zhang, L. Yang, N. Zhang, G. Pan, S. Yin, Y. Chen, and J. Wei, "Polymer Photovoltaic Cells Based on Solution-Processable Graphene and P3HT," Advanced Functional Materials, vol. 19, Mar. 2009, pp. 894-904.
6. H.-yu Chen, J. Hou, S. Zhang, Y. Liang, G. Yang, and Y. Yang, "Polymer solar cells with enhanced open-circuit voltage and efficiency," East, 3, 2009, pp. 649-653.
7. D. Mühlbacher, M. Scharber, M. Morana, Z. Zhu, D. Waller, R. Gaudiana, and C. Brabec, "High Photovoltaic Performance of a Low-Bandgap Polymer," Advanced Materials, 18, Nov. 2006, pp. 2884-2889.
8. Y. Zhang, S.K. Hau, H.-L. Yip, Y. Sun, O. Acton, and A.K.-Y. Jen, "Efficient Polymer Solar Cells Based on the Copolymers of Benzodithiophene and Thienopyrroledione," Chemistry of Materials, 22, May. 2010, pp. 2696-2698.

Acknowledgments

I would like to acknowledge the Center on Materials and Devices for Information Technology Research (CMDITR), the NSF Science and Technology Center No. DMR 0120967. I would also like to thank the Brédas research group, Georgia Institute of Technology, Olanda Bryant, Denisha Thomas, and Dr. Cam Tyson.

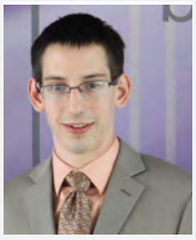

CURTIS DOIRON is a senior at the University of Oklahoma studying engineering physics. After graduating, Curtis plans to pursue a doctorate in applied physics or electrical engineering. His goal is to start up a nanofabrication plant.

Molecular Engineering of Heteroaryl-pyrylium Based Cyanines for All-Optical Switching

TIANZHU GE, University of Washington
Joshua A. Davies, Sei Hum Jang, Alex Jen, University of Washington

Introduction

In the past decade, there has been an increasing interest in the use of organic conducting materials, which are pi-conjugated materials, for applications such as optical communications, light emission, optoelectronics. Compared with inorganic materials, organic conducting materials can be easily controlled by modifying the molecular structures and manufactured in large scale at a lower cost.[1]

In optical communications, information travels optically with an input signal beam typically between 1.3 and 1.5 μm with minimized optical losses.[1] When compared with electronics, optical communication has many advantages including the ability to transmit a greater amount of information, over a longer distance, at a higher speed, and also less information loss. In all-optical switching an input control beam signal is used to change the refractive index of optical conducting material, which modulates the speed of the propagating input signal, as shown in Figure 1. All-optical switching is better than electro-optical switching in terms of speed, power and throughput,[2] which dramatically increases the efficiency of a variety of applications.

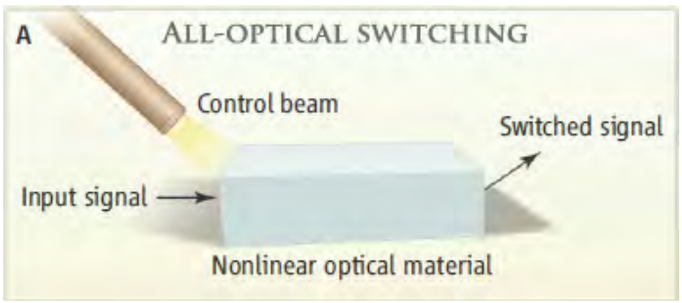

Figure 1: All-optical switching.[1]

For high-performance all-optical switching technology to become viable, the organic conducting materials should have properties such as strong optical nonlinearities, minimized linear and non-linear absorption loss, and translating molecular figures of merit (γ) to bulk properties. Researches have shown that symmetric, cyanine-like molecules (pi-conjugated), as shown in Figure 2, should not only possess the largest magnitude of γ for a given length of conjugation but also possess very sharp electronic transitions, which minimizes potential optical loss. Also, researches have shown that controlling aggregation and improving processability are keys to effectively translate into bulk properties susceptibility. Post-end-group modification is expected to be a very good way to accomplish this goal. Favorable J-type aggregation is shown in Figure 3.

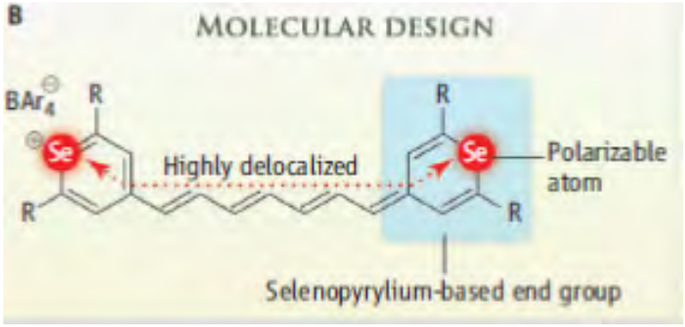

Figure 2: Selenopyrylium end group cyanine.[1]

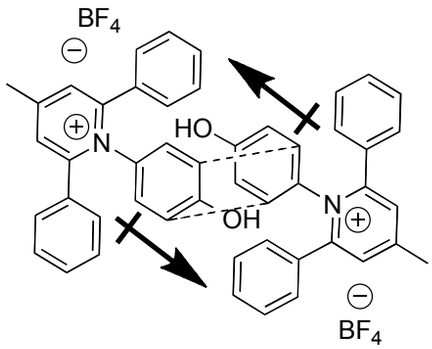

Figure 3: Favorable J-type aggregation.

The aim of this research is to control aggregation and improving processability of cyanine-like molecules through post-end-group modification in order to reach a large magnitude of γ and minimize optical loss. The first target end group was thiopyrylium and its derivatives, which are shown to be excellent end groups (Figure 4). In this work, a versatile synthetic route has been developed so that a wide variety of heteroaryl-pyrylium end groups can be made efficiently. This new synthetic route has a reduced number of steps, gives higher overall yields, and can be used to control the overall shape of the cyanine to promote favorable molecular J-type aggregation.

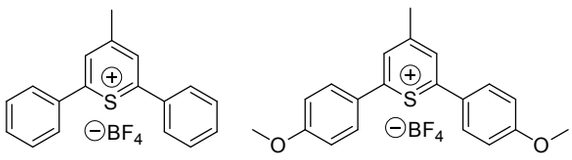

Figure 4: Thiopyrylium and its methoxy derivative.

Experimental Methods

The newly developed synthetic route for synthesizing thiopyrylium is shown in Figure 5. The thiopyrylium based cyanine is then made as shown in Figure 7. The H-NMR spectra were measured on a Bruker AVance series instrument 300 MHz. Mass spectra were collected on a Bruker Esquire LC-Ion Trap. UV-Vis spectroscopy was measured on a Perkin Elmer UV-Vis-NIR.

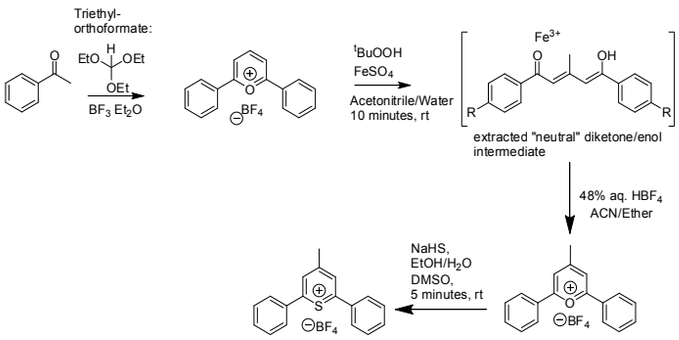

Figure 5: Three steps synthetic route for thiopyrylium end group.

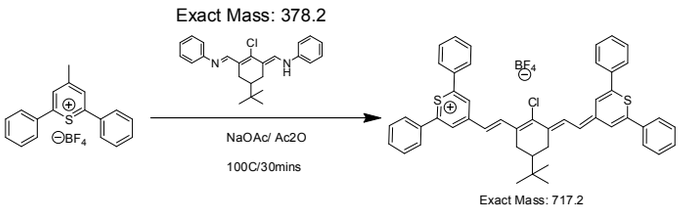

Figure 6: Synthesis of Thiopyrylium based cyanine.

1. Three-step synthetic route

Preparation of 2, 6-diphenylpyrylium tetrafluoroborate

2, 6-diphenylpyrylium tetrafluoroborate was prepared using an established procedure.

Preparation of 4-methyl-2, 6-diphenylpyrylium tetrafluoroborate

3.2 g of 2, 6-diphenylpyrylium salt (0.01 mole) was dissolved in a mixture of 20 ml of acetonitrile and 2 ml of 48% aq. HBF_4. 0.035 mol of both t-BuOOH and $FeSO_4$ (aq. solutions) were added drop wise into the reaction mixture at the same time. The reaction is allowed to stir for 10 minutes at room temperature before quenching with 10% aq. HBF_4. The precipitated pyrylium salt was collected by vacuum filtration in 99% yield as brown powder and the crude material was used without further purification. (ES) (+) m/z 247 [M^+].

Preparation of 4-methyl-2, 6-diphenylthiopyrylium tetrafluoroborate

0.5 g of 4-methyl-2, 6-diphenylpyrylium (0.0015 mole) was dissolved in 15 ml DMSO. A 3.75 ml of a solution of NaHS in EtOH and H_2O, which is prepared according to the literature,[4] was added drop wise into the reaction mixture. The reaction was run for 10 mins at room temperature. 48% aq. HBF_4 was added and the precipitated crude and complex product mixture was collected by vacuum filtration. Upon addition of water, a second precipitation yielded pure thiopyrylium and was collected separately by vacuum filtration at a 52% yield as greenish yellow powder. (ES) (+) m/z 263 [M^+].

2. Preparation of thiopyrylium based cyanine

0.0758 g of the diimine bridge compound (0.0002 mol), 0.21 g of thiopyrylium (0.0006 mol), and 0.0328 g of sodium acetate (0.0004 mol) were dissolved in 1ml of acetic anhydride and the mixture was heated at 100ºC for 30 min. After chilling, a mixture of hexane and ethanol was added into the reaction mixture and precipitated crude product was collected by vacuum filtration. The thiopyrylium tetrafluoroborate based cyanine (KG1003) was purified by column with 15% Acetone/DCM to obtain the thiopyrylium based cyanine salt. During a scale-up, the thiopyrylium based cyanine was subject to conditions of ion exchange by dissolving the crude product in DCM and adding 2 eq. of sodium tetraphenylborate. A column was the run with DCM to separate the thiopyrylium tetraphenylborate based cyanine (KG1014).

Results and Discussion

Thiopyrylium salts are reported to be successfully synthesized by a six-step synthetic route from corresponding pyrylium salts.[5] In comparison, the synthetic route that is described in this paper has fewer steps thus they are more convenient. In the three-step reaction, the thiopyrylium salt was obtained at a 30% overall yield as a greenish yellow powder. Mass-spectroscopy is used to indicate the existence of products and any possible impurities. As shown in Figure 8, for pyrylium salt, and Figure 9, for thiopyrylium salt, there are several impurities presented in the powder that were collected.

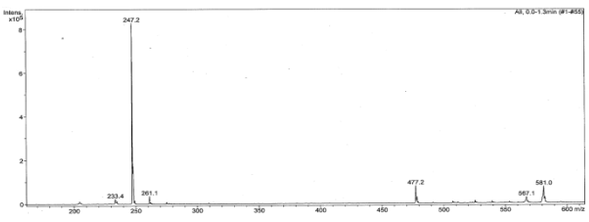

Figure 7: Mass-spectroscopy spectrum for 4-methyl-2, 6-diphenylpyrylium salt.

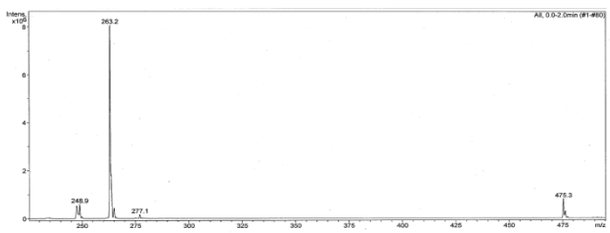

Figure 8: Mass-spectroscopy spectrum for 4-methyl-2, 6-diphenylthiopyrylium.

UV-Vis spectroscopy is used to evaluate the optical properties of the thiopyrylium based cyanine for intensity and range of absorption. As shown in Figure 11, a sampe of thiopyrylium based cyanine from Prof. Marder's group as shown in Figure 10,[6] which is prepared from the six-step synthetic procedure, is in comparison with the KG1003 made from the three-step synthetic route. The counter ion that is used for Marder's sample is tetra [3, 5-Bis (trifluoromethyl) phenyl] borate, while the counter ion used for KG1003 is BF_4^-. Both cyanine salts have expected intensive absorptions around 1000nm. However, KG1003 has a much broader absorption than Marder's sample therefore more optical losses. Also, there is large absorption in the 300 nm to 800 nm range for KG1003 but not for Marder's sample. Another UV-vis spectrum of KG1014 and Marder's sample is shown in Figure 12. Although the optical properties are much improved compared to the dye with the BF_4 counter ion, the absorption of KG1014 is slightly broader than the Marder group's. Absorption also occurs in the 300 nm to 800 nm range for KG1014.

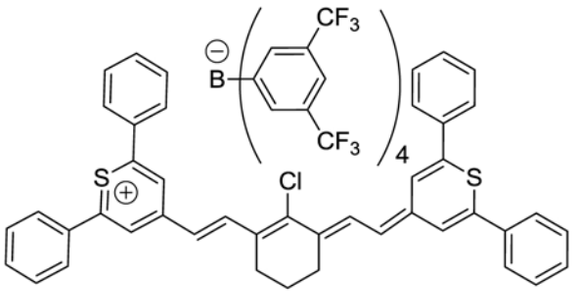

Figure 9: Marder's thiopyrylium based cyanine.

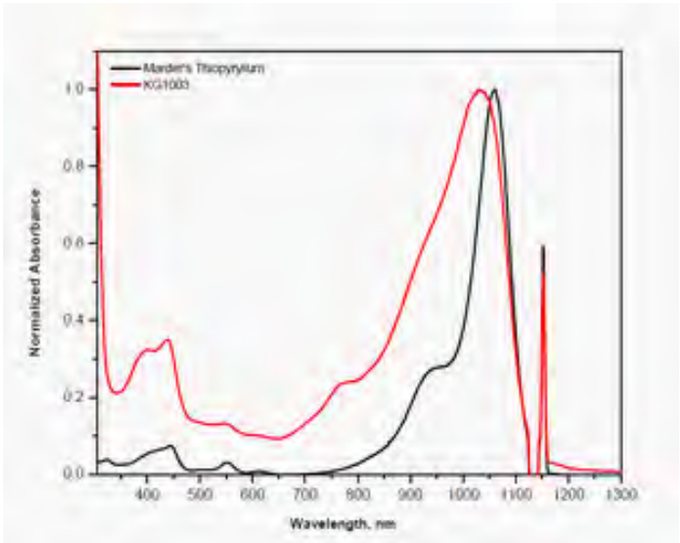

Figure 10: Marder's thiopyrylium Cyanine and KG1003.

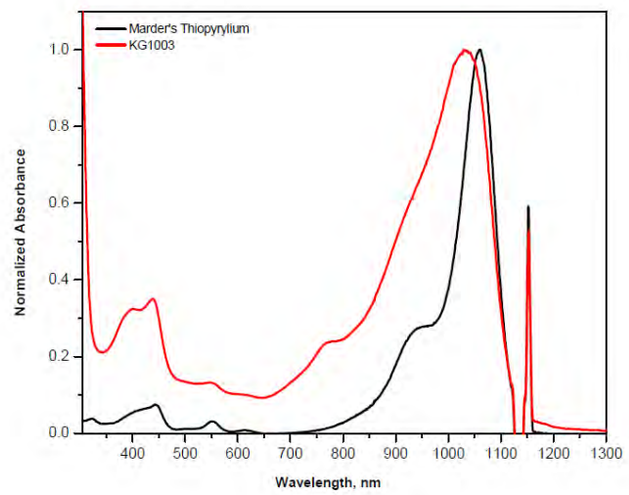

Figure 11: Marder's thiopyrylium Cyanine and KG1014

The broadness of the expected absorptions is different among these three thiopyrylium cyanine samples. This difference is thought to be caused by the difference in counter ion. KG1003 has BF_4^- as its counter ion and has the broadest absorption. KG1014 has tetraphenylborate as its counter ion and its absorption is sharper than KG1003 but broader than Marder's sample, which has tetra [3, 5-Bis (trifluoromethyl) phenyl] borate as its counter ion. Tetra [3, 5-Bis (trifluoromethyl) phenyl] borate has a much great charge delocalization than either BF_4^- or tetraphenylborate anions. It makes a better ion pair with thiopyrylim cyanine, which also has a similar delocalized charge through the pi-conjugated chain and therefore stabilizing the molecule. Another advantage of this anion is that its salts are more soluble in non-polar organic solvents and thus allow for facile purification and thin film device formation.

Conclusions

The thiopyrylium based cyanine was synthesized successfully from a synthetic route that is more efficient compared with the original six-step synthesis. Therefore, any modification of end groups can be done in a straightforward manner. Although our route has advantages in terms of efficiency, versatility, and simplicity of the steps involved, the existing procedure,[8] continues to show merit in terms of purity of the product. The usage of a counter ion that has a greater charge delocalization helps to sharpen the absorption of the thiopyrylium cyanine and minimized optical loss.

Synthesis of a methoxy derivative of the thiopyrylium salt using the synthetic route described is in progress. Upon successfully synthesize the methoxy thiopyrylium cyanine, UV-Vis spectroscopy will be used to explore optical properties and structure-property relationships. Comparison will be made between thiopyrylium cyanine and methoxy thiopyrylium cyanine for properties such as optical losses, processability, as well as solution and thin film third order properties for application in all-optical switches.

References

1. Haque S. A.; Nelson, J. Science 2010, 327, 1466.
2. Ye, X.; Akella, V.; Yoo, S. J. B. OSA/OFC/NFOEC. 2011.
3. (a) Marder, S. R.; Perry, J. W.; Bourhill, G.; Gorman, C. B.; Tiemann, B. G.; Mansour, K. Science 1993, 261, 186.
4. (b) Meyers, F.; Marder, S. R.; Pierce, B. M.; Bredas, J. L. J. Am. Chem. Soc. 1994, 116, 10703.
5. Yamamoto. N. I.; Okamoto T.Y. US Patent 2000, 6156, 506.
6. Hales, J. M.; Matichak, J.; Barlow, S.; Ohira, S.; Yesudas, K.; Bredas, J. L.; Perry, J. W.; Marder, S.R. Science 2010, 1185117.
7. Reference sample is provided by Professor Marder.

Acknowledgments

Funds for this research were provided by the Center on Materials and Devices for Information Technology Research (CMDITR), an NSF Science and Technology Center No. DMR 0120967.

Special thanks to Jen Research Group, the University of Washington Department of Material Science and Engineering, Dr. Joshua A. Davies, Brad Shigenaka, Dr. Sei Hum Jang, and Dr. Alex Jen.

TIANZHU GE is a transferring undergraduate student from Edmonds Community College. She is working to complete her BA in Chemistry at University of Washington. She is planing to pursue a PharmD degree and become a pharmacist.

Structure Relationship for Raman Scattering Cross-Sections of Carotenoids with Differing Electron-Acceptor Groups

KORIE GRAYSON, Norfolk State University
Anthony DeSimone, Joel Hales, Joseph Perry, Georgia Institute of Technology

Introduction

Raman Scattering

Raman spectroscopy is a vibrational spectroscopic technique that measures the light scattered by a sample. Most of the scattered light has the same frequency as the impinging radiation (Rayleigh scattering). A small portion (~ 1 in 10 million photons) has frequencies different from the incident beam demonstrating the Raman effect or Raman scattering.[1] This technique uses monochromatic laser light that interacts with molecular vibrations in a system. This interaction results in an energy shift of the scattered photons that provides information about the vibrational modes in a system.[1,2]

An excitation photon causes the molecule to go from a vibrational state in the electronic ground state to a virtual, not discrete, energy state. When the molecule relaxes, it returns to a different vibrational state and therefore light of a different frequency v_1 is emitted. This final vibrational state can be more or less energetic than the initial state. If the final state is more energetic than the initial, $v>v_1$, then a Stokes shift in frequency has occurred. If less, $v<v_1$, then an anti-Stokes shift in frequency has occurred. Stokes radiation will be the main focus for this project.[1]

Scientists hope to utilize this inelastic photon scattering process in devices for all-optical signal processing. The proposed research is mostly concerned with identifying molecules with large Raman scattering cross-sections (RSC) that could be processed into high number density films and could be suitable for device applications.[2,3] RSC is expressed mathematically with respect to experimental parameters as shown in Equation 1.

$$\frac{d\sigma}{d\Omega} = \frac{P^R}{P^L \cdot N \cdot \delta z \cdot \Delta\Omega}$$

Equation 1: The RSC expressed mathematically.[2]

P^R is the power of the scattered Raman light integrated over the entire vibrational band, P^L is the power of the incident light, N is the concentration of the sample, δ is the path length, and $\Delta\Omega$ is the solid collection angle.[2]

A potential class of molecules have been identified, namely carotenoids, consisting of conjugated organic molecules that are commonly terminated by rings. The chemical structures of these compounds are shown in Figure 1. Carotenoids are of special interest because they should possess relatively large RSC's and provide a means for structural modification that could lead to further optimization of these values. The large electron delocalization along the polyene chain has already been shown to exhibit large electron non-linear optical responses that are favorable for optical switching and photonics.[2,3,4,5,6,7]

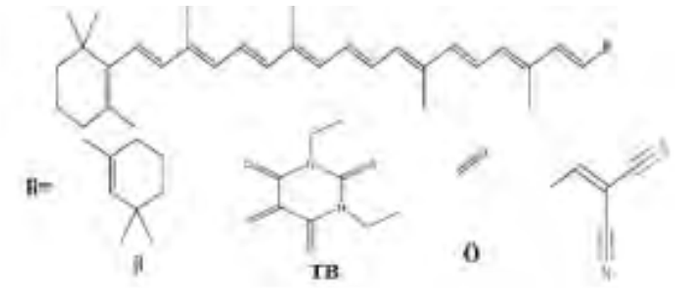

Figure 1: Structure of carotenoid molecules and various terminal groups.

The objective of this research is to develop a relationship between the structure of these carotenoids with different acceptor strengths and their RSCs. We will consider a valence bond-charge transfer (VB-CT) theory to help rationalize structure-property relationships for RSCs. Accordingly, carotenoids should exhibit an increase toward a maximal RSC as the acceptor group is tuned from weakly electron-accepting to strongly electron accepting.[3,4,8] Interestingly, a conceptually similar but more modest tuning route may be possible by changing solvent polarity.

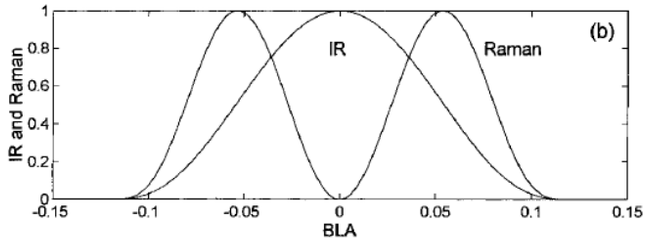

Figure 2: Raman intensities as a function of BLA.[4]

Polymer/Dye Films

As stated earlier, scientists hope to incorporate these carotenoids into high-performance photonic devices for all-optical signal processing. Devices incorporating similar chromophores have already been

successfully fabricated for other applications such as organic photovoltaics or organic LED's. The research of interest here focuses on processing these carotenoids in good quality films that exhibit strong Raman response, possess large chromophoric number densities, and are highly processible. This requires developing a suitable polymer/chromophore/solvent system to incorporate on films using different casting methods.

Materials and Methods

Raman intensity measurements were carried out using the MutliRAM Stand Alone FT-Raman Spectrometer with an Nd:YAG laser (1064 nm). The accompanying software, OPUS 6.5, collected all spectra taken. The carotenoids were dissolved in a variety of solvents ranging from nonpolar to extremely polar as shown in Table 1.

Solvent	Polarity index	Dipole Moment (D)
benzene	3.0	0.00
dichloromethane (DCM)	3.4	1.60
chloroform	3.4-4.4	1.04
tetrahydrofuran (THF)	4.2	1.75
1,4-dioxane	4.8	0.45
acetone	5.4	2.88
dimethyl sulfoxide (DMSO)	6.5	3.96

Table 1: Polarity and dipole moments of various solvents used in Raman experiments.

β-carotene, trans-β-apo-8'-carotenal (apocarotenal), and DCV-Apo were the carotenoids of interest, ranging from weak electron-accepting to strong electron-accepting groups. Approximately 1 mM solutions were prepared in 5 mL.

Absorptions measurements for the polymer/dye films were taken using the Shimadzu UV-Vis 3101PC Scanning Spectrophotometer. Apocarotenal was dissolved in solvents that are ideal for spin coating and casting as shown in Table 2. The host polymers were poly(methylmethacrylate) PMMA and polycarbonate resin.

Pictures of the film were taken using the Nikon Eclipse TE300 Microscrope and accompanying Nikon camera. The surface profile of each film was measured using the Veeco Dektak M6 Stylus Profiler.

Solvent	Density (g/cm^3)	Boiling Point (ºC)
cyclopentanone	0.95	131
chlorobenzene	1.11	131
dichlorobenzene	1.25	131
1,1,2-trichloroethane	1.44	133
dibromomethane	2.48	97

Table 2: Density and boiling points of solvents used in polymer/dye study.

First, polymer solutions were made with selected solvents (10% w/v). Solutions were heated to ~ 100 ºC to increase solubility. 40 uL of each solution was then added to 1 mg of apocarotenal. 10 uL of this solution was casted on a glass substrate using the pipette tip and dispersing the solution in every direction. Solutions were allowed to dry overnight in the dark in conditions that allowed for adequate ventilation and evaporation of solvent.

Results and Discussion

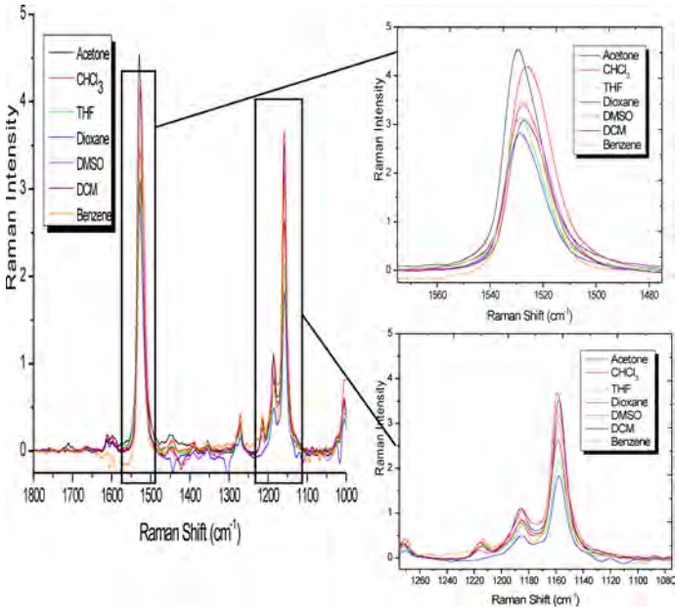

Figure 3: Raman spectra of apocarotenal.

Figure 3 portrays the Raman scattering spectra of apocarotenal. Apocarotenal includes a terminal aldehyde group, not a strong electron acceptor. Given that the C=C and C-C vibrational modes are of main interest to this research, these regions are magnified and studied for any systematic changes. It can be seen from the spectra that the Raman scattering cross sections of this carotenoid increases

with solvent polarity, acetone having the largest peak and cross section. Benzene and DMSO do not follow the expected trend that is based on the other sovents and the VB-CT prediction. This notable difference could be due to the large polarizabilities that benzene and DMSO possess.

The difference in solvent polarity and how that affects the Raman spectra of carotenoids was further studied by dissolving all three potential compounds in two different solvents—one more polar than the other—as shown in Figures 4 and 5.

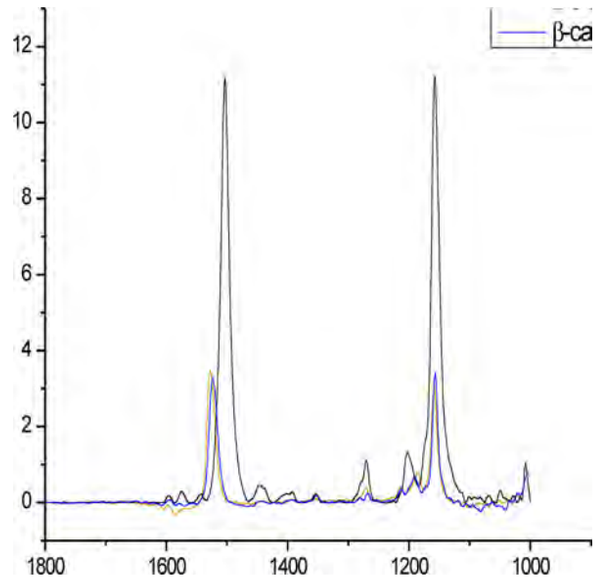

Figure 4: Raman spectra of β-carotene, apocarotenal, and DCV-Apo in benzene. (1 mM apocarotenal and β-carotene, 1.64 mM DCV-APO).

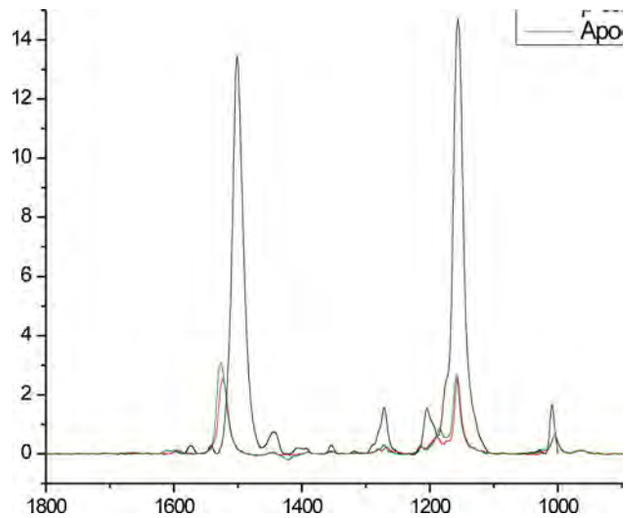

Figure 5: Raman spectra of β-carotene, apocarotenal, and DCV-Apo in DCM. (1 mM apocarotenal and β-carotene, 1.64 mM DCV-APO).

When compared to β-carotene, the carotenoid with the weakest electron-accepting group, DCV-Apo exhibits a cross section 2x greater in benzene and 4x greater in DCM for the carbon-carbon double bond region at 1550-1480 cm^{-1}. DCV-Apo exhibits cross section 3x greater in benzene and 6x greater in DCM for the carbon-carbon single bond region at 1200-1150 cm^{-1}. These values adhere to the theory that RSC's increase as the electron group is tuned from weak to strong.

Solvent	β-carotene	Apocarotenal	DCV-Apo
benzene	7.83E-32	7.63E-32	1.81E-31
DCM	5.19E-32	7.81E-32	2.29E-31
chloroform	6.54E-32	1.15E-31	------
THF	4.45E-32	7.86E-32	------
1,4-dioxane	6.20E-32	7.09E-32	------
acetone	------	1.02E-31	------
DMSO	------	8.15E-32	------

Table 3: C=C RSCs (m^2 $srad^{-1}$) of carotenoids in solvents.

Solvent	β-carotene	Apocarotenal	DCV-Apo
benzene	5.55E-32	5.38E-32	1.75E-31
DCM	3.71E-32	7.81E-32	2.44E-31
chloroform	3.75E-32	7.17E-32	------
THF	2.53E-32	4.16E-32	------
1,4-dioxane	3.40E-32	3.50E-32	------
acetone	------	5.91E-32	------
DMSO	------	5.43E-32	------

Table 4: C-C RSCs (m^2 $srad^{-1}$) of carotenoinds in solvents.

A qualitative study was conducted to determine the right combination and appropriate amount of polymer and apocarotenal necessary to produce optical quality guest-host films. Microscopy and profilometry were used to observe the surface roughness, homogeneity, and uniformity of the resulting films. UV/Vis spectroscopy is used to observe any degradation in the films and to determine if the film exhibits any optical (Rayleigh) scattering. Such measurements were necessary since by looking with a naked eye, all films looked homogenous and flat but with varying color. Some films displayed instant crystallization such as those containing chlorobenzene and 1,2-dichlorobenzene with polycarbonate resin. Microscopy confirmed that the films were homogenous but contained very small holes and/or defects. Some combinations like PMMA and 1,1,2-trichloroethane were unevenly distributed around the film and near edges. Profilometry provided a more detailed surface revealing that some films like those formed from PMMA and dichlorobenzene were not at all homogenous but rather contained many particles as shown in Figure 6.

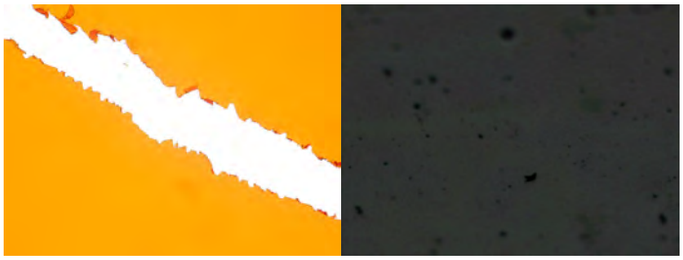

Figure 6: (a) Microscopic image of PMMA and dichlorobenzene. (b) Image taken using profilometry.

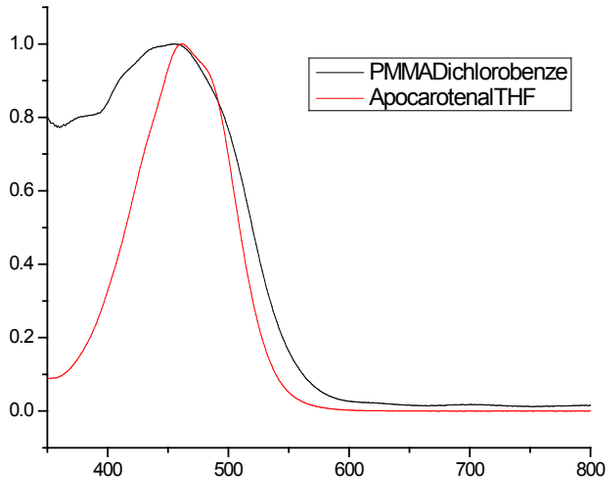

Figure 7: UV-Vis spectra of drop-casted film formed from p/c/s system and THF.

The UV-Vis spectra of the drop-casted film formed from p/c/s system and a similar solvent (THF) was taken and compared. The spectra show a common maximum peak and absorption contour suggesting that apocarotenal has not degraded in the new environment. No optical scattering is seen either. Due to the need for a film to be smooth, homogenous, and uniform, dibromomethane was chosen as the best solvent for the polymore/chromophore/solvent system. Films formed using this system had minimal surface roughness, consistent homogeneity, and uniformity. Figure 8 displays these qualities.

Figure 8: PMMA and dibromomethane.

Conclusions

For the Raman scattering project, the RSC of apocarotenal in different solvents showed a general increase with solvent polarity; however, this tendency was conflicting in solvents with a high polarizability. Carotenoids with stronger electron-accepting groups exhibited a more intense Raman spectra due to the large degree of intramolecular charge transfer that occurs between the pi-system and acceptor group.

In the polymer film project, the chromophore exhibited no degredation or optical scattering in a PMMA host. Solutions containing dibromomethane were chosen as the best system to begin spin coating or blade casting and running further tests.

Future Work

We will continue to establish a relationship between RSC and acceptor groups through further quantitative testing and map out RSC evolution as a function of solvent environment. There will also be more qualitative and quantitative work to determine an optimal polymer/dye combination and ideal conditions for film fabrication through either spin coating or blade casting.

References

1. Harris, Daniel C., and Michael D. Bertolucci. “Symmetry and Spectroscopy: An Introduction to Vibrational and Electronic Spectroscopy.” New York: Dover Publications, 1989.
2. DeSimone, Anthony. “Initial Research Review/Original Proposal.” Georgia Institute of Technology, April 2011.
3. Castiglioni, C., M. Veronelli., G. Zerbi, and M. Del Zoppo. “Nuclear Contribution to Hyperpolarizability of Polyconjugated Compounds: Role of Vibrational Intensities.” Synthetic Metals 55-57 (1993): 3919-3926.
4. Cho, Minhaeng. “Vibrational Characteristics and Vibrational Contributions to the Nonlinear Optical Properties of a Push-Pull Polyene in Solution.” J. Phys. Chem. A. 102 (1998): 703-707.
5. Castiglioni, C., G. Zerbi, and M. Del Zoppo. “Vibrational Raman Spectroscopy of Polyconjugated Organic Oligomers and Polymers.” Journal of Raman Spectroscopy 24 (1993): 485-494.
6. Castiglioni, C., M. Gussoni, M. Rui, G. Zerbi, and M. Del Zoppo. “Non-linear optical response to strong applied electromagnetic fields in polyconjugated materials.” Synthetic Metals 51 (1992): 135-146.
7. Müllen, K., G. Müller, M. Rehahn, M. Rumi, G. Zerbi. “Nonlinear optical and vibrational properties of conjugated polyaromatic molecules.” J. Chem. Phys. 106 (1997): 24-34.
8. Castiglioni, C., G. Zerbi, and M. Del Zoppo. “Molecular first hyperpolarizability of push-pull polyenes: Relationship between electronic and vibrational contribution by a two-state model.” Physical Review B 53 (1996): 319-325.

Acknowledgments

I would like to acknowledge the Center on Materials and Devices for Information Technology Research (CMDITR), the NSF Science and Technology Center No. DMR 0120967, Perry Research Group, Olanda Bryant, Denisha Thomas, Dr. Cam Tyson, and Dr. Keith Oden.

KORIE GRAYSON is a rising senior at Norfolk State University. Upon graduation, she plans to attend medical school to pursue her MD/Ph.D.

Spectral and Time-Dependent Photooxidative Degradation of Bulk Heterojunction Organic Thin Films

SARAH GRIESSE-NASCIMENTO, Boston University
Glennis Rayermann, David S. Ginger, University of Washington

Introduction

Solar cells from organic photovoltaics (OPVs) have the potential to meet market demands for energy consumption in the United States due to low production costs and the possibility to employ simple mass production techniques, such as roll-to-roll processing.[1,2] OPVs are also lightweight and flexible, adding advantages such as portability and potentially lower installation costs for a wider range of applications. However, challenges facing OPV commercialization are low efficiencies and short lifetimes. To achieve commercially competitive technology (3-5¢/kWh), efficiency levels must be higher than 10% in production.[3] The current record efficiency is ~8.3%, and the National Renewable Energy Laboratory reports that efficiency levels have been steadily increasing over the past decade, suggesting that >10% efficiencies could be attained in the future.[4] The goal for OPV lifetimes is five years or higher, depending on the application.[5]

Photooxidation is a process that can limit OPV lifetimes. It occurs when light interacts with the OPV material in air, leading to degradation of the active layer by formation of charge traps. Understanding the degradation mechanisms and kinetics for OPVs could help to guide solar cell design and encapsulation strategies for increased device lifetimes. Preliminary IR data suggested the possibility of second-order trap formation kinetics in the polymer. To continue studying the mechanisms of photooxidation, we conducted several experiments that involved photooxidizing two types of OPV thin films (Figure 1): a well-characterized model system of poly(9,9-dioctylfluorene-co-bis-N,N-(4-butylphenyl)-bis-N,N-phenyl-1,4-phenylenediamine) (PFB) blended with poly(9,9-dioctylfluoreneco-benzothiadiazole) (F8BT) and a widely-studied, efficient blend of poly(3-hexyl thiophene) (P3HT) and [6,6]-phenyl C61-butyric acid methyl ester (PCBM). We used attenuated total-reflectance Fourier transform infrared (ATR-FTIR) spectroscopy to study the resulting chemical degradation.

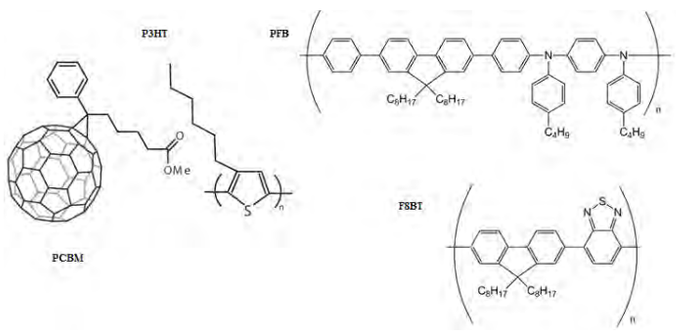

Figure 1: Chemical structures of P3HT, PCBM, PFB and F8BT.

Additionally, we began in situ photooxidation studies on these OPV blends using two atomic force microscopy techniques: time-resolved electrostatic force microscopy (trEFM) and fast-free trEFM. Both techniques measure the relative efficiencies of specifically photooxidized areas of the active layer with nanoscale resolution and allow us to study photooxidative damage at lower photon doses than with ATR-FTIR spectroscopy.[6]

Experimental Methods

Solutions of each polymer were prepared in a glovebox using anhydrous chlorobenzene at concentrations of 20 mg/mL (for PFB and F8BT) and 42 mg/mL (for P3HT and PCBM). The PFB and F8BT solutions were heated at 45 °C for ~ 4 hrs and P3HT and PCBM solutions at 55 °C for ~ 6 hrs. Solution pairs were mixed in a 1:1 ratio. Square glass substrates with side length 15 mm layered with indium-tin-oxide (ITO) were spin coated with ~ 40 nm PEDOT:PSS, annealed at 100 °C under nitrogen and then spin-coated with 60 µL of filtered polymer blend solution. P3HT:PCBM, films were annealed inside the glovebox for another 5 min at 125 °C.

Bulk photooxidation experiments were performed by photooxidizing the entire sample area under ambient conditions (22.1-28.9 °C and 21-34% relative humidity) using either an LED or a solar simulator. For the time-dependent PFB:F8BT photooxidations, samples were exposed to 405 nm LED illumination for varying amounts of time to achieve a range of absorbed photon doses in the film. This wavelength was chosen so that both components of the polymer blend had approximately the same absorbance. For P3HT:PCBM, we performed spectral-dependence experiments using 405, 455, 490, 532 and 630 nm LEDs as well as a solar simulator coupled with a bandpass filter to generate light between 300-400 nm. A bulk photooxidation was also performed using the solar simulator as a broadband light source and exposing it to a PFB:F8BT and a P3HT:PCBM sample for 40 h each (Figure 1).

IR measurements were performed on a ThermoFischer Scientific Nicolet-8700-FTIR equipped with a HgCdTe detector, Harrick GATR grazing angle ATR accessory with a 65° fixed incident angle, and a 56 in-oz slip-clutch. All spectra were signal-averaged over 256 scans with a resolution of 1 cm^{-1} and were baseline-corrected.

Localized photooxidation experiments were performed with an Asylum Research MFP-3D-BIO. Specific spots on the sample were exposed in air to a 405 nm (PFB:F8BT) or 532 nm (P3HT:PCBM) laser in a 3x3 matrix pattern. The array was bulk photooxidized in situ using an LED at the same wavelength as the laser. After each photooxidation step, imaging was performed using trEFM (for

PFB:F8BT) and FF-trEFM (for P3HT:PCBM). Experimental details about trEFM are provided elsewhere.[6,7]

a)

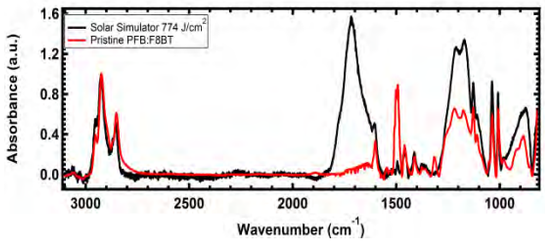

b)

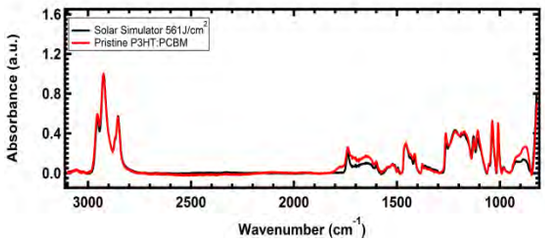

Figure 2: Absorbance spectra of pristine sample and broadband photooxidized sample (a) for PFB:F8BT blend (b) for P3HT:PCBM blend.

Results and Discussion

The objective of the bulk photooxidation studies with PFB:F8BT samples was to determine the kinetics of fluorenone trap formation and correlate results with data from the localized photooxidation experiment to test whether traps generated at low doses catalyze the formation of more charge trap species. The aim of the bulk P3HT:PCBM studies was to understand photoodegradation under ambient conditions, including whether photooxidation products depend on the wavelength of incident radiation.

At the highest photon dose (726 J/cm^2) the PFB:F8BT data show peak formation in the 1640-1750 cm^{-1} range consistent with the expected C=O stretch of the fluorenone photooxidation product;[8] however, the peak has a broader shape than was observed previously[6] (Figure 3a). The broad fluorenone peak shape is consistent with the spectrum of the PFB:F8BT film photooxidized with the broadband light source (Figure 1a). This deviation from previous results may have occurred due to a variety of factors: the PFB batch used was different, changing the UV/Vis absorbance; the total time for photooxidations was longer, and samples were stored covered in aluminum foil in the glovebox for up to ten days before IR measurements were taken, thus samples may have aged or come into contact with impurities. While precautions were taken to protect samples from other light sources during all experimental processes, samples had variable light exposure during experimental setup.

In addition, with increasing photon doses, we observe a decrease in the peak heights near 1490 and 1500 cm^{-1} (CH scissoring) and a small redshift in the methyl/methylene bend peaks at 2850, 2923 and 2952 cm^{-1}, which we attribute to changes in the local chemical environment as the sample becomes more photooxidized, suggesting a change in morphology (Figure 3b). This interpretation is consistent with the observed increase in the fluorenone peak, which is indicative of a local chemical change at higher photon doses.[8]

a)

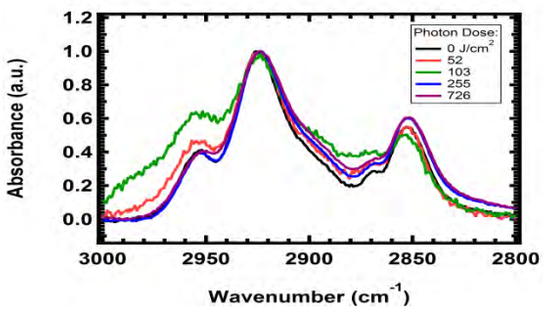

b)

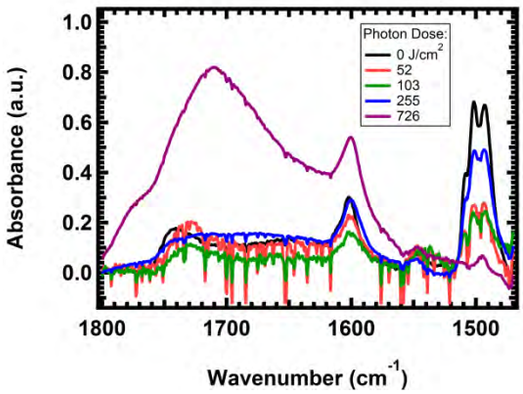

Figure 3: Absorbance spectra of PFB:F8BT time-dependent study samples (a) peak height decrease for CH scissoring (1490 cm^{-1}) and peak height increase for fluorenone centered at 1737 cm^{-1} (b) redshift for methyl/methylene stretching (2850, 2923 and 2952 cm^{-1}).

The P3HT:PCBM spectral study results indicate that specific photooxidative damage occurs at all wavelengths studied. An increase in the peak heights at 880 cm^{-1}, which we assign to the presence of a hydroperoxide moiety (-OOH), suggests that the thiophene alkyl chain is being photooxidized, as proposed by a mechanism from Manceau et al.[9] The hydroperoxide peak intensity increases with 490, 300-400, 405, 455, 532 and finally 630 nm light exposure. Similarly, we tentatively attribute the peak at 1261 cm^{-1} to epoxides formed during the photooxidation of PCBM.[10] This peak intensity increases from the pristine sample in ascending order by ultraviolet, 490, 405, 532, 630 and 455 nm light. Peaks corresponding to the C=C stretch in the thiophene rings (~1400-1500 cm^{-1}) did not change with exposure at specific wavelengths or with broadband illumination.[11] This suggests that the thiophene backbone remains intact over the photon doses studied. A very broad peak from ~1600-1730 cm^{-1} may be a convolution of further photooxidation products of the thiophene alkyl chain.[9] The spectral changes outlined above were also observed in the broadband photooxidized film (Figure 2b). It should be noted that there was some variation in photon dose at each wavelength, so

trends in the wavelength-dependence are tentative. We conclude from our results that photooxidation under ambient conditions in P3HT:PCBM films occurs in PCBM via epoxide formation and in P3HT at the alkyl chains but not at the sulfur on the thiophene ring.

a)

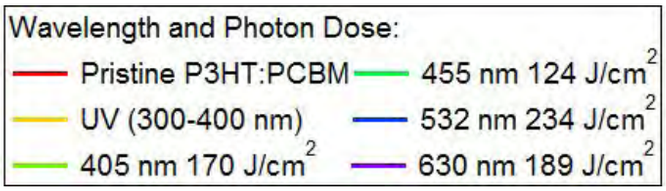

b)

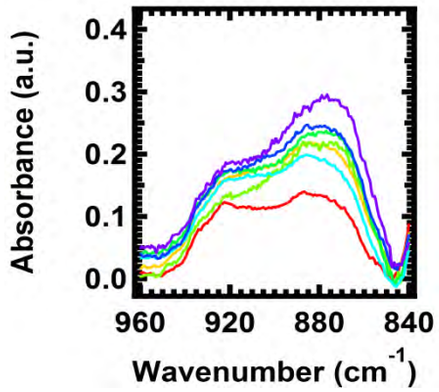

c)

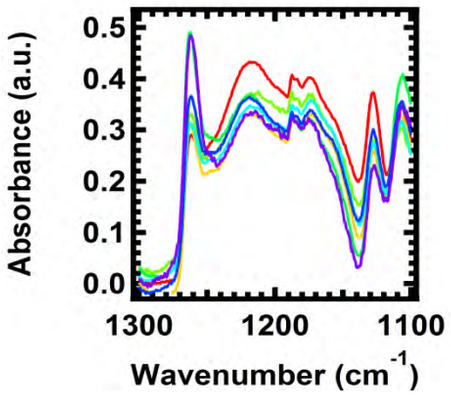

d)

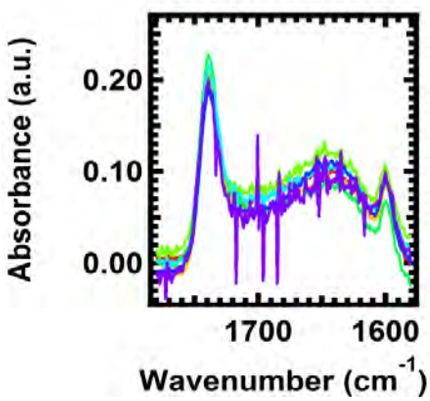

Figure 4: Absorbance spectra of spectral dependence study samples (a) legend with wavelengths and photon doses (b) change in peak at 880 cm^{-1} suggests thiophene alkyl chain photooxidation (c) C=C stretch at ~1400-1500 cm^{-1} suggest intact thiophene backbone (d) broad peak at 1600-1700 cm^{-1} also suggests alkyl chain photooxidation.

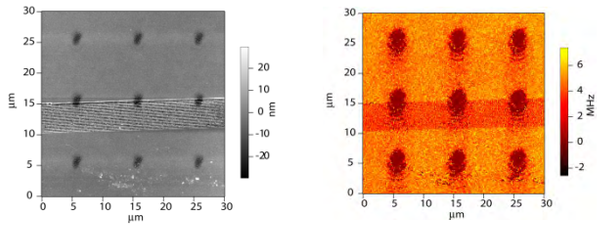

Figure 5: Topography (left) and charging rate image (right) of photooxidized array of spots in PFB:F8BT. Horizontal feature is a location marker made with the AFM tip.

The objective of the localized photooxidation study was to observe how the traps influence subsequent trap formation and if we could confirm second order kinetics. Difficulties in carrying out the entirety of the experiment led to changes in the methodology employed. Initial challenges involved finding the oxidized spots to perform the first set of trEFM imaging. To overcome this, the sample was marked using a diamond scribe and the AFM tip. The scribed scratches helped locate the vicinity of the spots (lowering the searching area to the order of 1 mm^2), and the smaller AFM tip scratches, typically made ~5 µm above and below the photooxidated area, helped in finding the exact location. Other problems encountered were the ease with which the tip location on the sample could drift or be shifted. Future work will include altering the gas lines in order to be able to purge with N_2 or inject air without disturbing the sample position.

Conclusions

Results from bulk photooxidation experiments show that the photooxidation of PFB:F8BT yields formation of fluorenones and possible changes in morphology, as suggested by the shift in methyl/methylene peaks. In P3HT:PCBM, out results suggest that photooxidation occurs more readily at thiophene alkyl chains than at the sulfur atoms along the thiophene backbone. Photooxidation also occurs in PCBM, via epoxide formation. Localized photooxidation study methodology must be improved in order to study possible second order kinetics in trap formation and photooxidation at lower photon doses.

References

1. Lee, M. R.; Eckert, R. D.; Forberich, K.; Dennler, G.; Brabec, C. J.; Gaudiana, R. A. Science 2009, 324, 232-235.
2. Peumans, P.; Bulovic, V.; Forrest, S. R. Applied Physics Letters 2000, 76, 2650-2652.
3. Singh, B., Davies, M.S. Green Econometrics. http://greenecon.net/solar-energy---closer-to-grid-parity/energy_economics.html (accessed August 25, 2011).
4. Servaites, J. D.; Ratner, M. A.; Marks, T. J. Energy & Environmental Science.
5. Nielsen, T. D.; Cruickshank, C.; Foged, S.; Thorsen, J.; Krebs, F. C. Solar Energy Materials and Solar Cells, 94, 1553-1571.
6. Reid, O. G.; Rayermann, G. E.; Coffey, D. C.; Ginger, D. S. Journal of Physical Chemistry C, 114, 20672-20677.
7. Coffey, D. C.; Ginger, D. S. Nature Materials 2006, 5, 735-740.
8. Bliznyuk, V. N.; Carter, S. A.; Scott, J. C.; Klarner, G.; Miller, R. D.; Miller, D. C. Macromolecules 1999, 32, 361-369.
9. Manceau, M.; Rivaton, A.; Gardette, J. L.; Guillerez, S.; Lemaitre, N. Polymer Degradation and Stability 2009, 94, 898-907.
10. Reese, M. O.; Nardes, A. M.; Rupert, B. L.; Larsen, R. E.; Olson, D. C.; Lloyd, M. T.; Shaheen, S. E.; Ginley, D. S.; Rumbles, G.; Kopidakis, N. Advanced Functional Materials, 20, 3476-3483.
11. Manceau, M.; Chambon, S.; Rivaton, A.; Gardette, J. L.; Guillerez, S.; Lemaitre, N. Solar Energy Materials and Solar Cells, 94, 1572-1577.

Acknowledgments

Funds for this research were provided by the Center on Materials and Devices for Information Technology Research (CMDITR), the NSF Science and Technology Center No. DMR 0120967. I would like to thank all the members of the Ginger group at the University of Washington for their support.

SARAH GRIESSE-NASCIMENTO is a rising senior at Norfolk State University. Upon graduation, she plans to attend medical school to pursue her MD/Ph.D.

Organic Field Effect Transistors (OFETs) as Tools for: Investigating the Relationship between the Morphology and the Charge Transport in Polythiophene Films.

JESSICA IZUMI, University of Maryland
Avishek Aiyar, Elsa Reichmanis, Georgia Institute of Technology

Introduction

Due to their low cost, large area coverage, and flexibility, OFETs have become very favorable in studying the conductivity and charge transport of solution processable organic polythiophene films.[1] Poly(3-hexylthiophene) (P3HT) has attracted many due to its' outstanding charge transporting characteristics in its' solution processable films. P3HT is easily solution processed and tends to form ordered films which allows for facile transport from the source to the drain. Charge transport has a high correlation to the microstructure of polythiophene films. By changing the reigioregularity of the alkyl side chains on the polythiophene backbone as well as increasing molecular weight, polythiophene films have performed with mobilities as high as $10^{-1}cm^2V^{-1}s^{-1}$ close to that of an amorphous silicon device.[2] Other factors such as changing the film processing method (dip coating, spin coating, drop casting), using different solvents, degree of ultrasonication and modifying the semiconductor dielectric interface all affect the microstructure and charge transport of the overall device.[2]

Various techniques have been performed to manipulate the microstructure of the thin films of solution processable conducting polymers. Surin processed films with three different film processing methods and tested each film's mobility to investigate the relationship between the structure of the film with it's mobility. Drop casting performed the lowest with mobilities ranging from 10^{-3}-10^{-4} V.[2] The highest mobility was found from dip coating (0.085 $cm^2V^{-1}s^{-1}$).[2]

Using high-intensity ultrasonic cleansing creates a high-order phenomenon.[3] In polymers, ultrasonication accelerates chemical reactions between liquids and solids by removing contaminating coatings within the solution mixture. By speeding up the chemical reaction, ultrasonication changes the solution's physical composition and lowers the chain length thus manipulating the microstructure of the polymer.[3] Ultrasonication is highly dependent on molecular weight and the microstructure of the polymer chain and will only lower the chain to a certain time limit.[3]

In this paper, we investigate the strong relationship between the microstructure of high regioregular P3HT films and their charge transport. A 92%-94% and a 96% regioregularity of the P3HT are used in all experiments. We manipulate the microstructure of the films by changing the film processing method(dip coating and spin coating) to experiment which process gives a more ordered film. Ultrasonication cleansing is used prior to film processing which produces more pi aggragates in the film allowing for improved charge transport. (see Figure 1.) Lastly, we modify the semi conductor dielectric interface by coating our substrates with Hexamethyldisilizane (HMDS). We keep the molecular weight and the solvent ($CHCl_3$) constant to analyze how these four variables improve the microstructure within the P3HT films.

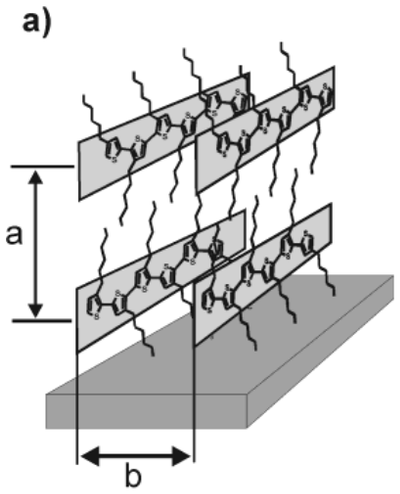

Figure 1: Pi aggregates of P3HT arranged in edge-on orientation.[4]

Experimental

The model solution was prepared by dissolving P3HT in anhydrous $CHCl_3$ to give a concentration of 4 mg/ml. All experiments were conducted in the glove box to eliminate any detrimental effects to the devices from oxygen or moisture in the air. The P3HT/$CHCl_3$ mixture was heated at 60°C and stirred inside the glove box on a hot plate. Each film was processed onto the device by either spin coating or dip coating and then thermally annealed for 10 h overnight. Prior to film processing, the P3HT/$CHCl_3$ was placed in a sonication bath for 7-10 min to create ordered precursors within the P3HT solution. The next day, each device was patterned with $CHCl_3$ to decrease gate leakage when tested.

Testing the device performance

Three probes were attached to the source, drain, and gate. (see Figure 2). Different voltages were applied to measure the current of each device. To measure the field effect mobility of the device, the following equation is used:

$$I_{SD} = \frac{W}{L}\mu C_0\left(V_G - V_T - \frac{V_{SD}}{2}\right)V_{SD}$$

I_{SD} is the measured drain current, μ is the carrier mobility, W and L represent the channel width and length, V_G is the gate voltage, VT is the threshold voltage, and C0 represents the capacitance of the gate dielectric per unit area.[2]

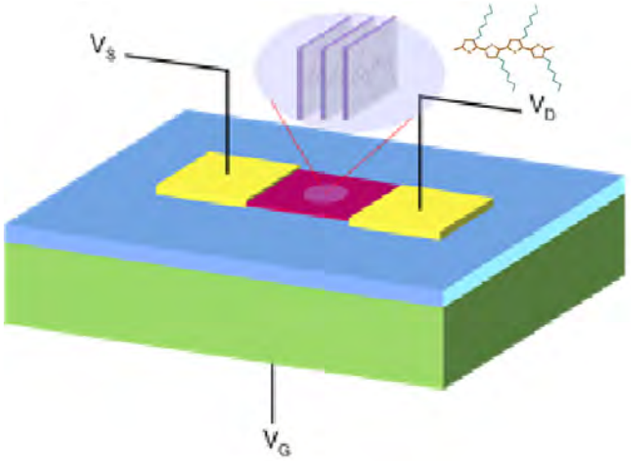

Figure 2: Bottom Contact, bottom gate OFET. Gold will serve as the source and drain electrodes with silicon dioxide (SiO_2) as the gate dielectric on the substrate. A poly(3-hexylthiophene) (P3HT) film will be processed over the channel. Inset shows the P3HT architecture.

Transfer and output characteristics were both measured. In testing the transfer characteristics, the gate voltage was changed as the drain voltage was kept constant. (see Figure 3). In testing the output characteristics, the drain voltage versus the drain current was measured for different Gate Voltages as shown in Figure 4.

The linear region and saturation region were both tested. The linear region was where the drain voltage depended on the gate voltage whereas in the saturation region, they were independent of each other. The mobility is extracted from the slope of each graph. (see Figure 3).

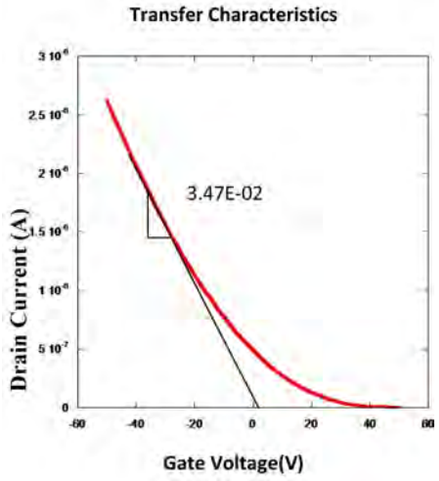

Figure 3: Transfer characteristics of a SiO_2 device that was spin coated.

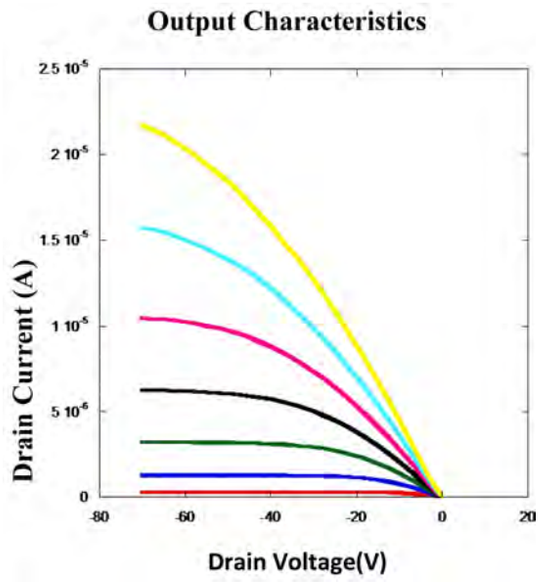

Figure 4: Output characteristics of a SiO_2 device that was spin coated.

Results

When placed in the sonication bath, the solution changed from a bright orange color to a deep brownish red color. The color change occurred at a faster rate with the higher regioregular P3HT.

From the comparison of average mobilities tested by changing variables such as regioregularity, film processing method, and ultrasonication, the highest mobility was found when the higher regioregular P3HT solution was processed through dip coating and sonicated prior to depositing the film. This mobility has high correlation to the high degree of order within the film due to the film processing method, sonication, and higher regioregular head-tail combinations, as shown in Figure 5.

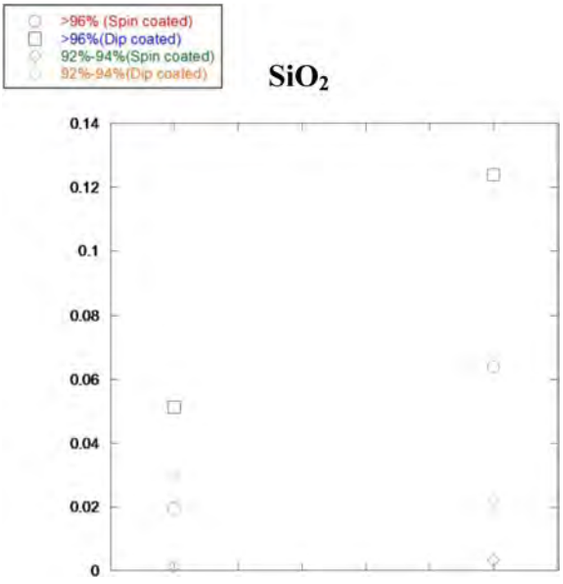

Figure 5: Average mobilities taken from experiments k where devices were tested on bare SiO_2.

Figure 6 show the comparison of average mobilities tested on bare SiO_2 and HMDS devices that were spin coated and dip coated as well as sonicated, the highest mobility was found from the HMDS device that was sonicated prior to being dip coated. By coating these devices with HMDS, the semi conductor dielectric interface was modified and improved the packing of the pi aggregates allowing for higher charge transport.

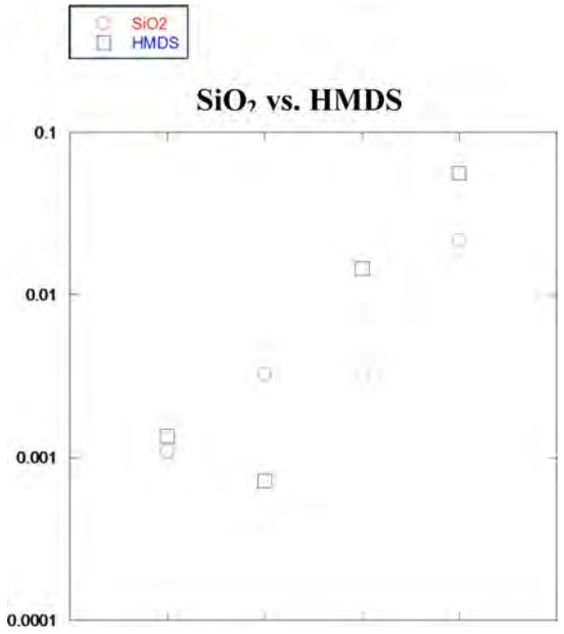

Figure 6: Average mobilities calculated from experiments where devices were tested on bare SiO_2 and HMDS.

Atomic Force Microscope and the Degree of Crystallinity

Due to complications, the Atomic Force Microscope was undergoing maintenance during the time period that I was here.

These images produced by the AFM above clearly show that by changing the film processing method as well as using ultrasonication prior to the film processing method both cause a difference in microstructure in a film.

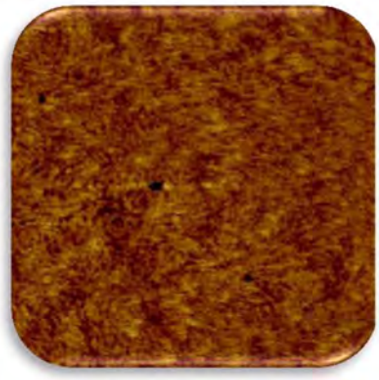

Prior to sonication (spin coated)

After sonication (spin coated)

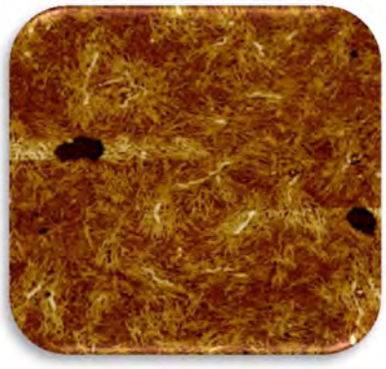

After sonication (dip coated)

Conclusion

The results shown in this paper show a strong relationship between the microstrucutre and charge transport in the P3HT films. Between the two film processing methods (spin coating and dip coating), dip coating the films gave the highest mobility of 0.12 $cm^2V^{-1}s^{-1}$. Also, using a higher regioregularity of 96% versus 92%-94% led to a higher mobility due to the higher degree of order in the films. Modifying the semiconductor interface by depositing hexamethyldisilizane on the device also showed improvements in device performance.

To further investigate the relationship between the morphology and charge transport in our P3HT films, we would need to examine each of the films with the Atomic Force Microscope. Afterwards, we would perform X-ray diffraction to give us a better understanding.

References

1. Sun,Y. Liu,Y. Zhu,D. “Advances in organic field-effect transistors.” Journal of Material Sciences, 2005, 15, 53–65.
2. Salleo, A. "Charge transport in polymeric transistors." Materials Today 10 (2007): 38-45.
3. K. S. Suslick , G. J. Price, Annu. Rev. Mater. Sci. 1999, 29, 295 – 326.
4. Sandberg, H.G.O., et al., Ultrathin regioregular poly(3-hexyl thiophene) field-effect transistors. Langmuir, 2002. 18(26): 10176-10182.
5. Pierret, R.F., Field effect devices1990: Prentice Hall.

Acknowledgments

I would like to strongly thank my faculty advisor Elsa Reichmanis and mentor Avishek Aiyar for allowing me to see how research is conducted at a graduate level by giving me this project and for allowing me to work in the Reichmanis lab. Appreciation also goes to the rest of the Reichmanis Group for their support and guidance throughout my time spent here at Georgia Institute of Technology. I would also like to thank the National Science Foundation for supplying funds necessary to perform my research and to CMDITR , DMR 0120967 and Georgia Institute of Technology for choosing me to participate in this wonderful research opportunity.

JESSICA IZUMI is a rising sophomore at the University of Maryland, Baltimore County majoring in Chemical Engineering.

Synthesis of a Squaraine-Based Dye for Dye-Sensitized Solar Cells

JULISHA L. JOYNER, North Carolina State University
Seth Marder, Tissa Sajoto, Georgia Institute of Technology

Introduction

Fossil fuels that are currently being consumed are projected to be depleted in the near future. Current developments in this field have been drifting toward advancements in alternative energy sources, especially in solar energy.[1] Solar energy is produced by harvesting radiation emitted from the sun. To collect solar rays, it is necessary to use a device called a solar cell. The dye-sensitized solar cell structure consists of a dye monolayer sandwiched in between an electrode and titania (TiO_2), a catalyst, conducting transparent layers, and a transparent substrate.[2] The device works by harvesting sunlight through a sensitizer (dye) attached to the surface of the semi-porous semiconductor. The beam excites the dye and causes electrons to shoot into the conduction band. The dye is then regenerated through electron donation from the iodide/triiodide redox mediator.[2] The dye-sensitized solar cell is the only solar cell that separates the process of collecting sunlight and electron injection.[2]

Currently dye-sensitized solar cells (DSSCs) contain dyes that have ruthenium complexes, but the metals that these dyes use are rare and expensive to implement.[1] Consequently, replacing the metal complex dyes with organic substitutes has become a trending topic in modern scientific research. Researchers have been studying these organic substitutes because they are cheaper to synthesize, have wider spectral distributions, potential for molecular design, and no resource limitations.[2]

The overall goal of this study is to synthesize a squaraine dye for DSSCs. By changing the x-bridge of the dye, the researchers hope to increase the spectral distribution range that the dye molecule can absorb, specifically in the red and near-infrared regions. The chemical structure of the target molecule is illustrated in Figure 1.

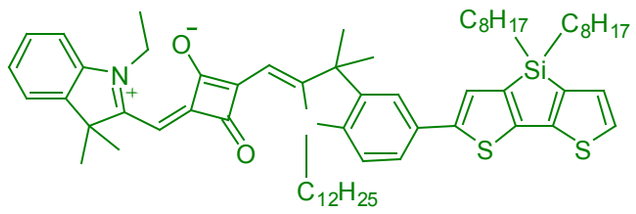

Sq-DTS (JJ-I-54)

Figure 1: Squaraine-dithienosilole dye.

Figure 1 is color-coded to reflect the different functionalities of the dye molecule. The substrate that is coded in red is the actual dye part of the molecule which absorbs different wavelengths of light to produce color (or energy when using DSSCs). Wide spectral distributions with high molecular extinction coefficients ultimately can increase the overall efficiency of DSSCs.[3] The dithienosilole (coded in green) not only provides a linkage between the squaraine dye and anchor but extends conjugation of the dye. This linkage hopefully will be able to absorb more from the red- near-infrared regions and may give more absorption coverage in the higher energy region leading to broader overall absorption. The section coded in blue is the anchor of the molecule. The anchor allows the dye to bind to the surface of the titania semi-conductor.[3]

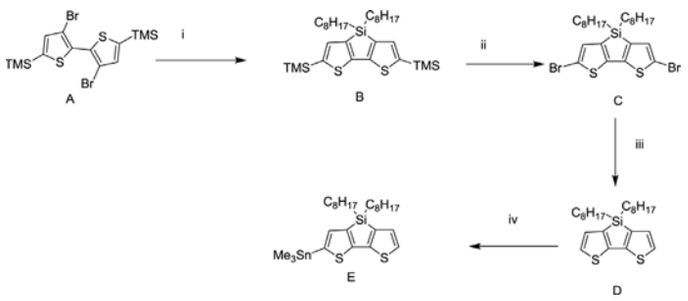

Figure 2: Synthesis of tributyltin-dithienosilole.

The synthesis of the target molecule is a two part synthesis that can further be broken down into a seven step process. The first part involves synthesizing a dithienosilole capable of linking the squaraine dye molecule with the anchor group. Figure 2 illustrates the complete scheme in part one.

Experimental Module

Materials & Instruments

Compound A (5,5'-Bis (trimethylsilole)-3,3'-dibromo-2,2'-bithiophene) in Figure 2 was provided by Solvay: Inc. The squaraine dye (the first molecule shown in Figure 3) was synthesized by Yanrong Shi.[4]

All synthesized compounds were characterized by gas chromatography used a mass spectrophotometer (GC/MS) on the Agilent 7890A GC system). The instrument's oven remained constant at 70°C (250°C at the injection port temperature), used a HP-5hs capillary column (50 m x 0.25 mm x 0.25 µm) with a.9 Column-1 Flow cal. All synthesized compounds were also characterized by ^1H NMR. Sample measurements were taken in chloroform using the

Varian 300MHz spectrometer. The dye compounds were analyzed on a HP 8453 UV Vis Spectrophotometer.

Step i

Compound A in Figure 2 was synthesized following the reported synthetic procedure.[5] Under N_2, reactant A (5,5'-Bis (trimethylsilole)-3,3'-dibromo-2,2'-dibromo-2,2-bithiophene) was placed in a three-neck round bottom flask and dissolved in 0.1 M tetrahydrofuran. The flask was then cooled in a dry ice/acetone bath to -78°C. After obtaining the desired temperature, 2.2 equivalents of n-butyl lithium were added dropwise. After thirty minutes of stirring at -78°C under N_2, 1.2 equivalents of di-n-octyl dichlorosilane were added into the reaction mixture. The flask was later removed from the ice bath and left to stir overnight to produce monomer B (5,5'-Bis (trimethylsilole)- 3,3'-dihexylsilylene-2,2'-bithiophene). To confirm product composition, samples were analyzed on the GC/MS. The reaction mixture was washed with water, extracted with ethyl ether and dried over anhydrous magnesium sulfate. The crude product was also purified through column chromatography. The reaction yielded 88.8% of compound B. At the end of the synthesis compound B appeared yellowish and oily.

Step ii

Step ii in reaction 2 was also based off of the same reaction referenced in step i.[5] Originally, step ii was not in the reaction scheme; the previous equation called for monomer B to be transformed directly into monomer D. However, each time the experiment was tried, monomer D was not produced, so step ii was inserted to remove both trimethylsilyl groups. Step ii's synthesis was conducted in a three-neck round bottom flask where monomer B was dissolved in tetrahydrofuran. Under N_2, N-Bromosuccinimide was added in portions to produce monomer C (5,5'-Dibromo-3,3'-dihexylsilylene-2,2'-bithiophene). After 30 min, the reaction mixture was extracted with ethyl ether, concentrated under pressure and purified through silicon column chromatography. After purification, the reaction was shown to produce an 87.2% yield.

Step iii

Step iii, illustrated in Figure 2, shows debromination of a dibromo dithienosilole and is based off a previous experiment.[6] To accomplish the debromination, monomer D was dissolved in excess propanol, and minute amounts of acetic acid and distilled water. The reaction mixture was refluxed at 110°C. After refluxing started, zinc was added in four portions 30 min after each other and left to react overnight. At the end of the experiment, monomer D (3,3'-dihexylsilylene-2,2'-bithiophene) was produced however, the product was not pure. To purify the mixture, the contents were extracted with ethyl ether and washed with water, saturated sodium bicarbonate, and brine. The solution was then dried with anhydrous magnesium sulfate and separated through silica gel column chromatography. After purification, the compound D was confirmed by GC/MS and the reaction was revealed to produce an 87.2% yield.

Step iv

Step iv (shown in Figure 2), the addition of a trimethyl-tin group and was based off a previous reaction.[7] In a 2-neck round bottom flask, the dithiosilole was dissolved by THF in a vacuum filled with nitrogen gas. The flask was placed in a dry ice/acetone bath at -78°C for 3 h. A small amount of the reaction mixture was added deuterium and checked in the GC/MS to confirm complete lithiation. After an additional 30 min at -78°C, trimethyltin chloride was added and allowed to reach room temperature naturally by letting the bath evaporate for 16 h.

Part II

The second part of the synthesis involves linking the squaraine dye and dithienosilole and creating the anchoring group as the final step. The squaraine dye (the first molecule shown in Figure 2) was synthesized by Yanrong Shi. The final target molecule shown in Figure 2 is the squaraine-dithienosilole dye. The synthesis of the squaraine-dithienosilole dye was largely based on a previous squaraine dye synthesized by Yanrong Shi.[4] The molecule synthesized by Yanrong is very similar to the desired product. The only difference is the x-bridge linkage between the squaraine dye and anchor group. Yanrong's x-bridge was a thiophene linkage. As stated previously, the change in linkage from thiophene to dithienosilole was in order to induce a bathochromic shift in the absorption spectra as well as to add more absorption coverage in the higher energy regions leading to a broader absorption.

Step v

In a two neck round bottom flask, the squaraine dye, trimethyltin chloride, and toluene were combined and left to stir under nitrogen gas for 15 min. Bis(triphenylphosphine) palladium chloride ($Pd(PPh_3)_2Cl_2$) was added and the mixture was heated at 90°C. After leaving the mixture for 16 h, the compound was poured into deionized water and extracted with dichloromethane. The compound was then purified through silica gel using dichloromethane first as the eluent. The eluent was then changed to ethyl acetate. The ethyl acetate fractions mixtures were rotovaped to obtain JJ-I-54.

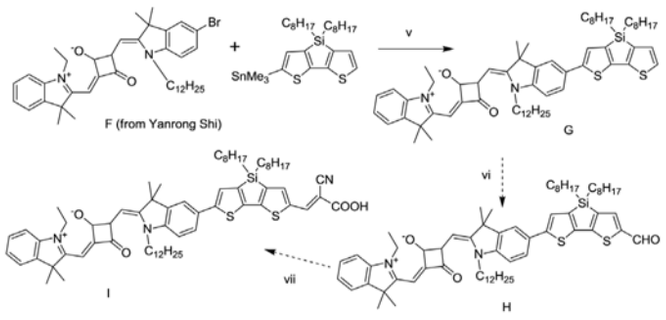

Figure 3: Synthesis of a squaraine-dithienosilole dye.

Results & Conclusions

The final compound JJ-I-54 was measured in UV-Vis spectrophotometer (Shown in figure 4) and shown to absorb around 665 nm (red - near-infrared region). This shows around a 25 nm bathochromic shift confirming the previous hypothesis that extending

the conjugation via x-bridge would shift the dye bathochromically in absorption and produce more coverage in the higher energy region of the dye absorption.

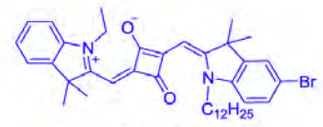

Sq- Br (from Yanrong Shi)

λ_{max}= 640 nm

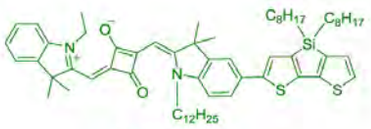

Sq-DTS (JJ-I-54)

λ_{max}= 665 nm

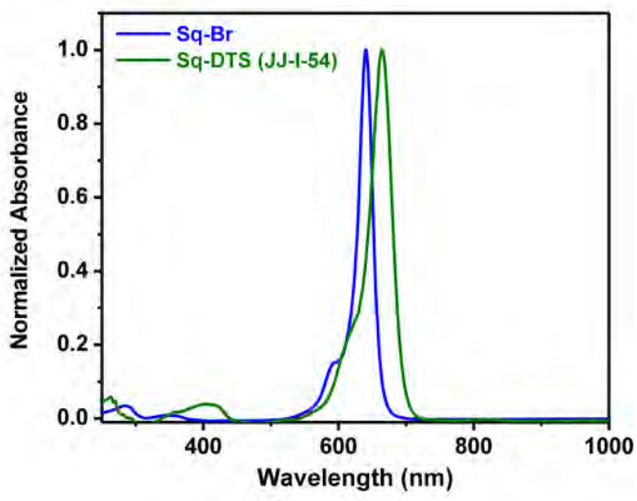

Figure 4: UV-Vis Absorption in CH_2Cl_2.

JJ-I-54 was also analyzed by the MALDI MS, with the corresponsing spectrum in Figure 5 confirms that the compound synthesized matches the molecular weight of the desired product. The nominal weight of the dye is 1008.5.

In the future, the anchor would need to be attached to the dye and x-bridge. After the desired molecule is produced it can be analyzed for solar cell efficiency in collaboration with another (namely the Grätzel) group.

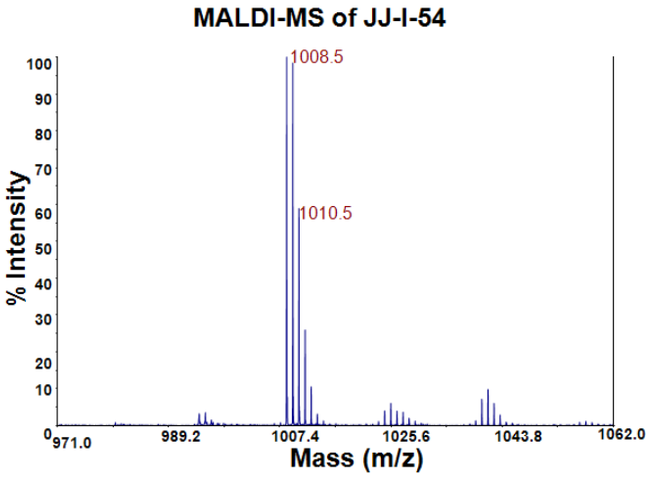

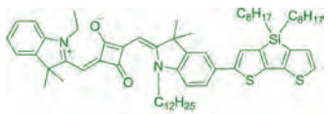

Sq-DTS (JJ-I-54)

Figure 5: Maldi MS of JJ-I-54.

References

1. Metal-Free Organic Dyes for Dye-Sensitized Solar Cells: From Structure: Property Relationship to Design Rules. Mishra, Amaresh, Fischer, Markus and Bäuerle, Peter. 2009, Angewandte Chemie International Edition, pp. 2474-2499.
2. Recent Advances in Sensitized Mesoscopic Solar Cells. Grätzel, Michael. 2009, Accounts of Chemical Research, pp. 1788-1798.
3. Molecular Designs and Syntheses of Organic Dyes for Dye-Sensitized Solar Cells. Ooyama, Yousuke and Harima, Yutaka. 2009, European Journal of Organic Chemistry, pp. 2903-2934.
4. Shi, Yanrong. Squaraine Sensitizers. Atlanta, Georgia : Georgia Institute of Technology School of Chemistry and Biochemistry, February 04, 2011.
5. Low Band Gap Dithieno[3,2-b:2',3'd]silole-Containing Polymers, Synthesis, Characterization and Photovoltaic Application. Huo, Lijun, et al. Berkeley : The Royal Society of Chemistry, 2009, The Royal Society of Chemistry, pp. 1-6.
6. Preparation of Organic Dyes Containing Different Heterocycle and Conjugated Units for Dye-Sensitized Solar Cells. Wang, P. et al. s.l. : Faming Zhuanli Shenqing Gongkai Shuomingshu, 2009, Vol. CN 101544845 A 20090930.
7. Tailoring Structure-Property Relationships in Dithienosilole-Benzothiadiazole Donor-Acceptor Copolymers. Beaujuge, Pierre M., et al.

Acknowledgments

I would like to thank Dr. Seth Marder and the Marder Group, especially Tissa Sajoto, for their outstanding support and help throughout the summer. I would like to thank Dr. Keith Oden, Olanda Bryant, Denisha Thomas, and Dr. Cam Tyson for giving me the opportunity to participate in this program. Finally, I would like to acknowledge the Center on Materials and Devices for Information Technology Research (CMDITR), the NSF Science and Technology Center No. DMR 0120967, and the 3M Corporation.

JULISHA JOYNER is currently a senior at North Carolina State University double majoring in Polymer & Color Chemistry and and Textile Engineering. After graduate school, she hopes for a career in engineering performance textiles and polymer coatings.

Synthesis, Crystal Growth and Characterization of New Chiral, Non-linear Optical Compounds

MAX KAGANYUK, University of Washington
Meghana Rawal, Werner Kaminsky, University of Washington

Introduction

As limitations of electronic signal processing are being reached, electro-optics are gaining more attention. The study of electro-optics deals with interactions between electrical and optical fields. Non-linear optics arise when interactions are non-linear. The focus of this paper is the relationship between molecular structure and non-linear effects in crystals. These effects have several applications in electro-optic modulation, telecommunication and frequency conversion. To investigate this relationship a series of structurally similar compounds were synthesized and characterized via NMR and x-ray diffraction. These compounds are either thiocarbamates prepared by reacting aryl iso-thiocyanates (ITC) with an enantiopure chiral alcohol, 2(S)-butanol, or they are thioureas which result upon the reaction of the aryl ITC with (S)-α-methylbenzylamine (MBA). The chirality of the starting material ensures the creation of molecules that are non-centrosymmetric, a required feature for a crystal to exhibit NLO properties. A lack of a center of symmetry removes the cancellation of non-linear responses in a molecule. The crystallization of the products is supported by the thiocarbamates and thioureas, which promote the formation of dimers through selected hydrogen bonding. Also, sulfur atoms in the products scatter X-rays well, allowing the definite determination of the products' structures via X-ray Diffractometry (XRD). For further characterization, these structures serve as input data for numerical model calculations of optical properties. Experimentally, it is difficult to measure NLO features in crystals; however, they can be calculated from a structure with electronic atomic polarizabilities as empirical input parameters. These models give detailed tensorial information on refractive indices, optical rotation, electro-optic coefficients and second harmonic generation (SHG) efficiency. The software was specifically developed to be applicable to crystals. Calculated properties were compared to Kurtz test results. These experimental measurements of SHG efficiency are compared to a standard electro-optic crystal, potassium dihydrogen phosphate (KDP). The overall goal is to observe how the NLO features in the compounds differ, as they vary slightly in structures. This would contribute to the understanding of the relationship between structure and NLO properties in crystals. For structural comparison, thiocarbamates were also prepared from a racemic mixture of 2-butanol, which resulted in centro-symmetric crystals.

Experimental Methods

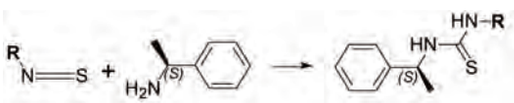

Scheme 1: Synthesis of Thioureas.

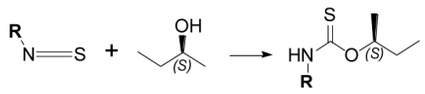

Scheme 2: Synthesis of Thiocarbamates.

	Compound	R	Scheme
1.	mk1-69	4-methoxyphenyl	1
2.	mk1-95	phenyl	1
3.	mk1-77	4-chlorophenyl	2
4.	mk1-73	4-nitrophenyl	2
5.	mk1-81	4-flurophenyl	2
6.	mk1-105	4-nitrophenyl	2*
7.	mk1-91	4-methoxyphenyl	2
8.	mk1-111	4-bromophenyl	2
9.	mk1-109	4-methoxyphenyl	2*
10.	mk1-107	phenyl	2*

Table 1: Compound Synthesized.
*racemic 2-butanol used instead of enantiopure 2(S)-butanol

Synthesis of compound 1 and 2.

A 4 mL vial was charged with a stir bar and cooled to 0°C in an ice bath. The aryl ITC (0.20 g, 1.2 mmol) was added to the vial and allowed to cool for 1 minute. MBA (0.29 g, 2.4 mmol) was added drop wise over a period of 30 seconds. The reaction was allowed to warm up over a period of 1 hour and tracked by thin layer chromatography (TLC) until all of the aryl ITC was consumed. The crude product was purified by flash column chromatography, eluting with 2:3 ethyl-acetate:hexanes. Factions were collected in 13x100mm test tubes and were spotted for TCL to locate the product. The fractions containing the product were rotovaped in a 25 mL round bottom flask to isolate the product. Compound 1: ^{1}H NMR (300 MHz, $CDCl_3$): δ 7.7209 (bs, ^{1}H), 7.2475 (m, 5H), 7.135 (d, J= 8.4 Hz, 2H), 6.929 (d, J= 8.4 Hz, 2H), 6.0468 (bs, 1H), 5.6839 (bs, ^{1}H), 3.8256 (s, 3H), 1.5302 (d, J=6.8 Hz, 3H). Compound 2: ^{1}H NMR (300 MHz, $CDCl_3$): δ 8.8139 (bs, ^{1}H), 7.3262 (m, 10H), 6.4061 (bs, ^{1}H), 5.7081 (bs, ^{1}H), 1.5452 (d, J= 6.9 Hz, 3H).

Synthesis of compounds 3-6

A 4 mL vial was charged with a stir bar, the aryl ITC (0.100 g, 0.555 mmol), and 2(S)-butanol (82.3 mg, 1.1 mmol). [For compound 6 the aryl ITC (0.200 g, 1.1 mmol) was reacted with racemic 2-butanol (.165 mg, 2.2 mmol).] Using a hot oil bath, the reaction was run at 108°C for 24 hours. After allowing the vial to cool, TLC was done to assure the completion of the reaction. Once the reaction was complete, the vial was covered with filter paper and left in the vacuum oven at 70°C. The crude product was purified by flash column chromatography, eluting with 1:4 ethyl-acetate:hexanes. Factions were collected in 13x100mm test tubes and were spotted for TLC to locate the product. The fractions containing the product were rotovaped in a 25 mL round bottom flask to separate the product. Compound 3: ^{1}H NMR (300 MHz, $CDCl_3$): δ 8.7150 (bs, ^{1}H), 7.2918 (d, J= 8.6 Hz, 2H), 7.2130 (bs, 2H), 5.5199 (m, 1H), 1.7269 (m, 2H), 1.3640 (d, J= 6.2 Hz, 3H), 0.9472 (t, J= 7.4 Hz, 3H). Compound 4: ^{1}H NMR (300 MHz, $CDCl_3$): δ 9.2638 (bs, 1H), 8.1926 (d, J= 7.1 Hz, 2H), 7.5520 (bs, 2H), 5.5528 (m, 1H), 1.7044 (m, 2H), 1.4038 (d, J= 6.3 Hz, 3H), 0.9634 (t, J= 7.4 Hz, 3H). Compound 5: ^{1}H NMR (300 MHz, $CDCl_3$): δ 8.8978 (bs, 1H), 7.2240 (bs, 2H), 7.0147 (t, J= 8.5 Hz, 2H), 5.0768 (m, 1H), 1.7280 (m, 2H), 1.3461 (d, J= 6.5 Hz, 3H), .9316 (t, J= 7.5 Hz, 3H). Compound 6: 1H NMR (300 MHz, (CD3)2CO): δ 10.3592 (s, 1H), 8.2148 (d, J= 7.4 Hz, 2H), 7.8926 (bs, 2H), 5.4897 (m, 1H), 1.7044 (m, 2H), 1.3557 (d, J= 6.1 Hz, 3H), 0.9358 (t, J= 7.4 Hz, 3H).

Synthesis of compounds 7-9

A 4 mL vial was charged with a stir bar and 2(S)-butanol (0.054 g, 0.726 mmol). [For compound 9 racemic 2-butanol (.054 mg, .726 mmol).] While stirring, triethylamine (0.011 g, 0.109 mmol) was added. After 5 min, the aryl ITC (0.100 g, 0.605 mmol) was added drop wise. The reaction was allowed to react for 24 h at 85°C. TLC was done to assure the completion of the reaction. Once the reaction was complete, the vial was covered with filter paper and left in the vacuum oven at 70°C. The crude product was purified by flash column chromatography, eluting with 1:4 ethyl-acetate:hexanes. Factions were collected in 13x100mm test tubes and were spotted for TLC to locate the product. The fractions containing the product were rotovaped in a 25 mL round bottom flask to isolate the product. Compound 7: ^{1}H NMR (300 MHz, (CD3)2CO): δ 9.7438 (s, 1H), 7.5813 (m, 2H), 6.9070 (d, J= 9.1 Hz, 2H), 5.4819 (bs, 3H), 3.7847 (s, 3H), 1.7022 (m, 2H), 1.2948 (s, 3H), 0.9184 (t, J= 7.4, 3H). Compound 8: ^{1}H NMR (300 MHz, $(CD_3)_2CO$): δ 10.115 (bs, 1H), 7.5386 (d, J= 7.0 Hz, 2H), 6.8768 (d, J= 8.6 Hz, 2H), 5.4904 (m, 1H), 1.7394 (m, 2H), 1.3332 (d, J= 6.0 Hz , 3H), 0.9388 (t, J= 7.4 Hz, 3H). Compound 9: ^{1}H NMR (300 MHz, (CD3)2CO): δ 9.7462 (bs, 1H), 7.5826 (m, 2H), 6.8412 (d, J= 9.1 Hz, 2H), 5.4990 (m, 1H), 3.7866 (s, 3H), 1.7012 (m, 2H), 1.3056 (d, J= 5.9 Hz, 3H), 0.9172 (t, J= 7.4 Hz, 3H).

Synthesis of compound 10

A flame dried 5 mL round bottom flask was charged with a stir bar. The flask was evacuated and backfilled with nitrogen. With a nitrogen flow, 2-butanol (0.219 g, 2.96 mmol) was added, followed by dry tetrohydrofuran (1 mL) obtained from the solvent dispensing system. Sodium hydride (0.0781 g, 3.25 mmol) was then added slowly. After adding the phenyl ITC (0.200 g, 1.48 mmol) the reaction was left to react overnight. The whole time the reaction was kept under nitrogen to avoid interaction between the sodium hydride and air. TLC was used to track the reaction. When the aryl ITC was complete, the product was left under vacuum overnight. A clear liquid was produced. Compound 10: ^{1}H NMR (300 MHz, $(CD_3)_2CO$): δ 9.9225 (bs, 1H), 7.3209 (m, 5H), 5.5038 (bs, 1H), 2.0499 (bs, 2H), 1.3020 (d, J= 8.4 Hz, 3H), .9311 (t, J= 7.4 Hz, 3H).

Recrystallization of compounds 1 and 3-9 for XRD

Once the product was isolated from column chromatography, it was left under vacuum on the Schlenk line overnight. Once removed from the Schlenk line, a solid was present in the round bottom flask. In a 1 mL vial, the product was dissolved in a 1:4 solution of methanol and ethanol. The vial was covered with aluminium foil and left on a shelf. To allow slow evaporation of the solvent a needle sized hole was punctured into the foil. The vial was left alone until crystals were observed.

Recrystallization of compound 2

Once the product was isolated from column chromatography, it was left under vacuum on the Schlenk line overnight. Once removed from the Schlenk line, a clear liquid was present in the round bottom flask. The liquid was transferred to a vial and allowed to sit at room temperature, until the formation of crystals, which occurred after two weeks.

Results and Discussion

After obtaining crystals of the newly synthesized compounds, characterization was done via XRD and software specifically developed to be applicable to crystals. Due to time constraints, the focus was narrowed to structure determination, morphology observations, and the calculation of the electro-optic effects. Also not all the compounds synthesized were characterized. Compound 10 was successfully synthesized; however, it was lost when it was left in the vacuum oven overnight. Compounds 3, 6, 8 and 9 are currently in the process of recrystallization and have not been characterized. A compound previously synthesized and characterized by a former REU student, Joel Zazueta, was brought in for comparison and will be referred to as compound 11.

Structures determined via XRD

The determination of the compounds' structures was done with a Bruker APEX II single crystal X-ray diffractometer. The structures obtained were of good quality.

In all the structures above, dimers are formed through the same selected hydrogen bonding. It is important to note that a non-centrosymmetric compound still remains. Since the products formed are enantiopure, only one enantiomer is present and the possibility of a center of inversion is avoided. The structural data obtained is used to calculate the electro-optic effect and other NLO features

Indexed Morphologies

The morphology of a crystal illustrates the shape and symmetry of

its crystal lattice. With the use of the WinxMorph software package, the morphologies of the crystals were indexed. Though morphologies have little impact on a compound's NLO features, they are results of a compound's structure.

Compound	Structure
1.N-(4-methoxyphenyl)-N-[1(S)-1phenylethyl]-thiourea	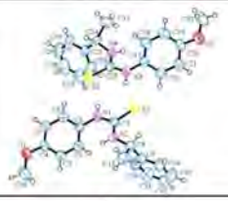
2.N-(phenyl)-N-[1(S)-1phenylethyl]-thiourea	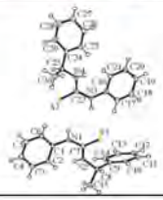
4. *i*-butyl-N-(4-nitrophenyl) thiocarbamate	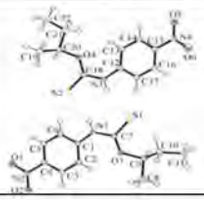
5. *i*-butyl-N-(4-flurophenyl) thiocarbamate	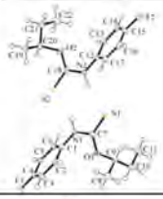
7. *i*-butyl-N-(4-methoxyphenyl) thiocarbamate	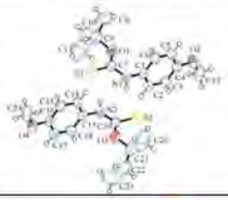
11.N-(4-nitrophenyl)-N-[1(S)-1phenylethyl]-thiourea	

Table 2: Structures determined from XRD measurements.

Indexed Morphologies

The morphology of a crystal illustrates the shape and symmetry of its crystal lattice. With the use of the WinxMorph software package, the morphologies of the crystals were indexed. Though morphologies have little impact on a compound's NLO features, they are results of a compound's structure.

Compound	Morphology	Crystal System	a (Å)	b (Å)	c (Å)
1		Monoclinic	8.78	8.28	21.4
2	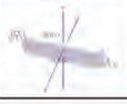	Monoclinic	15.6	6.01	16.0
4		Monoclinic	16.1	4.76	16.9
5		Monoclinic	6.97	20.2	8.28
7		Monoclinic	6.80	21.7	9.25
11		Triclinic	7.74	8.27	13.6

Table 3: Indexed morphologies.

The newly synthesis compounds all exhibit a monoclinic crystals structure, space group $P2_1$ with a twofold screw. It is observed that the largest crystal growth occurs along the shortest axis in the unit cell. This results in needle shaped crystals. When the two shorter axes are close in length, plate shaped crystals are observed as growth occurs in the direction of these two axes. This is due to the energetically enhanced crystal formation along shorter, hence stronger bonds. In compound 11, the crystal structure is triclinic. The only symmetry in this crystal is transitional symmetry.

Electro-optic Tensor Calculations

Using the OPTACT program, the electro-optic effects were calculated. This program needs the atomic structure and electronic polarizability volume parameters as input data. Each element, (H, C, S, O, N), reacts differently to light, represented by a polarizability value. A larger value indicates a stronger interaction with light. Polarizability values used for C, H, N, O, S were 0.09, .07, 0.005, 2.5, 5.3, respectively. Other elements were given standard values. The electro-optic tensors calculated with the OPTACT_DES program are rendered graphical to representations how the refractive index varies in the presents of an electric field. Since the crystals are anisotropic, the effects dependent on the orientation of the crystal and its alignment with the applied electric field. The calculations are also normalized to the dielectric constant. The validity of these calculations can be verified by comparing experimental SHG measurements to calculated values. Though not done for the newly synthesis compounds, SHG calculations were done previously on the earlier synthesized compound 11. Based on these calculations compound 11 should have a SHG efficiency three times greater than the standard, potassium dihydrogen phosphate (KDP). This was shown to be true, experimentally, by subjecting the compound to the Kurtz test.

Compound	Electro-Optic Tensor	Largest r-coefficient estimate
1	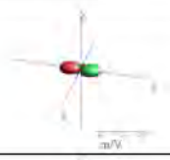	10 pm/V
2	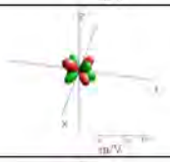	10 pm/V
4		10 pm/V
5	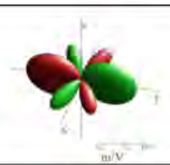	20 pm/V
7	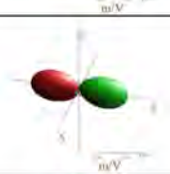	15 pm/V
11	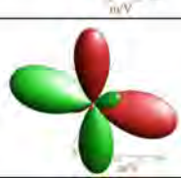	30 pm/V

Table 4: Electro-optic Tensors.

The largest r-coefficient is determined by assuming a realistic dielectric constant of 10 for the compounds. This is a safe assumption, as it prooves compound 11 to have a coefficient of 30 pm/V, which is three times greater than KDP (r ≈ 10 pm/V). SHG is related to the electro-optic effect through a Kleinman relation in which similar to our procedure, the electro-optic tensor is scaled to the SHG one via the dielectric constant. In the thioureas it can be seen that a more electronegative substitute, NO_2, yields a greater NLO response, by creating a larger inducible dipole. However, there appears to be little change in NLO features between compounds 1 and 2. In the thiocarbamates, no distinct pattern arises among the three compounds characterized. Compound 5, which has a highly electronegative substitute, F, has a high NLO response. This would suggest that compound 4's behavior would increase as its substitute is more electrons withdrawing. Instead, the NLO response decreases sharply. Also compound 7 has a greater effect than compound 4, though its substitute acts more as an electron donor. Thus the lattice symmetry must have a profound influence on the NLO where dimer formation and additional symmetry elements tend to quench NLO effects.

Conclusions

Of the ten compounds synthesized, five were optically characterized. Though no distinct trends were observed in the molecules in this paper, we plan to finish characterizing the compounds which are currently in the process of recrystallization. We are specifically interested in how the electro-optic effect varies in compounds 3, 5 and 8, where the substitutes are different halogens. In the future more compounds will be synthesized to observe patterns in a larger number of compounds. Also, we would like to obtain more experimental measurements to confirm our calculations, for example via the Kurtz test.

References

1. Kaminsky, W.; Responte, D.; Daranciang, D.; Gallegos, J. B.; Tran, B. N.; Pham, T. Structure, Morphology and Optical Properties of Chiral N-(4-Xphenyl)-N-[1(S)-1-phenylethyl]thiourea, X= Cl, Br, and NO2. Molecules 2010, 15, 554-569.
2. Sakamoto, M.; Yoshiaki, M.; Takahashi, M.; Fujita, T.; Watanabe, S. Photochemical Isomerization of O-Allyl and O-but-3-enyl Thiocarbamates. J. Chem. Soc. Perkin Trans 1995, 1, 373-377.
3. Kang, H.; Evmenenko, G; Dutta, P; Clays, K; Song, K; Marks, T. X-Shaped Electro-Optic Chromophore with Remarkably Blue-hifted Optical Absorption, Synthesis, Characterization, Linear/ Monlinear Optical Properties, Self-Assembly, and Thin Film Microstructural Characteristics. J. Am. Chem. Soc. 2006, 128, 6194-6205.
4. Bost, R; Andrews, E. Sulfer Studies. XIX. Alkyl Esters of Phenylthiocarbamic Acid. J. Am. Chem. Soc. 1943, 65 (5), 900-901.
5. Cesarini, S; Spallarossa, A; Ranise, A; Fossa, P; La Colla, P; Sanna, G; Collu, G; Loddo,R. Thiocarbamates as non-nucleoside HIV-1 reverse transcriptase inhibitors. Part 1: Parallel synthesis, molecular modeling and structure-activity relationship studies on O-[2-(hetero)arylethyl]-N-phenyl-thiocarbamates. Bioorg Med Chem. 2008, 16 (7), 4160-4172.
6. Hulme, K. F. Nonlinear optical crystals and their applications. Rep. Prog. Phys. 1973, 36, 499-534.
7. Kleinman, D. A. Nonlinear Dielectric Polarization in Optical Media. Phys. Rev. 1962. 126(6), 1977-1979.
8. Wang, F. Calculation of the electro-optical and nonlinear optical coefficients of ferroelectric materials from their linear properties. Phys. Rev. 1998. 59(15), 9733-9736.

Acknowledgments

This work was funded by the National Science Foundation (NFS) through the following grants:

NSF Science and Technology Center on Materials and Devices for Information Technology Research No. DMR 0120967 and NSF Research Experiences for Undergraduates Program Hooked on Photonics No. CHE 0851730. The authors would like to thank Donald Responte, Joel Zazueta, Dan Daranciang and Joe Gallegos for the previous work on this project. Also, special thanks to April Wilkinson and all the members of the Larry Dalton research group at the University of Washington.

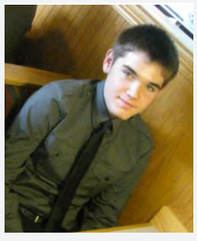

MAX KAGANYUK is currently a junior in the Department of Chemical Engineering at the University of Washington. At this point, he is considering graduate school to purse a doctoral degree in Chemical Engineering.

Characterization of Hole Only Devices for Organic Light Emitting Diode (OLED) Development

FARHAN KAMILI, Emory University
Wojciech Haske, Canek Fuentes-Hernandez, Bernard Kippelen, Georgia Institute of Technology

Introduction

Organic electronics, electronics that use organic polymers or small molecules in place of semiconductors, have the potential to replace or complement their traditional inorganic counterparts in many areas or electronics. This is mainly because of their mechanical properties; they are light weight, flexible, and relatively easy to process, which translates to lower production costs. In particular, there is large potential in using organic light emitting diodes (OLEDs) for display screens and lighting solutions. High efficiency OLEDs consist of multiple organic layers, which must have specific electronic properties depending on the function they play in the device.[1]

The working principle of an OLED is based on charge injection followed by recombination and radiation of light. This process is illustrated in Figure 1. An OLED device is composed of layers of organic thin films sandwiched between two electrodes, a cathode and an anode. When a voltage (V) is applied between the cathode and anode, electrons are transported from the cathode into the electron injection layer (EIL), and holes (i.e. "positive charge",) are transported from the anode into the hole injection layer (HIL). The electron transport layer (ETL) and the hole transport layer (HTL) carry the electrons and holes, respectively, into the emissive layer (EML). The charge combination of electrons and holes in the EML forms an exciton, which decays by emitting a photon either by fluorescence or phosphorescence (shown in green in Figure 1).

In a conventional OLED architecture, the light is emitted out of the device through a transparent anode, like indium-tin oxide (ITO), which is deposited on top of glass or a transparent plastic substrate. The top electrode is usually made from a highly reflective metal, e.g. aluminum (Al). Most organic layers in phosphorescent OLEDs are under a hundred nanometers thick.

Each of the materials used in OLEDs must be selected appropriately. The anode is selected so that its work function is desirable for injecting holes into the valance or highest occupied molecular orbital (HOMO) level of the HTL. The electrode work function can often be adjusted to some extent by using an injection layer. Most metals used as anodes have relatively low work functions compared to the HOMO level of the hole transport material, creating an energy barrier between the electrode and the HTL. Therefore an injection layer is used to decrease this energy barrier, thus increasing charge injection. Another reason for implementing HIL is to smooth the surface of the electrode. Even if the work function of the anode is suitable for injection into the HTL, rough morphology of the anode can create unwanted spikes in current. An intermediate HIL can be used to reduce these spikes.

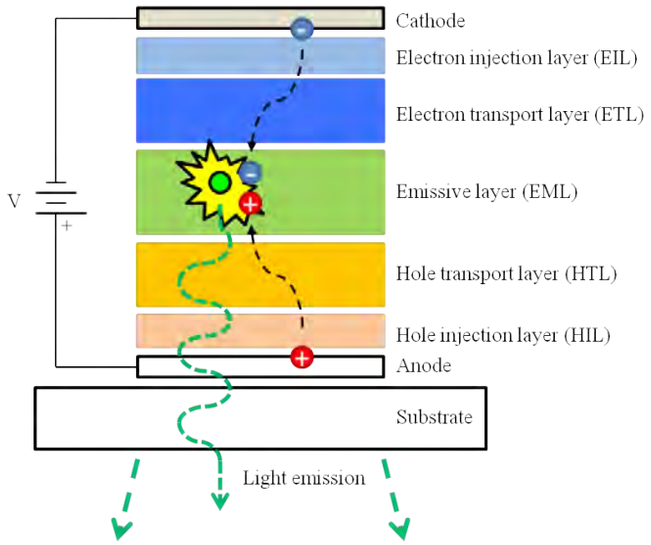

Figure 1: Structure and working principle of OLEDs.

The hole transport material is selected for its charge mobility properties and its HOMO level. Charge mobility is velocity of charges per voltage applied to a material. If the current is not limited by the injection barrier, which can be caused by the mismatch of the electrode work function and the HTL transport level (HOMO), then the intrinsic material charge mobility dictates current density in the device per applied voltage.

The emissive layer is selected based on its light emission and electronic properties. It is a combination of an organic charge transport material doped with a phosphorescent or fluorescent dye. The cathode, EIL, and ETL serve similar purposes as the anode, HIL, and HTL, respectively, except these considerations are for electrons instead of holes. In this case, the transport levels for electrons are the LUMO levels of the organic materials.

Figure 2 shows example energy levels of different layers and illustrates how each layer helps in overall charge transport of a full OLED device. In this figure, the black bars represent the work functions of the electrodes, the blue bars represent the LUMO levels, and the red bars illustrate HOMO levels.

Two key considerations in the development of efficient OLEDs are charge balance between the holes and electrons and the turn-on voltage. When the electrons and the holes move through the organic layers, it is important that they recombine in the EML. If there is an

imbalance of the hole and the electron current densities, then the charge recombination could shift into one of the other layers instead, which can lead to inefficient devices. In theory, charge densities are governed by the charge mobilities of the transport layers and the energy barrier of the injection layers of a device. However, in practical applications, interface interactions, like dipole formations, diffusion during fabrication, or morphology of the films at the interface, can strongly influence the current densities of a device. Furthermore, low turn-on voltage is highly desired in OLED devices. It can provide greater efficiencies and lower power consumption, which is important in large scale applications. Turn-on voltages are influenced by the energy barriers in the devices.

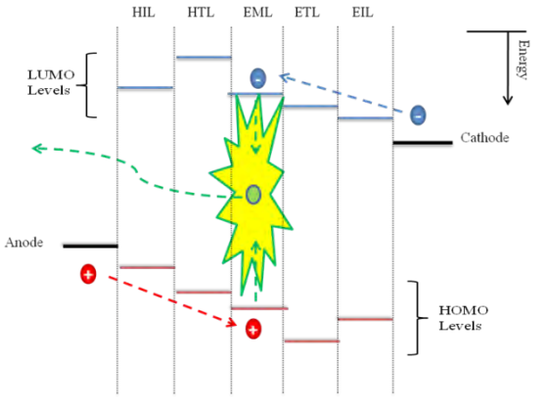

Figure 2: Energy level diagram of OLED layers.

Objective and Motivation

The goal of this experiment is to characterize the current density-voltage (J-V) behavior of hole only devices. A hole only device is one that transports holes from the anode through the HOMO levels of the HIL and HTL to the cathode of the device. The cathode is chosen to inhibit the injection of the electrons into the LUMO level of the hole transport material. A sample structure of such a hole only device is shown in Figure 3.

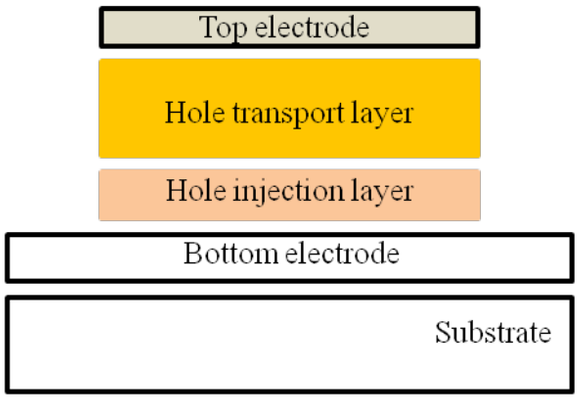

Figure 3: Schematics of a hole only device.

By comparing the J-V characteristics of the devices comprised of HTL/HIL layers in various combinations, one can gather information about the relative performance of one HIL/HTL layer combination over another. Another critical use of J-V characteristics is selecting electron transport and injection materials with similar electrical characteristics as the hole transport and injection materials when developing OLEDs. This is done in order to ensure charge balance in the devices, which leads to greater efficiency devices.

Materials

In this experiment, we considered three hole transport layers with two injection layer combinations, giving a total of six different devices. The hole transport layers were PVK (poly(*N*-vinylcarbazole)), α-NPD (4,4-bis[N-(1-naphthyl)-N-phenyl-amino]biphenyl), and CBP (4,4'-*N,N*'-dicarbazole-biphenyl). These are three well researched and widely used transport layers.[2,3,4] The two hole injection layers were PEDOT: PSS (poly(3,4-ethylenedioxythiophene): poly(styrenesulfonate)) and molybdenum trioxide (MoO_3). PEDOT: PSS is a commonly used injection layer for both its HOMO level and for its smooth morphology.[4] MoO_3 was chosen as an HIL due to the recent report by Meyer and Kahn showing that MoO_3 is better charge injector than PEDOT: PSS for the hole transport material TFB (poly(9,9'-dioctylfluorene-co-bis-N,N'-(4-butylphenyl) diphenylamine)).[2] The structure and energy levels of the hole transport and injection materials used in this experiment is shown in Figure 4.

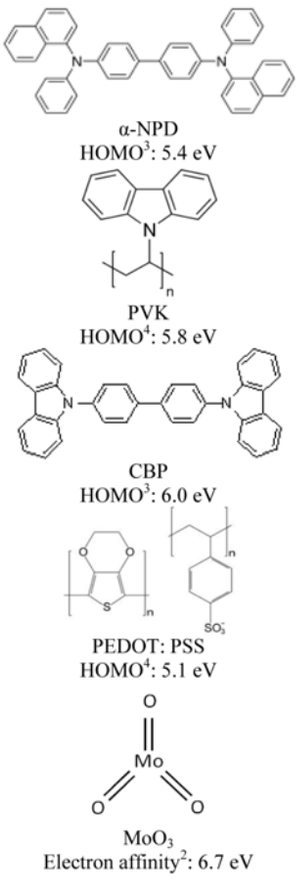

Figure 4: Structure and energy levels of the hole transport materials (a-NPD, PVK, and CBP) and hole injection materials (PEDOT: PSS and MoO_3).

For all of the devices fabricated in this experiment, oxygen plasma treated ITO was used as the anode and Al was used as the cathode.

The energy levels of all the materials used in this experiment are plotted in an energy level diagram in Figure 5.

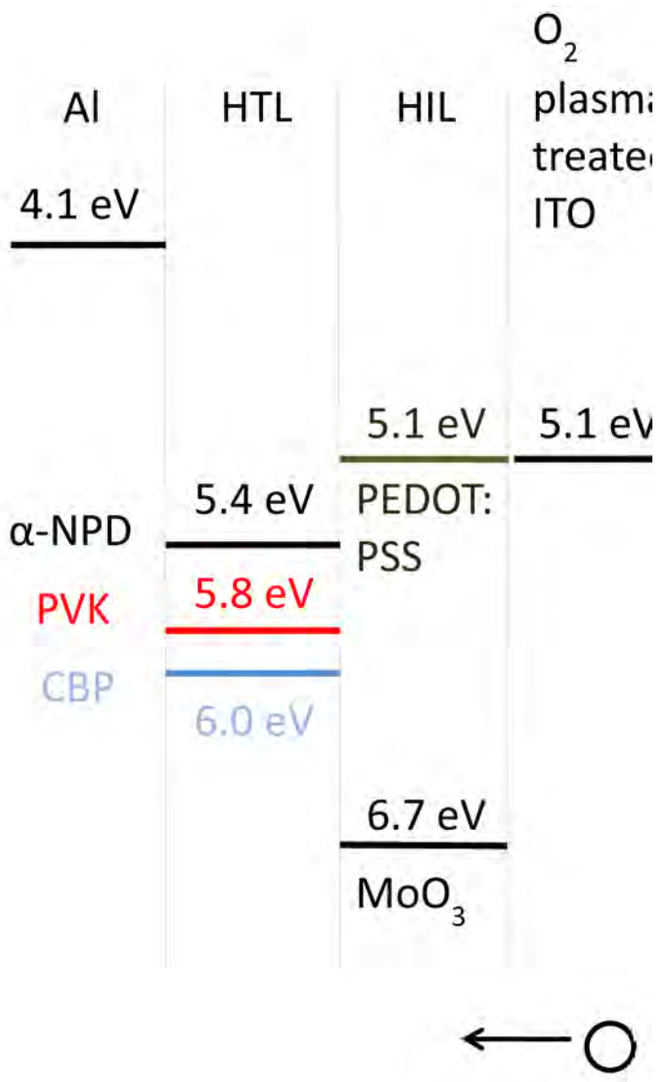

Figure 5: Energy levels of materials used in this experiment. The diagram shows the electron affinity of MoO_3, the work functions of Al and O_2 plasma treated ITO, and the HOMO levels of the organic molecules α-NPD, PVK, CBP, and PEDOT: PSS.

Methods

Figure 6 shows the completed structure and thicknesses of the hole only devices.

Fabrication of the devices involved cutting glass coated with ITO into 1 in x 1 in slides. The slides were then cleaned in a mixture of distilled water and soap, then distilled water, followed by acetone, and finally with isopropyl alcohol by ultrasonication for 20 min in each step.

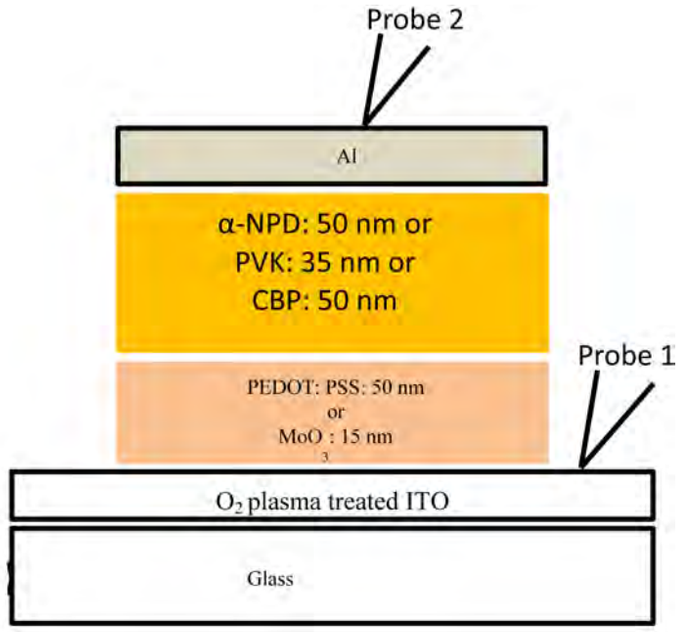

Figure 6: Structure and thickness of hole only devices fabricated in this experiment. The probes show how the measurements were performed.

After the cleaning process, the slides were O_2 plasma treated for two minutes, which increases the work function of ITO to 5.1 eV.[6] They were then immediately taken to a nitrogen filled glove box. PEDOT: PSS was spin-coated at 1500 rpm for one minute onto the ITO to create the thin film layer. These slides were dried on a hotplate set at 140°C for 15 min to remove solvent from the film. When MoO_3 was used as HIL instead of PEDOT: PSS, the O_2 plasma treated slides were transported to a thermal vacuum deposition system, where the MoO_3 was deposited at a rate of 0.2 Å/s.

Subsequently, the HTLs were deposited on top of the hole injection materials. Slides requiring PVK had the material spin coated on top of the injection layer at 1500 rpm for one minute. These slides were then dried on a hotplate at 120°C. For the slides requiring either α-NPD or CBP, these materials were deposited by thermal vacuum deposition. In the final process, Al was deposited also by thermal vacuum deposition on all the slides with a shadow mask, defining the size of the evaporated electrodes. The mask produced devices of two different areas, 1 mm^2 and 0.25 mm^2, as shown in Figure 7.

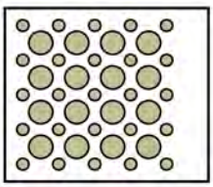

Figure 7: Top view of completed hole only device substrate.

The slides were then transferred to a glove box with an electrical probe apparatus. A voltage difference was applied to each individual device so that the bias was applied to the bottom electrode, as shown

in Figure 5. The output current data was collected in custom written LabVIEW program. The current density was calculated by dividing the current by the area of the device.

We measured eight small individual devices of each slide type, with each device tested three times. Of this data, the most consistent and failure free data was selected and averaged. It is this averaged data that is shown in the results section of this paper. For all of the slides and devices, the appropriate voltage range to test the devices over was selected by ensuring that the devices reached at least ~1 mA of current output, but did not breakdown. This data was then analyzed and plotted using the Origin plotting software.

Results

The data gathered from the experiment are shown in Figures 8 and 9. Note that these two figures show the same data sets, but plotted in two different ways.

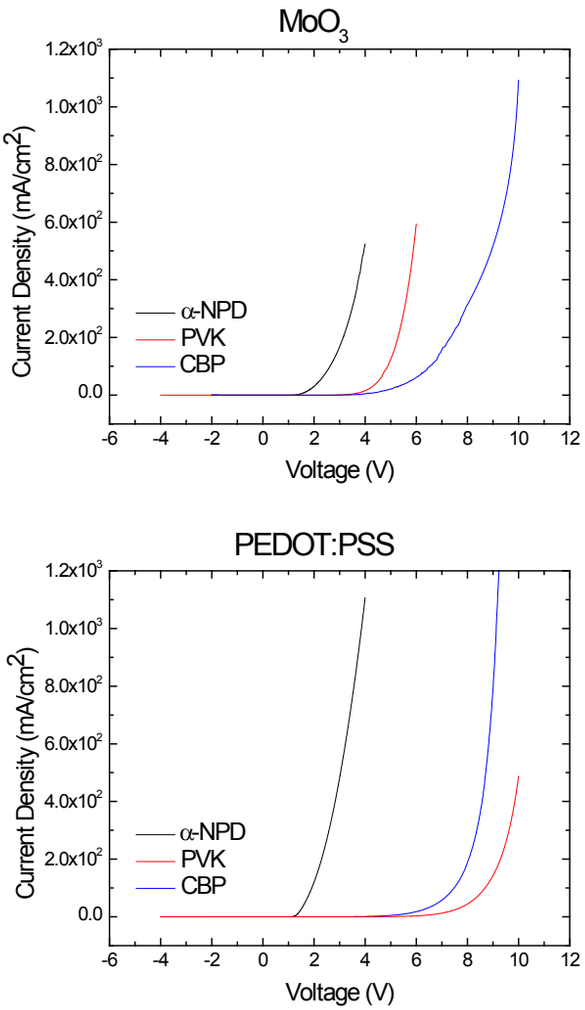

Figure 8: J-V characteristics of hole only devices with (a) MoO_3 and (b) PEDOT: PSS as injection layers, each of the plots showing results of devices with α-NPD, PVK, and CBP as the HTL.

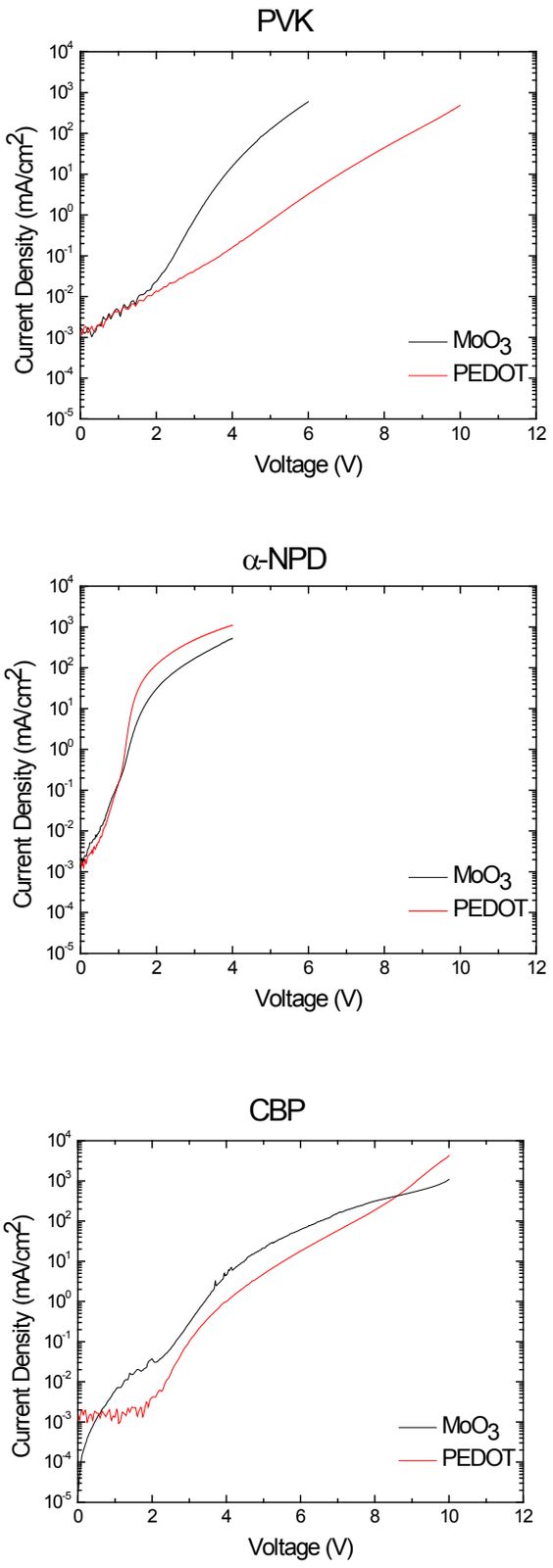

Figure 9. J-V characteristics of hole only devices with (a) PVK, (b) α-NPD, or (c) CBP as the HTL and with varying injection layers. Note that the current density is plotted on a log scale, while the voltage is plotted on a linear scale.

Discussion and Conclusions

From Figures 8(a) and (b), it is can be seen that α-NPD has lowest turn on voltage (~2 V) of the three transport materials. The turn on voltage of PVK shifts form 4 V with MoO3 to 8 V with PEDOT: PSS. There is a correlation between the turn on voltages, for the devices with MoO_3, and the HOMO level of the materials. The lower the HOMO level of the material, the lower its turn on voltage. This is not the case for the devices with PEDOT: PSS.

Figure 9(a) shows that α-NPD has slight decrease in charge densities for devices with MoO_3 as the hole injection layer. Figure 9(b) shows that PVK has significantly higher charge densities in devices with MoO_3 than with PEDOT: PSS. The results of CBP are unclear from Figure 9(c). From these figures, we can conclude that MoO_3 is a better charge injector for PVK only out of the three studied transport materials.

From Figure 5, it can be seen that MoO_3 has a higher electron affinity than HOMO levels of all three transport materials. This implies that MoO_3 should be a better charge injector than PEDOT: PSS for all the tested HTLs. However, as mentioned in the introduction, interface interactions of layers are an important factor in charge injection, and they can influence the relative position of the energy bands. Interface interactions are the most likely reason we do not see the expected increased charge injection when using MoO_3 with α-NPD or CBP.

References

1. S. Kappaun, C. Stefan, C. Slugovc, and E. J. W. List. Int. J. Mol. Sci. 2008, 9, 1527-547.
2. J. Meyer, and A. Kahn. J. Photon. Energy 2011, 1, 011109.
3. M. A. Baldo and S. R. Forrest. Phys. Rev. B 2000, 62, 10958.
4. F. So, B. Krummacher, M. K. Mathai, D. Poplavskyy, S. A. Choulis, and V.-E. Choong. J. Appl. Phys. 2007, 102, 091101.
5. H. Y. Yu, X. D. Feng, D. Grozea, Z. H. Lu, R. N. S. Sodhi, A-M. Hor, and H. Aziz. Appl. Phys. Lett. 2001, 78, 2595.
6. M. Yoshida, S. Mitui, N. Kobayashi, R. J. Hrohashi. Polym. Sci. Part B: Polym. Phys. 1999, 37, 61–69.

Acknowledgments

I would like to acknowledge the Center on Materials and Devices for Information Technology Research (CMDITR), the NSF Science and Technology Center No. DMR 0120967 for providing funding and support for this project.

FARHAN KAMILI is a senior at Emory University majoring in applied physics and applied mathematics. He plans on attending graduate school in applied physics or a related field following graduation.

Impact of Processing Method in the Fabrication of High Energy Density Nanocomposites Based on Surface-Modified $BaTiO_3$ and a Ferroelectric Polymer

ADRIENNE-ELAINE LAMPTEY, Clark Atlanta University
Yunsang Kim, Joseph W. Perry, Georgia Institute of Technology

Introduction

In today's world, technology has evolved and come to be better than ever. At some point with more technology, there is an even bigger need for electricity to take things to the next level and make it last longer and stronger. Capacitors are often used for this purpose and now need a higher density to work efficiently with new and improved equipment. Conventional capacitors are made of biaxially-stretched polypropylene film or stacks of thin ceramic film. Currently, polymer-metal oxide nanocomposites are of great interest because they are thin and light, easily processable in solution. Theoretically they can also achieve higher energy density. A previous study[1] incorporating surface-modified $BaTiO_3$ nanoparticles into a ferroelectric polymer, poly(vinylidene fluoride-co-hexafluoro propylene) (PVDF-HFP), achieved energy density of 3.2 J/cm^3. The authors utilized spin casting, which is a traditional way of fabricating films from solutions. Although spin casting is less time consuming and easy to use, it causes high porosity when it comes to higher loading of nanoparticles. This increased porosity may eventually lead to a decrease of breakdown strength. Alternative to spin casting, blade casting can be used to fabricate films of uniform thickness from solutions. In this technique, a blade is first placed at a fixed distance from the substrate before applying the coating solution. Finally the blade is pushed linearly across the substrate. When blade casting is used for the fabrication of dielectric films, the evaporation rate of the solvent is much slower than that of spin casting. That means the polymer chain in the solution will have enough time to relax and reach its equilibrium state, which is more favorable for densifying the structure and reducing its porosity. In this work, we will explore the impact of different processing methods for the fabrication of polymer-metal oxide nanocomposites for high-voltage applications. Both blade and spin casting will be used to compare physical properties of the films such as thickness, surface morphology, and porosity. Dielectric properties such as permittivity, breakdown strength, and energy density will also be assessed on films prepared by both methods.

Experimental Methods

Preparation of nanoparticle and polymer mixture

Barium titanate is an inorganic oxide with typical polar and hydrophilic properties. The surface modification of the oxide is necessary to preclude aggregation and to improve compatibility between the oxide and the organic host material. We designed pentafluorobenzyl phosphonic acid (PFBPA) for an organic linker (Figure 1), which has phosphonic acid for the surface modification of $BaTiO_3$ as well as pentaflurobenzyl group for the miscibility to host polymer. A nanocomposite consisting of surface modified $BaTiO_3$ in PVDF-HFP (Viton) was prepared by ball-milling the mixture in *N,N*-dimethylformamide (DMF) for two weeks.

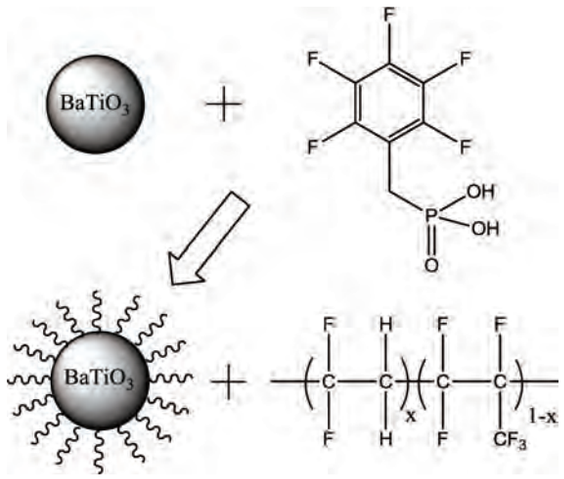

Figure 1: Surface-modified $BaTiO_3$ (nanoparticle) and PVDF-HFP (polymer matrix).

Blade casting

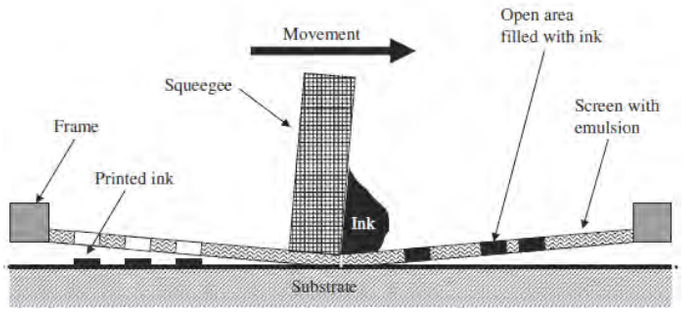

Figure 2: Schematic illustration of blade casting[2].

The glass substrate was cleaned with ethanol. Then ethanol was poured into cuvette, placed into a sonicator for 10 min, and substrate glass was dried with nitrogen gas. Substrate glass was then put in plasma cleaning for 3 min (also introduced oxygen gas into chamber). After cleaning, few drops of water were used to stick glass substrate to glass surfaced plate. A few drops of 50 vol% of PFBPA-BT in Viton in DMF solution were placed on glass substrate and a blade caster

(set to intended dial number) was slid to spread solution evenly across glass substrate. The thicker and/or thinner films were made with the blade caster of different height. Samples were then placed on a hot place with a temperature of 80°C for soft baking for a few minutes (DMF is evaporating during this process.) Hot plate was then turned off and samples were left there to cool down before removing. Samples were then placed in the vacuum chamber overnight with a temperature of 120°C for hard baking. After overnight baking, a channel is created within the film on the glass substrate with a razor blade. Samples are then placed on the stylus profiler so the thickness of the film can be measured.

Spin casting

The procedure of cleaning glass substrate was same to blade casting. A glass substrate was placed on a tube inside spin caster and the vacuum button was pressed so glass substrate would not move. A few drops of 50 vol% of PFBPA-BT in Viton in DMF solution were added to the glass substrate with a syringe and substrate was allowed to spin at the designated speed. While spinning, solution was evenly distributed. After spinning, samples went under soft and hard baking in the same manner of blade casting and the thickness of films were measured by stylus profiler.

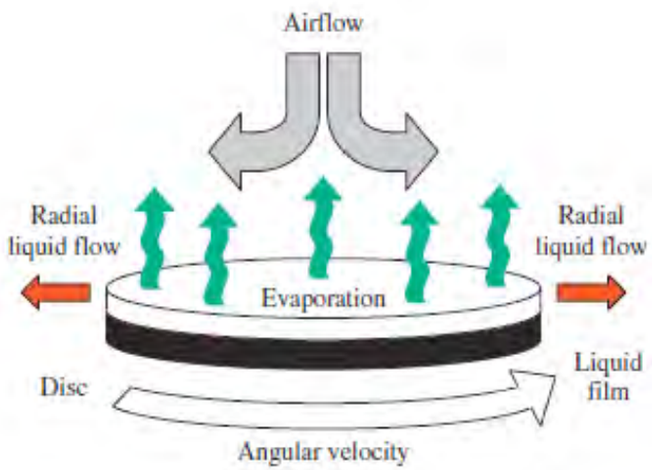

Figure 3: Schematic illustration of spin casting[2].

Electrode deposition

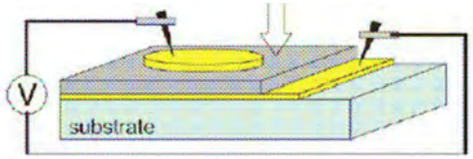

Figure 4: Geometry of thin film capacitor [1].

Parallel plate capacitors were fabricated by depositing an array of circular top aluminum electrodes on the dielectric nanocomposite thin films through a shadow mask by using a thermal evaporator at a deposition rate of 3 angstroms per second. The Al electrode was 480 nm thick.

Dielectric measurement

For the dielectric measurement composite thin films were processed on aluminum coated glass substrates, which was bottom electrode. Top Al electrode was deposited in thermal evaporator using a shadow mask, which led to a device with the area of 0.25 mm^2. Dielectric properties including capacitance, loss tangent and breakdown strength were measured by using Agilent 4284A LCR meter with parallel equivalent circuit and Keithley 248 high-voltage supply, respectively.

Results/Data/Figures and Discussion

Surface coverage of PFBPA to $BaTiO_3$ nanoparticle was calculated by TGA. From Figure 5, the coverage of PFBPA was a little bit excessive to ideal monolayer coverage. On top of that, significant weight loss below 100°C was observed which indicated some portion of PFBPA binding to nanoparticle was not strong enough that these physically adsorbed moieties will potentially lower effective permittivity and breakdown strength of the capacitor.

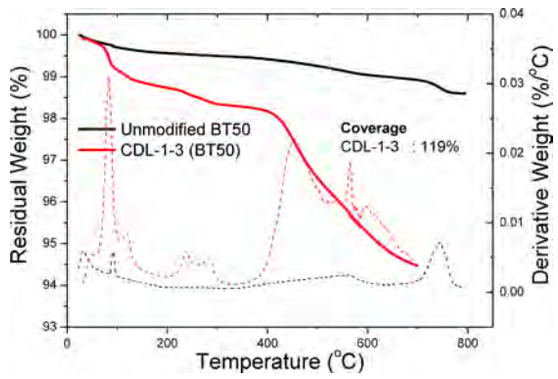

Figure 5: TGA result of PFBPA-modified $BaTiO_3$.

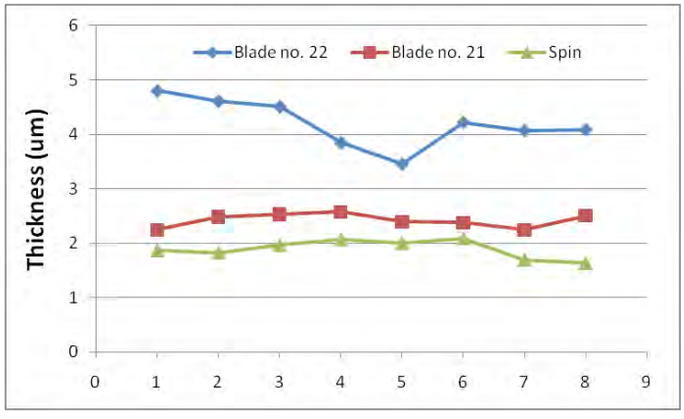

Figure 6: Thickness profiles of blade- and spin- casted films.

Figure 6 shows thickness profiles of the films prepared by both blade and spin casting. The average thickness of spin casted films was 2 um. With blade casting, much thicker and non-uniform films were made because of skewed height of blade caster. Now this problem has been fixed and more uniform films were prepared using four different height of blade caster. In the final paper, newly prepared films were used for further characterization.

$$U_{\max} = \frac{E_{\max}}{volume} = \frac{\frac{1}{2}CV_B^2}{A \times t} = \frac{1}{2}\frac{\varepsilon_0 \varepsilon_r (A/t) V_B^2}{A \times t} = \frac{1}{2}\varepsilon_0 \varepsilon_r E_B^2$$

Equation 1: The process of deriving U_{max} from measured variables.

Equation 1 shows how one calculate effective permittivity (ε_r) and breakdown strength (E_B) and eventually maximum energy density (U_{max}) from measured variables of capacitance, *C*, breakdown voltage, V_B, area, *A*, and thickness, *t*, of dielectric layer.

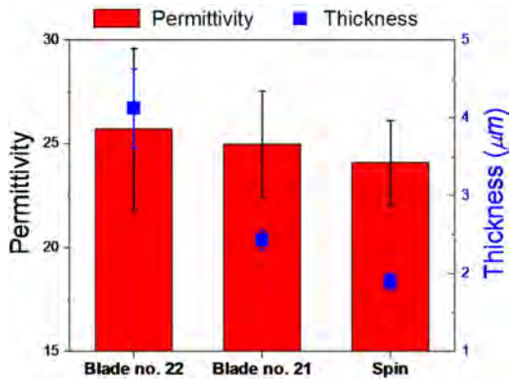

Figure 7: Average permittivity including standard deviation (left axis) and thickness (right axis) of spin- and blade-cast films.

Permittivity of both blade- and spin-casted films was similar on same thickness range of 2um and thicker films of 4 um by blade no. 22 (Figure 7). We can assume that permittivity is not sensitive to different processing method and thickness of dielectric film. In frequency dependence of permittivity and dielectric loss (Figure 8), both spin- and blade-cast films were also similar. Permittivity decreased when the frequency increased. Meanwhile, dielectric loss showed the opposite tendency. These behaviors occur because molecular resonance of Viton or PFBPA on nanoparticles becomes apparent in high frequency range.

Breakdown strength and calculated maximum energy density of both films are shown in Figures 9 and 10. The breakdown strength of blade-cast film is higher than spin-cast one and its lower standard deviation indicates blade casting provided more reliable dielectrics when it comes to electrical breakdown. In particular, reliability of dielectric film under high voltage is as important as the maximum electrical breakdown point. Within blade-cast films, thicker film prepared by blade no. 22 resulted in slightly higher breakdown strength and lower standard deviation.

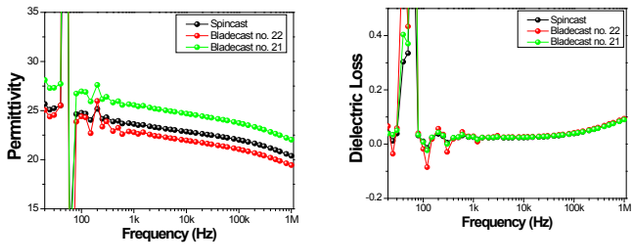

Figure 8: Frequency dependence of permittivity (left) and dielectric loss (right)

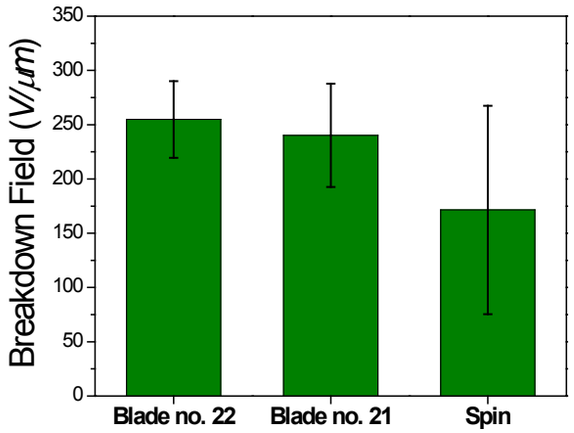

Figure 9: Breakdown strength of spin- and blade-cast films.

Maximum energy density of blade-cast film is 8.3 *J/cm*^{3}, which is 1.8 times higher than that of spin-cast film, 4.6 *J/cm*^{3}. The difference mainly comes out from enhanced breakdown strength of blade-cast film. We assume that blade casting makes much denser film than spin casting because of the slower evaporation time of blade casting that eventually allows enough time for polymer chain to relax and fill in the gaps between $BaTiO_3$ particles. To verify our assumption, cross sectional image of spin- and blade-cast films were taken and compared in Figure 11. In SEM image, spin-cast film looks much more porous and less dense than blade-cast film. It is obvious that the difference in the microstructure of both films gave rise to significant enhancement of breakdown strength of blade-cast film, which resulted in higher energy density.

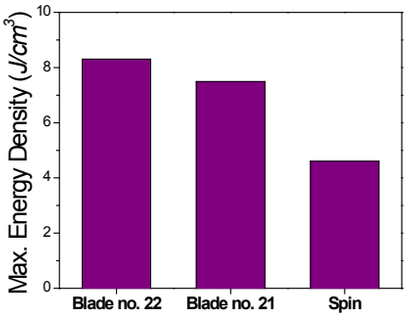

Figure 10. Calculated energy density of the films from spin- and blade-casting.

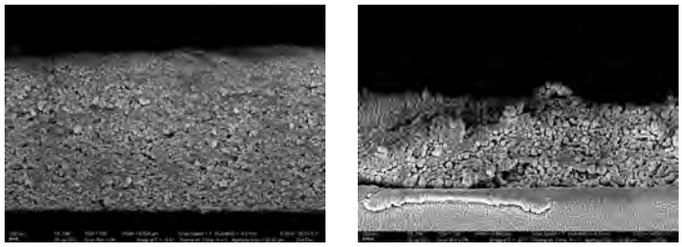

Figure 11: Cross-sectional SEM image of spin- (left) and blade-cast (right) films.

Conclusion

Blade casting increased maximum energy density of capacitor made of nanocomposite by 180% because of enhanced breakdown strength. Enhanced breakdown strength can be attributed to the densification of nanocomposite during blade casting because it allows enough time for polymer chains to relax and fill in the gaps between nanoparticles. Cross-sectional SEM image confirmed that blade-cast film had denser structure than spin-cast film.

References

1. Kim, P. Doss, N. M. Tillotson, J. P. Hotchkiss, P. J. Pan, M.-J. Marder, S. R. Li, J. Calame, J. P.; Perry, J. W. High Energy Density Nanocomposites Based on Surface-Modified $BaTiO_3$ and a Ferroelectric Polymer. ACS Nano 2009, 3, 2581-2592.
2. Krebs, F. C. Fabrication and processing of polymer solar cells: A review of printing and coating techniques. Solar Energy Materials and Solar Cells 2009, 93, 394-412.

Acknowledgments

Funds for this research were provided by the Center on Materials and Devices for Information Technology Research (CMDITR), the NSF Science and Technology Center No. DMR 0120967. I would like to thank Dr. Perry, Yunsang Kim, and all staff of Georgia Institute of Technology.

ADRIENNE-ELAINE LAMPTEY is a rising junior who attends Clark Atlanta University studying Computer Science and Mathematics. In the future, she plans to enroll in a PhD program with emphasis in Computer Information Systems.

Iron Pyrite (FeS_2) Nanocrystals Used in Bulk Heterojunction Photovoltaic Cells

ASHLEY MARSHALL, Pacific Lutheran University
Adam Colbert, David S. Ginger, University of Washington

Introduction

Semiconducting nanocrystals (NCs) have recently been under investigation as a low-cost material for use in the active layer of photovoltaic (PV) devices. NCs are advantageous due to their solution processability, strong light absorption, and size-tunable bandgaps.[1,2] The optical and electronic properties of these materials can be tailored by varying the size and shape of the nanoparticles due to the quantum size-effect.[2] Extensive research has been performed on several types of NCs, such as cadmium selenide (CdSe) and lead sulfide (PbS).[3,4] To address the issues of cost and toxicity with these materials, this study focuses on the PV applications of nanocrystals employing non-toxic, earth-abundant materials such as iron pyrite (FeS_2), copper sulfide (Cu_2S) and zinc oxide (ZnO).

Absorption of photons in the active layer of NC-based solar cells results in the formation of excitons. These devices rely on separation of the coulombically-bound charges to produce photocurrent, whereby electrons migrate to the cathode while the holes migrate to the anode and the affinity to recombine drives the external circuit (Figure 1).

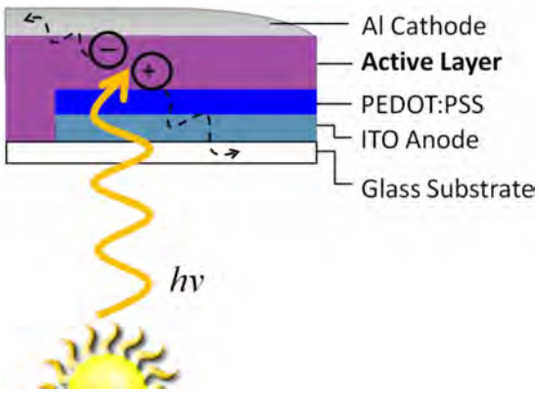

Figure 1: Basic design structure for a NC-based PV.

The anode consists of a transparent conductive oxide such as indium tin oxide (ITO), while the cathode is typically a low work-function metal such as aluminum.

Two different active layer designs were utilized in this study. The excitonic device architecture employs a NC film where photogenerated charge carriers are extracted from the NC layer into electron and hole transporting layers (Figure 2). Charge transfer occurs along the interface between the two types of materials, driven by a type II heterojunction, where the conduction band (CB) of the electron-transport layer lies at a lower energy than the light-absorbing NC layer.

In a bulk heterojunction (BHJ) design, the NCs are blended with a semiconducting polymer (Figure 3) where phase segregation drives the formation of polymer and NC domains throughout the film, giving high surface area contact between the materials. The polymer typically dominates light absorption in BHJ devices, as conjugated polymers generally have higher absorption coefficients than those of inorganic semiconductors. Excitons formed in the polymer domain diffuse to the interface between polymer and NC domains, where charge transfer occurs. The NCs act as electron acceptors, as most inorganic semiconductors have higher electron affinities than conjugated polymers, leaving a hole on the polymer and electron on the NC. Light may also be absorbed by the NCs, resulting in hole transfer to the polymer.

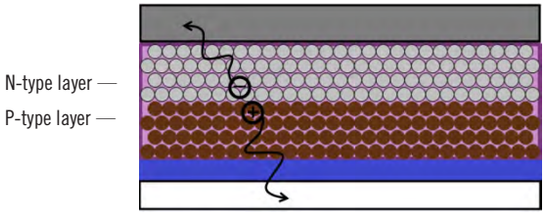

Figure 2: Device structure for an excitonic PV.

Photoinduced absorption (PIA) spectroscopy is a "pump-probe" technique capable of detecting long-lived (μs-ms) photogenerated charge carriers. A modulated pump beam is used to excite the sample, while the transmission (T) of a probe beam is monitored. A lock-in amplifier referenced to the modulation frequency of the pump is used to detect the fractional changes in probe beam transmission (ΔT), and the signal is normalized with respect to the steady-state transmission (ΔT/T). When charge transfer occurs between donor and acceptor species, a positive charge (or hole) is left on the p-type polymer resulting in formation of a polaron. These polaron states possess sub-bandgap absorption bands that give rise to new optical transitions detected by the ΔT in the probe beam.[5]

Significant research has been performed on semiconducting NCs composed of toxic materials (CdSe, PbS, etc.) which are not ideal for commercial applications. The focus of this research is to study nanocrystals produced with non-toxic, earth abundant materials for photovoltaic applications. Specifically, this study investigated the

synthesis and charge-transfer processes involving iron pyrite (FeS_2) NCs. The synthesis of these particles is not thoroughly studied so this research focused on the synthesis of FeS_2 nanocrystals and incorporating them into BHJ photovoltaic devices. BHJ and bilayer films of FeS_2 and regioregular poly 3-hexylthiophene (P3HT) were examined with PIA to determine whether charge-transfer occurred between the NCs and polymer to determine the merit of developing a working PV device.

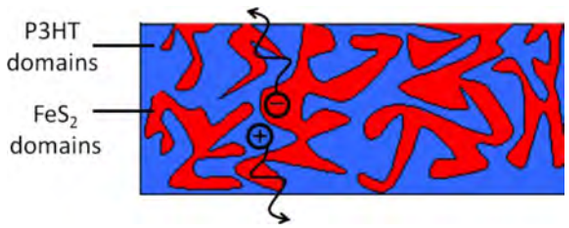

Figure 3: Active layer for a bulk heterojunction photovoltaic device.

Experimental Methods

All chemicals for the synthesis were used as received from Sigma-Aldrich and reactions carried out under N_2 (*g*) on a Schlenk line. Solvents which were not anhydrous were dehydrated with molecular sieves and bubbled with N_2 (*g*).

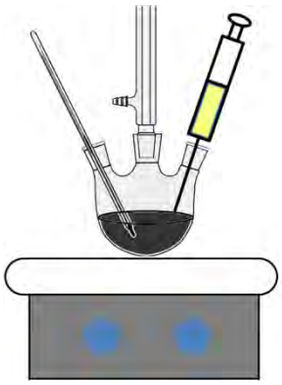

Figure 4: Reaction scheme for the hot-injection synthesis of FeS_2 nanocrystals.

Iron Pyrite (FeS_2) nanocrystals were synthesized by a hot-injection reaction (Figure 4).[6] In a 50 mL 3-neck flask, $FeCl_2 \bullet 4H_2O$ (100 mg, 0.5 mmol) was dissolved in octadecylamine (10 g, 0.037 mol) and heated to 120°C. In a second flask, sulfur (96 mg, 3 mmol) was mixed with diphenyl ether (90% tech. grade, 5 mL) and heated to 70°C for the injection mixture. Both flasks were degassed under N_2 (g) for 1 hour. Flask 1 – containing iron – was heated to 220°C, and the contents of flask 2 were injected. The reaction ran for 3 hours at 220°C and was subsequently quenched by partially submerging the flask in a water bath. When the reaction had cooled to 100°C, 9 mL of chloroform was injected to keep the octadecylamine from solidifying. After cooling to room temperature, 4 mL aliquots of the reaction were transferred to centrifuge tubes and precipitated with ethanol. An extra 6 mL of cholorform added to the empty reaction flask helped wash any residual product off the flask walls; this was also precipitated with ethanol. The product was dispersed in chloroform and added to potassium dodecanethiolate (0.2 g, 0.83 mmol). The mixture stirred overnight to ligand exchange the nanoparticles.

Potassium dodecanethiolate was prepared by mixing dodecanethiol (2 mL, 12 mmol), potassium hydroxide (0.75 g, 13 mmol), and methanol (10 mL). This was stirred until dissolved then placed on a hot plate. The solution was heated until dry then dissolved in chloroform. The salt was precipitated with ethanol and dried with N_2 (g).

The ligand exchange mixture was centrifuged at 4000 RPM for 5 min to remove the excess salt and any large nanocrystals. The supernatant was transferred to a new centrifuge tube and left to under N_2 (g) flow to evaporate the chloroform until the volume had decreased to 0.5 mL.

In a N_2 (g), water-free glove box, poly(3 hexylthiophene) (P3HT) was dissolved in chloroform (20 mg/mL) by stirring at 50°C for at least 4 hours. The nanocrystals were filtered through 1 µm and 0.45 µm filters and mixed with 150 µL of P3HT solution. This mixture stirred for 1 hour at 50°C. The blend was spun on clean glass slides at 2000 RPM (255 acceleration) for 1.5 min.

For FeS_2 nanocrystals used in bilayer films, the overnight ligand exchange was not performed. After spin casting a layer of FeS_2 a ligand exchange was performed directly on the film by covering with 1 mM acetonitrile solution of 1,2-ethanedithiol (EDT) and letting it set for 1 minute. The EDT solution was then spun off at maximum acceleration (255) and successive layers of FeS_2 were laid down. P3HT was spun on top of the final FeS_2 layer.

Photoinduced absorption (PIA) spectroscopy and UV-Vis were used to characterize the films. PIA was measured using a 455 nm LED pump beam and a continuous wave (CW) probe beam from a tungsten-filament lamp scanning from 550-1750 nm.

Results and Discussion

FeS_2 nanocrytals were successfully synthesized using the hot-injection technique. Figure 5 shows a transmission electron micrograph of the synthesized nanocrystals which met our expectations as spherical particles, 5-10 nm in diameter.

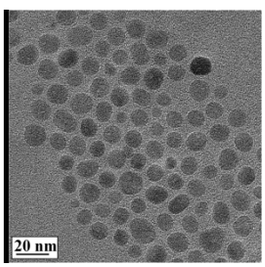

Figure 5: TEM of FeS2 nanocrystals.

UV-Vis absorption spectroscopy further corroborated the synthesis of FeS_2 nanocrystals (Figure 6). The measured absorption spectra matched the literature spectra for phase-pure FeS_2 NCs.[5] While we do not stipulate our nanocrystals are phase-pure, our product looks similar to the desired nanocrystals.

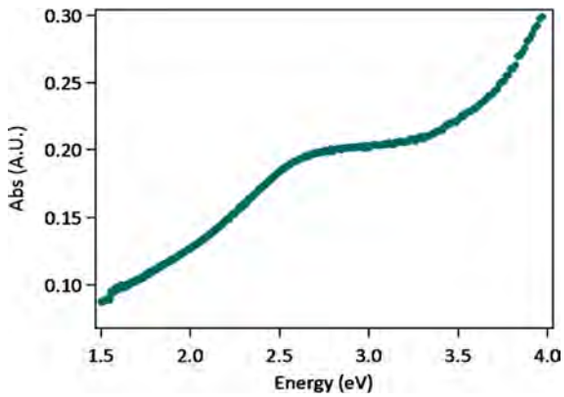

Figure 6: UV-Vis absorption of FeS_2 nanocrystals.

PIA spectra of films containing FeS_2 and P3HT blended in a 50:50 weight ratio exhibited an absence of long-lived photogenerated charges (Figure 7).

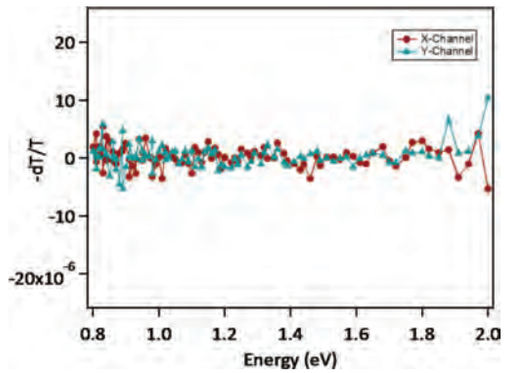

Figure 7: PIA spectra of FeS_2/P3HT blended film.

If efficient charge transfer occurred between donor and acceptor species, a P3HT polaron feature would be expected at ~1.2 eV. The polaron peak was identified by measuring a known, functional BHJ (Figure 8) – a blend of P3HT and PCBM ([6,6]-phenyl-C61-butyric acid methyl ester).

The UV-Vis absorbance spectra also showed a deficiency of FeS_2 in the 50:50 weight percent blend (Figure 9), which explains the absence of the P3HT polaron peak. If there is not enough FeS_2 nanocrystals, charge transfer cannot occur and the excited polymer will relax without charge-transfer occurring.

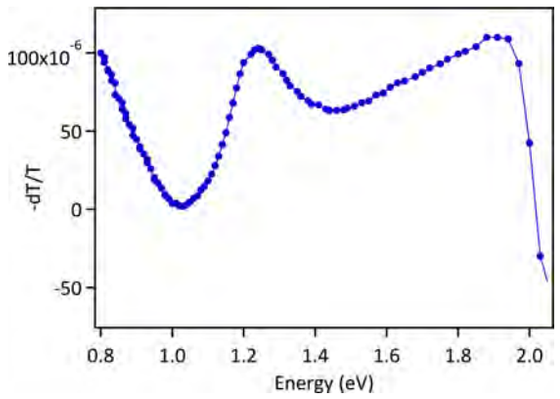

Figure 8: PIA of P3HT:PCBM blend exhibiting charge transfer between the polymer domains. The peak just to the right of 1.0 eV is the polaron peak of P3HT.

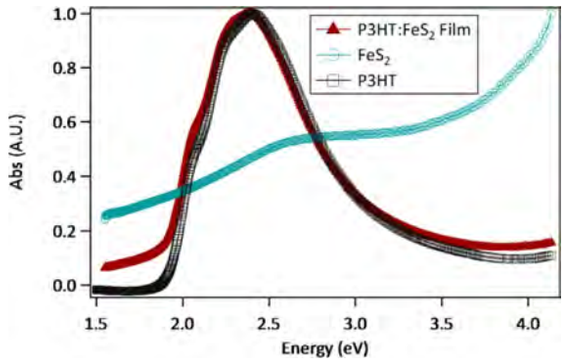

Figure 9: Absorbance spectra for each FeS_2 (open blue circles), neat P3HT (open black squares), and the blended film (filled red triangles).

Blends consisting of a higher fraction of FeS_2 (~90% by weight) were also tested, as this corresponds to a volume fraction of approximately 50%. Although the presence of FeS_2 was detected in the film (Figure 10), the PIA spectrum of these blends also yielded no detectable signal.

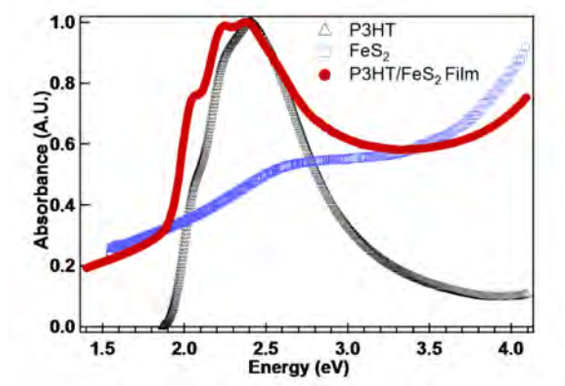

Figure 10: Absorption spectra of the higher weight percent (FeS_2) blended film. Enhanced absorbance in both the IR and UV regions on either side of the P3HT peak indicates the measurable presence of FeS_2 nanocrystals in the final film.

A higher weight percent of FeS_2 nanocrystals were included in the blended film by evaporating solvent to concentrate the initial FeS_2 solution. This prevents us from calculating the exact concentration of FeS_2, but from the absorption spectra (Figure 10) it is clear that a larger amount of the film consists of nanocrystals. The peaks observed at 2.3 and 2.4 eV likely correspond to vibrational transitions of P3HT, suggesting more ordered packing of the polymer chains in the blend film relative to the neat polymer film.

Since the higher weight percent film still did not yield any significant PIA signal, a FeS_2/P3HT bilayer was fabricated. A layer of FeS_2 NCs, which had not been previously ligand exchanged, were spin-cast and treated with 1,2–ethanedithiol (EDT) directly on the film to cross-link the particles. P3HT was then spin cast on top of the FeS_2. Again, the PIA spectrum was absent of any features indicating the presence of long-lived charges.

Conclusions

The successful synthesis of FeS_2 NCs was verified through TEM imaging, and UV-Visible absorption spectra. No long-lived charged species were detected in the PIA spectra of FeS_2:P3HT BHJ blends or initial tests of the bilayer. Spin casting multiple FeS_2 layers under the P3HT may result in better contact between the NC and polymer layers.

Photoluminescence (PL) lifetime studies will be carried out to determine whether charge transfer occurs between the donor and acceptor materials followed by rapid recombination. This would be evident by a shorter PL lifetime of a blend film relative to a neat P3HT film. Further future work on this project will also include testing a long chain dithiol ligand in place of the potassium dodecylthiolate to increase the reaction yield and allow a more thorough cleaning of the product.

References

1. Choi, Joshua J.; Lim, Yee-Fun; Santiago-Berrios, Mitk'El B.; Oh, Matthew; Hyun, Byung-Ryool; Malliaras, George G.; Sun, Liangfeng; Bartnik, Adam C.; Goedhart, Augusta; Abruna, Hector D.; Wise, Frank W.; Hanrath, Tobias. Nano Lett., 2009, 9 (11), 3749-3755.
2. Tang, Jiang; and Sargent, Edward H. Adv. Mater. 2011, 23, 12–29.
3. Noone, Kevin M.; and Ginger, David S.; ACS Nano., 2009, 3 (2), 261-265.
4. Noone, Kevin M.; Strein, Elisabeth; Anderson, Nicholas C.; Wu, Pei-Tzu; Jenekhe, Samson A.; and Ginger, David S. Nano Lett. 2010, 10, 2635–2639.
5. Heinemann, M.D.; Von Maydell, K.; Zutz, F.; Kolny-Olesiak, J.K.; Borchert, H.; Riedel, I.; Parisi, J. Adv. Funct. Mater. 2009, 19, 3788-3795
6. Puthussery, James; Seefeld, Sean; Berry, Nicholas; Gibbs, Markelle; Law, Matt. J. Am. Chem. Soc., 2011, 133 (4), 716-719.

Acknowledgments

Funds for this research were provided by the Center on Materials and Devices for Information Technology Research (CMDITR), the NSF Science and Technology Center No. DMR 0120967. I would like to acknowledge the members of the Ginger Lab for their help and support and especially my lab mates Eric Janke and Stephen Hsieh.

ASHLEY MARSHALL is a senior Chemistry major at Pacific Lutheran University, planning on pursuing a Ph.D. in Chemistry and continuing research on nanomaterials and energy production.

Magneto Optic and Chemical Characterization of MRTILs for use in Broadband Isolators

JASMYN MORTON, Fort Lewis College
Palash Gangopadhyay, Nasser Peyghambarian, University of Arizona

Introduction

Magnetic room temperature ionic liquids (MRTILs) are liquids at room temperature and display magnetic properties. The project goal is to synthesize new liquids that are transparent over broad range of wavelengths and characterize their magneto optic (MO) and chemical properties for future use in liquid core fiber isolators. The liquids described in this paper are composed of transition metal ions or lanthanides. The organic components were 1-butyl-3-methylimidazolium $[Bmim]^+$, and 1-decyl-3-methylimidazolium, $[Dmim]^+$. During this project four MRTILs, $BmimCoCl_4$, $[Bmim]_3ErCl_6$, $BmimNiCl_4$, and the first colorless liquid $[Dmim]_3GdCl_6$.

Present materials for optical isolators include glass, magnetic garnet crystals, e.g. Bi:YIG (bismuth doped yttrium iron garnets) and TGG (terbium gallium garnet crystals), and colored glasses. Both garnet crystals are absorbing and have magnetic properties but can only be applied to infrared lasers and visible lasers respectively. One disadvantage of the crystals and glass is the quantity of material needed. Generally, 500 micron of garnet and 3 mm length of TGG is used. A liquid core isolator composed of photonic crystal fiber (Holey fiber) and a colorless MRTIL would be ideal because of the reduced volume and the broad range of wavelengths from visible to infrared. In addition, a large part of the manufacturing cost goes to cutting and polishing the crystals that will not be required in the proposed liquid core isolators.

MO characterization consists of measuring the Verdet constant of the material at various wavelengths of interest. Ideal optical isolators have high Verdet constants and low absorption of light. Faraday rotation is a MO property used for isolators to achieve required 45 degrees of polarization rotation. Magnetic properties of the material and the magnetic field, both affect the Faraday rotation strongly. The Faraday rotation of a TGG isolator is 45 degrees.The purpose of this project is to characterize the MRTILs with a focus on the colorless $[Dmim]_3GdCl_6$ liquid. The colorless Gd liquid is a strong candidate for an isolator because colorless materials absorb less light and the magnetic properties of the liquid can produce a larger Verdet constant. To obtain a 45 degree Faraday rotation, the length of a fiber filled with the liquid can be suitably adjusted.

Experimental Method

The MRTILs were synthesized using metal ions and cationic organic materials using a similar process as described in a paper from 2004.[1] Metal oxides (Er, Co, Gd, and Ni) were heated under reflux with excess HCl to produce metal chlorides. The crystals were dried in a vacuum oven for 1-2 h.The metal chloride crystals were reacted with equimolar amounts of Bmim under reflux for 1-2 h. The liquid was left to cool to room temperature then placed in a rotary evaporator bath until the water evaporated. The liquids were transferred to glass vials. After separation the top layer was removed. $ErCl_3$ and $GdCl_3$ crystals did not react with Bmim. Dmim was chosen because of its long chain possibly inducing disorder into the molecular packing and in lieu turning it into a liquid at room temperature.

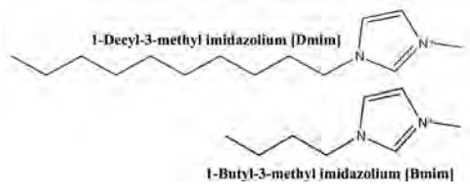

Figure 1: Structures of Dmim and Bmim.

The $[Dmim]_3GdCl_6$ liquid did not separate when left to sit in a vial and instead crystallized at the bottom leaving a clear liquid at the top.

Reults and Discussion

Five different characterization techniques were employed; differential scanning calorimetry (DSC), Fourier transform infrared spectroscopy (FTIR), scanning electron microscopy-energy dispersive microscopy (SEM-EDS), micro Raman spectroscopy, and ultraviolet - visible - nearinfrared spectrophotometry (UV-VIS-NIR).

Differential Scanning Calorimetry

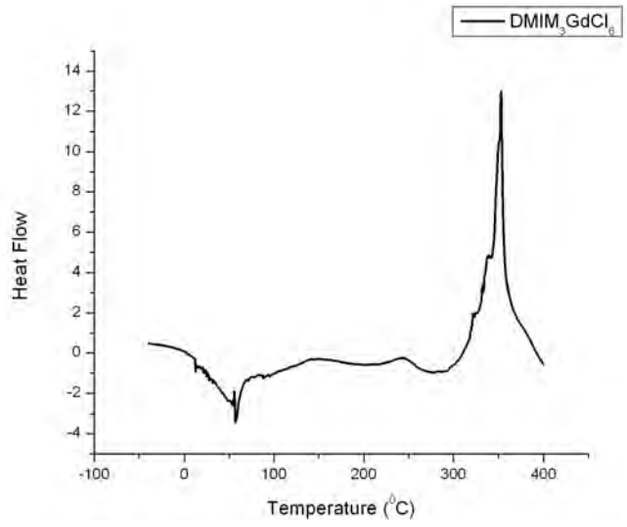

Figure 2: DSC plot of $[Dmim]_3GdCl_6$.

The DSC plot shows the phase changes of the material from -40°C to 400°C. $[Dmim]_3GdCl_6$ starts crystallization at or below 12.5°C and is liquid at room temperature. Decomposition of the liquid starts at ~ 300°C indicating thermal stability over a large range of temperature. Note that crystallization is an exothermic process and appears as a dip in the DSC heat flow map, reverse is true for decomposition, melting and boiling points. The dip at ~65°C is the crystallization point for DmimCl and indicates free organic components that is not attached to the metal.

Fourier Transform Infrared Spectroscopy

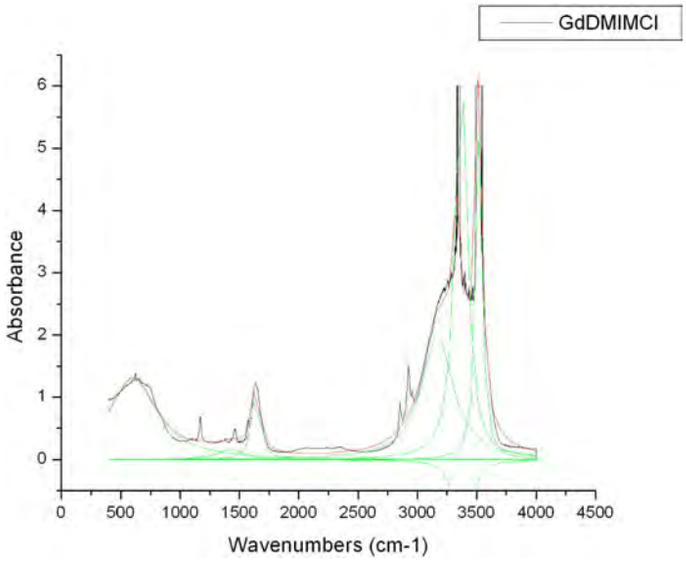

Figure 3: FTIR spectra of $Dmim_3GdCl_6$ The FTIR spectra shows constituents of the liquid. This was done to determine the purity of the material. There was trace amounts of water in the liquid which was an expected byproduct.

SEM-EDS

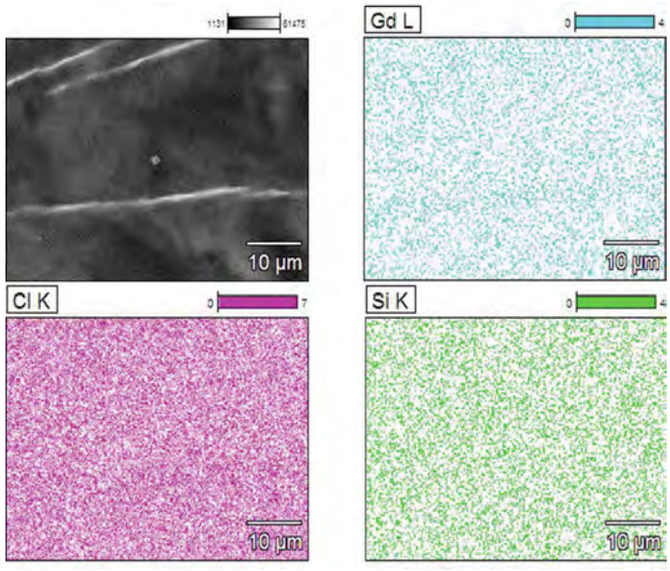

Figure 4: SEM image and 3 EDS maps.

The top left image is a SEM micrograph of the Gd liquid. The liquid at the time of the SEM crystallized although the liquid itself did not change. The EDS maps show the homogeneity of the gadolinium and chloride ions in the liquid. The silicon was from the substrate the liquid was placed on.

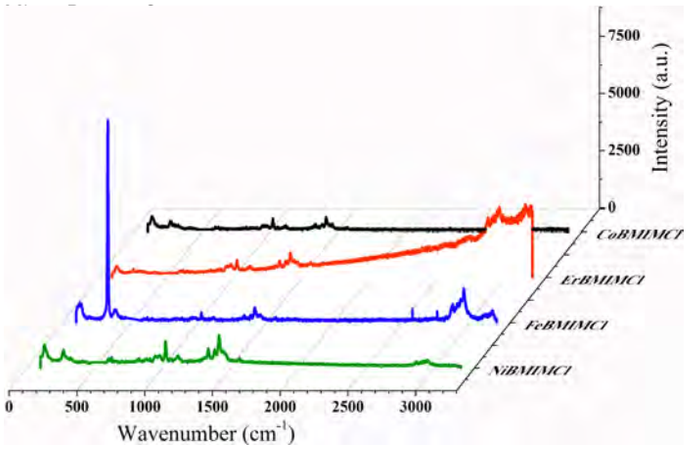

Figure 5: Micro Raman of Co, Er, Fe, and Ni liquids.

The peaks from 1500-1000 cm^{-1} of each liquid correspond to the organic cation Bmim. The $Dmim_3GdCl_6$ liquid micro Raman spectra is not shown. The downfield peaks between 500-0 cm^{-1} correspond to the metal anions in the liquid. The peaks themselves do not show changes in frequency, polarization, and show good quality (narrow peak width). The large peak from 3000-2500 cm^{-1} for $BmimErCl_4$ is due to the fluorescent property of erbium.

Magneto Optic Characterization

Faraday rotation, or the Faraday effect is a MO property that rotates the plane of the linear polarization as a result of changing the magnetic field.

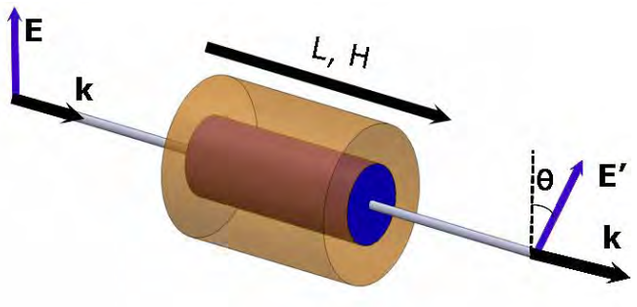

Figure 6: A diagram of the Faraday effect.

The Faraday rotation is expressed as θ=VBl, where V is the Verdet constant, B is the magnetic field, and l is the length of the material. Measuring the Faraday rotation one can measure the Verdet constant

of the materials. Current isolators have Verdet constants that are used as reference for the rotation of light at that wavelength. The Faraday rotation of the Gd liquid was found for two visible wavelengths; 532 nm and 670 nm using a setup from a previous paper published by this group.[2]

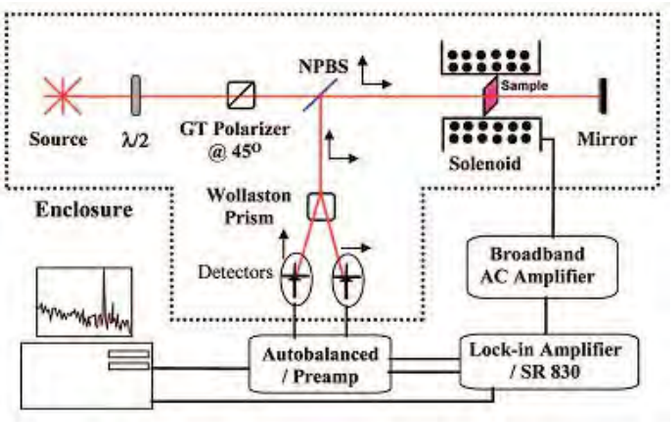

Figure 7: The Faraday rotation measurement setup.

A comparison of the Faraday rotation measurements of the reference BK7 glass and $[Dmim]_3GdCl_6$ liquid. The Faraday rotation measurements of the Gd liquid showed less absorbance than the glass samples and had a better Verdet constant.

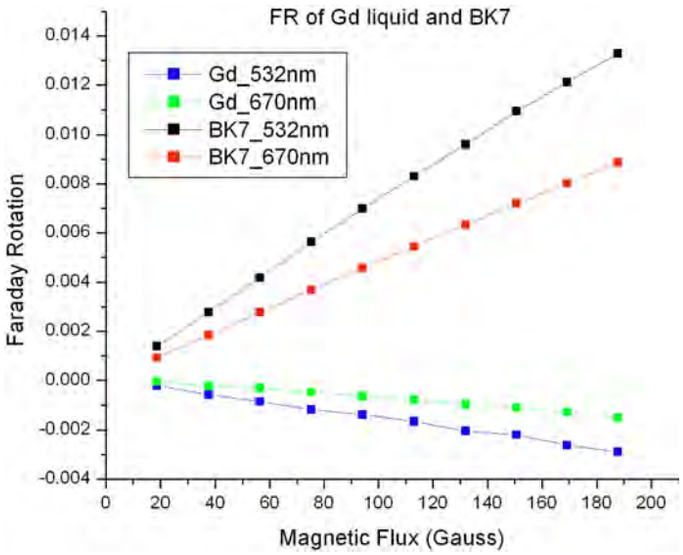

Figure 8. Comparison of BK7 and Gd Liquid Faraday rotation (α) at 532 nm and 670 nm.

Conclusion

The first colorless magnetic room temperature ionic liquid $[Dmim]_3GdCl_6$ is synthesized and we have demonstrated that this is a promising material for future magneto optic research. More work will be required to determine the feasibility of using the liquid in liquid core isolators. The Verdet constants of the liquid at 532 nm and 670 nm are consistent which is promising for its use with visible wavelengths. As MRTILs are fairly new materials, more work can be done to further the understanding of its properties and potential.

References

1. Hayashi, Satoshi; Hamaguchi, Hiro-o. Chem. Lett. 2004, 33, 1590-1591.
2. Gangopdhyay, Palash; Voorakaranam, ramakrishna; Lopez-Santiago, Alejandra; Foerier, Stijn; Thomas, Jayan; Norwood, Robert; Persoons, Andre; Peyghambarian, Nasser. J. Phys. Chem. 2008, 112, 8032-8037.

Acknowledgments

Funds for this research were provided by the Center on Materials and Devices for Information Technology Research (CMDITR), the NSF Science and Technology Center No. DMR 0120967. Authors also acknowledgeCollege of Optical Sciences at the University of Arizona, and Hooked on Photonics for their support.

JASMYN MORTON is a junior at Fort Lewis College studying chemistry. She plans to apply to graduate programs in physical chemistry or materials science within the next two years.

An Investigation into the Resistance and Electron Selectivity of Ultra-Thin Titanium-Oxide Films

MICHAEL NGUYEN, San Diego State University
Delvin Tadytin, Kai-Lin Ou, Neal R. Armstrong, University of Arizona

Introduction

The overall goal of our project in the Armstrong group is to produce an efficient, flexible, inexpensive, inverted organic photovoltaic (OPV) cell out of earth abundant materials. As of now, reports have indicated power conversion efficiencies (PCE) from 3-4% for inverted architectures. [1] We are striving to increase the PCE of these OPV's near 12% so they may become commercially viable.[2] Our understanding of the interfacial contacts within these devices is limited. Therefore, we planned to build upon our understanding of these inverted solar devices by focusing on the charge injection into titanium oxide (TiO_x) and indium tin oxide (ITO) layers. TiO_x functions as the electron injection layer (EIL), sometimes referred to as the electron-selective layer or the hole-blocking layer. The EIL is displayed as the blue TiO_x layer in Figure 1 below. The transparent conductive oxide (TCO), ITO, can be seen as the grey layer in Figure 1.

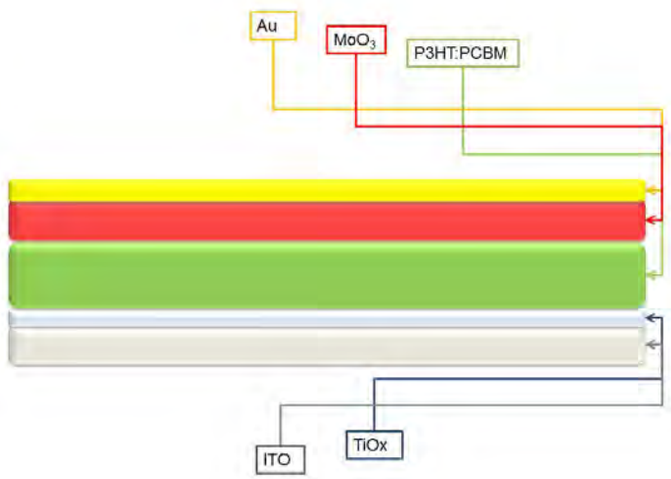

Figure 1: Schematic of the targeted inverted solar device.

TiO_x is inherently transparent, possesses hole-blocking properties, it is also, however, relatively non-conductive.[1] By decreasing the thickness of TiO_x to nanometer lengths we aim to reduce the resistance of the ultra-thin film while retaining the electron-selective properties. This can be extrapolated from the resistance equation shown in Equation 1, where if we decrease the thickness or length the current must travel to reach ITO, we can effectively lower the resistance.

Currently, TiO_x is deposited via metalorganic chemical vapor deposition (MOCVD), sputtering, and spin coating;[3-5] some of these techniques, however, also require high annealing temperatures with excess of 400°C and even up to 1000°C; they may often require ultra-high vacuum (UHV) conditions. Despite these extreme conditions, the Armstrong group has developed a more commercially viable method to deposit ultra-thin TiO_x films at low temperatures onto ITO substrates at mTorr-vacuum conditions. This method also enables the group to deposit TiOx onto sensitive OPV platforms. This technique utilizes ultra-violet (UV) light or light-enhanced chemical vapor deposition (LECVD) to decompose titanium tetraisopropoixde (TTIP) precursor into the desired TiO_x film. We address whether or not the UV light has any effects on the electrical and morphological properties of the ultra-thin films. We also address the conductance of the ultra-thin films as a function of film thickness and morphology.

$$R = \frac{\rho L}{A}$$

Equation 1: Resistance equation $R = \rho L/A$; where ρ is resistivity ($\Omega \bullet m$) of the given material, L is the length (m), and A is the cross-sectional area (m^2).

Experimental Methods

The TiO_x was deposited on glass and ITO substrates were purchased from Colorado Concepts. The ITO substrates were oxygen plasma cleaned for 15 min. The LECVD method was used to deposit TiO_x onto the ITO substrates. The deposition parameters: furnace temperature was at 180°C, substrate temperature was at 210°C, and pressure was at 500 mTorr. The ultraviolet light source was a 250 nm mercury vapor lamp with 8 watts of power. Our approach to understanding these relationships utilized conductive tip atomic force microscopy (C-AFM) to build current maps for the TiOx ultra-thin films. Figure 2 shows a simplified diagram of how we analyzed our samples via C-AFM. To further analyze the effectiveness of this low temperature and mTorr- vacuum deposition technique, we harnessed the ability to compare the topography of the TiO_x film in conjunction with the current map to provide insight into what thickness is optimal for decreasing resistance and what morphologies promoted a decrease in resistance. We accessed the Agilent 5500 AFM to collect our images using a Veeco (DDESP-FM-10) doped diamond coated conductive probe. A concept map of our research method is displayed on Figure 4. To conclude our study, we hope to construct an inverted solar cell using ITO, TiO_x, P3HT:PCBM, MoO_3, and Au as shown in Figure 1. In concurrence with the C-AFM studies, cyclic voltammetry was employed to monitor the hole blocking properties of the four TiO_x films. To lessen the effects of impurities in the study, the sample was prepared in inert (N_2) conditions. To accomplish this

electrochemical analysis, the cell was assembled in the glove box while all solvents were purged under argon for more than 12 hours. The cell was machined out of Teflon, with the supporting electrolyte MeCN/TBAPF$_6$ (0.1 M), Ru(bpy)$_3^{2+}$ as the probe molecule, a Pt wire as the counter electrode, and TiO_x or ITO as the working electrode.

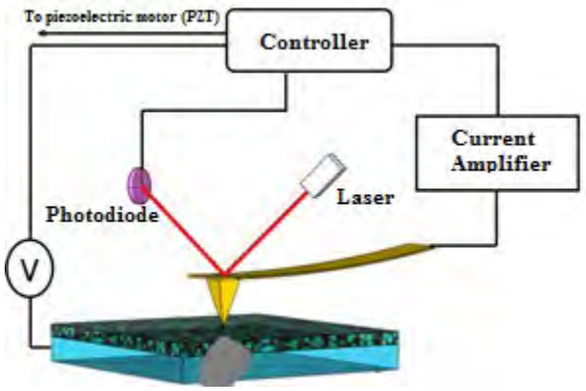

Figure 2: A schematic of the C-AFM setup used to shed light on the topography and current maps of TiO_x/ITO film. Adapted from http://www.nanowerk.com/spotlight/spotid=18038.php

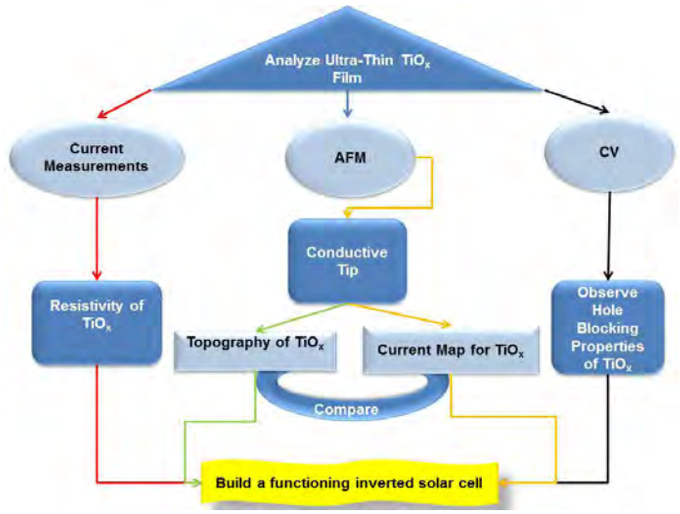

Figure 3: A schematic to the research plan for this project.

Results and Discussion

In order to facilitate the process into preparing OPV's for commercial scale, the interfacial TiO_x must be analyzed to enhance the overall PCE. Results toward this goal will be stated herein. C-AFM images in Figure 4 display the topography and corresponding current maps of the four films in question. Here the top row is displayed as the topography of each film by contrasting the z-height of the film; the darker areas are the shorter features, while the lighter areas are the taller features. On the 30 nm film topography, one can see the tall, white features that are presumed to be large aggregations of TiO_x. With C-AFM, there is often a sacrifice of topography image quality for the current measurements. The elongation of the features at the bottom of the 20 and 30 nm films is an indication of hysteresis. These artifacts can be attributed to tip defects. The 10 nm film has the most well-defined topography; this may be due to optimal combination of settings such as tip force, scan rate and scan size. For the current maps, one may catch the subtle lines for the 30 nm film. This may be attributed to the probe dragging dust or material across the surface; this may occur until the material falls or rubs off the probe. This image also shows how the tall features relate to areas of high resistance. For the current maps of the 10 and 20 nm thicknesses, we see a fairly even distribution of current. With the 5 nm film, high current dominates the area with only small areas of resistance; we do see, however, an area at the bottom of high resistance. This area may be largely attributed to the probe picking up an impurity and sliding it on the surface. These images indicate that as the film thickness of the TiO_x layer was tuned thinner, the resistance decreased. This finding confirms the hypothesis using the resistance equation provided in Equation 1, by lowering the length (thickness) the electrons must travel, the resistance can be lowered. These images also suggest that there tends to be larger areas of resistance perhaps due to the taller aggregations of TiO_x. In Figure 5, the cross-sectional study shows a 10 nm TiO_x film of the topography along with the corresponding current measurements. It can be seen that with respect from the taller to the shorter features, there is relatively even intensity of current flowing through the sample. In order to selectively harvest electrons only from the acceptor phases in OPVs, we require an interlayer (5-50 nm) which is robust, easily processed at low temperatures, and will only allow for electrons to pass to the underlying contact (ITO). It is shown with cyclic voltammetry conducted on all four thicknesses studied, 5 nm, 10 nm, 20 nm, and 30 nm, the hole blocking properties of TiO_x is retained; this is shown in Figure 6 with a comparison to ITO. This was shown using tris(bipyridine)ruthenium(II) chloride (Ru(bpy)$_3^{2+}$) as our probe molecule and an ITO sample as the comparison to show the preservation of this property. When performing this electrochemistry with the control ITO sample, three reductions are apparent in the negative voltage bias while one oxidation occurs in the positive voltage bias. When each of the respective TiO_x films are introduced, the oxidation is no longer present. We observe, however, incidental leakage of current in the 10 nm film thickness, but this leakage does not follow the same trend as the oxidation peak. This occurrence is indicative of the TiO_x film providing and energy barrier where the oxidation cannot occur. This data is also indicative that the LECVD setup the Armstrong group developed is able to effectively deposit an ultra-thin conformal hole-blocking layer.

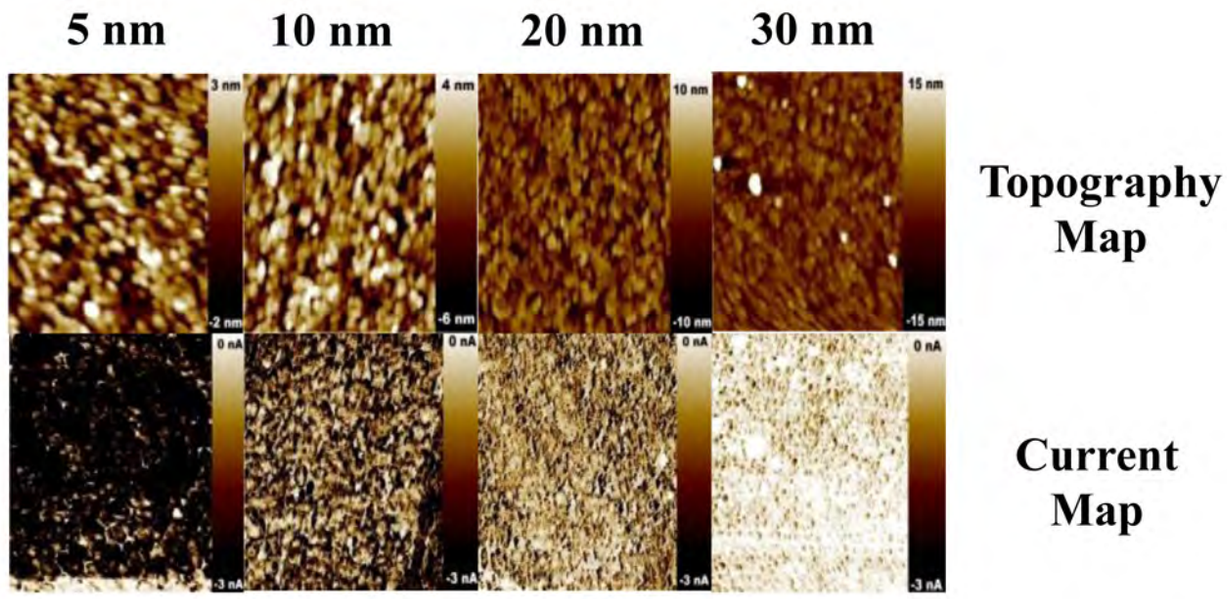

Figure 4: Topography and current maps of TiO_x deposited onto ITO via LECVD: Top row being the topography and bottom row being the corresponding the current maps. A, 5 nm; B, 10 nm; C, 20 nm; D, 30nm. All images are on a 5µm x 5µm scale where the current maps are scaled from 0 (white) to -3 nA (black).

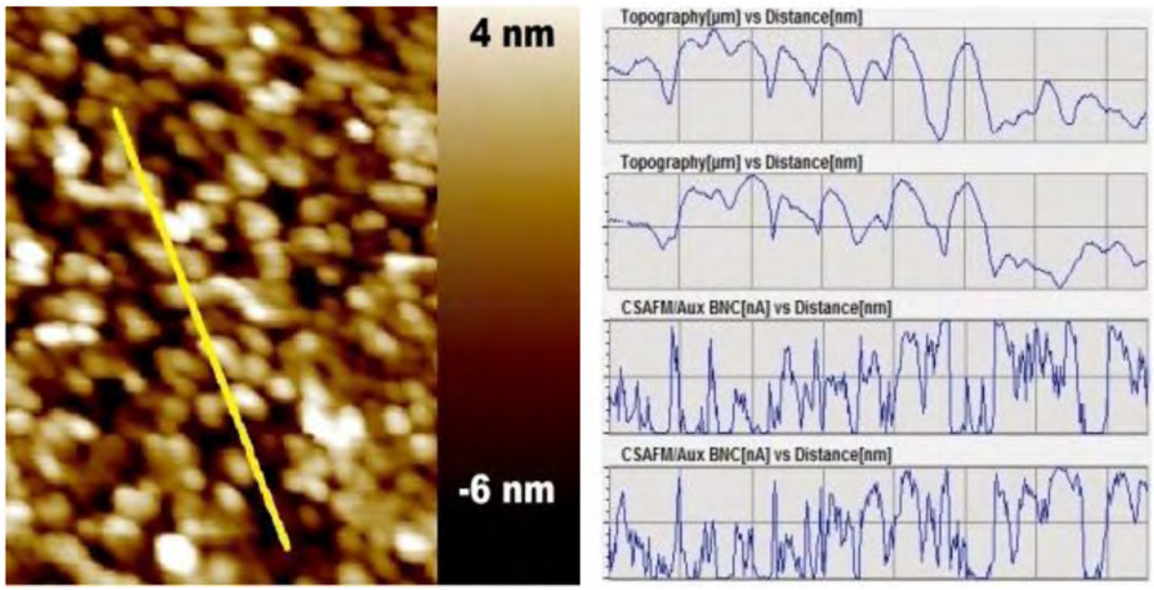

Figure 5: The cross-sectional analysis of TiO_x/ITO shown with a yellow marker, passes through taller and shallower areas to display how the topography and corresponding current measurements indicate that the TiO_x ultra-thin film is conformal to the ITO substrate. The 10 nm film is on a 5µm x 5µm scale where the current map is scaled from 0 (white) to -3 nA (black).

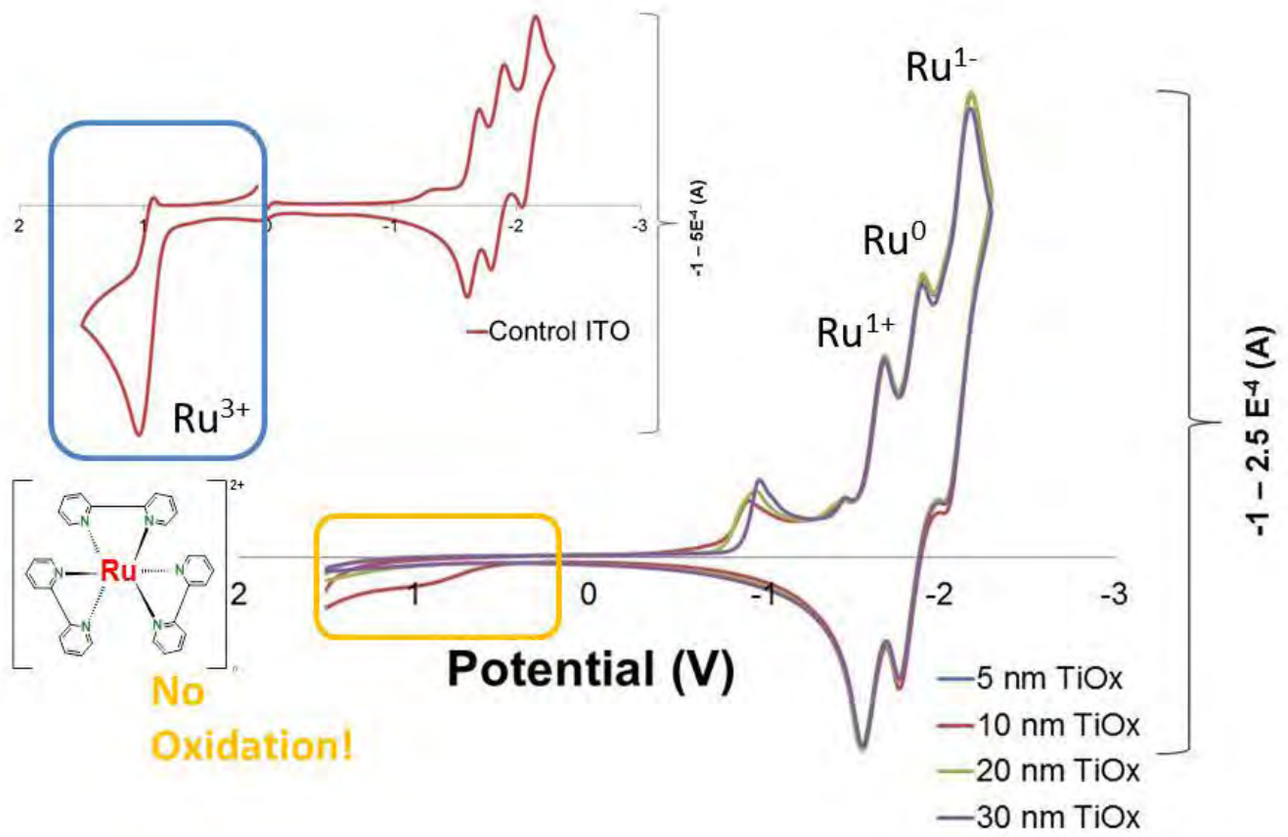

Figure 6: Cyclic voltammograms displaying the ultra-thin TiO_x films' hole-blocking ability at all thicknesses versus the ITO control. Supporting electrolyte was $TBAPF_6$/MeCN, with $Ag/AgNO_3$ as the reference electrode and $Ru(bpy)_3^{2+}$ as the probe molecule.

Conclusion

We investigated the properties and electron transfer between small solution probe molecules and TiO_x ultra-thin films over indium tin oxide (ITO). TiO_x and ITO are both increasingly common materials found in "inverted" organic photovoltaic (OPV) architectures. We utilized a light enhanced chemical vapor deposition (LECVD) technique where a titanium alkoxide precursor was activated by heat and ultra-violet light to deposit ultra-thin and conformal TiO_x films. Despite the inherent transparency and electron-selective properties, it is also intrinsically non-conductive. Therefore, we addressed the resistance of the ultra-thin films by decreasing the thickness. We have shown that as the film thickness was reduced to less than 10 nm, the net resistance of the film was shown to decrease according to our conductive-tip atomic force microscopy results. Current maps indicate that our film becomes increasingly and uniformly conductive compared to the film thicknesses greater than 15 nm. In addition to this work, we have seen that short areas of TiO_x/ITO have a decrease in resistance than in adjacent tall areas. In conjunction with conduction studies, cyclic voltammetry was utilized to monitor the electron selective properties of TiO_x, where probe molecule $Ru(bpy)_3)^{2+}$ was utilized to indicate electron selectivity was preserved at from 5 nm to 30 nm film thicknesses. These findings will help foster our understanding into solar electric materials and provide insight into the successful building of an inverted OPV.

References

1. Steim, R., Kogler, F. R., & Brabec, C. J. (2010). Interface materials for organic solar cells. Journal of Materials Chemistry, 20(13), 2499-2512.
2. Krüger, R. A., Gordon, T. J., Baumgartner, T., & Sutherland, T. C. (2011). End-group functionalization of poly(3-hexylthiophene) as an efficient route to photosensitize nanocrystalline TiO_2 films for photovoltaic applications. ACS Applied Materials & Interfaces.
3. Lee, D. H., Cho, Y. S., Yi, W. I., Kim, T. S., Lee, J. K., & Jin Jung, H. (1995). Metalorganic chemical vapor deposition of TiO_2:N anatase thin film on si substrate. Applied Physics Letters, 66(7), 815-816.
4. Ren, D., Zou, Y., Zhan, C. Y., & Huang, N. K. (2011). Study on the porosity of TiO_2 films prepared by using magnetron sputering deposition. Journal of the Korean Physical Society, 58(4), 883-885.
5. Sudou, S., Kado, K., & Nakamura, K. (2010). Optical properties of ga-doped TiO_2 films prepared by spin-coating method. Transactions of the Materials Research Society of Japan, 35(1), 171-174.

Acknowledgments

This work was also made possible by the NSF sponsored Science and Technology Center on Materials and Devices for Information Technology Research, No. DMR-0120967 and the Center for Interface Science: Solar Electric Materials, an Energy Frontier Research Center Funded by the U.S. Department of Energy, Office of Science, Office of Basic Energy Sciences under Award Number DE-SC0001084.

I would also like to acknowledge my faculty mentor Dr. Neal R. Armstrong, graduate student mentors Delvin Tadytin and Kai-Lin Ou, Hooked on Photonics (HoP) administrative assistant Amanda Anderson, and HoP program coordinator Kimberly Sierra-Cajas for all their help and support.

MICHAEL NGUYEN is a fourth year chemistry undergraduate at San Diego State University aiming to procure a doctoral degree in the chemical sciences from a research oriented university.

Interfacial Adhesion Strength Analysis of SiN_X/Ag Contacts in Photovoltaic Modules

ANTHONY P. NICHOLSON, Colorado State University
Yongjin Kim, Samuel Graham, Georgia Institute of Technology

Introduction

Efficiency of solar modules is a major figure of merit which must be addressed in order to help further the market penetration of solar cells. However, just as equally important is the reliability of these photovoltaic (PV) cells which are expected to last 20-25 years. One of the influences which impacts the degradation and reliability of PV cells is exposure to the environment or more specifically, oxygen, water vapor, temperature, and chemical species.[1] To aid the long term reliability, PV modules are typically encapsulated to prevent the ingress of water vapor and oxygen which can cause corrosion of contacts and electrodes as well as degrade active layers especially in the case of organic photovoltaics. For thin film, photovoltaics consisting of CIGS and OPV, thin barrier films are utilized during manufacturing processes of PV cells to protect them from water vapor and oxygen. In the case of inverted OPVs and CIGS cells, these barrier films may be deposited in direct contact with the back silver electrode which is used to collect charge generated in the solar cell. As these cells undergo thermal cycling and changes in stress during operation, there is a possibility that delamination could occur within the PV cell, initiating at the barrier film-Ag electrode interface. Such delaminations will then allow for the rapid ingress of water vapor and oxygen, leading the rapid degradation of the PV module. At present, the adhesion of barrier films to Ag electrodes has not been quantified. Thus, it is not possible to model the strength of the interfaces and make an assessment of the potential failure during PV operation. In addition, the aging and degradation of this interface has not been studied. Such values are critical to the assessment of PV module long term reliability.

The objective of this work is to study the adhesion of barrier films to Ag electrodes, providing the first measurements of the Critical Strain Energy Release Rate (Gc). Analyzing this mechanical property value will allow for quantification of the adhesion strength which can then be used in subsequent failure analysis models. In addition, we will investigate methods to improve adhesion to the Ag electrodes and determine the ability of these interfaces to resist aging in solar environments. The predicted outcome of the experiments is that using TiN on the Ag layer will significantly increase the critical strain energy release rate of the interface and resist the degradation which may occur in thermal cycling or exposure to solar environments.

Experimental Methods

A series of Double Cantilever Beam (DCB) mechanical tests were conducted to analyze the fracture energy toughness between the Ag and a SiN_x barrier film. A depiction of the DCB tests is shown in Figure 1, where mode 1 fracture of the prepared samples occurs.

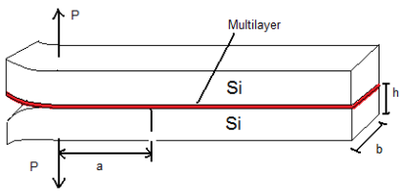

Figure 1: Schematic of the targeted inverted solar device.

The Ag layer was deposited on a Si wafer using a Ti adhesion layer for the Ag. The Si wafer is used as a strong elastic member to transfer the mechanical energy to the interface for controlled crack propagation. After the Ag is deposited, deposition of a SiN_x layer directly onto the Ag layer took place using plasma enhanced chemical vapor deposition. Next, we attached a Si wafer to the SiN_x layer using epoxy. Samples were cut into beams for DCB testing in a mechanical test frame. Three separate procedures were conducted: First a baseline test was performed to obtain the initial G_c values of the interface. Second tests included an enhanced interface using TiN were tested to determine if the adhesion between the SiN_x and Ag can be improved. Third, another modified interface using Al was used to examine how alternative materials compare to TiN regarding adhesion strength. Each sample used had a total height of approximately 1 mm, width of 5 mm, and a length of 45 mm. Typical thicknesses for the Si wafers were around 400 μm. The bottom Si wafer contained the thin Ti (30 nm) and Ag (300 nm) deposited layer and was coated with 100 nm of SiN_x. The top layer only consists of Si and was placed on top of the preceding layers. In between these two layers, < 1 μm EPO-TEK ® 301 Epoxy was used to join both layers. A C-Clamp device was required to compress the epoxy to a thickness on the order of 1 μm. In order to ensure a crack is initiated, 30 nm of Au was placed between the Ag and SiN_x at the front edge of the sample. The entire configuration of the sample is illustrated in Figure 2(a). The primary mechanism used for testing the fracture energy of the adhesive bonds between the Ti/Ag deposition and SiN_x layer is mechanical loading in a tabletop test frame (DTS Delaminator) as shown in Figure 2(b).

The results were compiled into a graph measuring specific loading magnitudes dependent on bond displacement. The critical fracture energy G_c can then be calculated from the load-displacement data to establish the amount of applied energy used to debond Ti/Ag from the SiN_x barrier layer.

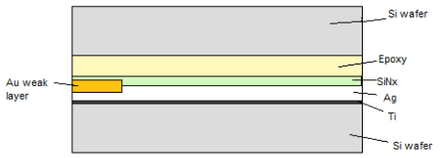

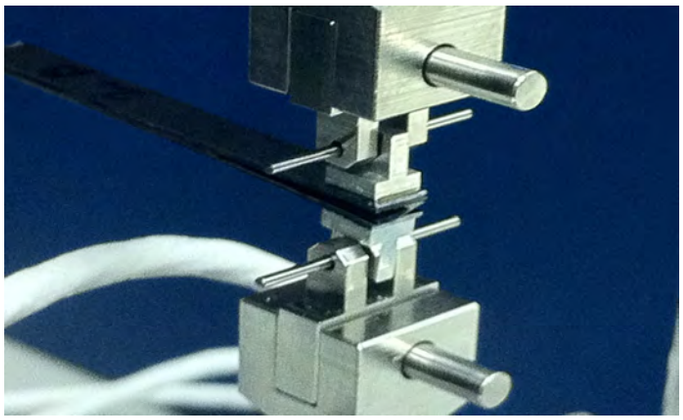

Figure 2: (a) Illustration of sample layers being tested (initial samples only). Enhanced samples include either TiN or Al deposited between the SiN_x and Ag layers. Each sample was tested upside down to this configuration. (b) Double Cantilever Beam set-up using the DTS Delaminator. The clevis grips and holding pins ensure that crack propagation is moving straight along the interface of interest.

Results

An understanding of Beam Theory and Fracture Mechanics is required for determining the critical strain energy release rate that is derived from the double cantilever beam test. The double cantilever beam (DCB) interfacial fracture toughness equation used during these experiments is as follows:

$$G_c = \frac{12(1-\nu^2)P_c^2 a_c^2}{Eb^2h^3}$$

where ν=Poisson's ratio, P_c=Critical Load, a_c=crack length, b=base of beam sample, h=half height of beam sample, and E=Young's modulus. Since a_c, h, b, E, and ν are all controlled parameters within the experiment, it is only necessary to find critical loading and crack length values in order to calculate G_c^2. This was detected through critical points indicated on the Load vs. Displacement graph of the sample as shown in Figure 3.

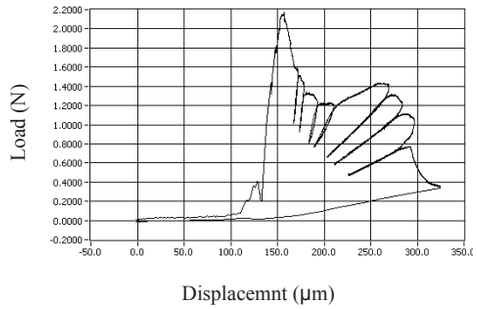

Figure 3: Load-Displacement Graph of the DCB mechanical testing analysis. The critical points are marked by the arrows above and are used to determine the G_c value at that specific crack length.

Out of 10-15 tested samples, only five of each sample type yielded sufficient data for the DCB testing. Five critical points were found for each sample to provide enough evidence of a consistent trend in the adhesive strength throughout the sample interfaces, seen in Table 1.

Sample	P_c (N)	a_c (mm)	G_c value (J/m^2)
1	0.7	10.3	1.181
	0.68	11.51	1.392
	0.58	13.45	1.383
	0.48	16.98	1.509
	0.43	19.92	1.667

Table 1: Recorded data of the critical loads and crack lengths for five critical points in one sample. The critical strain energy release rates were also calculated for each critical point.

Average critical strain energy release rate values for the five best initial and enhanced test samples (TiN and Al) are displayed in Tables 2. Table 3 compares the total average Gc sample value for the three varying samples.

Sample #	Av. G_c value (J/m^2)
1	1.426
2	0.718
3	1.698
4	1.207
5	0.659

(a)

Sample #	Av. G_c value (J/m^2)
1	0.838
2	5.667
3	1.412
4	0.611
5	1.327

(b)

Sample #	Av. G_c value (J/m^2)
1	3.249
2	2.410
3	2.307
4	1.384
5	1.184

(c)

Table 2: (a) Initial sample results for average G_c values. (b) TiN enhanced sample results. (c) Al enhanced sample results.

Sample Modifier Type	Av. G_c value (J/m^2)
No modifier	0.778
TiN	1.482
Al	1.633

Table 3: Comparison of the three total adhesion energy averages of each different test sample type.

Discussion

Most of the initial samples did not provide high Gc results as expected. The crack propagated along the SiN_x/Ag interface of interest due to the Au weak region. As for the enhanced samples, adhesion energy improvements were seen in both TiN and Al modifiers. However, the two enhanced sample types did not contain a weak Au region because of the issue with deposition temperature for TiN and Al layers. In particular, TiN deposition occurs at 450°C; this temperature range is too high for Au and will actually cause it to diffuse during the process. Therefore the modified samples were tested without controlled crack propagation, allowing for debonding in subsequent interfaces other than SiN_x/Ag. This may explain why some fracture energy values in both Tables 3 and 4 were inconsistent in magnitude. Further examination reveals valid evidence as to where these enhanced samples most likely debonded. Using Energy Dispersion Spectroscopy (EDS) on the Scanning Electron Microscope (SEM), we determined the weight percentage of certain elements found on the top and bottom piece of a fractured sample for TiN and Al. Doing so indicated which elements were on the surface where debonding took place as depicted in Figure 4.

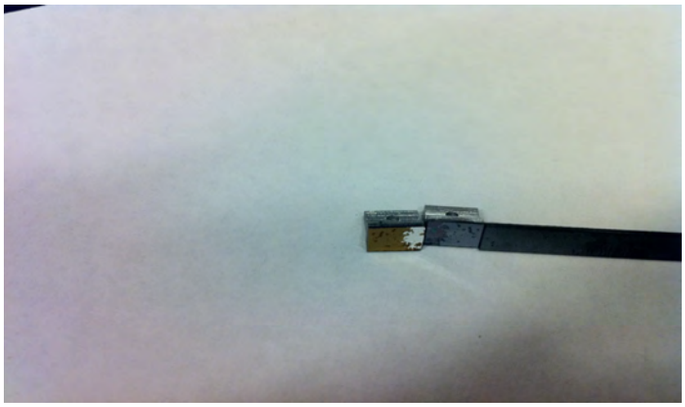

Figure 4. View of debonded sample at the TiN (yellow) and SiNx (Grey) interface. Most TiN enhanced samples did not separate at the interface of interest as in this case.

Concerning the TiN fracture sample, Figure 5(a) shows a high Ag and SiN_x concentration on the top half while Figure 5(b) contains large amounts of carbon and oxygen for the bottom surface, which are main components found in epoxy. Based off these results, it is reasonable to assume that the interface at which delamination occurred for this sample was at the SiN_x/Epoxy interface. This interface is not the correct one for testing the adhesion strength between the thin SiN_x film barrier and the Ag electrode. Although we know that TiN creates a stronger bond, the specific magnitude of TiN adhesion strength is inconclusive in these results. However, the Al fracture sample yielded a different result than that of TiN. As Figures 5(c) and 5(d) suggest, respectively, the top half consisted of Ag and Al and the bottom half only had SiN_x. Therefore, it is evident that this sample debonded at the desired Al-Ag/SiN_x interface of interest, demonstrating that data for Al was more consistent than TiN. Yet is still difficult to compare both TiN and Al merely by their average sample Gc value. Since debonding for the preceding fracture sample type did not happen at the TiN/SiNx interface as expected, the adhesion strength is believed to be higher for TiN than Al because of this interfacial discrepancy.

a)

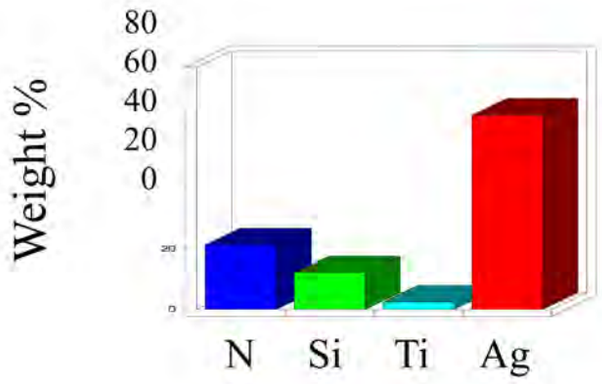

b)

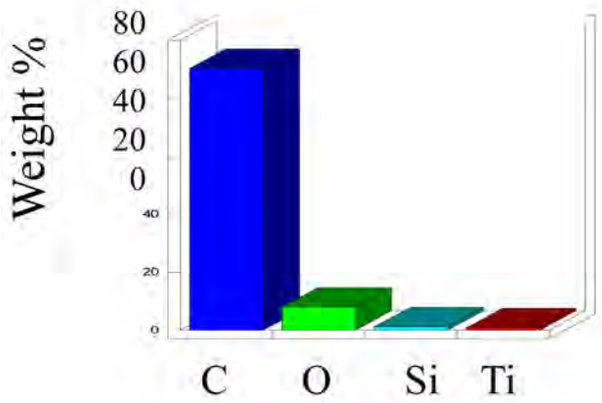

c)

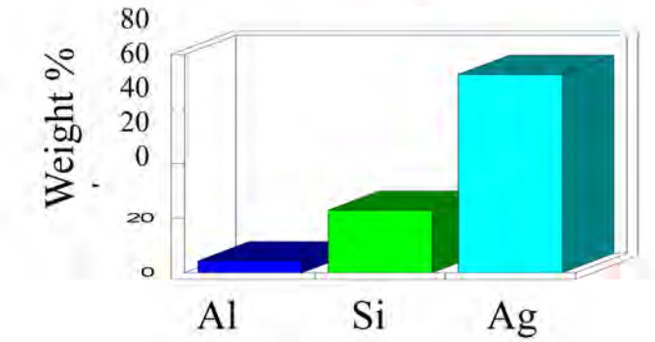

d)

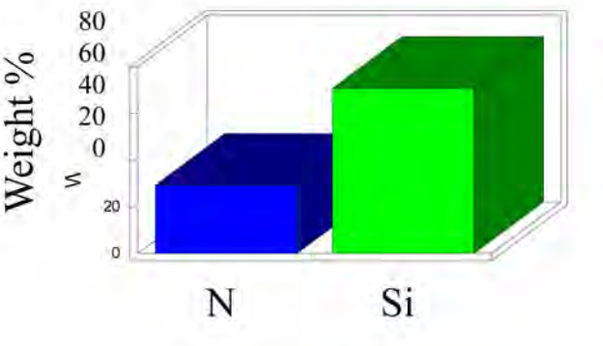

Figure 5: Weight percentages of certain elements found on the surface of the (a) top and (b) bottom of a TiN enhanced fracture sample, and the (c) top and (d) bottom half of an Al enhanced fracture sample.

Conclusion

By analyzing the interfacial adhesion strength of the SiN_x barrier and Ag electrode, we conclude that using TiN and Al materials between the two layers does improve the amount of energy required to delaminate that interface. Despite not having a weak region at the front of each sample for controlled crack propagation, TiN and Al still provide viable results, which indicated significantly better fracture energy values as oppose to the initial samples. Both enhanced sample batches provided at least a 90% increase in the adhesion strength when compared to the typical SiN_x/Ag arrangement. When using EDS for evaluating the bottom and top surface of the fractured TiN sample, the elemental composition indicates debonding at the incorrect interface, thus making it difficult to draw conclusions on the exact adhesion strength of TiN. In contrast, the composition found in the Al fractured sample's separated interface signifies a successful crack propagation along the interface of interest. By looking at not only the data but also these observations, it may inferred that TiN has better adhesive properties than Al because TiN did not delaminate from the SiN_x layer, as in the case of Al and SiN_x. In the end, the quantification of the critical strain energy release rate shows promises of progress in determining the reliability of thin film PV cells and in methods on how to improve adhesion.

Future Work

More research must be conducted on the morphology, or surface roughness,[3] of the SiN_x and Ag electrode. The more asperities that form on either layer actually create a larger surface area of contact in the SiN_x/Ag interface. Upon observation, all samples were relatively smooth at those layers, therefore providing less area of contact for adhesion to occur. It may be reasonable to assume that at least some of the inadequate G_c values were caused by a design parameter like surface roughness. Therefore studying the effects of morphology on certain interfaces may lead to deeper insights on how to improve adhesion strength.

Another possible extension for this research is the utilization of the four-point bend method instead of the DCB method. Using this technique may provide more accurate results in quantifying the G_c values due to its use of fracture modes I and II that give better control of crack propagation along a particular interface. This will allow for further intrinsic observations of the fracture and a better simulation of actual delaminations that occur with PV cells in commercial use.

References

1. Lane, M. W.; Snodgrass, J. M.; Dauskardt, R. H. Environmental Effects on Interfacial Adhesion. Microelec. Rel. 2001, 41, 1615, 1616.
2. Dauskardt, R. H. DTS Delaminator Manual, 2004, 10, 11, 23, 40-42.
3. Dauskardt, R. H.; Lane, M.; Ma, Q.; Krishna, N. Adhesion and debonding of multi-layer thin film structures. Engr. Frac. Mech. 1998, 61, 143.

Acknowledgments

Funds for this research were provided by the Center of Materials and Devices for Information Technology Research (CMDITR), the NSF Science and Technology Center No. DMR 0120967. I would like to personally thank Dr. Samuel Graham, Yongjin Kim, and Hyungchul Kim for all of their help and support during this research experience.

ANTHONY NICHOLSON is a junior majoring in mechanical engineering and minoring in mathematics at Colorado State University in Fort Collins. His prospective goals after obtaining his Bachelor of Science degree are to pursue a career in the solar renewable energy field and continue fulfilling future aspirations as an engineer.

Single Molecule Measurements of Dielectric Domains in Polymers

JORGE PALOS-CHÁVEZ, University of Texas
Erin A. Riley, Chelsea Hess, Philip J. Reid, University of Washington

Introduction

Advancements in photovoltaics, LEDs, and other solid state devices have been achieved through continued characterization of nano-scale structure in device materials. Much remains to be discovered about the electronic properties of materials at the nano-scale such as how charge distributes itself and re-arranges. In my research we began to answer this question using single molecule (SM) microscopy to determine how distributed the dielectric constant is in poly methyl methacrylate (PMMA).

Single molecule (SM) spectroscopies reveal phenomena that are obscured by ensemble measurements. Monitoring the fluorescence of a single molecule can provide information on the nano-scale structure of the supporting lattice, as the fluorescence of a dye is solvent dependent. This is of particular interest for deducing the structure of soft and complex matter which possesses both static and dynamic heterogeneity.

One hypothesis that has come of previous SM studies, which monitored the rotation of fluorophores embedded in polymer films, is that super-cooled polymers are comprised of domains that interchange at varying rates.[1] The existence of domains is an important consideration in the design of organic electronics especially if charge is moving inhomogeneously due to these domains. These domains also may affect the efficiency of "poling" where an external field is used to induce molecular alignment of polar molecules in a material. Inefficient poling of organic nonlinear optical materials is a major obstacle in the development of organic based devices.[2]

To determine the existence of "dielectric domains" a highly solvochromatic fluorophore, nile red, is doped into polymer films to probe the local dielectric constant by monitoring the color of the dye using confocal microscopy.

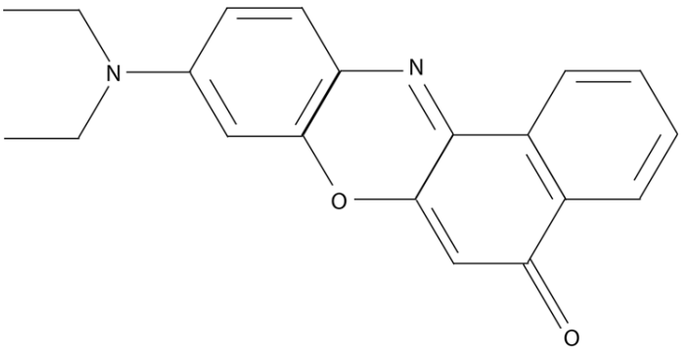

Figure 1: The chemical structure of Nile Red.

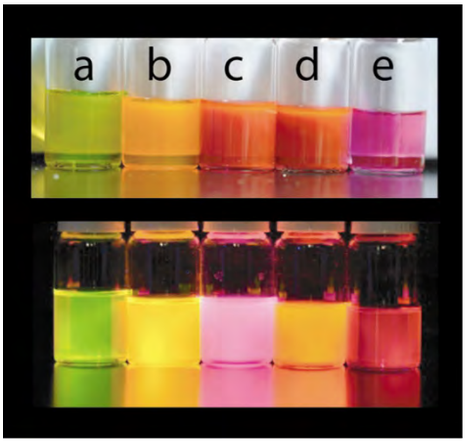

Figure 2: Nile Red in various solvents, showing its solvochromatic properties. Bottom photograph is of the fluorescence. Solvents shown are: a. hexane, b. toluene, c. cyclopentanone, d. acetone, e. methanol.

Experimental Methods

Nile Red (318.7 g/mol) was dissolved in toluene to produce ~$3x10^{-5}$ M solutions. This concentration was experimentally determined to be appropriate for bulk film absorption and fluorescence measurements. PMMA was dissolved into HPLC-grade toluene in order to form 4% wt. polymer-dye solutions for heavily dyed films and 1% for microscopy measurements. The solutions were rotated overnight.

Thick films were made by drop casting 8-10 drops of polymer dye-solution on a glass cover slip and then immediately placing the cover slip under vacuum at approximately -10 atm. The films were allowed to settle for 10 min and gradually brought back to atmospheric pressure under nitrogen fed from an outside line. Absorption measurements were taken using a dual-beam spectrophotometer. Fluorescence and excitation measurements were done using a steady-state fluorimeter.

To prevent fluorescence contamination, all glassware were cleaned by first treating in an isopropanol/KOH base bath overnight and rinsed thoroughly with nanopure DI water, and HPLC grade acetone and dried with nitrogen. Blank cover slips were cleaned by boiling in a solution of 3:2:1, nanopure DI water: ammonium hydroxide: hydrogen peroxide for 3 h. The solution then cooled for 1 h before being doused individually with nanopure DI water. The cover slips were quick-dried with nitrogen.

1% wt PMMA in toluene stock solution was placed in a UV box (320 nm $\leq \lambda \leq$ 420 nm) for 4 h to reduce fluorescence contamination

present in the polymer or solvent. This procedure had no effect on the chemistry of the polymer.[3]

Thin films for microscopy were produced by spin coating. Approximately 8-10 drops of polymer solution were dropped on a clean cover slip. The spin coating program was 60 s at 500 rpm followed by 45 s at 2000 rpm.

The thin film samples studied in this experiment were a) a "blank" sample consisting of a SM clean cover slip and 1% PMMA/toluene solution with no dye present, b) a "bulk" sample consisting of 10^{-7} M Nile Red in 1% PMMA/toluene, and c) a "SM dye" sample consisting of ~$5x10^{-11}$ M Nile Red in 1% PMMA/toluene. The SM concentration was tailored to space the molecules ~2 microns apart.

Measurements were taken using a custom-built diffraction-limited confocal laser microscope. Two avalanche photodiode (APD) detectors collect light of wavelengths i. 550-600 nm and ii. >600 nm. 3.1 microwatts of a 532 nm CW diode laser were focused into a 1.3 NA objective to provide excitation.

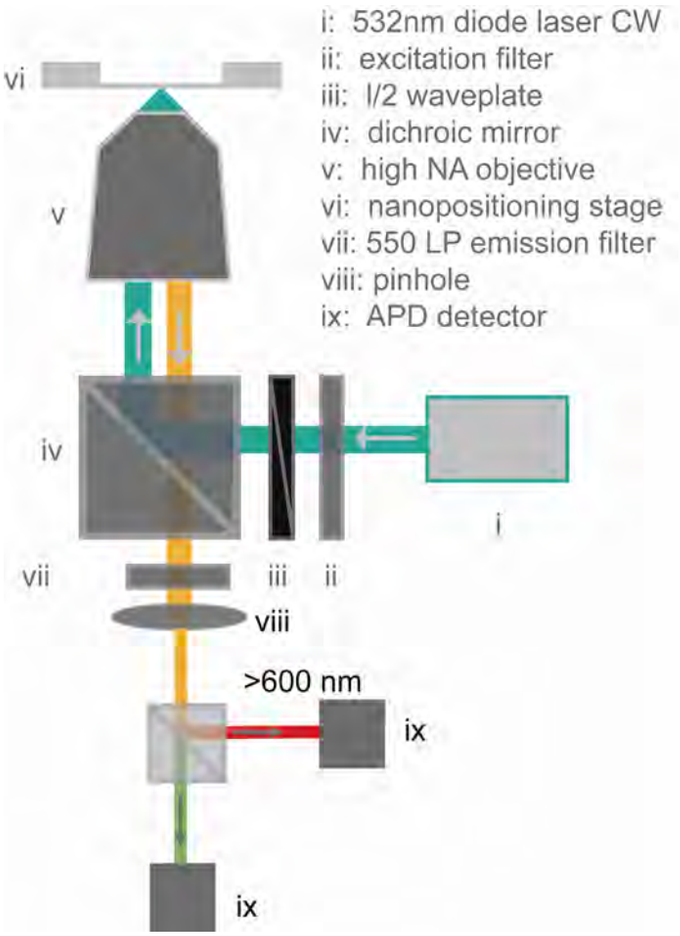

Figure 3: Schematic of the confocal microscope used to obtain SM fluorescence images.

Results and Discussion

Excitation and fluorescence spectra for 'bulk' dye-polymer thick films reveal a very symmetric and well-defined distribution of emission frequencies. This is in stark contrast to distributions obtained by observing the fluorescence of single molecules in thin films, demonstrating the importance of understanding single molecule pheonomena.

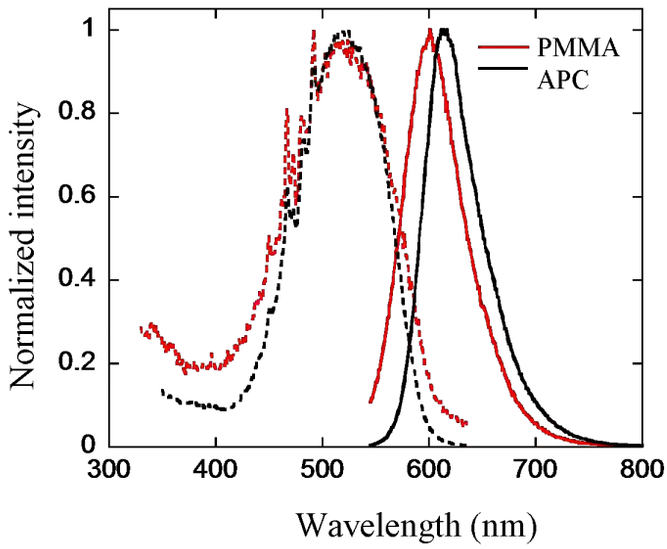

Figure 4: Bulk excitation and fluorescence spectra for Nile Red doped PMMA and APC (amorphous polycarbonate) thick films.

Figure 5 is a false color image of the fluorescence of single nile red molecules. These images were processed to remove aggregates based upon size and intensity of the spots, and the back ground removed. Then the ratio of the two channels was computed in ImageJ and histograms of the resulting pixels were complied.

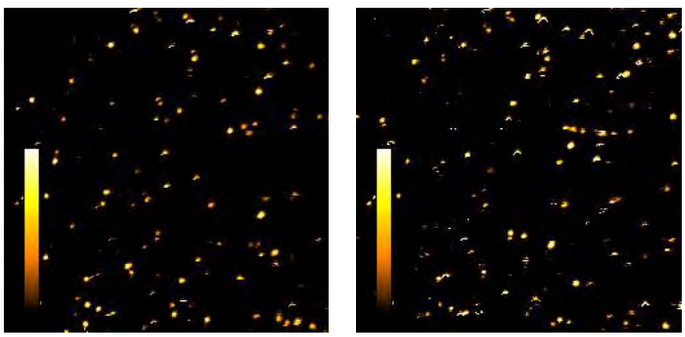

Figure 5: 25 x 25 micron scan of nile red in PMMA. False color scale 50-500 counts/100 ms. Left >600 nm detector, and right 550 nm-600 nm detector.

Figure 6 demonstrates the distribution of fluorescence intensities for PMMA with 10^{-7} M Nile Red. The ensemble histogram is representative of the bulk spectrum in Figure 4 as recorded by the two APDs. The histogram constructed out of several scans like the one in Figure 5 of single Nile Red molecules shows a much broader distribution. The tail of the distribution in Figure 7 seems to be partly due to background contamination from the polymer as can be seen in Figure 8.

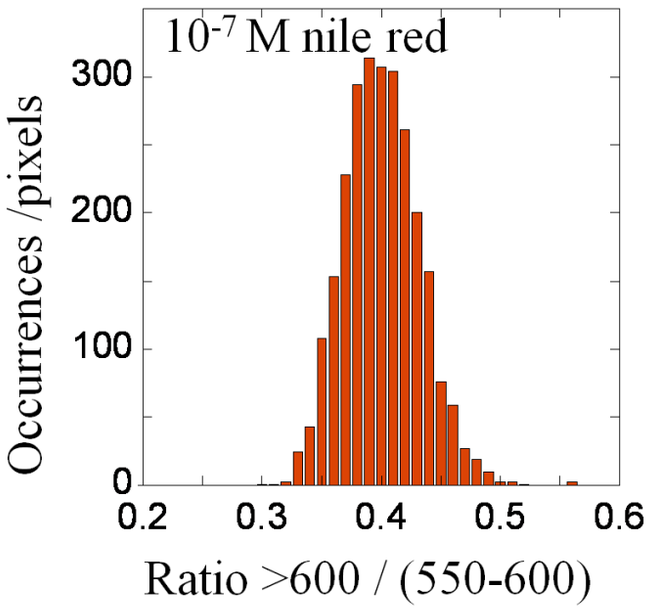

Figure 6: Fluorescence distribution of bulk Nile Red doped PMMA film.

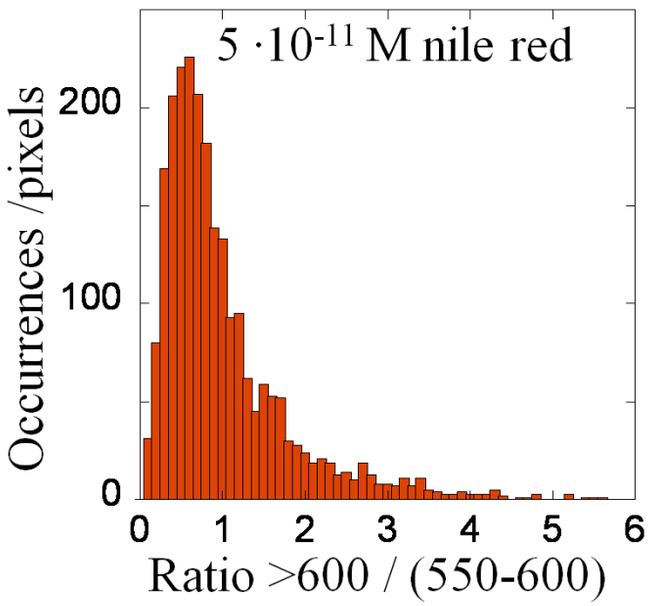

Figure 7: Fluorescence distribution of Nile Red doped PMMA film.

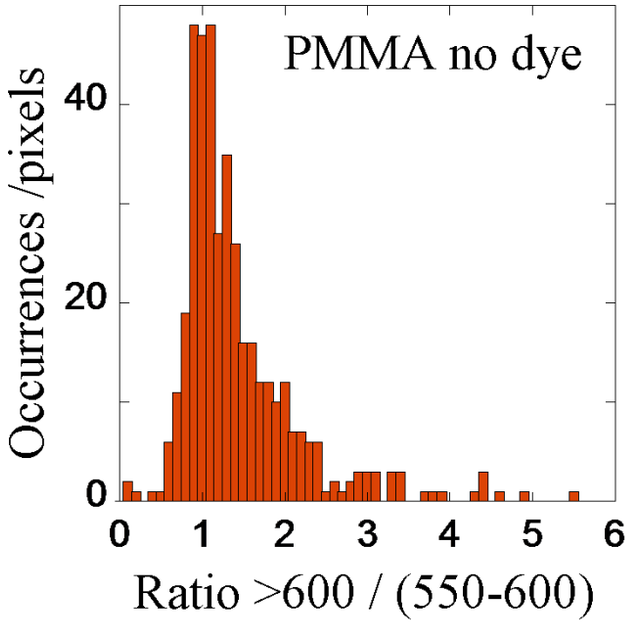

Figure 8: Fluorescence distribution of blank PMMA film. Contamination is present.

The wide spread in the ratio of the two channels for the single molecule intensities is related to shifts in the fluorescence spectrum of Nile Red. There exists a much broader spread in SM emission wavelengths then can be detected in the bulk measurement. Since Nile Red is solvochromatic, it stands to reason that this supports the hypothesis of the existence of distributed dielectric domains within PMMA.

Future Studies

Future work will include correlating the spectral shifts seen in the SM experiments to actual values of the dielectric constant of each nano-environment that is sampled by individual nile red molecules. From this we can determine how wide the distribution of dielectric environments is expected to be.[3]

This experiment will be performed on two other polymer films which are in preparation. These are amorphous polycarbonate (APC), and a ferroelectric polymer PVDF. The single molecule histograms will be analyzed based upon the known dielectric properties of Nile Red to determine the spread in dielectric constants in the polymer films.

Once this initial characterization is complete, then dynamic studies will be performed to measure the time dependence of the dielectric constant in the vicinity of each molecule. We would also like to determine the influence of an electric field on the distribution of dielectric environments to see if poling has a influence during and after the application of a field. The ferroelectric polymer will be used to test the hypothesis of switchable domains since ferroelectric materials are comprised of domains that can have their polarization changed by the application of an external field. It will be interesting to observe the switching *in situ*.

These experiments are important in understanding both the structure of polymer films as well as how much the structure can be manipulated externally. Currently poling is used to induce alignment of molecules in nonlinear optical devices, but is very inefficient. We would like to gain a molecular understanding of this process to improve upon it.

References

1. F. Kulzer, T. Xia, M. Orrit. Single Molecules as Optical Probes for Soft and Complex Matter, Angew. Chem. Int. Ed. 2010, 49, 854 – 866.
2. M. Orrit. Single Molecule Microscopy, Universiteit Leiden, Netherlands. http://www.molphys.leidenuniv.nl/monos/students/index.html?smo.htm
3. Torikai, A., Ohno, M. and Fueki, K. (1990), Photodegradation of poly(methyl methacrylate) by monochromatic light: Quantum yield, effect of wavelengths, and light intensity. Journal of Applied Polymer Science, 41, 1023–1032.

Acknowledgments

Funds for this research were provided by the Center on Materials and Devices for Information Technology Research (CMDITR), the NSF Science and Technology Center No. DMR 0120967.

Special thanks to Chelsea Hess, Erin Riley, and Patrick Whitham of the Reid lab for their guidance and assistance in accomplishing these studies.

Partially funded by NIH/NIGMS MARC U*STAR GM07717.

JORGE PALOS-CHÁVEZ is a senior Physics major at the University of Texas at San Antonio planning on pursuing a Ph.D. in Physics.

Molecular Design, Synthesis and Characterization of Thiophene-based Organic π-conjugated Semiconducting Polymers

CARYN PEEPLES, Norfolk State University
Boyi Fu, Elsa Reichmanis, Georgia Institute of Technology

Introduction

Polymer semiconductors refer to polymers having π-conjugated polymer backbone. Coupled unsaturated units, e.g. aromatics, lead to the polymer having extended π orbitals along the backbone. Currently, polymer semiconducting materials are widely investigated due to their applications in opto-electronics, such as organic field-effect transistors (OFETs),[1] organic photovoltaic devices (OPVs), and organic light-emitting diodes (OLEDs).[2]

Compared with traditional silicon semiconductors, organic semiconducting devices have advantages in the solution processing availability.[1] This will allow them to be made economically light weight in large area flexible plastic optoelectronic devices.

Poly-3-hexylthiophene, P3HT, is the most widely studied π-conjugated material in organic optoelectronics, which exhibits high charge carrier mobility up to 0.3 $cm^2/(V.s)$ in OFET and high power conversion efficiency beyond 5% in OPV.[3] This polymer; however, has severely decreased performance when exploring to oxygen and humid environments. These disadvantages are attributed to its high highest occupied molecular orbital (HOMO) energy levels. In addition, its relatively large bandgap (~ 2.0 eV) limits the sunlight harvesting when it is employed to OPV.[3] It is therefore necessary to enhance the oxidative stability and bandgap of polythiophene by utilizing molecular modification.[4]

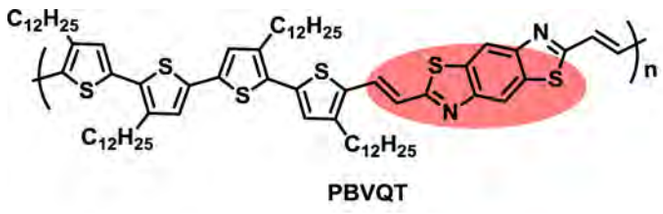

Figure 1: Poly-benzobisthiazole-vinylene-quarterthiophene (PBVQT). Highlighted areas indicate vinylene linkage and fused rings.

We have proposed to develop a new regioregular poly-benzobisthiazole-vinylene-quarterthiophene (PBVQT, Figure 1). The HOMO energy level of the polymer will be reduced by incorporating vinylene linkages in the polythiophene backbone. This will assist with enhancing π-conjugation by lowering intra-chain torsion; while the bandgap of the polythiophene will be narrowed after incorporating electron deficient benzobisthiazole.

The synthetic strategy for making PBVQT is outlined in Scheme 1. The synthesis will be completed using several reactions: including copper coupling (1), bromination (2), Stille coupling (3) reaction, formylation reaction (M1), and Horner Wadsworth Emmons reaction (PBVQT).

Experimental

Preparation of 4,4'-didodecyl-2,2'-bithiophene (1)

Tetramethylethylenediamine (TMEDA) (0.213 mL, 1.42 mmol) and 3-dodecylthiophene (0.3 g, 1.19 mmol) were dissolved in tetrahydrofuran (THF) (20 mL) and n-butyllithium (0.57 mL, 2.5 M in hexanes) was added dropwise at -78°C. The reaction was allowed to warm to room temperature before heated to 70°C and refluxed for one hour. Copper chloride (0.208 g, 1.55 mmol) was quickly added at -78°C. The reaction mixture was stirred overnight, during which period the temperature rose to room temperature.

The organic product was extracted with hexane. The combined organics were washed with brine (250 mL), dried (magnesium sulfate), filtered and concentrated under reduced pressure. The hexane in the mixture was then removed using rotary evaporator. The resulting yellow oil was purified by column chromatography (hexane as the eluent). The resulting product was recrystallized in acetone and ethanol (1:1, v/v) to get 0.4 g of target product. ^{1}H NMR:(400 MHz, $CDCl_3$, ppm): 6.95 (s, 2H); 6.74 (s, 2H); 2.53 (t, J = 7.6 Hz, 4H); 1.56 (t, 4H, J = 6.6 Hz); 1.29 (m, 20H); 0.85 (t, J = 7.1 Hz, 3H).

Preparation of 5,5'-Dibromo-4,4'-didodecyl-2,2'-bithiophene (2)

To a solution of 4,4'-didodecyl-2,2'-bithiophene (0.4 g, 79.5 mmol) in $CHCl_3$/HOAc (1:1) (Vt = 10.0 mL) at 0°C was added NBS (0.297 g, 1.67 mmol) in portions over a period of 1 h. The reaction mixture was stirred for 1 h at 0 °C, and overnight at room temperature.

The reaction mixture was then washed with brine (50.0 mL) and extracted with chloroform (3×50.0 mL). The combined organic phases were dried over $MgSO_4$. The chloroform in the mixture was then removed using rotary evaporator to produce a yellow powder. 1H NMR (CDCl3): 1H NMR ($CDCl_3$): ^{1}H NMR (400 MHz, $CDCl_3$) δ 6.77 (s, 2H), 2.51 (t, J=19.6 Hz, 4H), 1.57 (m, 4H), 1.31(m, 28H), 0.89 (t, J=13.6 Hz, 6H)

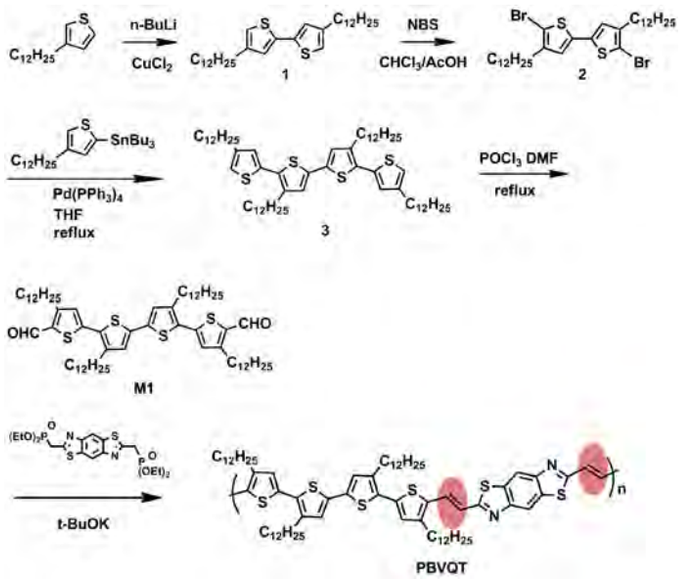

Scheme 1: Synthetic route of PBVQT.

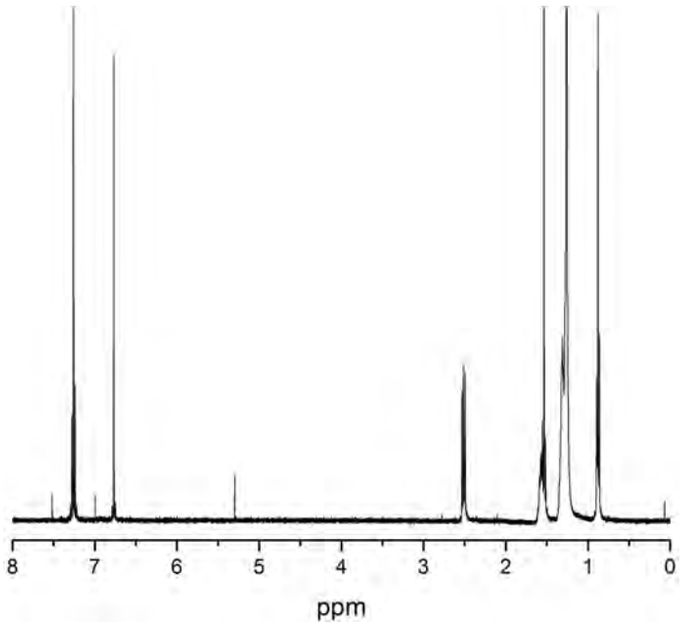

Figure 2: 1H NMR of 4,4'-didodecyl-2,2'-bithiophene.

Characterization

1H NMR (nuclear magnetic resonance) spectra were measured with a Varian Mercury 400 at room temperature. (see Figure 2 and 3).

Results and Discussion

The synthesis began with a copper chloride after butyllithium to obtain 4,4'-didodecyl-2,2'-bithiophene (1). The reagents in this step were very sensitive to water and oxygen environment. The reaction formed a crystallized yellow product after column chromatography. After recrystallization the product was light yellow cotton textured solid.

The product identity was confirmed to be 4,4'-didodecyl-2,2'-bithiophene (1) using NMR.

The product then underwent bromination using n-bromosuccinide (NBS). The reaction was carried out under the dark situation. A clear, amber liquid was produced after washing. The product's identity was confirmed using ^{1}H NMR.

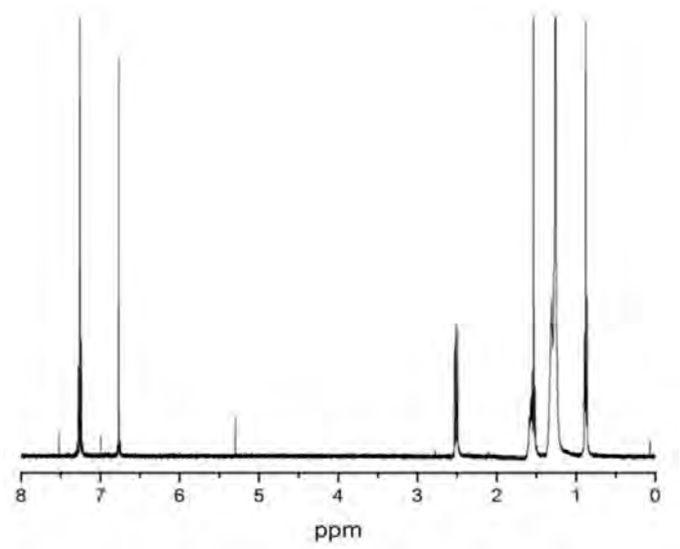

Figure 3. 5,5'-Dibromo-4,4'-didodecyl-2,2'-bithiophene.

Conclusion

The first two monomers that are essential for the synthesis of PBVQT were successfully synthesized and characterized.

In the future, the later three steps for making M1 will be synthesized. M1 will undergo Horner polymerization to produce our target polymer, PBVQT. The charge transport property of PBVQT will be tested by field effect transistor; while the photovoltaic properties of PBVQT will be tested by organic photovoltaic devices.

References

1. Osaka, I. ; Abe, T.; Shinamura, S.; Takimiya, K. Impact of Isomeric Structures on Transistor Performances in Naphthodithiophene Semiconducting Polymers. J. Am. Chem. Soc. 2011, 133, 6852-6860.
2. Blouin, N.; Michaud, A.; Gendron, D.; Wakim, S. Toward a Rational Design of Poly(2,7-Carbazole) Derivatives for Solar Cells. J. Am. Chem. Soc. 2008, 130, 732-742.
3. Ma, W.; Yang, C.; Gong,X.; Heeger, A. Thermally Stable, Efficient Polymer Solar Cells with Nanoscale Control of Interpenetrating Network Morphology, Adv. Funct. Mater. 2005, 15, 1617-1622.
4. Kong, H.; Cho, S; Lee,H.; Cho,N. The Influence of Electron Deficient Unit and Interdigitated Packing Shape of New Polythiophene Derivatives on Organic Thin-Film Transistors and Photovoltaic Cells. Journal of Polymer Science Part A Polymer Chemistry. 2011, 49, 2886-2898.

Acknowledgments

I would like to acknowledge the Center on Materials and Devices for Information Technology Research (CMDITR), the NSF Science and Technology Center No. DMR 0120967. I would also like to thank Boyi Fu, Dr. Elsa Rechmanis, the Rechmanis Research Group, Olanda Bryant, Denisha Thomas, Dr. Cam Tyson, Dr. Keith Oden, and fellow CMDITR participants.

CARYN PEEPLES currently attends Norfolk State University where she is pursuing a chemistry concentration. She will be attending Old Dominion University to major in biochemistry in Fall 2011. Future endeavors include attending graduate school and studying biochemistry or biomedical research.

Donor Materials for Organic Photovoltaics

CHIARA PETRUCCI, University of Perugia
Raghunath Reddy Dasari, Seth R. Marder, Georgia Institute of Technology

Introduction

Organic Photovoltics (OPV) materials being widely investigated as alternatives to inorganic photovoltaic devices due to their potential advantages such as low fabrication cost, light weight, and fast production of large area devices by roll-to-roll processes.[1]

Power conversion efficiencies of OPVs are steadily increasing although, still lower than the silicon-based solar cells (8% versus 20%) which limit their widespread implementation. Strategies to improve OPV performance include developing new materials with broader optical absorption and higher charge carrier mobility, and developing a better understanding of active layer morphology.

Recently, donor (push) and acceptor (pull) systems have gathered greater attention to effectively reduce the energy gap, which is the difference between HOMO and LUMO of the donor, and broaden the optical absorption. Moreover, the intramolecular charge transfer (ICT) from the donor moiety to the acceptor moiety inside a D–A molecule can efficiently extend the absorption spectrum of the molecule for better matching the solar spectrum.[2]

The purpose of my research is to synthesize and study electronic, electrical behavior of donor-acceptor (D-A) copolymers, where donor is benzodithiophene and dithienosilole derivative and acceptor is pyromellitic diimide.

Both acceptor and donor monomers are consist of rigid fused-ring units, which could lead to π-π intermolecular interaction, high charge carrier mobilities and also the planarization of polymer chain, and reduced band gap. The presence of alkyl chains renders the molecules more soluble and easier to process as thin films by solution processing.

Results and discussion

Synthesis of N,N'-dialkylpyromellitic imide reported in Scheme 1 followed the procedure reported in literature,[3,4] it was performed reacting pyromellitic anhydride with alkylamine in DMF at 140 °C overnight. However, ^{1}H NMR of crude product showed only mono substituted anhydride. The reaction was further continued with heating at reflux for 12 h. The crude product was then purified by column chromatography using DCM and hexane as eluent. ^{1}H NMR in $CDCl_3$ confirmed the product.

The following bromination of diimide was not successful due to non reactivity of the starting material.

Scheme 1: Synthesis of N,N'-dialkyldibromopyromellitic imide.

The bromination of pyromellitic anhydride showed in scheme 2 was not successful

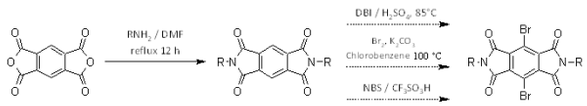

Scheme 2: Bromination of pyromellitic anhydride.

The desired product was prepared according to procedure reported in the literature and described in Scheme 3.[5] The bromination of the commercially available 1,2,4,5-tetramethylbenzene (durene) was performed in refluxing CH_2Cl_2, the product was then oxidized with $KMnO_4$ in a two-step process, first using pyridine and then in aqueous NaOH conditions. Upon the oxidation, the pH of the resulting solution was optimized to obtain dibromopyromellitic acid.[6] The formation of anhydride was conducted in refluxing acetic acid and acetic anhydride for 3 h. The condensation reaction between dibromopyromellitic anhydride and alkylamine was carried out in refluxing acetic acid for 2 h. The crude product was purified recrystallization from ethyl acetate.

The synthesis of the copolymers was performed in a small scale, through microwave assisted Stille coupling, using $Pd(PPh_3)_2Cl_2$ as catalyst and o-xylene as solvent. Dibromopyromellitic imide acceptor was coupled with stannyl derivatives of benzodithiophene and dithienosilole respectively. Molecular weights of new copolymers were estimated by Gel Permeation Chromatography (GPC) and their absorption properties were measured by UV-Vis spectroscopy in THF. The absorption spectra of the crude polymeric samples in THF show high energy absorption bands in the range of 250-400 nm and broad charge-transfer type absorption bands between 400-600 nm for each copolymer. However copolymer of a stronger donor P2, showed red-shifted and intense charge-transfer band.

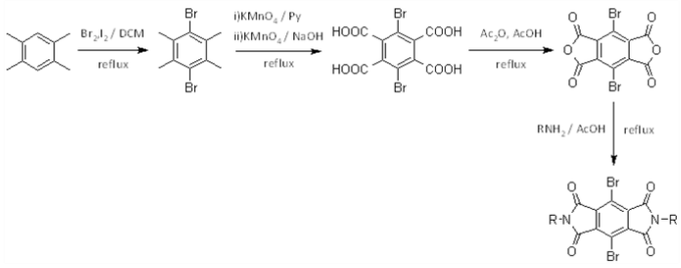

Scheme 3: Synthesis of N,N'-dialkyldibromopyromellitic imide.

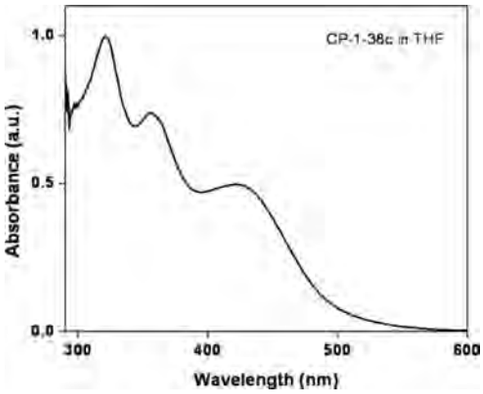

Figure 1: UV-Vis spectrum of polymer P1.

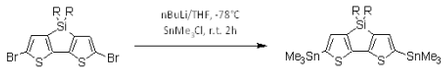

Scheme 4: Synthesis of di-trimethyltin-dithienosilole.

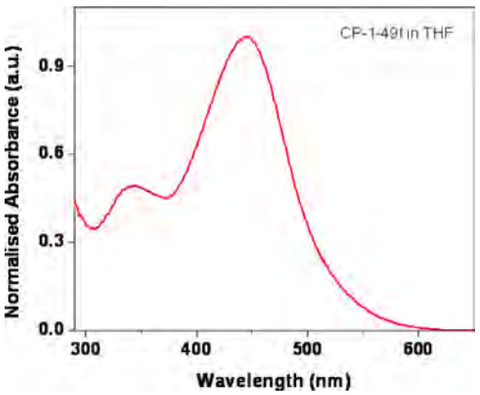

Figure 2: UV-Vis spectrum of polymer P2.

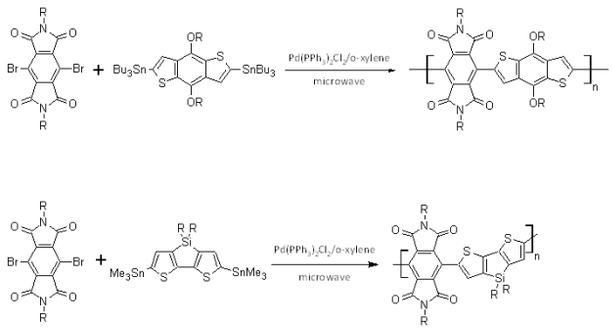

Scheme 5. Synthesis of conjugated D-A polymers P1 and P2.

Experimental

Synthesis of N,N'-dialkylpyromellitic imide

Pyromellitic anhydride (10 g, 46 mmol) was placed in a 500 ml multi-neck RBF. DMF (185 mL) and alkylamine (184 mmol) were added under N_2 flux and the mixture was heated at 140°C for 24 hrs. The reaction mixture was cooled in a refrigerator and subsequently filtered; the precipitate was washed with methanol. The crude product was dissolved in DCM, dry-packed onto a silica gel column and desired product was eluted with DCM:Hexanes in ratio 1:1. Yield: 5.4 g. ^{1}H NMR ($CDCl_3$, 300 MHz) δ 8.26 (s, 2H), 3.73 (t, 4H, J = 7.2 Hz), 1.71-1.67 (m, 4H), 1.32-1.26 (m, 20H), 0.87 (t, 6H, J = 6.6 Hz).

Synthesis of 3,6-dibromo-1,2,4,5-tetramethylbenzene

Durene (15 g, 112 mmol) and iodine (0.6 g, 4.48 mmol) were placed in a 500 mL multi-neck RBF and dissolved in CH_2Cl_2 (90 mL). Bromine (14.5 mL) in CH_2Cl_2 (60 mL) was added drop wise and the reaction mixture was heated under reflux for 1 hr, which was subsequently neutralized with 5N NaOH solution (30 mL). The organic phase was separated and washed with water twice, the organic layer was dried over $MgSO_4$. The solvent was removed by evaporation; 25.7 g of product was obtained (yield 78%).

Synthesis of 1,4-dibromopyromellitic acid

Dibromodurene (8 g, 27 mmol) was placed in a 500 mL multi-neck RBF. Pyridine (270 mL) and water (36 mL) were added and the mixture was heated at 100°C. $KMnO_4$ (21.6 g, 135 mmol) was added in small portions and the mixture was heated to reflux for 5 h. MnO_2 was removed through filtration; the solvent was removed under reduced pressure to obtain pale-white solid.

Above crude solid was suspended in 5N NaOH (17.9 g, 400 mL of H_2O) solution and the mixture was heated at 100°C. $KMnO_4$ (21.6 g, 135 mmol) was added in small portions and the reaction mixture was heated under reflux for 5 h. The reaction was quenched with the addition of ethanol (20 mL) and MnO_2 was removed through filtration. The filtrate was acidified by addition of HCl to reach pH 1, the solvent was removed by evaporation and the resultant solid was stirred with acetone for 30 min. After separation of NaCl by filtration, the solvent was evaporated and the solid was dried. The oxidation was performed twice, 6.2 g of product was obtained (yield 27%).

Synthesis of dibromopyromellitic anhydride

Dibromopyromellitic acid (6.2 g, 15 mmol) was placed in a 250 mL multi-neck RBF. Acetic acid (89 mL) and acetic anhydride (4.9 mL) were added and the mixture was heated under reflux for 3 h. The reaction mixture was filtrated at RT, the solid was washed with acetic acid and hexane successively. Product was obtained as colorless solid (yield: 3.9 g, 70%).

Synthesis of N,N'-dialkyldibromopyromellitic imide

Dibromopyromellitic anhydride (0.3 g, 0.9 mmol) was placed in a 25 mL multi-neck RBF. Acetic acid (8.1 mL) and alkylamine (7 mL) were added under N_2 flux and the mixture was heated under reflux for 2 h. After filtration, the precipitate was washed with acetic acid and dried under reduced pressure. The crude product was purified by recrystallization from ethyl acetate. Pure product was obtained as pale white solid (0.46 g, 84%). ^{1}H NMR ($CDCl_3$, 300 MHz) δ 3.72 (t, 4H, J = 7.2 Hz), 1.72-1.61 (m, 4H), 1.33-1.26 (m, 20H), 0.87 (t, 6H, J = 6.6 Hz). ^{13}C NMR ($CDCl_3$, 75 MHz) 163.69, 136.39, 31.97, 29.30, 29.26, 28.41, 27.01, 22.82, 14.29. LRMS (MALDI) m/z $[M]^+$ calc for 598.4; found, 600.[1]

Synthesis of ditrimethyltin-dithieno silole

Dibromodithienosilole (2 g, 3.47 mmol) was dissolved in THF (30 mL) under N_2. The reaction flask was cooled to -78°C using dry ice/acetone bath, *n*-Buthyllithium (2,44 mL, 7.18 mmol) was added drop wise and the mixture was stirred at -78°C for 15 minutes. Trimethyltin cloride (1.39 g, 7.07 mmol) was dissolved in THF (1.4 mL) and added to the reaction mixture. The reaction mixture was allowed to warm upto to RT and stirred at RT for 2 h. Water was added to the reaction mixture; the product was extracted with ethyl ether, washed with brine and dried over sodium sulphate. The solvent was removed by evaporation and the product was dried under reduced pressure. ^{1}H NMR is an agreement with the literature.

Synthesis of P1

N,N'-dialkyldibromopyromellitic diimide (0.030 g, 0.050 mmol) and $Pd(PPh_3)_2Cl_2$ (0.0017 g, 0.0025 mmol, 5%) were placed in a glass tube, benzodithiophene tin-derivative (0.039 g, 0.051 mmol) was placed in a microwave vial and both containers were transferred into a glove box.

All the reagents were transferred into a microwave vial, *o*-xylene (0.4 - 0.5 mL) was added and the vial was transferred out of the glove box. The reaction was performed under microwave irradiation at 140°C and 180°C for 1 h and 2 h, respectively. The resulting mixture was dropped into methanol, and the precipitate was collected by filtration, washed with methanol and dried. GPC (THF): M_n= 49.4 kD, M_w= 141.5 kD, PDI= 2.9. UV-Vis (THF) λ_{max}, nm: 320, 440.

Synthesis of P2

N,N'-dialkyldibromopyromellitic diimide (0.030 g, 0.050 mmol) and $Pd(PPh_3)_2Cl_2$ (0.0017 g, 0.0025 mmol, 5%) were placed in a glass tube, dithienosilole tin-derivative (0.038 g, 0.051 mmol) was placed in a microwave vial and both container were transferred into a glove box.

All the reagents were transferred into a microwave vial, o-xylene (0.5 mL) was added and the vial was transferred out of the glove box. The reaction was performed under microwave irradiation at 140°C and 180°C for 1 h and 2 h, respectively. The resulting mixture was dropped into methanol, and the precipitate was collected by filtration, washed with methanol and dried. GPC (THF): M_n= 14.9 kD, M_w= 63.2 kD, PDI= 4.2. UV-Vis (THF) λ_{max}, nm: 350, 450.

Experimental Methods

^{1}H NMR and ^{13}C NMR spectra were measured on a Mercury-300

MHz; UV-Vis spectra were measured on a Cary UV-Vis-NIR Spectrophotometer; polymerizations were performed in Biotage Initiator microwave.

Conclusions

Pyromellitic diimide acceptor monomer was synthesized and coupled with two different donors, a benzodithiophene and a dithienosilole. Two new copolymers were characterized by GPC and UV-vis absorption spectroscopy. The strength of the donor can influence the absorption of the polymer: a strong donor causes a red-shifted absorption. In this case, dithienosilole is a stronger donor then benzodithiophene and the UV-Vis spectrum of P2 is effectively red-shifted. Purification and full characterization of the polymers is not complete and currently ongoing.

References

1. Günes, S. et al., Chem. Rev. 2007, 107, 1324-1338.
2. Li, Y. et al., Energy Environ. Sci., 2010, 3, 1427-1436.
3. Darren, G. et al., J. Chem. Soc., Perkin Trans. 1, 1999, 1063.
4. Gosztola, A. et al., J. Phys. Chem., 2000, 26.
5. Suh, D. H.et al., Angew Makrom. Chem., 1998, 254, 33-38.
6. Cerar, J. et al., Acta Chim. Slov., 2008, 55, 999-1008.

Acknowledgments

This research work was made possible by the help and guidance of Dr. Ragunath Reddy Dasari, Prof. Seth Marder and Marder Research Group.

A special thanks goes to Dr. Cameron Tyson, Denisha Thomas, Olanda Bryant, Keith Oden (Georgia Institute of Technology), Prof. Antonio Laganà, Prof. Assunta Marrocchi, Prof. Luigi Vaccaro, (University of Perugia).

Funds for this research were provided by University of Perugia – Department of Chemistry, European Chemistry Thematic Network and American Chemical Society.

CHIARA PETRUCCI goals are to obtain a Bachelor degree in Chemistry and a Master degree in Organic Chemistry. The REU project gave her the possibility of gaining skills in laboratory work and led her to think about a PhD. This experience will help her to achieve her goals successfully.

Fabrication and Characterization of Phosphonic Acid Functionalized Oligothiophene Monolayers

D. PLOEGER, University of Washington

Introduction

Organic electronics are being developed due to their benefits in regards to chemical design, cost, and processing parameters in comparison to their inorganic counterparts.[1] One possible application of organic electronics is in the field of renewable energy, particularly in photovoltaic cells.

Most organic photovoltaic (OPV) cells consist of several layers; the substrate, hole-selective layer, the bulk heterojunction, and an electrode. Current organic photovoltaic cells are limited in their capacity to produce a high device efficiency, due to limitations in their architecture.[2]

One possible way to increase the device efficiency may be to optimize the chemical composition of the hole selective layer.[2] Many OPVs employ PEDOT:PSS [poly(3,4-ethylenedioxythiophene): poly(4-styrenesulfonate)] as the hole selective layer, spincoated onto an ITO-coated substrate, although it has been shown that the PEDOT:PSS/ITO interface is unstable and degrades when exposed to air.[4]

Another possible material for use as the hole selective layer is a phosphonic acid-functionalized 5-thiophene molecule, covalently bound to our substrate. This material has several potential benefits over PEDOT:PSS, such as an increase in the control over monolayer formation, density, and roughness, which in turn may increase the hole mobilities and thus, the overall efficiency of the OPV.

In this project, we seek to develop substrates with monolayers made up of our phosphonic acid-functionalized oligothiophene. We also want to optimize the uniformity and density of the monolayer in an attempt to make high quality films. Eventually, we would like to measure the hole transport properties of these films and incorporate them as a hole transport layer in organic photovoltaic devices.

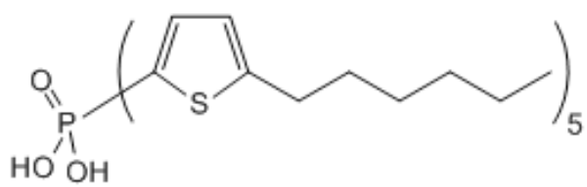

Figure 1: Phosphonic acid functionalized 5-thiophene molecule.

Experimental Methods

We develop 4 pairs of substrates, the first pair corresponding to our control, and each additional pair corresponding to 1, 2, and 3 processing cycles, respectively. We cut our substrates from SiO_2 coated silicon wafers, with each substrate having dimensions of 1.50 cm x 1.50 cm. The substrates are then rinsed and sonicated in acetone, methanol, and isopropanol, respectively, for 15 min each. Afterwards, the substrates are dried under a stream of nitrogen gas and placed in an air plasma cleaner for 10 min to remove any remaining organic material.

We then develop our substrates by placing them in a beaker with 50.0 μM of a solution consisting of our phosphonic acid functionalized 5-thiophene as the solute, and THF as the solvent, making sure to fully immerse the substrates into the solution. We let the solution evaporate until the meniscus drops below our substrate, and our entire substrate has been coated with the solution via the T-BAG method.[5]

After our substrates are coated with the solution, we place them in a Petri dish and onto a hot plate at 140°C for 48 h. Heating enables our monolayer to covalently bond to our substrate, and allows for aggregation of the individual molecules of the monolayer.

After the substrates are removed from the hot plate, we sonicate them in THF and methanol respectively, for 15 min each in an attempt to remove any remaining materials other than our monolayer. For some of the substrates, we altered the cleaning method by sonicating in 0.5 M K_2CO_3 / [2:1 ethanol, water] rather than THF and methanol. Afterwards, our substrates are dried under a stream of nitrogen gas. We repeat the T-BAG method as necessary to create substrates with our desired properties.

After we have created our substrates, we use atomic force microscopy (AFM) to characterize monolayer coverage, surface roughness and surface thickness. We further characterize our substrates by using a goniometer to measure the contact angles to evaluate the surface energy of our films. For each substrate, we perform four contact angle measurements, and take the average of those measurements to determine the average contact angle and thus, the surface energy of our films.

Our goal is to produce smooth, dense homogenous monolayers of phosphonic acid functionalized 5-thiophene, which can later be incorporated into OPV cells.

Results and Discussion

The primary scope of this project consists of developing films with the appropriate characteristics which can later be tested using field effect transistors (FETs), and eventually be incorporated into OPV cells.

There are two processes inherent to our project – development and characterization of our substrates.

For our first set of substrates, the surface roughness has been measured at 0.715 nm, 1.169 nm, and 3.815 nm, respectively (see Figures 2-4).

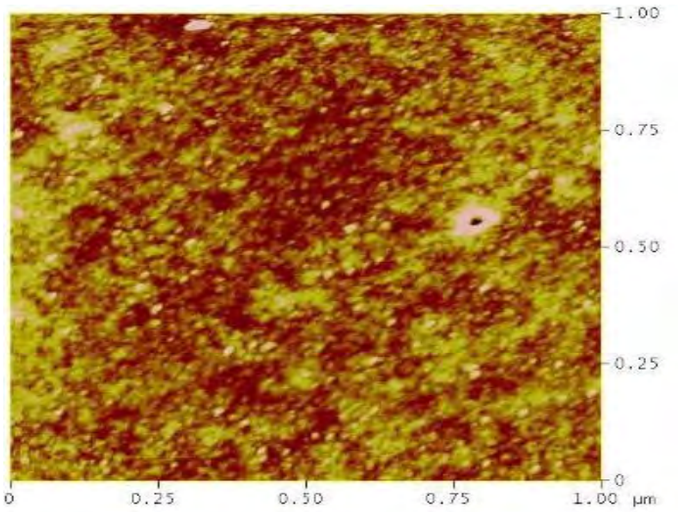

Figure 2: AFM image of substrate surface after 1 T-BAG cycle (first set).

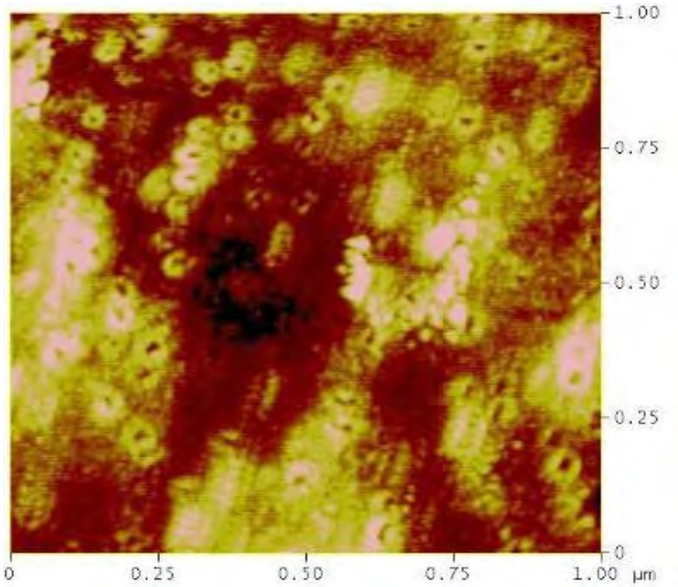

Figure 3: AFM image of substrate surface after 2 T-BAG cycles (first set).

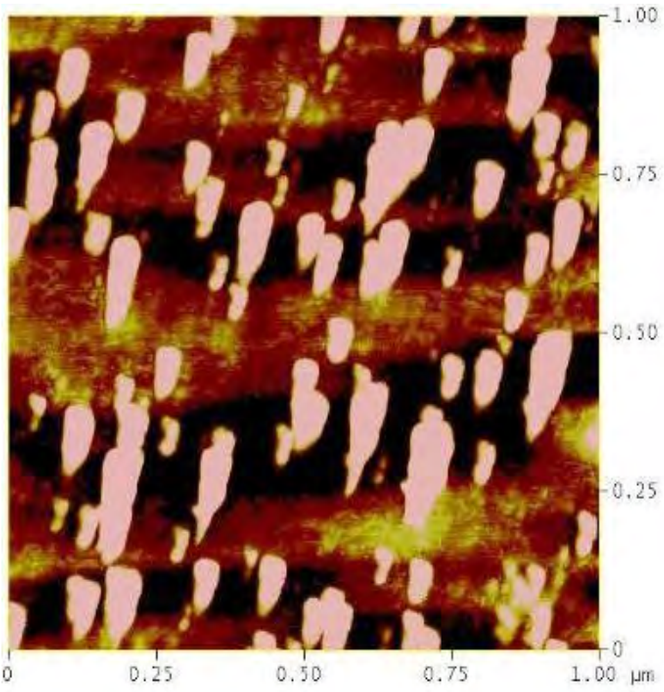

Figure 4: AFM image of substrate surface after 3 T-BAG cycles (first set).

This demonstrates that we have significant surface coverage on all three substrates, and that our films deviate from being perfectly flat.

The step height measurements describe the thickness of our films applied to our substrates under the T-BAG method. For our first set of substrates, the step height has been measured at 11.555 nm, 33.837 nm, and 46.517 nm, respectively (see Figures 5-7).

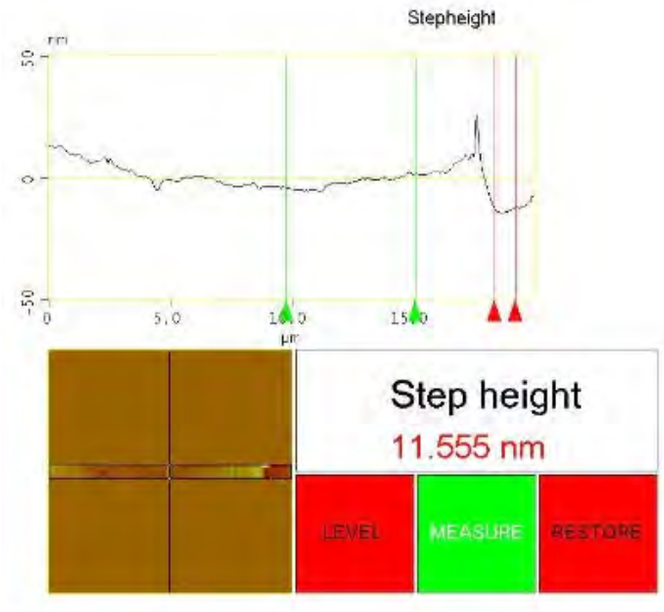

Figure 5: Step height measurement of substrate after 1 T-BAG cycle (first set).

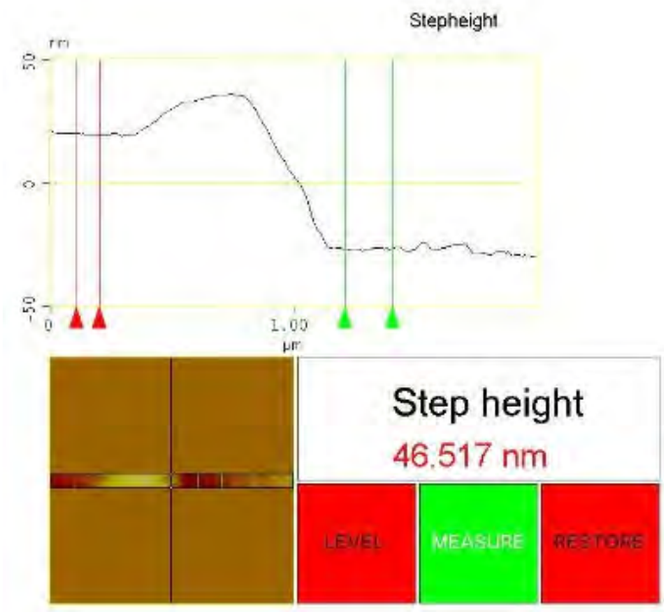

Figure 6: Step height measurement of substrate after 2 T-BAG cycles (first set).

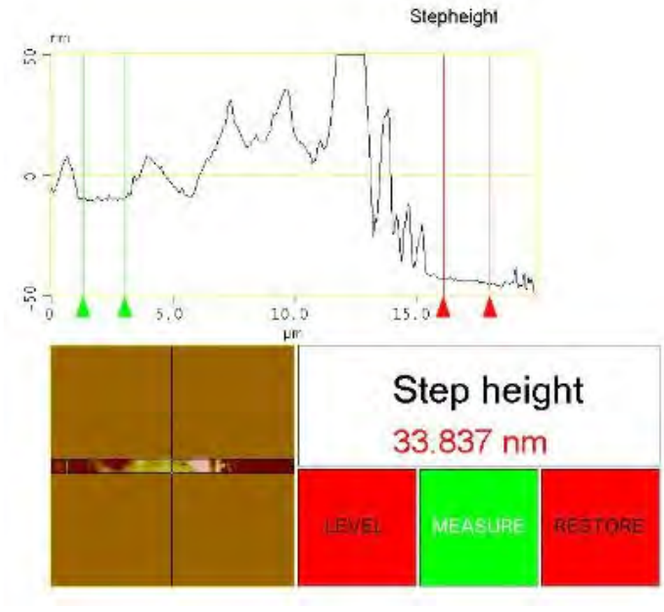

Figure 7: Step height measurement of substrate after 3 T-BAG cycles (first set).

These results are much larger than our anticipated thickness of ~3 nm, which is what we would expect due to the molecular length of our phosphonic acid functionalized 5-thiophene. These results indicate that we have nonhomogenous film layer thicknesses, and that we have more than a single monolayer of film on our substrates.

From visual inspection of the AFM images, we observe that the surfaces are increasingly less homogenous, and contain increasing numbers of 'islands' of our film, rather than the smooth, homogenous molecular aggregate films we had been seeking from this process. From this, we can conclude that each subsequent T-BAG cycle has corresponded to additional layers of coverage, rather than the intended homogenous aggregation we were seeking.

We have also performed contact angle measurements on the first set of substrates by taking four contact angle measurements of each of our substrates and averaging them.

The contact angle measurement on the clean SiO_2 is 33.40°, whereas the contact angle measurements on the substrates that have undergone the T-BAG cycles average out at 88.20°, 89.10°, and 91.90° respectively (see Figures 8,9).

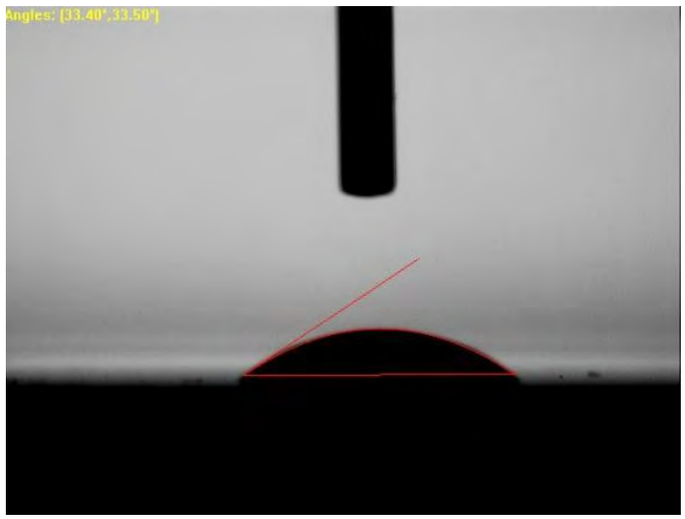

Figure 8: Contact angle measurement of clean SiO_2 substrate (first set).

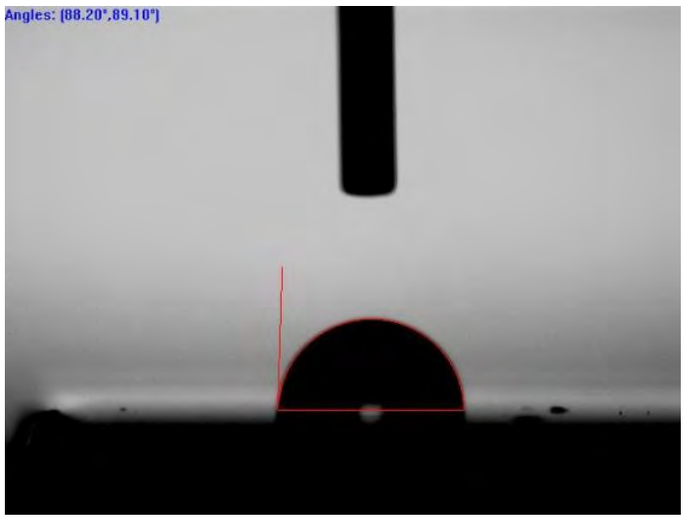

Figure 9: Contact angle measurement of substrate after 1 T-BAG cycle (first set).

This indicates that the surface energy of our clean, unprocessed SiO_2 substrate is higher than that of the substrates processed using the T-BAG method. The similarities in contact angle measurements for the substrates that have undergone the T-BAG cycles indicates that their surface energies are similar, meaning that they have similar surface coverage in regards to the monolayers. This also demonstrates that our films are not altered significantly after undergoing multiple T-BAG cycles. At this point, we derive little benefit from subsequent T-BAG cycles.

For the first set of films, we found that they were not as smooth and homogenous as we would like, and that we had too much surface coverage (more than just our monolayer). These additional layers could be the result of a variety of factors; however, we can potentially attribute this to our cleaning methods (sonication in THF and methanol), and thus, we have begun cleaning our substrates by sonicating them in 0.5 M K_2CO_3 / [2:1 ethanol, water]. We have performed this cleaning method with one set of substrates (our second set), and the results appear to be promising. From visual inspection of the results of the first two substrates taken from AFM (substrates corresponding to 1 T-BAG and 2 T-BAG cycles, respectively), we have obtained more surface coverage of our monolayer, as well as a 'smoother', more homogenous surface. For the substrate corresponding to 1 T-BAG cycle, we have noticed that the islands are similar in height, around ~3-4 nm tall, and that the percentage of the surface covered by the islands is around 5%. After performing a second T-BAG cycle on our substrates cleaned with 0.5 M K_2CO_3 / [2:1 ethanol, water], we have been able to obtain films that were more continuous, and that were approximately ~10 nm thick (9.052 nm), which is much less than the thickness obtained from the substrate undergoing 2 T-BAG cycles from the first set (33.837 nm).

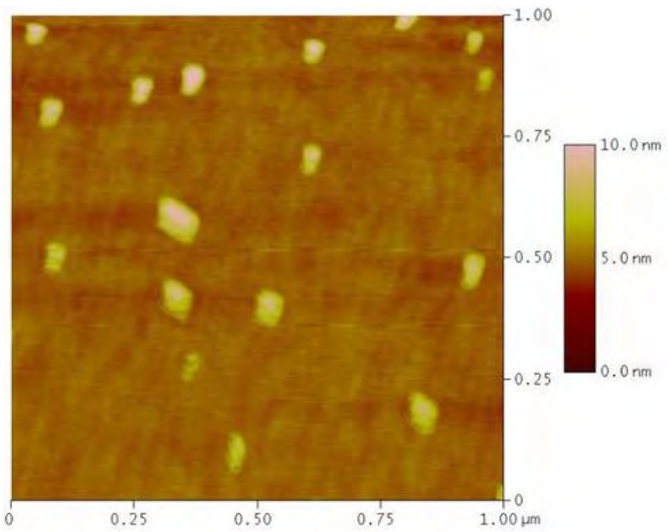

Figure 10: AFM image of substrate surface after 1 T-BAG cycle (second set).

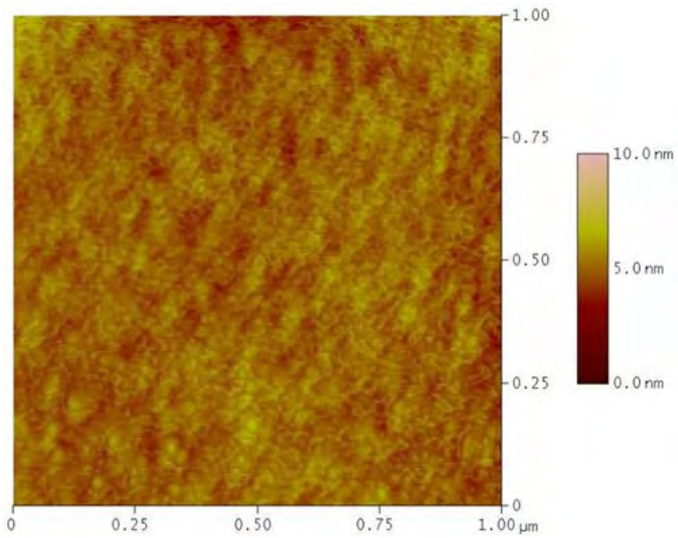

Figure 11: AFM image of substrate surface after 2 T-BAG cycles (second set)

Conclusions

The goal of this project was to fabricate substrates with optimized uniformity and density of the monolayer, and optimized surface energy, for which we would later examine the hole-transport properties, and incorporate into OPV cells. To determine the uniformity and density of the monolayer, we relied on AFM to measure our thickness, and to provide images of our surface. To determine the surface energy, we utilized a goniometer to perform contact angle measurements.

The results obtained for surface thickness of the first set of substrates (11.555 nm, 33.837 nm, and 46.517 nm, respectively) have been larger than the results we would hope to acquire from this process (~ 3 nm). The contact angle measurements we obtained were able to demonstrate that our surface energies of our treated substrates were similar and lower than that of our untreated SiO_2 substrate, but since we have not conducted actual surface energy measurements via Young's equation, we cannot elaborate on the values for surface energy.

We have also observed that our surfaces became increasingly less homogenous with additional T-BAG cycles, and we inferred that the additional T-BAG cycles may correspond with additional monolayers of coverage rather than providing us with homogenous aggregation of the surface molecules of our film.

These additional layers could be attributed to our cleaning methods, which were discussed in the Results and Discussions portion of this paper. For the second set of substrates, we altered the cleaning method to incorporate sonication of 0.5 M K_2CO_3 / [2:1 ethanol, water] rather than sonication in THF and methanol. The preliminary results demonstrated that we had smoother, more homogenous surface coverage, as well as more continuous surfaces and less surface thickness.

Another possibility which may affect the aggregation of our surface

molecules is the number of, and process inherent with, the T-BAG cycles. We plan on changing the number of T-BAG cycles and evaluating whether or not that affects our surface coverage. We will also investigate changing the volume and/or the exposed surface area of the phosphonic acid functionalized 5-thiophene/ THF solution, which would serve to change the time required for the solvent evaporation. We may also alter the molarity of our solution, or possibly change the solvent. Yet another possibility we may explore is changing the heating time or temperature of our substrates after processing.

In the future, we plan on testing the hole-transport properties of our substrates, and later, incorporating them into OPV cells. After we have characterized our films, we will test the hole transport properties by fabricating FET devices from the substrates by using thermal deposition to evaporate a composite of lithium fluoride/ aluminum (LiF/Al) electrodes onto the substrates. We will then characterize the completed FETs by measuring the current-voltage (IV) characteristics. After we have obtained sufficient hole mobilities, we will incorporate our monolayer into specifically designed OPV cells to test the change in efficiency. After we have tested the efficiency of our OPV cells, we should be able to demonstrate the usefulness of our films within the provided OPV architecture.

References

1. Ma, Hong, Hin-Lap Yip, Fei Huang, and Alex Jen. "Interface Engineering for Organic Electronics."Advanced Functional Materials 20. (2010): 1371-1388.
2. Thompson, Barry C., and Jean M. J. Frechet. "Polymer-Fullerene Composite Solar Cells."Angewandte Chemie 47, (2008): 58-77.
3. Zhan, Xiaowei, and Daoben Zhu. "Conjugated polymers for high-efficiency organic photovoltaics." Polymer Chemistry 1, (2010): 409-419.
4. de Jong, M. P., L. J. van IJzendoorn, and M. J. A. de Voigt. " Stability of the interface between indium-tin-oxide and poly(3,4-ethylenedioxythiophene)/poly(styrenesulfonate) in polymer light-emitting diodes." Applied Physics Letters 77, 2255 (2000).
5. Hanson, Eric L., Jeffrey Schwartz, Bert Nickel, Norbert Koch, and Mehmet Fatih Danisman. "Bonding Self-Assembled, Compact Organophosphonate Monolayers to the Native Oxide Surface of Silicon." Journal of the American Chemical Society 125, (2003) on 16074-16080.

Acknowledgments

This research was conducted under the supervision of Andrew Rice in the laboratory of Dr. Christine Luscombe at the University of Washington.

Funds for this research were provided by the Center on Materials and Devices for Information Technology Research (CMDITR), the NSF Science and Technology Center No. DMR 0120967.

D. PLOEGER is an undergraduate at University of Washington.

Investigation of Commercially Available Cyanine Molecules for Use in All-Optical Signal Processing

BRANDON SHARP, Lincoln Memorial University
Anselmo Kim, Joseph Perry, Georgia Institute of Technology

Introduction

All-optical signal processing – controlling light using another light in a purely optical domain – is of great interest to scientists as it will obviate the need for expensive electrical-to-optical, and optical-to-electrical conversions of signals. The difficulty in building an all-optical switch – a device that allows one optical signal to control the transmission of another optical signal – is in the fact that photons normally behave as non-interacting particles. While this is ideal for transmitting the signal over long distances, as the signals will be insensitive to the environmental disturbances, performing switching function on these signals would prove challenging as it requires interaction of a photon with another photon.[1] Often, nonlinear optical media that permit light-matter interaction are employed to mediate the control of a photon with another photon.

One such medium is a class of organic molecules called cyanines. Cyanines, because of the extensive delocalization of their π-electron rich polymethine bridge, are highly polarizable, and thus exhibit high optical nonlinearity.

However, because of this high polarizability, they also show strong tendencies to exhibit aggregation, ion-pairing, and symmetry-breaking, all of which alter their ground state geometry and consequently optical properties, often resulting in excessive light, and/or reduction in nonlinear response.

The objective of this project is to find the conditions in which the distortion of the ground state geometry occurs in quinolinium-terminated cyanine molecules in order to identify the source of this phenomenon, and quantify its effect on linear and nonlinear optical properties so that the dye molecules can be easily integrated into devices.

The two dyes that will be studied are 1,1'-diethyl,2,2'-quinotricarbocyanine iodide (Figure 1) and 1,1'-diethyl,4,4'-quinotricarbocyanine iodide (Figure 2).

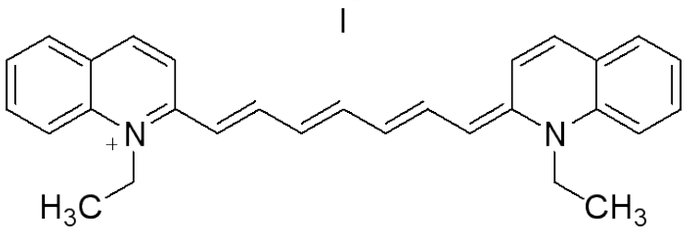

Figure 1: Structure of 1,1'-diethyl,2,2'-quinotricarbocyanine iodide.

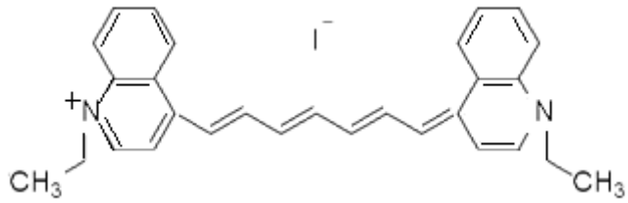

Figure 2: Structure of 1,1'-diethyl,4,4'-quinotricarbocyanine iodide.

Experimental Methods

In order to understand the nonlinear properties of the two cyanine molecules being studied, it will be necessary to characterize the dyes by performing linear absorption measurements using an ultraviolet-visible/near-infrared (UV-Vis/NIR) spectrometer. A solvatochromic study was first performed by preparing solutions of the two dyes in six separate solvents. The solvents used, in the order of increasing polarity index, were: toluene, o-dichlorobenzene (DCB), dichloromethane (DCM), tetrahydrofuran (THF), acetone, and dimethylsulfoxide (DMSO). The results of the solvatochromic study prompted a binary solvent experiment using DCB and acetone. The compositions of the solutions used in this study are included in Table 1. The absorption spectra from this study of the dyes in binary solvent system with varying compositions revealed the dielectric environment in which the dyes were no longer solvated as independent cyanine units and began to form H-aggregate.

Solution	Composition
1	0mL acetone + 20mL DCB
2	2mL acetone + 18mL DCB
3	6mL acetone + 14mL DCB
4	10mL acetone + 10mL DCB
5	14mL acetone + 6mL DCB
6	18mL acetone + 2mL DCB
7	20mL acetone + 0mL DCB

Table 1: Binary solvent study compositions. Both dyes were dissolved in each of the above solutions and their spectra taken.

The degree of delocalization along the polymethine bridges of the dyes was observed using spontaneous Raman spectroscopy. Since the C-C stretch and C=C stretch show distinct Stokes shifted bands at approximately 1100 cm^{-1} and 1600 cm^{-1}, the delocalized C-C bond of the polymethine chain is expected to show a band somewhere within this window.

Non-linear optical characterization of the quinolinium-terminated cyanine dyes – the extraction of the real and imaginary part of third-order polarizability – was performed using non-degenerate two-photon absorption spectroscopy and Z-scan. The details behind these advanced Pump-probe laser techniques are beyond the scope of this study, but they have been well-documented in literatures.[2,3,4]

Results and Discussion

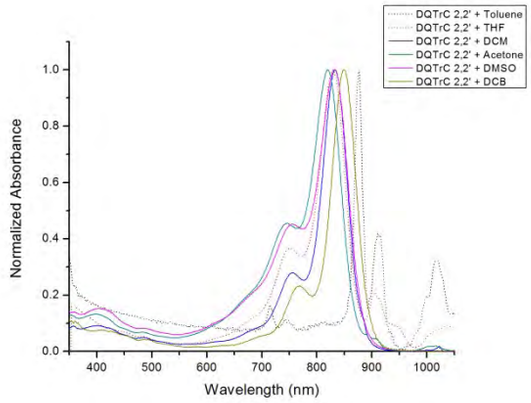

Figure 3: Solvatochromic study data for 1,1'-diethyl, 2,2'-quinotricarbocyanine iodide. The dotted black and red lines indicate limited solubility of the dye in both toluene and THF, respectively.

The results of the solvatochromic study of both dyes (Figure 3 and 4) showed a blue shift with increasing solvent polarity. The exception to this general trend was DCB, which has a polarity comparable to DCM, but showed a significantly red-shifted spectrum compared to the other solvent because of its high polarizability.

The binary solvent study results (Figure 5 and 6) show that with an increase in acetone, the spectra became increasingly blue-shifted. As the amount of acetone was increased, the higher-energy peak on the blue side became increasingly pronounced, indicating an increased contribution from the 0,1' vibronic transition. This reduced the sharp, narrow transition characteristic of cyanine dyes. For 1,1'-diethyl, 4,4'-quinotricarbocyanine iodide, this vibronic shoulder shows a greater increase in magnitude with the addition of more acetone, indicating that the 4,4'-DQTrC is more susceptible to ground-state geometry change than 2,2'-DQTrC counterpart. This study also revealed that the dyes performed best in slightly less-polar solvents, o-DCB in the study, and worst in acetone. o-DCB provided an excellent environment for the characterization of the two dyes because the cyanine-like character of the dyes was most retained in this solvent. However, because the polarizability of o-DCB, it is unwise solvent choice for two-photon absorption experiments because there is a chance that the response received will be from the solvent and not the cyanine dyes.

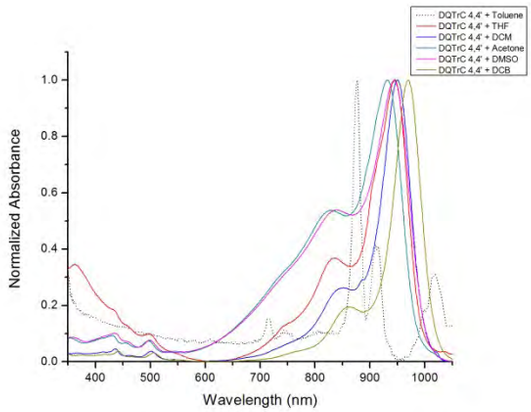

Figure 4: Solvatochromic study data for 1,1'-diethyl, 4,4'-quinotricarbocyanine iodide. The dotted black line is used here to indicate limited dye solubility in toluene.

Transient absorption measurements (Figure 7) provided the wavelengths (1400 nm and 2000 nm) at which to pump the samples in other nonlinear absorption measurements. The results of our non-degenerate two-photon absorbance experiment (Figure 9) showed a small two-photon cross-section for both dyes. It also revealed that neither dye possessed a transparency window near current telecommunication wavelengths (1300-1550 nm).

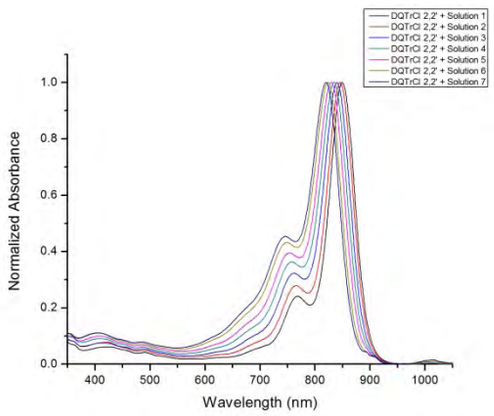

Figure 5: Binary solvent study results 1,1'-diethyl, 2,2'-quinotricarbocyanine iodide. The amount of acetone in solution increased from solution 1-7, as shown in Table 1.

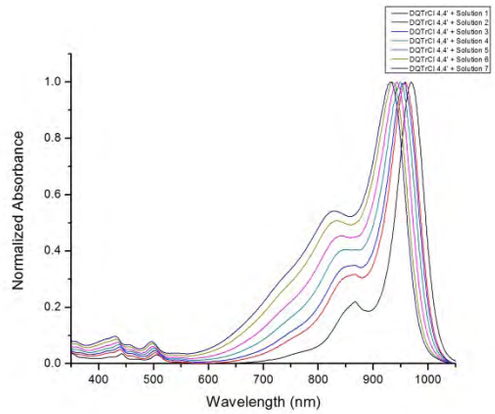

Figure 6: Binary solvent study results for 1,1'-diethyl, 4,4'-quinotricarbocyanine iodide. The amount of acetone in solution increased from solution 1-7, as shown in Table 1.

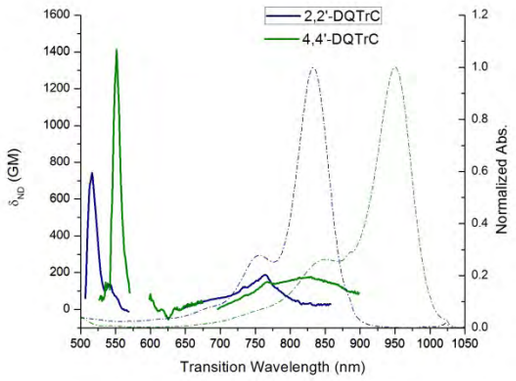

Figure 9: Results of non-degenerate two-photon absorption (NDTPA) experiment.

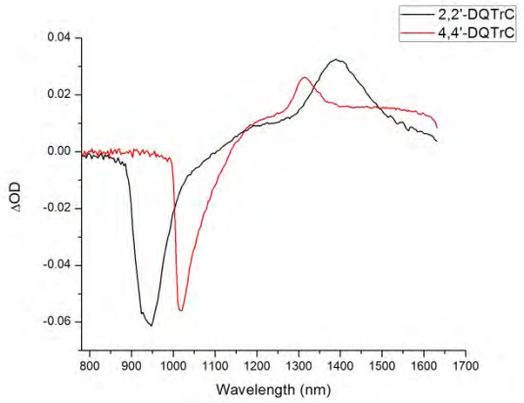

Figure 7: Transient absorption spectra of the two cyanines.

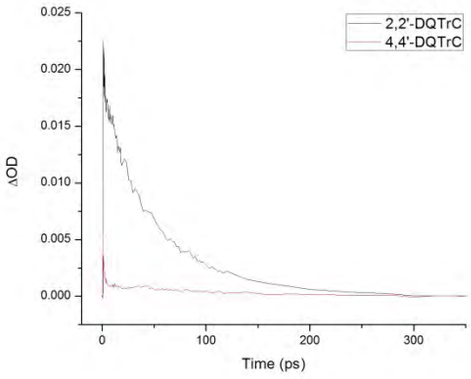

Figure 8: Excited state lifetimes for the cyanines.

Conclusion

The results of our solvatochromism and binary solvent studies indicated that the cyanine-like character of the dyes was preserved in the less-polar solvents and that earlier-onset symmetry-breaking occurred in 1,1'-diethyl, 4,4'-quinotricarbocyanine iodide. The non-degenerate two-photon cross sections of the two dyes were not particularly high. Furthermore, the two cyanines lacked a transparency window at current telecommunication wavelengths, indicating some absorption in this region. This is an undesired effect as the materials will absorb light if integrated into all-optical devices, resulting in light/signal loss.

References

1. Ramaswami, R.; Optical Networks: A Practical Perspective.
2. Campo, J.; Makarov, N. S.; Hales, J. M.; Perry, J. W.; (2011).
3. Sheik-Bahae, M.; Said, A. A.; Wei, T. H.; Hagan, D. J.; and Van, E. W.; Stryland, Quantum Electronics, IEEE Journal of 26 (4), 760-769 (1990).
4. Negres, R. A.; Hales, J. M.; Kobyakov, A.; Hagan, D. J.; and Van Stryland, E. W.; Quantum Electronics, IEEE Journal of 38 (9), 1205-1216 (2002).

Acknowledgments

I would like to acknowledge the Center on Materials and Devices for Information Technology Research (CMDITR), the NSF Science and Technology Center No. DMR 0120967.

BRANDON L. SHARP is a rising senior chemistry major at Lincoln Memorial University. He plans to attend graduate school in chemistry upon completing his B.S. degree and eventually work in industry.

Development of a High-Q Fabry-Perot Cavity for Linewidth Narrowing of High Power Guide Star Laser

ALICIA SWAIN, Norfolk State University
Chris Hessenius, Mahmoud Fallahi, University of Arizona

Introduction

Currently, a Vertical External Cavity Surface Emitting Laser (VECSEL) is being developed to use as an efficient guide star laser. A VECSEL is made of a semiconductor chip consisting of a multiple quantum well gain region and a distributed bragg reflector which acts as a mirror on the back of the chip. An external cavity is then created with a separate mirror that is used as an output coupler. A guide star laser is used to excite sodium in the atmosphere in order to assist in obtaining clear images with adaptive optic telescopes. Because the band for sodium is very narrow, it is necessary for the linewidth of the guide star laser also be very narrow. Typically, a linewidth narrowed system results in a system that has decreased efficiency and less output power from the laser.

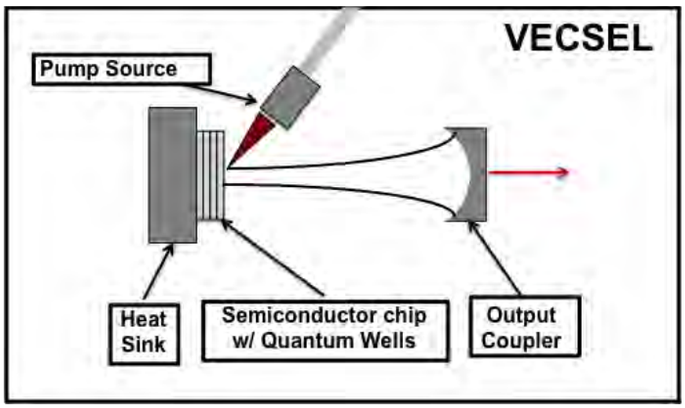

Figure 1: Diagram of VECSEL.

Because of the linewidth needs of the guide star laser, work was done to narrow the linewidth of the VECSEL by the development of an external Fabry-Perot (FP) cavity. The external Fabry-Perot cavity will eventually become a reference source to assist in the linewidth narrowing. Currently the line narrowing is accomplished with the use of intra-cavity components of the high power semiconductor laser, whose fundamental wavelength is 1178 nm and frequency doubled by a non-linear optic (NLO) crystal to the visible wavelength of 598 nm needed for guide star applications.[1] Prior to this work, a linewidth of 20 MHz and a maximum output power of 4 W was observed. The intra-cavity components of the laser promote loss and the objective to create an external Fabry-Perot cavity narrow the linewidth and increase the stability of the high power VECSEL.[2]

Also necessary for this objective is isolating the external Fabry-Perot cavity from the VECSEL. Failure to do so creates instability in the VECSEL due to feedback from the Fabry-Perot cavity to the VECSEL. This can be done with the application of an optical isolator, which can be composed of two major components, which are a polarizing beam splitter (PBS) and a quarter wave plate (QWP). The Optical Isolator ensures that as little light as possible will return from the external cavity back toward the laser, by changing the polarization of the light and deflecting it away through the PBS.[3]

A third very important component of the project is to understand and apply mode-matching concepts. Mode-matching is done by the use of lenses, other optical components, and free space areas, which allows a Gaussian beam's characteristics to be altered to match that of new required characteristics.[4] Without correct mode-matching, the Fabry-Perot cavity will be unstable and unpredictable.

Experimental Methods

There were three parts of the experiment to consider, the FP, the optical isolator, and the mode-matching optics. There are several aspects of the FP, which are important it's design, some of which are the Free Spectral Range (FSR, ν_F), the linewidth, and the beam waist of the cavity (W_o).

The FSR of the FP describes the distance between the peaks that are shown in a graph of the spectrum of the light leaving a cavity. When the spectrum is taken of the output, the FSR should be easily identifiable. It can be calculated in terms of frequency by

$$\Delta f \approx \frac{c}{2nl\cos\theta}$$

where C is the speed of light, n is the index of refraction, and L is the cavity length of the Fabry-Perot, and converted to wavelength units to be seen in a graph of the spectrum.

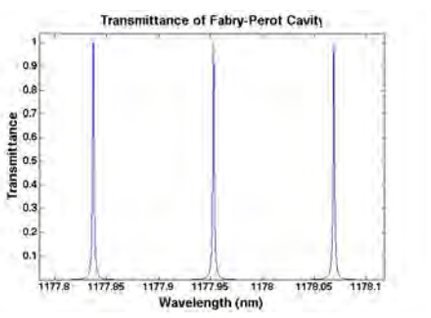

Figure 2: Theoretical Output of FP.

The linewidth of the FP, also sometimes written as the Full Width Half Max (FWHM) defines the width of each peak of the spectrum. Specifically, at the FWHM, the width of the spectrum peak is being described at half of the max intensity of the peak. The linewidth is defined as a ration between the FSR and the finesse. The finesse is another characteristic of the FP that assists in the description of the spectrum and its peaks. The higher the finesse that a FP has, the greater the quality of the peaks will be. The finesse of the FP is

$$F = \frac{\pi\sqrt{R}}{1-R}$$

where R_1 is the reflectivity of the first mirror and R_2 is the reflectivity of the second mirror of the FP. Knowing the FSR and the finesse, the FWHM and the linewidth can be written as

$$\Delta\nu = \frac{\Delta\lambda}{F}$$

A narrow linewidth FP is desirable in this project.

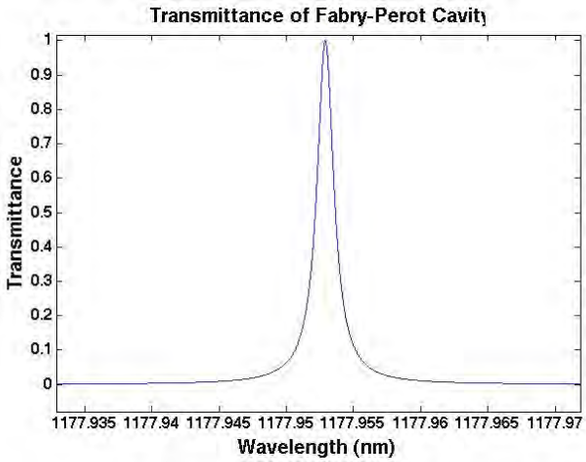

Figure 3: Theoretical Output of FP.

The beam waist of the FP is very important because it is necessary to use the beam waist information in order to mode-match the VECSEL to the FP. The beam waist is the smallest radius of the Gaussian beam that is the predominant beam in the cavity. Knowing the beam waist allows one to know almost every other aspect of the Gaussian beam and its shape along the optical path.

Figure 3 shows the shape of the Gaussian beam inside the Fabry-Perot cavity. It is difficult to see the expansion of the beam because the small length of the cavity but the beam at the end of the cavity is slightly bigger. The beam waist at the beginning of the cavity was 135 microns, compared to the 280 micron beam waist of the VECSEL. Using the beam waist of the VECSEL, through use of the ABCD Matrices and the Gaussian paramater q, correct locations of the lenses could be determined to ensure that the beam entering the FP was the correct mode.

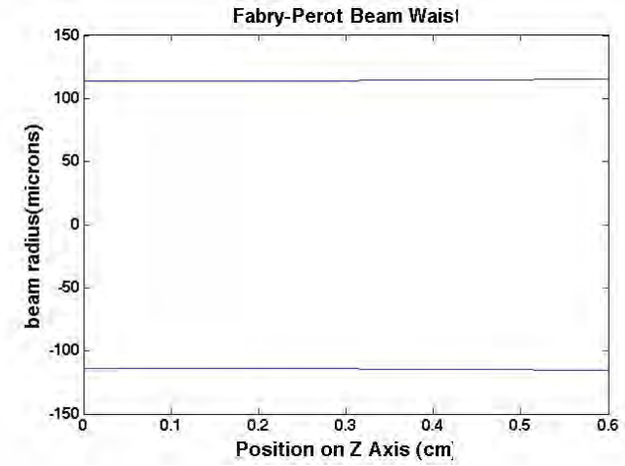

Figure 4: Beam Waist W(z) of FP.

$$R_2 = \frac{A^2{q_1}^2 - B^2}{AC{q_1}^2 - BD}$$

$$q_1 = \frac{-\pi {W_1}^2}{i\lambda}$$

$$W_2 = \sqrt{\frac{A^2{W_1}^2 - B^2\left(\frac{\lambda^2}{\pi^2{W_1}^2}\right)}{AD - BC}}$$

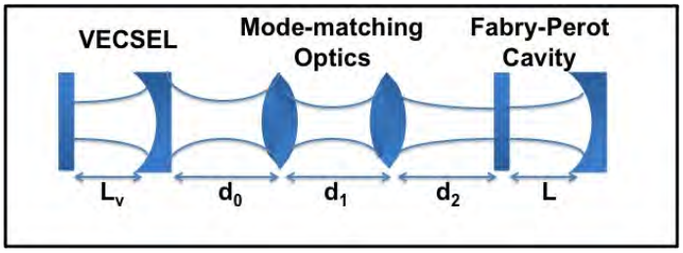

Figure 5: Diagram of components.

In determining the accurate distances for mode-matching, distances d_0 and d_1, and the lens focal lengths were set as a constant, and varying distances d_2 were plotted to determine where the beam waist would be and if it would match the FP's 135 microns.

Experimental Design Information		
Length of VECSEL Cavity	L_V=7.5 cm	L_V=7.5 cm
Output Coupler	R = 75cm	R = 75cm
Distance to Lens 1	d_0 = 15cm	d_0 = 22.5cm
Distance to Lens 2	d_1 = 29.5cm	d_1 = 30cm
Distance to FP	d_2 = 21.8cm	d_2 = 22.5cm
Lens 1, Focal Length	f_1 = 10cm	f_1 = 10cm
Lens 2, Focal Length	f_2 = 10cm	f_2 = 10cm
FP Cavity Length	L = 6mm	L = 3mm
Radius of Curvature of First Mirror	$R_1 = \infty$	$R_1 = \infty$
Radius of Curvature of Second Mirror	R_2 = 40cm	R_2 = 40cm
Theoretical Results		
FP Cavity Beam Waist	135µm	113.8µm
Linewidth (Δλ)	325MHz	650MHz
Free Spectral Range (FSR)	0.12nm	0.23nm

Table 1: Experimental Setup Information.

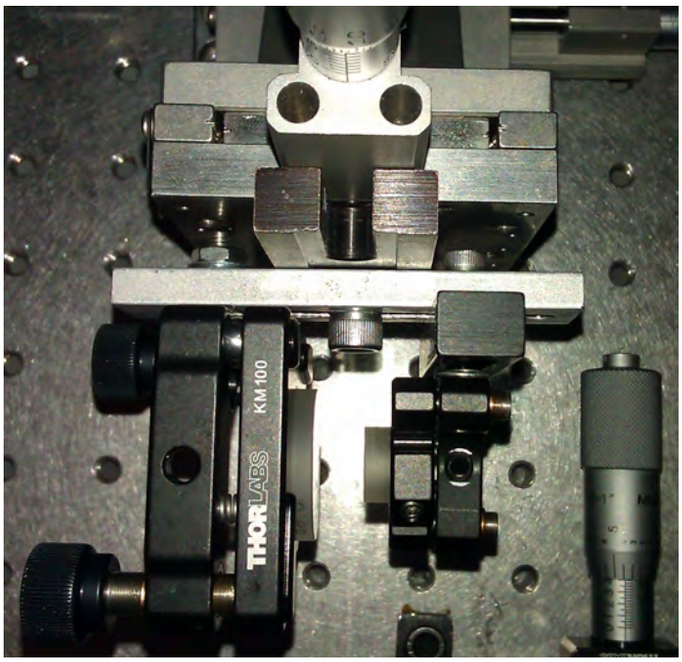

Figure 6: 6 mm Fabry-Perot cavity.

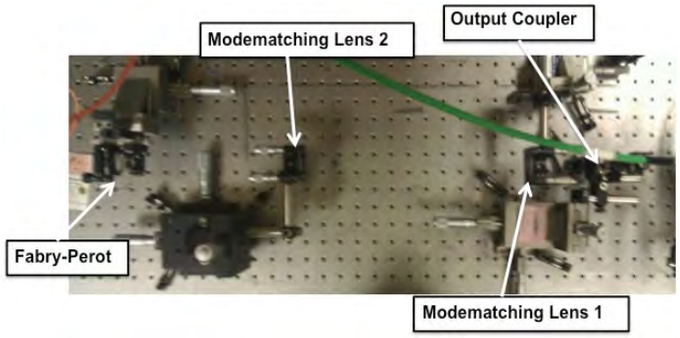

Figure 7: Optical Setup.

Results and Discussion

Initial results from attempts to build a correctly mode-matched optical system were mostly unsuccessful. Stability problems caused the spectrum to make many abrupt shifts and changes. Sometimes, spectrums were very noisy and peaks were difficult to determine. This could be caused by instability, misalignment, or incorrect mode matching.

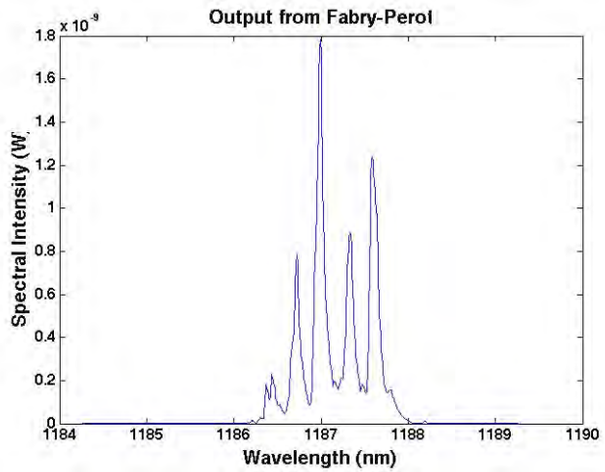

Figure 8: Output spectrum of 6mm FP.

Figure 8 shows the output spectrum of the FP taken by the Optical Spectrum Analyzer (OSA). The spectrum is incorrect because when looking at the Free Spectral Range, the distance between the peaks, though they are the same, they are incorrect distances a part from each other. This is because the OSA only has a resolution of 0.1 nm. The expected FSR is 0.12 nm which is considerably low for the OSA to accurately measure.

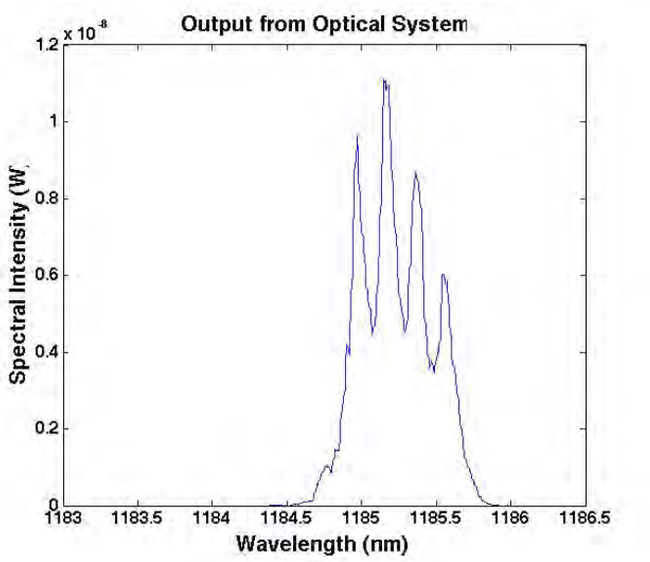

Figure 9: Output spectrum of 3 mm FP.

Figure 9 shows an accurate measurement of the FSR of the 3 mm cavity taken by the OSA. The spacing is rather consistent and shows a pretty accurate reading of its calculated value of 0.23 nm.

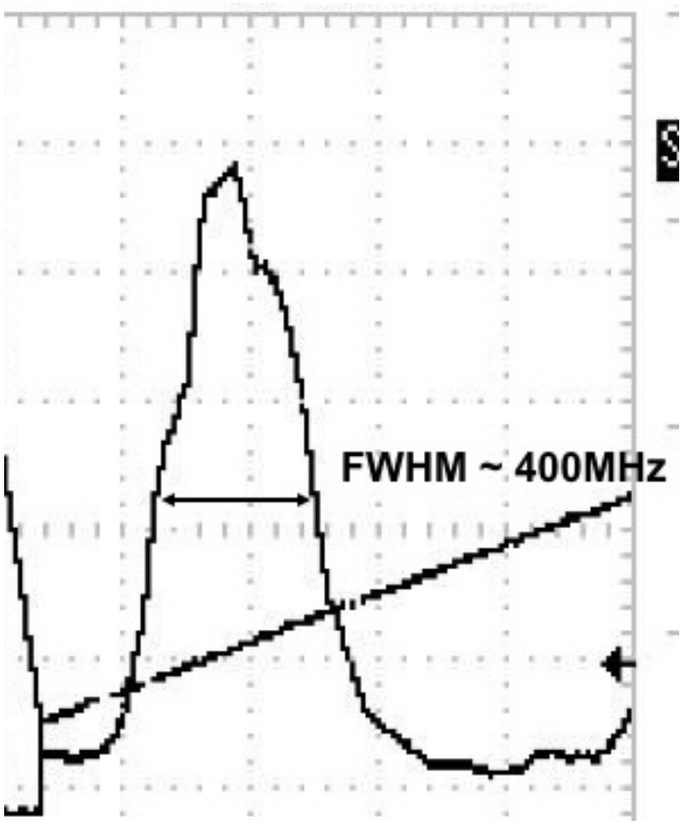

Figure 10: Linewidth measurement of 6 mm FP.

Figure 10 shows the linewidth measurement taken from a commercially available Scanning FP whose FSR is 1.5 GHz. The calculated linewidth we were expecting to see for the 6 mm cavity was 325 MHz. 400 MHz is not too far from the calculated value and its slight shift can be from the optical setup not being fully optimized. This measurement confirms our theoretical calculations. A linewidth measurement was not taken for the 3 mm cavity because the expected value was too large to be very accurately measured by the equipment that we have.

Conclusions

A couple of important conclusions can be drawn about the FP cavity, the optical isolator, and the mode-matching optics. The FSR was confirmed as calculated in the simulations. Clearly defined peaks were able to be able to obtained once the system was correctly mode-matched. Prior to accurate mode-matching, clear peaks could not be achieved and all spectrums obtained were relatively noisy.

It was also shown that as the over all power of the optical system is increased, an optical isolator is more necessary. For this setup, the power was relatively low, but when power was increased, the reflections back into the VECSEL caused instability and affected the lasing quality of the semiconductor chip.

Also to be noted was the sensitivity of the Fabry-Perot. To take accurate measurements it was necessary to temporarily remove vibration sources from the VECSEL by turning of the water chiller for short periods of time. The water chiller uses circulating water to cool the semiconductor chip to a desired temperature, and the water flow causes vibration in the system. Abrupt air currents also caused alteration to the system. It would have been desirable to eliminate instability caused by vibrations by mounting the mode-matching optics and the FP cavity together, but it was found that the system was nearly impossible to align correctly.

Overall, the Fabry-Perot cavity and mode-matching optics showed to be successful. Measurements confirmed the simulations made in MATLAB to determine the correct placement of the components.

References

1. Fallahi, Mahmoud; Fan, Li; Kaneda, Yushi; Hessenius, Chris; Hader, Jörg; Li, Hongbo; Moloney, Jerome; Kunert, Bernadette; Stolz, Wolfgang; Koch, Stephan; Murray, James; Bedford, Robert; IEEE Photonics Technol. Lett., 2008, 20, 1700-1702.
2. Lally, Evan; "A Narrow-Linewidth Laser at 1550 nm using the PDH stabilization technique," M.S. Thesis, Dept. Elect. Eng., Virginia Polytechnic Institute and State University, Blacksburg, VA, 2006.
3. Saleh, B.; Teich, M.; Fundamentals of Photonics, Wiley, 1991, Ch. 6, 1, 193-203.
4. Siegman, A.; Lasers, University Science Books, 1986.

Acknowledgments

Funds for this research were provided by the Center on Materials and Devices for Information Technology Research (CMDITR), the NSF Science and Technology Center No. DMR 0120967 as well as NSF award No. 0823795. I would also like to acknowledge graduate student mentor Chris Hessenius, faculty mentor Dr. Mahmoud Fallahi, and program coordinator Kimberly Sierra-Cajas.

ALICIA SWAIN is currently a senior at Norfolk State University studying Optical Engineering with ambitions to pursue a Ph.D. in optical sciences or electro-optics.

Inverted Organic Solar Cells with Zinc Oxide and Cesium Carbonate Interlayers

MICHELLE WANG, Cornell University
Yinhua Zhou, Canek Fuentes-Hernandez , Bernard Kippelen, Georgia Institute of Technology

Introduction

Organic solar cells have been receiving considerable attention because of their potential for low cost, flexible, and large-area applications. Recently, power conversion efficiencies (PCE) in the range of 6 to 8% have been reported.[1] Most solar cells generally use a low work function metal as the top electrode to collect electrons. However, these low-work function metals are very chemically active and easily oxidized in the presence of oxygen and water. Organic solar cells with an inverted structure typically have better air stability because of the use of a high work function metal as the top electrode. In inverted structures, transparent conducting oxides (such as indium tin oxide, ITO) are used as the bottom electrodes for collecting electrons. Therefore, the low work function metals are not included in the solar cells, which results in better air stability. To collect electrons efficiently, the work function of ITO needs to be lowered by interlayers. So far, semiconducting metal oxides with lower work function, such as ZnO and TiO_X, or a thin layer of insulators, such as cesium carbonate (Cs_2CO_3) and polyethylene oxide (PEO), have been deposited onto ITO to lower the work function.[2-5]

In this work, we used different interlayers: ZnO, Cs_2CO_3, ZnO:Cs_2CO_3, and ZnO/Cs_2CO_3 to modify ITO for inverted solar cells. Figure 1a is a schematic structure of a solar cell, where transparent ITO was used as bottom electrode for light going through. Coated by interlayers, ITO was tuned to collect electrons. Organic blends of poly(3-hexylthiophene) (P3HT) and [6,6]-phenyl C61-butyric acid methylester (PCBM) (Figure 1b) were used as the photo-active layer for light absorption and generating free carriers. The top electrode of MoO_3 and Ag was used for collecting holes.

With different interlayers of ZnO, Cs_2CO_3, ZnO:Cs_2CO_3 and ZnO/Cs_2CO_3, the devices we fabricated were:

(a) ITO(Plasma)/P3HT:PCBM/MoO_3/Ag

(b) ITO(Non-plasma)/P3HT:PCBM/MoO_3/Ag

(c) ITO/ZnO/P3HT:PCBM/MoO_3/Ag

(d) ITO/Cs_2CO_3/P3HT:PCBM/MoO_3/Ag

(e) ITO/ZnO:Cs_2CO_3/P3HT:PCBM/MoO_3/Ag

(f) ITO/ZnO/Cs_2CO_3/P3HT:PCBM/MoO_3/Ag

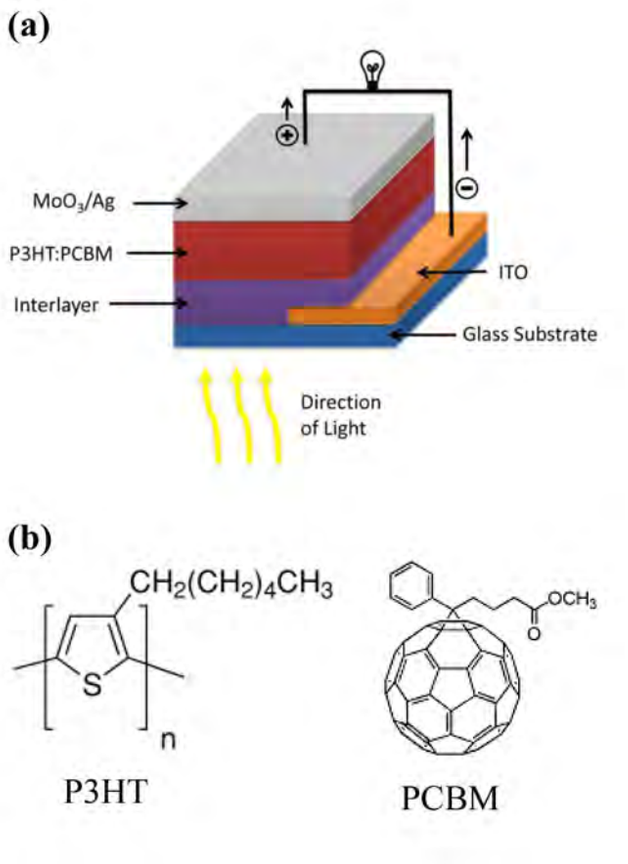

Figure 1: (a) Schematic structure of an inverted solar cell; (b) Chemical structure of P3HT and PCBM.

Research Methods

One inch by one inch squares of glass substrates coated in ITO (from Colorado Concept Coatings LLC) were patterned by covering half of each substrate with kapton tap and etching it with HCl:HNO_3 (3:1 volume ratio) at 70°C for a period of 5 min. After acid etching, the substrates were lined up in a tray and cleaned. The tray was placed in an ultrasonic bath of deionized water and detergent. Following this, the tray was then put in subsequent baths of deionized water, acetone, and isopropanol. Each bath was at room temperature (23°C) and lasted for 20 min. Between each bath, the substrates were dried with nitrogen. Some ITO substrates were treated with a 3 minute O_2 plasma treatment in order to tune its surface to be more hydrophilic for better wetting for the interlayer coating.

The layers used to coat ITO to lower its work function, ZnO, Cs_2CO_3, and ZnO:Cs_2CO_3, were processed from solution. ZnO was derived from a precursor, zinc acetate dihydrate, $Zn(O_2CCH_3)_2(H_2O)_2$. The concentration of each compound used is as follows: ZnO, 100 mg/ml; Cs_2CO_3, 5 mg/ml (used for the singular layer of Cs_2CO_3), 20 mg/ml (used for the ZnO: Cs_2CO_3 blend). The blend of ZnO and Cs_2CO_3 was mixed with a 1:1 weight ratio. The solvent used in all three solutions was 2-methyloxyethanol. Each solution was stirred at 500 rpm overnight. In addition, ethanolamine was added to the $Zn(O_2CCH_3)_2(H_2O)_2$ at a ratio of 0.168 g ethanolamine per 0.6 g zinc acetate dihydrate to help dissolve the solute. The active layer, P3HT:PCBM (1:0.7, weight ratio), was also processed from solution with a total concentration of 34 mg/ml. The solvent was chlorobenzene. This solution was stirred at 500 rpm overnight as well. The prepared solutions were filtered through 0.2 µm pore PTFE filters before spin coating.

The layers of ZnO, Cs_2CO_3, or ZnO:Cs_2CO_3 were spin coated onto the ITO glass for 1 minute at a rate of 3000 rpm for compounds containing ZnO and 5000 rpm for Cs_2CO_3. Samples containing ZnO were annealed at 200°C for 30 minutes and samples containing only Cs_2CO_3 were annealed at the same temperature for 10 min.

Samples were then loaded into a nitrogen-filled glovebox and P3HT:PCBM was spin coated onto each sample at a speed of 700 rpm for 1 minute and annealed at 160°C for 10 minutes. After spin coating, layers of MoO_3 (15 nm) and Ag (150 nm) were deposited in a vacuum system (EvoVac, Angstrom Engineering Inc.). A completed solar cell is shown in Figure 2.

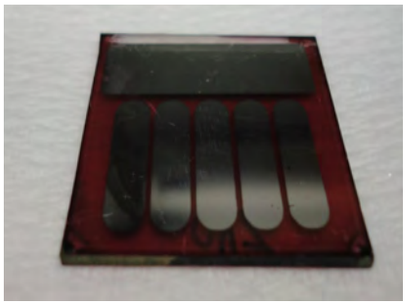

Figure 2: A picture of the fabricated devices.

Device performance of the solar cells was tested in a nitrogen-filled glovebox using LabVIEW program-controlled sourcemeter (Keithley 2400). Graphs based on the data obtained from LabVIEW of current density (*J*) vs. voltage (*V*) were generated using Origin 7.0.

Lifetime tests were also performed on the ITO/ZnO/P3HT:PCBM/MoO_3/Ag and the ITO/ZnO/Cs_2CO_3/P3HT:PCBM/MoO_3/Ag cells, three times the first day and then once every subsequent day.

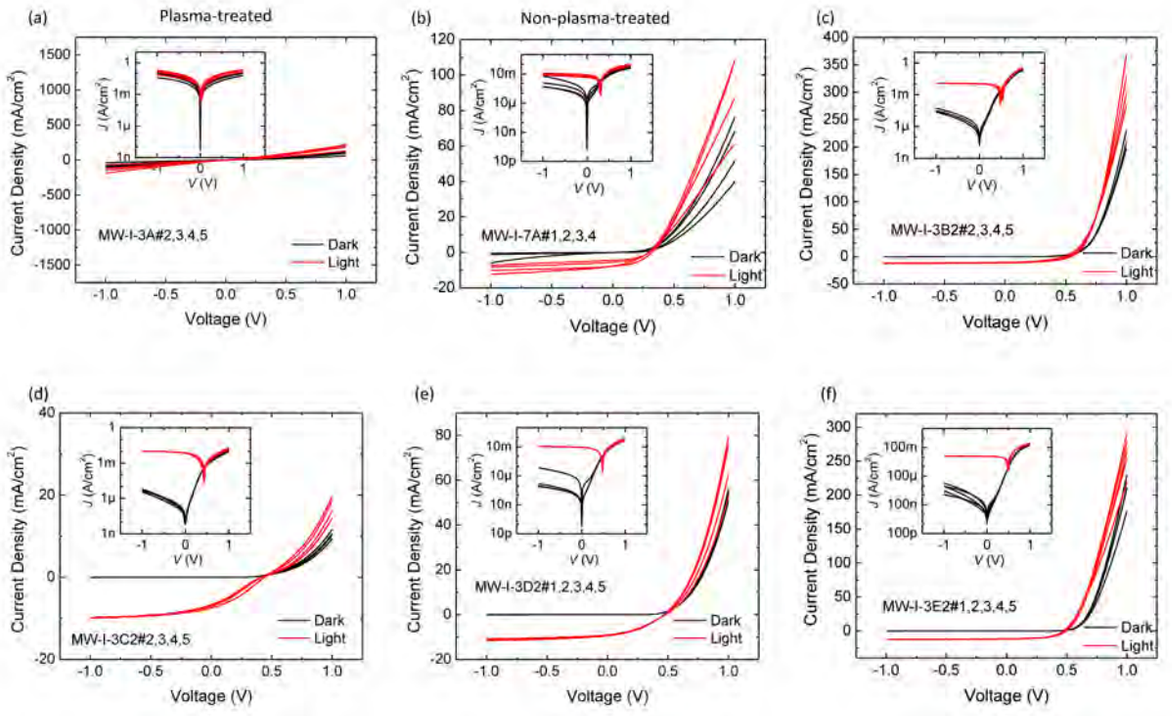

Figure 3: *J-V* characteristics of devices under 100 mW/cm² AM 1.5 illumination and in the dark.

(a) ITO(Plasma)/P3HT:PCBM/MoO_3/Ag
(b) ITO(Non-plasma)/P3HT:PCBM/MoO_3/Ag
(c) ITO/ZnO/P3HT:PCBM/MoO_3/Ag
(d) ITO/Cs_2CO_3/P3HT:PCBM/MoO_3/Ag
(e) ITO/ZnO:Cs_2CO_3/P3HT:PCBM/MoO_3/Ag
(f) ITO/ZnO/Cs_2CO_3/P3HT:PCBM/MoO_3/Ag

Results and Discussion

Device performance was measured using an AM 1.5G solar simulator (Model 91160 Solar Simulator, Oriel Instruments) with an irradiance of I_L = 100 mW/cm^2. Figure 3 shows the *J-V* characteristics of each device, observed both under illumination and in the dark. Device performance is summarized in Table 1.

The best device consisted of the ZnO/Cs_2CO_3 bilayer, with an average PCE of 3.0 ± 0.3%, an open-circuit voltage (V_{OC}) of 0.50 ± 0.02 V, a short-circuit current density (J_{SC}) of 10.7 ± 0.8 mA/cm^2, and a fill factor (FF) of 0.55 ± 0.02. In comparison, the device with a single ZnO layer showed similar results, including an average PCE 2.9 ± 0.7%, a V_{OC} 0.50 ± 0.04 V, a J_{SC} of 11.4 ± 1.3 mA/cm^2, and a FF of 0.50 ± 0.05. Compared to these two kinds of devices, the device with the single layer of Cs_2CO_3 showed significantly lower overall performance with an average PCE of 1.2 ± 0.4%, a V_{OC} of 0.43 ± 0.04 V, a J_{SC} of 7.6 ± 1.3 mA/cm^2, and a of FF of 0.35 ± 0.04. The blend of ZnO and Cs_2CO_3 showed slightly better performance with an average PCE of 1.4 ± 0.5%, a V_{OC} of 0.48 ± 0.03 V, a J_{SC} of 7.7 ± 1.7 mA/cm^2, and a FF of 0.36 ± 0.05.

After initial testing, three devices were selected for lifetime tests to be measured and recorded for a period of 20 days; two were inverted solar cells (ITO/ZnO/P3HT:PCBM/MoO_3/Ag and ITO/ZnO/Cs_2CO_3/P3HT:PCBM/MoO_3/Ag, the two best performing devices) and one was a conventional structure (ITO/PEDOT:PSS/P3HT:PCBM/Ca/Al) for comparison. Each device was kept in a drawer for storage while being exposed to air. Results show while the PCE of the conventional structured solar cell degraded very rapidly, reaching almost zero percent efficiency within 3 days, both inverted solar cells retained roughly 50% efficiency by day 20. The PCE change as a function of exposure time to air is shown in Figure 4.

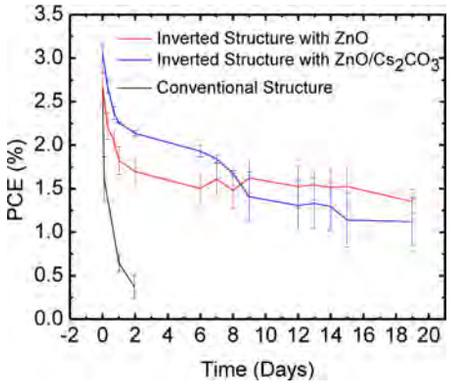

Figure 4: PCE change of devices after kept in air in the dark up to 20 days.

Conclusion

In summary, we have shown that the inverted organic solar cells with ZnO/Cs_2CO_3 interlayer (with an PCE of almost 3%) performed better significantly better than the devices with Cs_2CO_3 and the ZnO:Cs_2CO_3 blend interlayers and slightly better than the ZnO interlayer. In addition, we have also demonstrated that inverted organic solar cells exhibit remarkably better air stability than their conventional structure counterparts, maintaining around 50% of its initial efficiency by day 20 while conventional cells lost most of their efficiency by day 3.

Device	V_{OC} (V)	J_{SC} (mA/cm^2)	FF	PCE (%)
(a) ITO(plasma)/P3HT:PCBM/MoO_3/Ag [a]	0.02 ± 0.02	1.4 ± 1.1	0.1 ± 0.1	0
(b) ITO/P3HT:PCBM/MoO_3/Ag [b]	0.33 ± 0.02	7.1 ± 1.6	0.43 ± 0.03	1.0 ± 0.1
(c) ITO/ZnO/P3HT:PCBM/MoO_3/Ag [c]	0.50 ± 0.04	11.4 ± 1.3	0.50 ± 0.05	2.9 ± 0.7
(d) ITO/Cs_2CO_3/P3HT:PCBM/MoO_3/Ag [c]	0.43 ± 0.04	7.6 ± 1.3	0.35 ± 0.04	1.2 ± 0.4
(e) ITO/ZnO:Cs_2CO_3/P3HT:PCBM/MoO_3/Ag [c]	0.48 ± 0.03	7.7 ± 1.7	0.36 ± 0.05	1.4 ± 0.5
(f) ITO/ZnO/Cs_2CO_3/P3HT:PCBM/MoO_3/Ag [c]	0.50 ± 0.02	10.7 ± 0.8	0.55 ± 0.02	3.0 ± 0.3

Averaged over a: 5 devices; b: 10 devices; c: 20-30 devices

Table 1: Average Device Performance.

References

1. S. H. Park, A. Roy, S. Beaupre, S. Cho, N. Coates, J. S. Moon, D. Moses, M. Leclerc, K. Lee and A. J. Heeger, Nature Photon., 2009, 3, 297.
2. C. Waldauf, M. Morana, P. Denk, P. Schilinsky, K. Coakley, S. A. Choulis and C. J. Brabec, Appl. Phys. Lett., 2006, 89, 233517.
3. C. Y. Li, T. C. Wen, T. H. Lee, T. F. Guo, J. C. A. Huang, Y. C. Lin and Y. J. Hsu, J. Mater. Chem., 2009, 19, 1643.
4. G. Li, C. W. Chu, V. Shrotriya, J. Huang and Y. Yang, Appl. Phys. Lett., 2006, 88, 253503.
5. Y. H. Zhou, F. H. Li, S. Barrau, W. J. Tian, O. Inganas and F. L. Zhang, Sol. Energy Mater. Sol. Cells, 2009, 93, 497.

Acknowledgments

Funding for this research was provided by the Center on Materials and Devices for Information Technology Research (CMDITR), the NSF Science and Technology Center No. DMR 0120967 and 3M Corporation. Special thanks to Dr. Bernard Kippelen, Dr. Yinhua Zhou, Dr. Canek Fuentes-Hernandez, and the Kippelen Research Group. Also, thanks go to the REU program coordinators who made this whole experience possible: Olanda Bryant, Denisha Thomas, Dr. Cam Tyson, and Dr. Keith Oden.

MICHELLE WANG is currently a sophomore at Cornell University. After completing her degree in Chemical Engineering, she plans on attending graduate school in pursuit of an advanced degree.

Hydrothermal Synthesis of Magnetite Nanowires

SAMANTHA WHEELER, University of Washington
Paden Roder, Peter Pauzauskie, University of Washington

Introduction

Magnetite, Fe_3O_4, is a naturally occurring ferrimagnetic phase of iron oxide that has an especially interesting set of magnetic, optoelectronic, and biological properties. Magnetite particles occur naturally in living organisms; magnetotactic bacteria have been making magnetite nanoparticles for billions of years, and magnetite is found in the brains of many species, including humans. This integration into natural processes suggests significant biocompatibility. Consequently, magnetite nanoparticles are a promising material in nanomedicine applications including targeted drug delivery, gene therapy, and as MRI contrast agent.

Magnetite crystals have an inverse spinel structure, as indicated by their formula: $Fe^{2+}Fe_2^{3+}O_4$. This represents an equal quantity of Fe^{2+} ions and Fe^{3+} ions in the lattice, shown in Figure 1 as blue and red atoms, respectively.

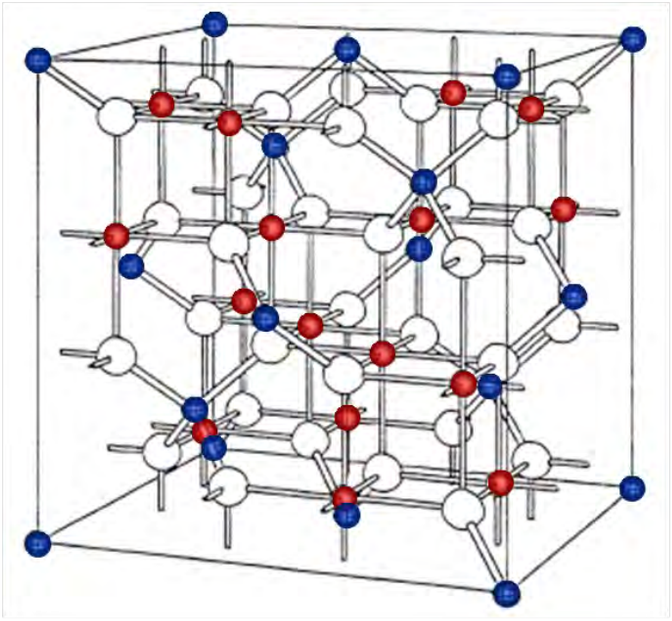

Figure 1: Crystal structure of magnetite. Blue atoms are tetrahedrally coordinated Fe^{2+}, red atoms are octahedrally coordinated Fe^{3+}. White atoms are oxygen.[1]

As with many materials, the manifestation and relative importance of properties can change when the scale of the particles changes from the macro-scale to the nano-scale. The one-dimensional shape of nanowires may improve cell uptake, or even enable them to puncture cells like a needle, and their magnetism could provide unprecedented spatial control. Laser tweezers use highly focused laser beams to induce dipole moments within particles. At the same time, they produce an electromagnetic field with a dramatic gradient that ultimately leads to a local three-dimensional potential well. The radiation pressure helps align optoelectronic nanomaterials that have the requisite one-dimensional geometric morphology. Trapping single wires enables isolation and manipulation useful for diagnostic research in nanomedicine and other applications. Magnetic nanoparticles have not yet been extensively explored with laser trapping technology, mostly due to a lack of commercial suppliers of one-dimensional magnetite materials with deeply subwavelength cross sections.

Given the lack of commercial suppliers, magnetite nanowires must be synthesized for research applications. This project uses a hydrothermal surfactant-assisted method of synthesizing nanowires published by Harraz et al. in 2008.[2] The surfactant polyethylene glycol (PEG) constrains the direction of crystal growth, and successful synthesis produces high-purity monocrystalline single-domain wires with a high aspect ratio. Several methods of characterization confirm the material's suitability for possible applications.

Experimental Methods

Synthesis Process

The method of synthesis is based on the procedure outlined by Harraz et al. A 2:1 molar ratio of hydrated ferrous sulfate ($FeSO_4 \bullet 7H_2O$) and hydrated sodium thiosulfate ($Na_2S_2O_3 \bullet 5H_2O$) was mixed and ground uniformly using a ceramic mortar and pestle, and added to a 23 ml Teflon-lined stainless autoclave. A 1:2 volume ratio solution of liquid PEG ($M_w = 4000$) and deionized water was prepared and added to the autoclave. A constant amount of NaOH was added to the autoclave. The autoclave was kept at 150°C for 24 h in a stirred silicone oil bath. It was then cooled naturally to room temperature. The product was washed with deionized water and ethanol, sonicated, and separated by centrifugation; this process was repeated several times.

Characterization

Several methods were used to characterize the material. The wires were imaged using scanning electron microscopy (SEM, JSM-7000F), and energy-dispersive x-ray spectroscopy (EDAX) was used for elemental composition analysis. Imaging was also conducted using transmission electron microscopy (TEM, Tecnai G2 F20). Phase analysis was performed using a Renishaw inVia Raman microscope as well as with a Bruker D8 Focus x-ray diffractometer (XRD).

Results and Discussion

Characterization of Nanowire Structure

Large numbers of nanowires were clearly visible using SEM. Wires appeared to stick together readily in the dry vacuum conditions of SEM, which made conclusive size analysis difficult. In areas where individual wires were separated, as in Figure 2, the diameters appeared to be on the order of 20-30 nm, while the lengths tended to be 1-2 microns, leading to nanowire aspect ratios ranging between 30 and 100.

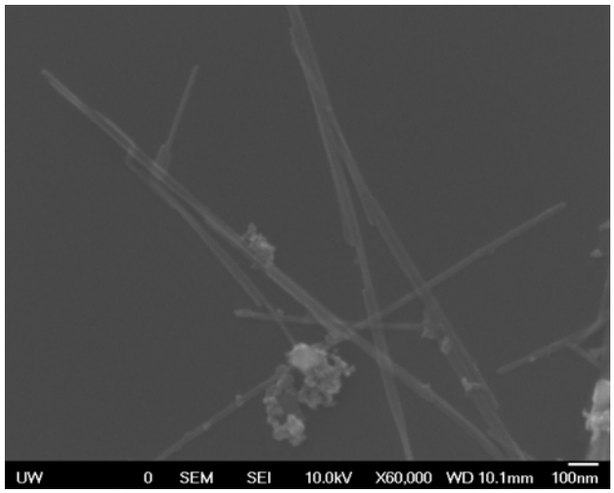

Figure 2: SEM image of several nanowires. Diameter estimates of 20-30 nm are supported by the individual wires visible here. The nature of the cluster of particles at the bottom of the image is unknown.

The apparent dimensions of the wires agreed closely with the average wire dimension reported by Harraz, 25 nm diameter and 1.5 microns in length.[2]

Elemental analysis (EDAX) was performed at the same time as SEM images were obtained. As seen in Figure 3, peaks for both iron and oxygen are prominent. The silicon peak is due to the silicon substrate holding the sample, and the sodium is expected due to its presence in both the sodium thiosulfate and sodium hydroxide precursors in synthesis. The small peak at the right is the Fe-kα peak.

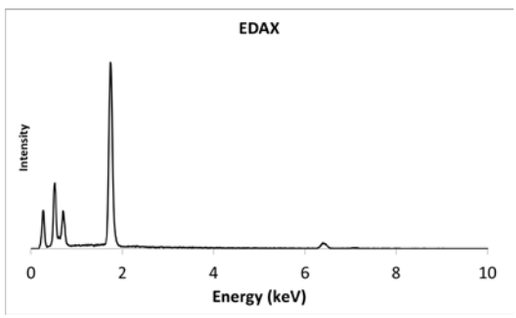

Figure 3: EDAX composition analysis of the sample. Expected iron and oxygen peaks are present. Silicon peak is contributed by the silicon substrate, and sodium peak is from two precursors. The small peak at 6.5 keV is iron.

Morphology and nanostructure were also evaluated using TEM. Lattice fringes were visible in individual wires, as in Figure 4. Several wires were inspected, and no changes in fringe direction within a wire, or apparent grain boundaries, were observed. This supports the supposition that the wires are growing in a monolithically single-crystalline form.

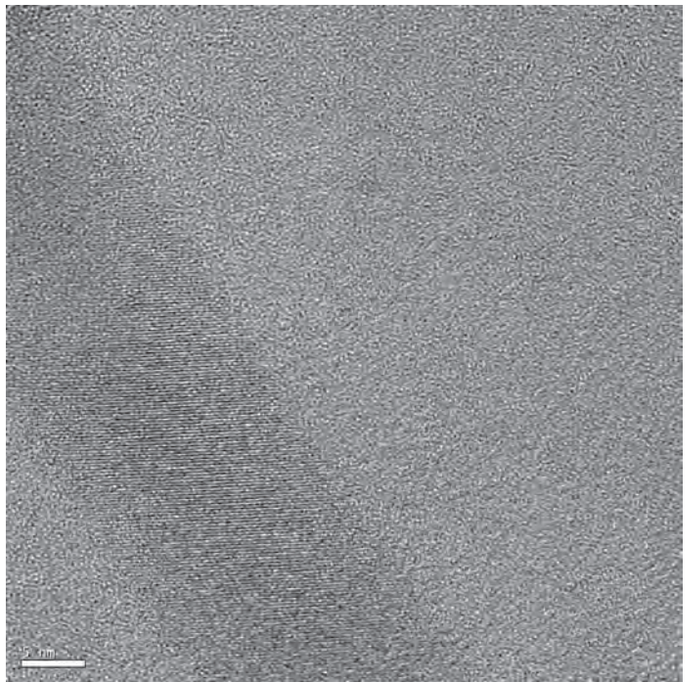

Figure 4: TEM image of a single wire. Lattice fringes suggest a monocrystalline structure. Apparent diameter agrees with the order indicated by SEM analysis.

Phase and Composition Characterization

Initial phase information was gathered using Raman spectroscopy. The collected data presented in Figure 5 represents a 6-point moving average in order to reduce noise and enhance signal. The magnetite and hematite spectra were extracted from Shebanova et al. using the GRABIT package in MATLAB.

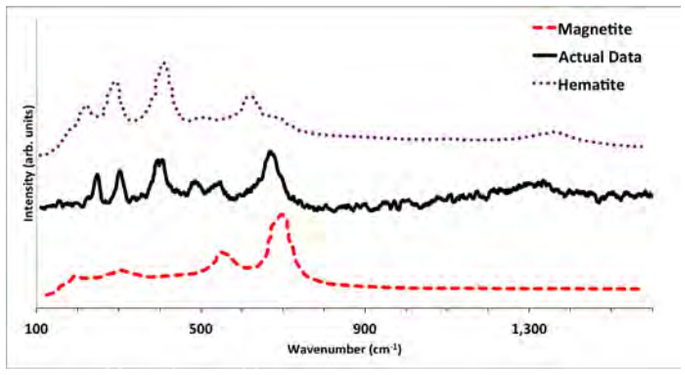

Figure 5: Spectrum obtained using Raman spectroscopy compared to spectra for magnetite and hematite. Peaks from both phases are prominent in the data, indicating both phases are present. Data extracted from Shebanova et al.[3]

Shebanova showed that high laser powers oxidize magnetite samples, producing a hematite phase. Because of this, some peaks characteristic of hematite have been reported in literature for magnetite.[3] This data shows the resulting spectra using the extreme high and low power lasers used by the paper.

The spectrum contains peaks characteristic of both magnetite, at 250 cm^{-1}, 300 cm^{-1}, and 400 cm^{-1}, and hematite, at ~550 cm^{-1} and ~700 cm^{-1}. Because of the possibility of oxidation during laser exposure, it is possible that the hematite is a result of the characterization method, and was not previously present in the sample.

Further phase analysis was performed by powder x-ray diffraction (XRD). The sample yielded the diffraction pattern in Figure 6.

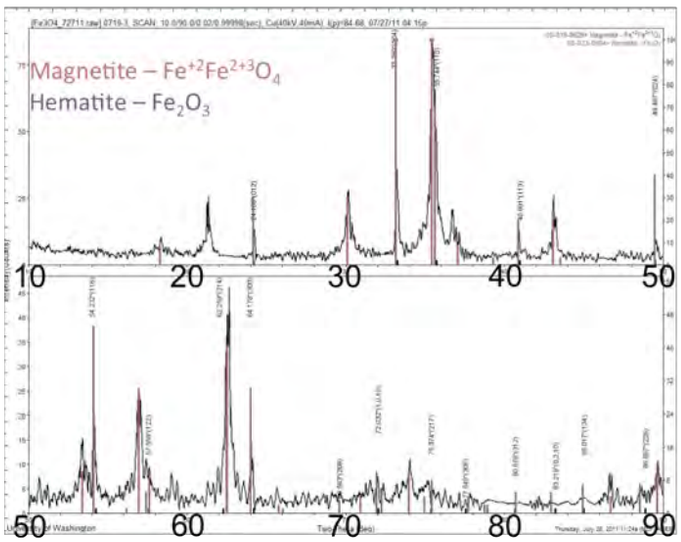

Figure 6: XRD pattern from the sample. Peaks from both magnetite and hematite are present, with few other unidentified contaminant peaks. The intensity of magnetite peaks seems to be relatively higher than that of the hematite.

The standard characteristic patterns for magnetite and hematite are overlaid to identify the origin of individual peaks. There are few unidentified contaminant peaks. The relative intensity of the magnetite peaks seems to be greater than those of the hematite peaks, compared to their corresponding reference patterns. These results seem to support the Raman spectroscopy data indicating the presence of hematite in the as-synthesized material.

Laser Tweezer Trapping Results

As synthesized, the particles visibly respond to a nearby magnetic field both while in solution and when dried. Wires were located using dark field microscopy, but were not convincing in their response to a magnetic field. Bright field microscopy was used in conjunction with a laser tweezer apparatus to locate wires in solution. While they still showed little response to a magnetic field, we were able to trap individual wires, frequently along with other particles in solution. The wire oriented along the axis of the laser, as in Figure 7, and remained in the trap while being moved relative to the other particles in solution.

Figure 7: Nanowire oriented along the axis of the trapping laser, with a profile of laser intensity.

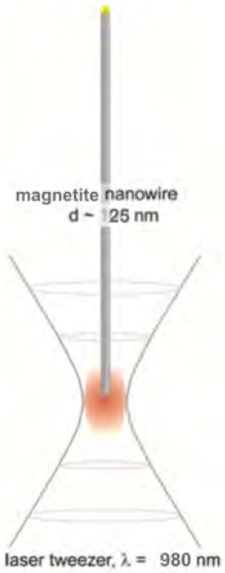

Preliminary Power Spectral Density data was obtained, which can be used to measure the temperature and size of an individual wire with a known geometry. Currently further spatially resolved x-ray diffraction is necessary to positively identify the phase of hydrothermally synthesized nanowires. Nanowire samples are being prepared on silicon nitride membranes for synchrotron XRD measurements at the Lawrence Berkeley National Laboratory's Advanced Light Source, beamline 10.3.2.

Conclusions

SEM and TEM images depict wires that correspond closely to the sizes reported by Harraz et al. SEM shows the presence of other unidentified nanoparticles, while TEM indicated that the wires produced are indeed monocrystalline, as desired. Phase information from Raman spectroscopy and XRD suggests the presence of both magnetite and hematite phases in the produced material. These results indicate that while each individual wire is one phase, other wires and the nanoparticles present could be different phases. It will be important to determine whether the wires are all the same phase, or whether different phases are growing with the nanowire morphology. If hematite wires are forming, it may be of interest to determine whether they show promise in nanomedicine or other research.

Wires appeared to be magnetic as expected, since magnetite and hematite both are naturally magnetic materials. They also appeared to have desirable optoelectronic properties for use with the laser tweezer apparatus, as they trapped readily. Power spectral density information will be useful in investigating potential heating phenomena during optical trapping as well as hydrodynamic nanowire radii during following surface functionalization research.

Surface functionalization is necessary to ensure biocompatibility for future nanomedicine applications. Laser tweezers will measure the hydrodynamic radii of individual functionalized nanowires, measuring the effects of trapping and magnetic fields on the particles, and finding a method for controlling initial interactions between magnetite nanowires and the cancer cells they are designed to label or destroy.

Furthermore, size distribution analysis will be helpful in characterizing the uniformity of wires, and will indicate whether the current morphology is appropriate for future applications.

References

1. "Strongly correlated nanostructures: magnetite", Natelson Group, Rice University. Accessed Aug. 15, 2011. http://www.ruf.rice.edu/~natelson/research.html.
2. Harraz, F. Physica E: Low-dimensional Systems and Nanostructures 2008, 40, 3131–3136.
3. Shebanova, O. N.; Lazor, P. J. Raman Spectrosc. 2003, 34, 845–852.

Acknowledgments

Funds for this research were provided by the Center on Materials and Devices for Information Technology Research (CMDITR), the NSF Science and Technology Center No. DMR 0120967. The authors acknowledge Frances Hocutt for advice and assistance, and April Wilkinson for support.

SAMANTHA WHEELER plans to complete a BS in Materials Science & Engineering at the University of Washington. She is interested in further research in the field of nanomedicine, as well as in the application of Materials Science to the field of archaeology.

Characterization of Chromophores for Non-Linear Optical Devices

WESTON C. WINN, Green River Community College
Andreas F. Tillack, Bruce H. Robinson, University of Washington

Introduction

As telecommunications become more prominent, bandwidth demands continue to increase. Most notably this is due to demand for internet services by corporations, governments and individuals. Such demands include television and movie streaming, as well as multi-directional communication (conference calling, video chat, etc.) over the internet. Furthermore improved latency and increased bandwidth are important in other computing areas such as data transfers between individual components or between cores within a single chip. Optical connections could be used as a solution to reduce latency and increase bandwidth.

Compared to conventional inorganic materials such as $LiNbO_3$, organic non-linear optical materials pose great advantages. Greater speeds (bandwidth in tens of terahertz) are feasible because of their fast response time to applied electric fields. Additionally, organic materials are easier to process than their inorganic equivalents.

For the development of such devices, it is crucial to find materials with a strong electro-optic effect, and a high level of photochemical stability. In order to obtain a strong electro-optic effect, acentric dipolar order is necessary. This order is typically obtained using electric field poling. Preparing a sample for poling entails embedding chromophores into a polymer matrix and heating, then spin-coating the resulting mixture onto a conducting substrate. Upon annealing, the chromophores are able to rotate, and they are subjected to an electric field, which creates a dipole. The sample is then cooled while under the electric field. This fixes the dipolar order in place and the system solidifies into a film. Much of the current research in the Dalton/Reid/Robinson groups is focused on making more efficient films and finding chromophores yielding improved electro-optical activity.

Experimental Methods

DNA Intercalation

Several chromophores were tested for DNA intercalation. The procedure for each chromophore was similar. The chromophore was diluted in solution and placed in a cuvette. A detailed list of the solutions and concentrations used are in Table 1. The absorbance of the solution was measured, and the molarity of the solution was adjusted until the absorbance around π_{max} was close to 1.000 a.u. We then placed a small stir rod into the cuvette and took absorbance measurements using an Ocean Optics UV-Vis spectrometer with the sample holder on a stir plate. The temperature was controlled at 25.0°C. π_{max} and absorbance were recorded. Increments of 30 µL of sodium DNA were added and the cuvette was shaken and left to stir for ~30 s. This process was repeated until absorbance measurements began to level off (usually between 300-600 µL).

Chromophore Films

We began with a control experiment using the chromophore YLD-124 and poly(methyl methacrylate) (PMMA) dissolved in trichloroethylene (TCE), using 2.5% YLD-124, 7.5% PMMA and 90% TCE wt/wt. Film solution was drawn into a syringe and pushed through a 0.2 µm filter onto an indium tin oxide (ITO) glass slide. The slide was then spin coated. The slides were annealed overnight at 65°C. Gold electrodes were evaporated onto the slides (se Figure 1). The film thickness was measured using a Wykoprofilimeter at the Applied Physics Lab. By making a small scratch into the film using a razor blade, the resulting gap was measured for thickness in several places to ensure accuracy.

We attached wires to the gold electrode on the glass side and one to the ITO (see Figure 2). We placed the films into a custom-built in-situ poling apparatus (Teng-Man II) and heated them above their glass transition point (T_g). An electric field is applied above the T_g and the film is then cooled below the T_g and the electro optic coefficient (r_{33}) was measured using software developed by Ben Olbricht and Jeff Hurst of the Dalton Group.

Initial testing of the chromophores DAST and LL-1 in films with cetyltrimethylammonium deoxyribonucleic acid (CTDA-DNA) was done by mixing 1% chromophore, 9% CTAB-DNA and 90% n-Butanol. Film solution was drop casted onto glass slides unfiltered. Slides were observed under 20x magnification microscopy. New DAST films were spin coated onto ITO slides unfiltered using the same procedures as above, but annealed at 50°C.

Coumarin Crosslinking

A coumarin surfactant synthesized by Lewis E. Johnson and Stephanie J. Benight was tested for crosslinking under UV light. The Coumarin surfactant was diluted to $1x10^{-4}$ M and 3 mL was placed into a cuvette. Absorbance was measured on a Varian Cary 5000 UV-Vis spectrometer. Coumarin was then placed under UV light from a 500 W mercury arc lamp for one minute intervals between absorbance measurements for a total combined 5 min of exposure.

Results

DNA Titration

Absorbance measurements of the Na-DNA titration into EtBr are in Figure 1. After adding 600 µL of Na-DNA, π_{max} shifted approximately 40 nm. Identical procedures were used for the LL-1 and Na-DNA

titration and similar results were observed, including a π_{max} shift of approximately 40 nm. Conversely, crystal violet Na-DNA titration showed no shift in π_{max}.

Monte Carlo Fit Analysis

In the Monte Carlo Fit (MCfit) software n represents the ration of base pairs to dye molecules. The best fit of EtBr showed a binding curve with a value of n = 2.

Chromophore Films

Control tests of poling the YLD-124/PMMA in TCE films on ITO showed r_{33} values of 80 ± 5 pm/ V.In figures 3 and 4 are 20x magnification microscope images of the CTAB-DNA with DAST and LL-1 films respectively. We observed that the CTAB-DNA and DAST film was very evenly distributed and with very few inclusions, especially for having no filtration before making the film. However, the DAST and PMMA in acetonitrile film appeared to partially crystallize. The CTAB-DNA and LL-1 film appeared to have cracks throughout the film and the edges were not smooth, however throughout the film there were many smooth areas without inclusions.

Spin coating the CTAB-DNA and DAST films onto ITO slides yielded several smooth films. While the film solution appeared much less viscous, it did attach to the ITO slides through the same spin coating procedure.

Coumarin Crosslinking

Figure 5 shows the absorbance measurements of the coumarin crosslinker. Each line represents a one minute interval of UV exposure. After each exposure, the π_{max} lowered roughly 0.2 A.U. which was one sixth of the original π_{max}.

Discussion

Titration of Na-DNA into EtBr was used as a control test, because EtBr is a known to intercalate with DNA. The π_{max} shift and the MCfit showing n = 2 both confirm this, as n = 2 represents one dye molecule for each two base pairs. Our results were consistent with known behavior of EtBr in DNA, suggesting that our methods were sound.

LL-1 also showed a shift in π_{max}. The MCfit software provided an n value of 0.45189, which is lower than the previous value recorded in our lab. The molarity used was 0.25mM, as opposed to 0.5mM used in previous experiments. One possible explanation is that LL-1 was found to be extremely hygroscopic (microgram changes within a few seconds of removal from vacuum.)

The first films we made were YLD-124 with PMMA dissolved in TCE, and these were used as a control. The r_{33} values obtained in the poling tests coincided with past values obtained in experiments in the Robinson lab. When we drop casted the DAST and CTAB-DNA in n-Butanol and found the slides to be so smooth with such few inclusions, results were very encouraging. While the results of the LL-1 films weren't as clean, the fact that films with clean spots were formed does make future investigation look promising. Another promising result is that the DAST and CTAB-DNA film solution was able to be spin coated onto ITO slides. The strong donor and acceptor in DAST due to it carrying a charge intercalated in DNA could mean a film with a very strong electro-optical effect.

Conclusions

Due to the similarities between DAST and LL-1, much of the work done was with DAST. It was found to make clean films with CTAB-DNA and n-Butanol and current work involves spin coating the DAST film solution onto ITO slides and attaching gold electrodes to the slides as we did with our YLD-124 control tests. Future work will involve testing the r_{33} values of the DAST/CTAB-DNA films. Once DAST is characterized, characterization of LL-1 films will begin. The problems with LL-1's seemingly brittle films will have to be worked out and procedures for spin coating will be developed. Later work will involve using the coumarin surfactant and attempting to make dye/DNA films crosslinked with coumarin for increased structural integrity and hopefully an increased r_{33} value.

References

1. S. J. Benight, D. H. Bale, B. C. Olbricht, L. R. Dalton, Journal of Materials Chemistry, Vol 19, No 40, 7381-7568 (2009).
2. E. M. Heckmann, P. P. Yaney, J. G. Grote, F. K. Hopkins, Proc. of SPIE 593408 (2005).
3. S. R. Trenor, A. R. Shultz, B. J. Love, T. E. Long, Chem. Rev. 104, 3059-3077 (2004).

Acknowledgments

Thank you very much to Lewis Johnson for guidance and support and hours spent on explanation of concepts and helping with the project inside and outside the lab.

Many thanks to all of the members of the Robinson and Dalton groups for their assistance and guidance throughout the project, especially Diana Yugay and Dr. Jinsheng Song for assistance with poling.

Much gratitude for financial assistance from the National Science Foundation STC-MDITR (DMR-0120967), REU Hooked on Photonics (CHE 0851730), the Air Force Office of Scientific Research (FA9550-09-1-0589), Air Force Research Labs (UTC Subcontract 8650-06-D-5401/0005).

A special thanks to Rainbow Photonics (Zürich) for supplying DAST, Luke Latimer for his prior work on LL-1, and Dr. Stephanie Benight for developing the coumarin surfactant.

Finally, thank you to Professor Bruce Robinson, who always kept an open door.

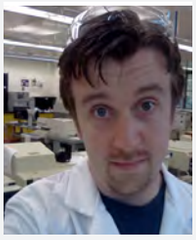

WESTON C. WINN is a student at the University of Washington Bothell in Computing and Software Systems and hopes to pursue a double degree and attend graduate school in chemistry.